


Small-scale temperature fluctuations in atmospheric flows

A doctoral dissertation by

Robert Grosz 

Supervisor: **Prof. Szymon P. Malinowski** 
Institute of Geophysics, Faculty of Physics, University of Warsaw

Co-supervisor: **Prof. Raymond A. Shaw** 
Department of Physics, Michigan Technological University



University of Warsaw

Warsaw 2025

to all my teachers

Acknowledgements

Since this is probably the only section not being evaluated on substance, I'll take the opportunity to get a few honest words in. To keep things balanced, I'll start by thanking myself for my determination and consistency—which, let's be honest, fluctuated more than the quantities discussed in this thesis. Apparently, that's normal. During those moments, I could always count on my supervisors, Szymon and Raymond, who are, without a doubt, my reference points and people I truly respect for what they stand for. The best summary? If I could choose again, I'd pick the same. Sycophancy? No need. But I do genuinely need to thank them.

This work came together with help from many who shared their knowledge and experience. Among them, I fondly remember Marta Waławczyk, Dennis Niedermeier, Jun-Ichi Yano, Stanisław Król, Jakub Nowak, and Maciej Lisicki, along with the research teams at the LACIS-T and the II Chamber facilities. I can't forget Katarzyna Dyl and Dąbrówka Stępniewska, who were my lifelines in the world of bureaucracy.

I also owe thanks to Lidia, who endured all of this with me—and probably saw the light at the end of the tunnel more often than I did. Thanks for being there—it meant more than you know. I'll do my best to pay that debt back.

Lastly, thanks to the many people who, over the years, were there to help without asking for anything in return. Most of them are smart and bold women who taught me a lot. These include my family and friends. To make sure I don't leave anyone out, I dedicate this work to everyone I've learned from along the way.

Statement of originality

The thesis I am submitting was composed and written by myself. The work presented herein is my own, except where explicitly stated otherwise. I have clearly indicated all quoted material from other sources, including diagrams, charts, and graphs. Additionally, all paraphrased material is properly referenced. This work has not been submitted for any other degree or professional qualification.

The data analyzed in this thesis was collected from three different experiments: one field campaign, EUREC⁴A, and two laboratory experiments conducted in the LACIS-T wind tunnel (Leibniz Institute for Tropospheric Research, Germany) and the II Chamber (Michigan Technological University, USA).

The multidisciplinary EUREC⁴A campaign was carried out by a team of scientists, whose names are listed among the co-authors of the overview paper of [Stevens et al. \(2020\)](#). The data used in this study originates from airborne operations performed by the Twin Otter aircraft (operated by the British Antarctic Survey), which carried out flights equipped with the UltraFast Thermometers (UFTs) over the Atlantic Ocean. I was not personally involved in the data collection during this campaign; this task was performed by S. P. Malinowski, M. Posyniak and W. Kumala, along with the aircraft crew. My role focused on high-resolution data processing, in which I received partial support from S. Król, who was responsible for temperature time series pre-processing and cloud identification. The analysis and interpretation of this dataset are my own work, conducted under the guidance and advice of S. P. Malinowski, M. Lisicki, and S. Król. To date, the results have not been published.

The experiment in the LACIS-T wind tunnel was designed and conducted by J. L. Nowak, S. P. Malinowski, W. Kumala, and D. Niedermeier as part of the EUROCHAMP-2020 initiative. The subsequent analysis and interpretation of the collected UFT temperature time series are my own work, carried out with consultations from S. P. Malinowski, D. Niedermeier, and S. Schmalfuß. I also acknowledge that the initial data pre-processing was performed by J. L. Nowak. The results from this experiment have not been published.

The analyses from the second laboratory experiment, conducted in the II Cham-

ber, are presented in the following preprint: Grosz, R., Chandrakar, K. K., Shaw, R. A., Anderson, J. C., Cantrell, W., and Malinowski, S. P.: High-resolution temperature profiling in the II Chamber: variability of statistical properties of temperature fluctuations (Grosz et al., 2024). I played a major role in this research, as reflected in the author contribution statement of the manuscript:

„RG, RAS, JCA, WC, and SPM designed the study. RG and JCA adapted the UFT instrument and the II Chamber facility for the measurements. RG and JCA performed the UFT measurements. KKC performed DNS. RG processed and analyzed the collected data with advice from RAS, SPM, and KKC. RG wrote the manuscript with contributions from RAS, SPM, and KKC (who wrote Subsection 2.2).”

At the time of this thesis submission, the manuscript has been accepted and for the reader’s convenience this version is provided in Appendix C.

In this thesis, the material presented in the manuscript has been expanded with additional details. Since I am the primary author of the manuscript, I do not quote or paraphrase the paper directly but instead provide a concise summary of the most significant results in Sec. 3.2, along with appropriate references to the text.

Abstract

Atmospheric flows represent a wide range of fluid motions, spanning various spatial and temporal scales, driven by diverse forcing mechanisms, thermodynamic and microphysical changes, and interactions with other phenomena. These overlapping processes give rise to complex dynamics that manifest differently at different scales. To better understand these processes, two main experimental approaches are typically employed. One approach involves isolating specific phenomena in laboratory settings under controlled conditions, allowing for a more selective analysis of flow properties. The alternative relies on deploying multiple instruments in field measurements to capture a broader spectrum of atmospheric variability. This study investigates small-scale temperature fluctuations across the full range of scales in both laboratory facilities and real atmosphere conditions during airborne measurements. The data were collected using miniaturized UltraFast Thermometers, which enable undisturbed, high-resolution (2 kHz or 1.5 kHz, depending on the experiment) scalar field measurements.

The first part of this study focuses on the LACIS-T wind tunnel (TROPOS, Germany), one of the newest operational aerosol–cloud research chambers. As a closed-loop wind tunnel, it enables turbulent, isobaric mixing of two humidified, aerosol-free air streams under independently controlled and repeatable thermodynamic conditions. This work presents results from two dry and clean experiments conducted with temperature differences of 25 K and 16 K between the air streams. These experiments revealed intensified scalar field variability in the central region, recognized thermal inhomogeneities, and examined influence of outside conditions on experiments. Moreover, the study identified four distinct power-law spectral regimes, and provided a comparative analysis between scalar and energy-based approaches in the dissipative range.

The second facility examined was the II Chamber, a convection-cloud chamber operating on the principle of induced Rayleigh–Bénard convection, where air is heated from below and cooled from above. This study analyzed temperature fluctuations under three different temperature differences between the bottom and top plates (10 K, 15 K, and 20 K), corresponding to a Rayleigh number of appro-

ximately 10^9 and a Prandtl number of about 0.7. The results revealed significant variability in both the standard deviation and skewness of temperature fluctuations near the top and bottom plates, as well as in the central region—variations linked to local thermal plume dynamics. Additionally, three spectral regimes were identified, and a power-law relationship was established between the periodicity of the large-scale circulation and the temperature difference. Notably, the experimental results aligned well with Direct Numerical Simulations conducted under similar thermodynamic conditions.

Finally, this study investigated temperature dissipation during airborne operations in the EUREC⁴A campaign. The collected temperature time series were categorized into three horizontal segments: clouds (liquid water content $\geq 10^{-3} \text{ g m}^{-3}$), boundary layer (pressure $\geq 1010 \text{ hPa}$), and free atmosphere (pressure $< 1010 \text{ hPa}$). These classifications enabled statistical analyses of a normalized temperature dissipation rate. The histograms of this quantity exhibited a robust power-law distribution, except for elongated tails at both high and low values of dissipation rates across all segment types. Laboratory datasets displayed similar behavior, albeit with some limitations. Furthermore, the study demonstrated that the power-law coefficients are not interdependent and can be described by a logarithmic relationship—suggesting that this may be a more universal feature of atmospheric flows.

Streszczenie

Przepływy atmosferyczne obejmują szeroką gamę ruchów płynów, występujących w różnych skalach czasowych i przestrzennych. Są one napędzane przez różnorodne mechanizmy wymuszające, przemiany termodynamiczne i mikrofizyczne oraz wzajemne oddziaływania z innymi procesami. Nakładanie się tych zjawisk prowadzi do skomplikowanej dynamiki, która objawia się różnie w zależności od skali. W badaniach eksperymentalnych stosuje się dwa główne podejścia. Jednym z nich jest izolowanie wybranych procesów w warunkach laboratoryjnych, co pozwala na dokładniejszą analizę właściwości przepływów. Alternatywną metodą są pomiary terenowe z wykorzystaniem wielu instrumentów, które pozwalają uchwycić pełniejsze spektrum zmienności atmosferycznej. W niniejszej pracy badano drobnoskalowe fluktuacje temperatury, obejmując zarówno eksperymenty laboratoryjne, jak i pomiary wykonywane w rzeczywistych warunkach atmosferycznych na pokładzie samolotu. Dane zostały zebrane za pomocą miniaturowych termometrów UltraFast, umożliwiających niezakłócone i wysokorozdzielcze (2 kHz lub 1.5 kHz, w zależności od eksperymentu) pomiary pola skalarne.

Pierwsza część pracy koncentruje się na tunelu aerodynamicznym LACIS-T (TROPOS, Niemcy), jednym z najnowocześniejszych obecnie działających obiektów badawczych przeznaczonych do badań aerozoli i chmur. Tunel ten ma budowę zamkniętą oraz umożliwia turbulentne, izobaryczne mieszanie dwóch nawilżonych, wolnych od aerozoli strumieni powietrza w ściśle kontrolowanych i powtarzalnych warunkach termodynamicznych. W pracy przedstawiono wyniki dwóch eksperymentów przeprowadzonych w warunkach suchych i czystych, przy różnicy temperatur między strumieniami odpowiednio 25 K i 16 K. Eksperymenty wykazały wzmogoną zmienność pola skalarne w centralnym obszarze tunelu, pozwoliły na identyfikację niehomogeniczności termicznych oraz analizę wpływu warunków zewnętrznych na przebieg eksperymentów. Ponadto zidentyfikowano cztery wyraźne zakresy spektralne o potęgowych zależnościach oraz porównano podejścia analityczne oparte na polu skalarne i energii w reżimie dyssypacyjnym.

Drugim analizowanym obiektem było II Chamber, czyli komora konwekcyjno-chmurowa działająca na zasadzie wymuszonej konwekcji Rayleigha-Bénarda, w któ-

rej powietrze jest podgrzewane od dołu i chłodzone od góry. Badania dotyczyły fluktuacji temperatury dla trzech różnych różnic temperatur pomiędzy dolną i górną płytą (10 K, 15 K i 20 K), co odpowiada liczbie Rayleigha rzędu 10^9 i liczbie Prandtla około 0.7. Analiza wykazała istotne zmiany zarówno odchylenia standardowego, jak i skośności rozkładu temperatury w pobliżu płyt oraz w centralnej części komory – zmienność ta została powiązana z lokalną dynamiką strug termicznych. Ponadto zidentyfikowano trzy zakresy spektralne oraz wykazano zależność potęgową między okresem cyrkulacji wielkoskalowej a różnicą temperatur. Co istotne, wyniki eksperymentalne dobrze pokrywały się z symulacjami Direct Numerical Simulations przeprowadzonymi w zbliżonych warunkach termodynamicznych.

Ostatnia część pracy dotyczyła problemu dyssypacji temperatury podczas lotów badawczych w ramach kampanii EUREC⁴A. Zebrane serie czasowe temperatury podzielono na trzy grupy poziomych segmentów: chmury (zawartość ciekłej wody $\geq 10^{-3} \text{ g m}^{-3}$), warstwę graniczną (ciśnienie $\geq 1010 \text{ hPa}$) oraz swobodną atmosferę (ciśnienie $< 1010 \text{ hPa}$). Klasyfikacja ta umożliwiła przeprowadzenie analiz statystycznych dla wprowadzonej znormalizowanego tempa dyssypacji temperatury. Histogramy tej wielkości wykazały wyraźną zależność potęgową w rozkładach, z wyjątkiem wydłużonych ogonów dla bardzo wysokich oraz bardzo niskich wartości dyssypacji we wszystkich typach segmentów. Dane laboratoryjne wykazały podobne zależności, choć z pewnymi ograniczeniami. Ponadto analiza wykazała, że współczynniki potęgowe są ze sobą powiązane i można je opisać zależnością logarytmiczną, co sugeruje, że może to być bardziej uniwersalna cecha przepływów atmosferycznych.

Contents

1	Introduction	1
1.1	Convective processes	2
1.1.1	Range of scales	3
1.1.2	Climate change	4
1.1.3	Clouds	5
1.1.4	Rayleigh-Bénard convection	7
1.2	Scalar turbulence	9
1.2.1	Kolmogorov-Obukhov-Corrsin picture	10
1.2.2	Scalar spectra regimes	13
1.2.3	Cascade picture	15
1.2.4	Active scalars	18
1.3	Temperature dissipation rate	19
1.4	Scope of work	21
2	Measurements	23
2.1	UltraFast Thermometers	23
2.2	LACIS-T	25
2.2.1	Facility	25
2.2.2	Experimental strategy & data	26
2.3	Π Chamber	28
2.3.1	Facility	28
2.3.2	Experimental strategy & data	29
2.4	EUREC ⁴ A	30
2.4.1	Campaign overview	30
2.4.2	Experimental strategy & data	32
2.5	General data methodology	35
3	Laboratory experiments	36
3.1	LACIS-T	36
3.1.1	Basic thermal characterization	36

3.1.2	Spectral analysis	39
3.2	Π Chamber	49
4	Field experiments	53
4.1	Cloud boundaries	53
4.2	Temperature dissipation in atmosphere	55
4.3	Temperature dissipation in laboratory	63
5	Summary and discussion	67
A	Temperature time series from EUREC⁴A	74
B	Additional χ statistics from EUREC⁴A	78
C	Accepted manuscript version	80
C.1	Introduction	81
C.2	Methods	85
C.2.1	Setup and experimental strategy	85
C.2.2	DNS methodology	88
C.3	Results	90
C.3.1	Determination of basic characteristics of temperature profile	90
C.3.2	Power Spectral Densities	95
C.3.3	DNS versus experimental data	101
C.4	Summary	102
C.5	Quicklooks of temperature fluctuations	105
C.6	Non-dimensional representation of standard deviations	108
C.7	Power Spectral Density in wavenumber space	109
C.8	Standard deviation scaling	111
	List of Symbols	113
	Bibliography	118

Introduction

Some see turbulence as chaos—an unpredictable mess of swirls and eddies. But whether in Van Gogh’s post-impressionist brushstrokes or in fluctuating data from research facilities, hidden patterns emerge—if one knows where to look. And while these small-scale structures may not transform into large atmospheric patterns as effortlessly as Tom Waits turns emotions into a forecast in *Emotional Weather Report*, they still deserve a *voice* beyond the noise.



Figure 1.1: *The Starry Night* by Vincent van Gogh, painted in June 1889. The original painting is housed at the Museum of Modern Art, New York City. Image by Giorgio Morara, Adobe Stock (ID: 421043104), used under standard license.

The painting above is here for a reason—it is yet another example of where art meets science. Van Gogh captured a swirling sky just before sunrise, as seen from his room in a mental asylum. In a recent study, [Ma et al. \(2024\)](#) analyzed the

luminance of the paint, identifying eddies and whirls that remarkably resemble real turbulent flows. Their findings confirmed just how perceptive Van Gogh was—his brushstrokes unintentionally mirrored the structure of atmospheric turbulence. Fourier power spectrum analysis revealed a Kolmogorov $-5/3$ scaling, followed by a -1 Batchelor-type range under a high Schmidt number regime, a consequence of both his paint composition and painting technique.

This study, in contrast, takes a closer look at small-scale fluctuations, focusing on the scalar field of temperature. It presents previously unreported results from both laboratory and field experiments. To highlight the significance of this topic, the following sections systematically introduce key aspects of atmospheric physics, guiding the reader down to the finest scales of turbulent flows.

1.1 Convective processes

The phenomenon of convection encompasses an extraordinarily broad spectrum of problems in atmospheric physics, driving processes across a wide range of scales—from microscale turbulence and local heat transfers to large cloud systems that form integral parts of global circulation. Despite significant advances, this jigsaw puzzle remains incomplete. Roots of the early studies are stretching back to Aristotle and Seneca the Younger, who sought to link heat, air movement, and cloud formation to explain weather and atmospheric dynamics. It was Descartes though, in his essay *Meteorology*, who introduced more advanced concepts and laid the groundwork for modern meteorology by applying early scientific reasoning. (Descartes, 1637; Lafleur, 1950). Over the years, different physics fields like thermodynamics, fluid dynamics, and statistical mechanics developed more qualitative frameworks to describe complex processes that compromise convection. At its simplest, an atmospheric model of convection involves fluid being heated from the surface, which absorbs solar radiation. This isobaric heating reduces the density of the affected volume, referred to as an air parcel. Buoyant forces acting on the parcel initiate then vertical motion, lifting it to higher altitudes. Simultaneously, the principle of mass conservation results in the sinking of nearby air. This exchange creates a continuous cycle that drives weather and climate systems. As the parcel rises, it expands adiabatically and cools, potentially reaching conditions favorable for phase change. Water vapor may then transform into cloud droplets or ice crystals by condensing onto cloud condensation nuclei (CCNs) or ice-nucleating particles (INPs), respectively. Even this crude description rises more questions than answers, opening a vast array of scientific challenges. In the following paragraphs, the current state of knowledge on convection will be

outlined along with the most active research areas.

1.1.1 Range of scales

The annual mean cloud cover over land and oceans is approximately 54% and 68%, respectively, underscoring the critical role of large-scale circulation processes in redistributing water within the Earth’s system (Siebesma et al., 2020). Oceans and the atmosphere interact intensively, promoting convective motions in the lower troposphere and creating conditions favorable for shallow convection (see Fig. 1.2). This phenomenon is particularly characteristic of trade wind regions with weakly unstable atmospheric conditions. The exchange of water and energy between these two mediums results in various mesoscale cloud patterns (Denby, 2020; Stevens et al., 2020; Bony et al., 2020a; Schulz et al., 2021; Janssens et al., 2021) and mesoscale circulations (George et al., 2023).



Figure 1.2: Shallow clouds captured by B. Stevens during the first NARVAL expedition (Stevens et al., 2019). Photo posted on the EUREC⁴A campaign website (access: Feb. 28, 2025).

Shallow convection sets the stage for deep convection under stronger sensible and latent heat fluxes from the surface and weaker atmospheric stability. It is a dominant phenomenon in the tropics, marked by vigorous vertical motions that produce substantial precipitation and drive global-scale circulation. Deep convection is also associated with highly complex processes, such as the spontaneous emergence of self-organized structures, which can expand to synoptic scales without any external perturbation (Haerter and Muller, 2023). The potential for deep convection is primarily governed by sea surface temperature and wind shear magnitude. These factors, along with spatial convection variability and lower-

tropospheric instability, significantly influence the radiation budget (Bony et al., 2020b; Hsiao et al., 2024). When precipitation occurs, cold pools form, further enhanced by air mass circulation. The associated gust fronts and temperature gradients often trigger new convective cells (Chakraborty et al., 2023). Despite advancements, achieving a comprehensive understanding of convection organization remains challenging due to methodological discrepancies, which complicate comparisons across different studies (Janssens et al., 2021; Biagioli and Tompkins, 2023). A broader discussion of atmospheric convection organization can be found in Emanuel (1994) and Trapp (2013), while a historical perspective is provided by Houze (2018).

Past years were very rich in measurement campaigns that targeted convective processes across diverse environments, ranging from the tropical Atlantic (BOMEX (Holland and Rasmusson, 1973), GATE (Greenfield and Fein, 1979), RICO (Rauber et al., 2007), EUREC⁴A (Stevens et al., 2021), along with its U.S. counterpart ATOMIC (Quinn et al., 2021)), low-mountain regions in Europe (COPS (Wulfmeyer et al., 2011)), midlatitude continental Oklahoma (MC3E (Jensen et al., 2016)), to the Indian Ocean (CINDY /DYNAMO (Zhang and Yoneyama, 2016)). Among these, the EUREC⁴A experiment introduced innovative approaches, particularly in quantifying convective strength, vertical motions, and governing cloud formation processes across a wide range of scales. Additional details on this campaign are provided in Subsec. 2.4.1, with small-scale temperature analyses from aircraft operations presented in Chapter 4. One of the campaign objectives was to evaluate the extent to which changing environmental conditions could influence low-cloud feedback in a warming climate. As indicated in Vogel et al. (2022), trade cumulus clouds exhibit weaker feedback than many models predict, primarily due to inadequate representation of mesoscale circulation variability.

1.1.2 Climate change

Predictions regarding the effects of a warming climate on atmospheric phenomena and their associated feedback mechanisms remain highly problematic. Much of the difficulty arises from the complexity of properly parameterizing convection (Kendon et al., 2021; Lin et al., 2022). Recent studies indicate that mesoscale convective systems are likely to become both more frequent and intense in a changing climate (Aumann et al., 2018; Schumacher and Rasmussen, 2020). On the other hand, observations suggest that the most intense convective cores are predominantly localized over land, including at higher latitudes where mean surface tem-

peratures have increased most significantly (Houze Jr et al., 2019; Zipser and Liu, 2021). Trade cumulus clouds’ cooling effects are projected to diminish as greenhouse gas concentrations rise, with the magnitude of this reduction depending on the clouds’ organizational state (Kazil et al., 2024). This reduction in cooling is expected to exacerbate energy and moisture accumulation, promoting the formation of long-lived, clustered mesoscale convective systems associated with extreme tropical precipitation (Roca and Fiolleau, 2020; Angulo-Umana and Kim, 2023; Roca et al., 2024). By the end of the century, global precipitation extremes are projected to increase by $32 \pm 8\%$ under a medium-emissions pathway and by $55 \pm 13\%$ under a high-emissions pathway (Thackeray et al., 2022). Earth’s climate modeling is highly challenging due to the vast number of variables that must be reliably predicted in models. Pioneers in this field, Syukuro Manabe and Klaus Hasselmann, were awarded the Nobel Prize in Physics in 2021 „for groundbreaking contributions to our understanding of complex physical systems” (see the [press release](#), access: Feb. 28, 2025).

It is widely recognized within the atmospheric science community that cloud formation and development processes remain among the largest sources of uncertainty in climate projections (IPCC, 2021). Presently, the reduction of low clouds in northern mid-latitudes and the tropics is believed to be a primary driver of the record-low planetary albedo, which may have significantly contributed to the recent global mean temperature records (Goessling et al., 2024). Current estimates of future cloud responses place climate sensitivity between 2–3 K (Ceppi and Nowack, 2021; Myers et al., 2021). However, these estimates often do not account for potential tipping points within the climate system or disruptions in the carbon cycle (Sherwood and Forest, 2024). Alternative perspectives emphasize the role of anthropogenic aerosols, which have gained attention due to their involvement in new particle formation (Zaveri et al., 2022; Zhao et al., 2024). Such aerosol effects could further disrupt the hydrological cycle, amplifying the challenges of climate prediction and adaptation (Allan et al., 2020).

1.1.3 Clouds

As discussed in Sec. 1.1.1, mesoscale convection processes play a dominant role in shaping regional weather and climate systems, which are undergoing significant changes due to anthropogenic influences. Under favorable conditions, these processes result in cloud formation, comprising microscale droplets embedded in rapidly evolving fields of velocity, humidity, temperature, and aerosol concentration. As noted by Bodenschatz et al. (2010), this *mixture* is further influenced

by complex turbulent flows, which drive mixing, entrainment, and stirring mechanisms (see Sec. 1.2). It might be more precise to describe these dynamics as local turbulence, as field experiments have shown substantial spatial variability in temperature fields within different cloud regions (see Fig. 1.3) (Jen-La Plante et al., 2016; Ma et al., 2017; Nowak et al., 2021; Siebert et al., 2021). Such variability leads to scalar fluctuations that drive supersaturation changes on small spatial scales, which depend on the ratio of phase relaxation time to turbulent mixing time (Siebert and Shaw, 2017). Laboratory experiments have further demonstrated that supersaturation fluctuations contribute to aerosol removal (Chandrakar et al., 2017) and are not mitigated by droplet growth or evaporation (Anderson et al., 2024). Turbulence also impacts aerosol activation rates, thereby influencing cloud formation processes. Recent laboratory studies have combined relative humidity changes with three cloud formation regimes characterized by different mean saturation ratios, revealing scenarios for droplet activation and deactivation (Prabhakaran et al., 2020b). Subsequent research concluded that supersaturation fluctuations are critical for the activation and initial growth of small droplets (Prabhakaran et al., 2022). Additionally, once activated, particles persist in subsaturated regions, leading to increased overall droplet concentrations (Anderson et al., 2023).

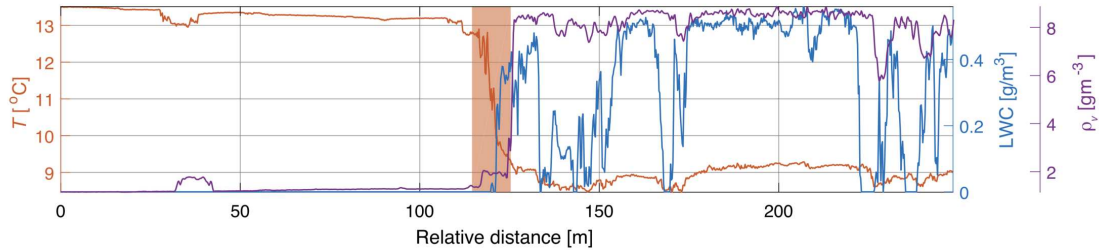


Figure 1.3: Stratocumulus top penetration during ACORES campaign. The aircraft gradually descended intruding the thin inversion layer exhibiting sharp temperature gradient of about 4 K over approximately 0.8 m of vertical path. Picture from Siebert et al. (2021).

The primary method for identifying cloud presence and its boundaries relies on liquid water content (LWC) data, a classical approach. However, more comprehensive studies on cloud shells suggest that, instead of water content, dynamic boundaries should be considered—where thermodynamic and microphysical properties change gradually. Key processes include entrainment and detrainment, which control evaporative cooling in the cloud margin ($\sim 10\%$ of the cloud diameter) and the negatively buoyancy forces driving subsidence of air masses around a cloud forming a subsiding shell at cloud boundary (Wang et al., 2009; Wang

and Geerts, 2010; Katzwinkel et al., 2014). This region is also characterized by intensified turbulent motions (Siebert et al., 2006b).

Due to the inherent limitations of small-scale experiments, particularly under real atmospheric conditions, numerical simulations have become indispensable for gaining deeper insights into the complexity of turbulence processes. Active areas of research include the broadening of droplet size distributions caused by turbulence fluctuations during entrainment and mixing (Li et al. (2019); Chandrakar et al. (2021); Grabowski et al. (2022); Grabowski (2025) and references therein) and the effects of turbulence on droplet collision-coalescence mechanisms (Chandrakar et al. (2024b) and references therein). Li et al. (2019) demonstrated also that the magnitude of turbulence-induced fluctuations increases with the Reynolds number (see Eq. 1.3). Other studies have investigated the locality of supersaturation fluctuations, particularly at warm cloud-top mixing regions (Fossà et al., 2022), and within the framework of the RBC problem (Chandrakar et al., 2020a,b, 2022; Salesky et al., 2024). These efforts collectively contribute to a better understanding of the multiscale interactions governing cloud microphysics and atmospheric turbulence.

The previous discussion focused on convection processes where supersaturation fluctuations lead to condensation which is a typical mechanism for forming convective clouds. However, convection does not always result in a phase change; it is generally responsible for the intense mixing of air masses, which can subsequently lead to the development of convection cells and complex particle transport. This is why laboratory-simulated convection provides a controllable framework for investigating this physical phenomenon.

1.1.4 Rayleigh-Bénard convection

Both measurements or simulations within the framework of large-scale convection presents significant operational and computational challenges. Accurate descriptions of convective phenomena require data on e.g. sea or ground surface temperatures, humidity, temperature fluxes, atmospheric stability which often require the deployment of multiple measurement platforms. While simulations may initially appear simpler, they require parameterization of complex physical processes or solving governing equations under various assumptions.

As mentioned earlier, the crude model of convection is conceptually straightforward. This simplicity has allowed laboratory environments to successfully simulate convective phenomena, where input parameters can be controlled, and experiments repeated. Laboratory setups retain sufficient complexity to encompass

the key features of convective turbulence. Natural convection systems are typically categorized into three main types: horizontal convection, vertical convection (Fan et al. (2021) and references therein), and Rayleigh-Bénard convection (RBC) (the phenomenon was first described by Henri Bénard and Lord Rayleigh (Bénard, 1900; Rayleigh, 1916), while a comprehensive overview of the current state of the art can be found in Fan et al. (2021); Lohse and Shishkina (2024) and the references therein). Among these, RBC has been the most extensively studied, given its relevance to geophysical and astrophysical systems (Busse, 2006) and industrial applications. RBC involves a fluid confined between two isothermal horizontal surfaces maintained at different temperatures. When the Rayleigh number (Ra , defined in Eq. 1.3) exceeds a critical threshold, convective motion begins (Jeffreys, 1928; Reid and Harris, 1958). As Ra increases further, both flow dynamics and heat transport become increasingly influenced by the Prandtl number (Pr , also defined in Eq. 1.3). In RBC, the flow becomes more turbulent with rising Ra , driven by the temperature difference between the horizontal surfaces and the height H of the system. Another key control parameter is the aspect ratio $\Gamma = D/H$, where D represents the diameter (for cylindrical setups) or the length of the longest side (for rectangular geometries). This parameter governs the number of convective rolls and the properties of the large-scale circulation (LSC). Optimal values of Γ under the Oberbeck-Boussinesq approximation are discussed in Shishkina (2021). Further insights into recent RBC studies can be found in Grosz et al. (2024) and in Sec. 1.3, where thermal dissipation is explored, as well as in Subsec. 1.2.4, which focuses on active scalar analysis.

Experimental RBC studies often utilize relatively small containers for ease of adjustment and conversion. However, larger facilities provide unique opportunities for studying atmospheric phenomena across a wide range of conditions and scales, enabling the simulation of such processes for durations ranging from minutes to days. Notable examples include the High Pressure Convection Facility (HPCF) at the Max Planck Institute for Dynamics and Self-Organization in Göttingen (Ahlers et al., 2009), the Scaled Convective Airflow Laboratory Experiment (SCALEX) at Technische Universität Ilmenau (Sharifi Ghazijahani et al., 2023), and the II Chamber at Michigan Technological University (Chang et al. (2016)). The II Chamber, in particular, is discussed in detail in Subsec. 2.3.1, where an overview of its measurements is also provided.

While this work focuses primarily on classical RBC, other important variations of the problem exist. For example, rotating RBC is used to study the influence of the Coriolis force (Ecke and Shishkina (2023) and references therein), while other extensions include magnetohydrodynamics (Aurnou and Olson, 2001; Burr

and Müller, 2001; Burr and Müller, 2002; Akhmedagaev et al., 2020; Yang et al., 2021), the effects of thermal radiation (Ebert et al. (2008); Kogawa et al. (2019)), double-diffusive flows (Li et al., 2016; Zhang et al., 2017a), electric field influences (Yoshikawa et al., 2013; Lu et al., 2021; Peng et al., 2024), and porous media convection (Liu et al., 2020; Zang et al., 2023).

Advancing our understanding of turbulence and scalar fluctuations in convection is crucial for addressing gaps in our knowledge of atmospheric processes in the lower troposphere, particularly regarding cloud development. While experimental and numerical studies have provided valuable insights, they have also highlighted new challenges. The next section delves into theoretical details of scalar dynamics, focusing on spectral regimes and energy cascades.

1.2 Scalar turbulence

Turbulence is regarded as field of unsolved problems with pivotal applications in domains of engineering, geophysics, astrophysics, and cosmology. The despair desire to uncover its complexity has led many renowned scientists to eventually abandon the field, often with a sense of *failure*. Even after almost hundred years of advanced research there is still no comprehensive theory that may be regarded as universal across specific cases, scales or regimes. The main challenge lie in the strong non-linearity of the fundamental Navier–Stokes equations (see Eq. 1.1) coupled with the non-equilibrium properties of statistical profile of turbulent flows. Turbulence impenetrability ultimately reveals the weaknesses in prevailing ideas and highlights conceptual limitations.

An extended history of various turbulence theories developments can be found in e.g. Monin and Yaglom (1975), Pope (2000), Davidson (2015), Zhou (2021), and Benzi and Toschi (2023). Davidson et al. (2011) provides more biographical perspective and insight into the personal backgrounds of those involved in the field. This section is dedicated to outline the key steps in progress that reshaped our understanding of how scalar quantities, such as temperature, substance concentration, or humidity, act in turbulent flows. Unlike velocity fields, scalars represent properties that are not vectors, but still interact with the turbulent motion of the fluid. Over time, scientists began to distinguish between passive and active scalars, marking a significant shift in approach. More comprehensive passive scalar problem reviews can be found in Warhaft (2000), Shraiman and Siggia (2000), Falkovich and Sreenivasan (2006), Gotoh and Yeung (2012) and Sreenivasan (2019) whereas for active scalars the recommended overview papers are Celani et al. (2002), Celani et al. (2004), and Alexakis and Biferale (2018).

1.2.1 Kolmogorov-Obukhov-Corrsin picture

For the following considerations the generic form of governing equations is listed below including momentum, advection/diffusion, and continuity equations for incompressible flows:

$$\partial_t \mathbf{U} + (\mathbf{U} \cdot \nabla) \mathbf{U} = -\frac{1}{\rho} \nabla p + \mathbf{f} + \nu \nabla^2 \mathbf{U}, \quad (1.1)$$

$$\partial_t \theta + (\mathbf{U} \cdot \nabla) \theta = \xi \nabla^2 \theta, \quad (1.2)$$

$$\nabla \cdot \mathbf{U} = 0.$$

They illustrate flow $\mathbf{U} = (u, v, w)$ variability under the influence of local pressure p , kinematic viscosity ν , and embedded in the medium of density ρ . The abstract forcing \mathbf{f} may denote e.g. buoyancy input $\rho\psi(T - T_0)g$ with thermal expansion coefficient ψ , gravitational acceleration g , as well as local and ambient temperatures of fluid, T and T_0 respectively. The subscript t stands for partial time derivative here. Equation 1.2 is valid for scalar fields θ like temperature or mass concentration with ξ representing e.g. thermal (κ) or molecular (α) diffusivity respectively. The formula has a number of limitation (elaborated more in [Landau and Lifshitz \(1987\)](#)) but gives a good model for multiple purposes in e.g. engineering and geophysics. The turbulent nature of \mathbf{U} converts Eq. 1.2 into a stochastic differential equations with only statistical averages of quantities. Based on the given formulas one can derive dimensionless numbers which describe different properties of a flow. Four that will be most relevant in this work are given below

$$\text{Re} = \frac{uL}{\nu}, \quad \text{Ra} = \frac{g\Delta TH^3}{T_0\nu\kappa}, \quad \text{Sc} = \frac{\nu}{\alpha}, \quad \text{Pr} = \frac{\nu}{\kappa}. \quad (1.3)$$

The Reynolds number (Re) measures the ratio between inertial and viscous forces (here L denotes characteristic length), the Rayleigh number (Ra), associated with natural convection driven by temperature difference ΔT , the Schmidt number (Sc) characterizes fluid flows with simultaneous momentum and mass diffusion processes, and its analogue for heat transfer is the Prandtl number (Pr).

The beginnings of modern turbulence theories follow the crude concepts of eddy viscosity ([Boussinesq, 1877](#)) and mixing length theory ([Prandtl, 1925](#)), which laid the foundation for understanding how flow properties (including scalars) are mixed and transported. In meantime, L. F. Richardson introduced the notion of the energy cascade ([Richardson, 1922](#)) and the diffusion law in turbulent flows, leading to the well-known four-third law ([Richardson and Walker, 1926](#)). G. I.

Taylor's statistical description of turbulence established the relationship between velocity and scalar fields, introducing the concept of isotropic turbulence (later developed by [von Kármán and Howarth \(1938\)](#)) and microscale (Taylor microscale)

$$\lambda = \sqrt{\frac{15\nu}{\langle \epsilon \rangle}} u'_{\text{rms}},$$

which characterize the viscosity influenced flow regime ([Taylor, 1935](#)). In above angular brackets introduce the average of ϵ which is turbulent kinetic energy dissipation per unit mass and time across scales, and u'_{rms} is the root mean square of velocity fluctuation i.e. $u'_{\text{rms}} = \frac{1}{\sqrt{3}} \sqrt{(u)^2 + (v)^2 + (w)^2}$. Taylor also proposed the frozen turbulence hypothesis ([Taylor, 1938](#)), assuming that turbulent eddies and flow properties remain "frozen" as they are advected by an incompressible fluid while undergoing some small amount of molecular diffusion. This hypothesis can be considered as an early indication of the concept of passive scalars – quantities that have no dynamic effect on the fluid motion itself.

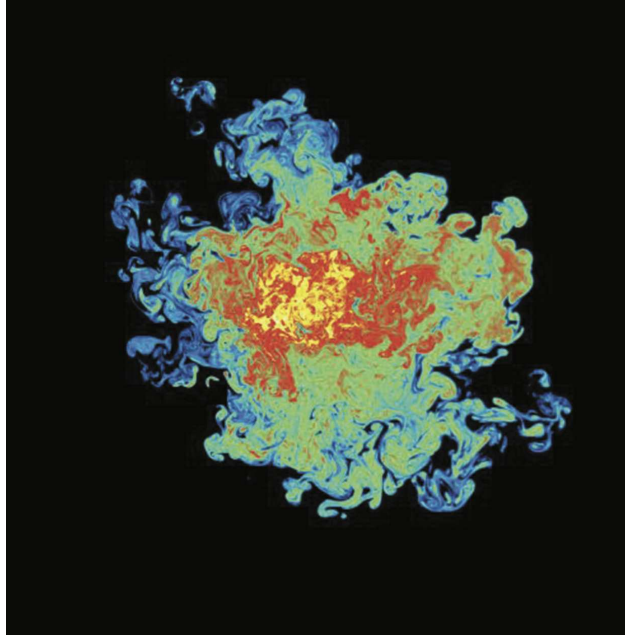


Figure 1.4: Cross section through a turbulent jet carrying a passive scalar (concentration changes color marked). Figure from [Davidson \(2015\)](#).

A cornerstone in turbulence research was Kolmogorov's K41 theory ([Kolmogorov, 1941a,b,c](#)), which unified previous theories and provided postulates on the structure of turbulence in fully developed flows. The notion focused on velocity field and expanded the concept of inertial range, a scale regime between large scales, characterized by integral scale l where energy is injected, and small scales,

where viscosity dominates and dissipates energy as heat at the Kolmogorov length scale

$$\eta = \left(\frac{\nu^3}{\langle \epsilon \rangle} \right)^{1/4}.$$

The above considerations holds $\eta \ll \lambda \ll l$. The theory also assumed local isotropy and homogeneity of turbulent statistics, a direct energy cascade, and self-similar stochastic flow processes (i.e., invariant in distribution under time and space scaling). Additionally, Kolmogorov derived the key scalings laws for longitudinal n -order structure functions i.e. moments of velocity component differences, of a form $S_n \equiv \langle [(\mathbf{U}(\mathbf{r}, t) - \mathbf{U}(0, t)) \cdot \mathbf{r}/r]^n \rangle \equiv \langle (\delta u_r)^n \rangle$, introducing separation between two points \mathbf{r} at a distance r . According to Kolmogorov's theory they should follow $\langle (\delta u_r)^n \rangle = C_n (\langle \epsilon \rangle r)^{n/3}$, where C_n are constants. However, only S_3 exhibits a rigorous result providing a measure of skewness of velocity difference and introducing so-called four-fifth law. The second-order structure function S_2 is the energy contained in all Fourier modes for wavelengths larger than $1/r$ and its scaling is currently recognizable as two-third law. The energy spectral density is given below with its Kolmogorov-Obukhov (KO) scaling

$$S_2 \sim (\langle \epsilon \rangle r)^{2/3}, \quad S_3 = -\frac{4}{5} (\langle \epsilon \rangle r), \quad \eta \ll r \ll l,$$

$$E(k) = C_K \langle \epsilon \rangle^{2/3} k^{-5/3}, \quad \eta \ll r \ll l. \quad (1.4)$$

Here k stands for wavenumber and C_K denotes Kolmogorov constant which universality is widely discussed (Sreenivasan, 1995; Yeung and Zhou, 1997; Heinz, 2002; Donzis and Sreenivasan, 2010; Imomov and Murtazaev, 2024). The analogical formulation can be obtained for scalar field. Its second-order structure function S_2^θ was derived independently by Obukhov (1949) and Corrsin (1951). The analog of Kolmogorov's four-fifth law for scalars was proposed by Yaglom (1949) and gives an exact form of third order mixed structure function of the scalar field and velocity, currently known as Yaglom's four-third law. Both are printed below

$$S_2^\theta \sim \langle \epsilon_\theta \rangle \langle \epsilon \rangle^{-1/3} r^{2/3}, \quad \langle \delta u_r \cdot (\delta \theta_r)^2 \rangle = -\frac{4}{3} (\langle \epsilon_\theta \rangle r), \quad \eta \ll r \ll l,$$

where $S_n^\theta \equiv \langle [(\theta(\mathbf{r}, t) - \theta(0, t)) \cdot \mathbf{r}/r]^n \rangle \equiv \langle (\delta \theta_r)^n \rangle$, and ϵ_θ denotes scalar dissipation which is more extensively discussed in 1.3. Similarly, the scalar spectrum (whose

integral is the scalar variance) was derived yielding same scaling factor as in velocity spectrum with constant C_O considered to be universal (Sreenivasan, 1996; Watanabe and Gotoh, 2004). In the literature it is usually regarded as Obukhov-Corrsin (OC) scaling

$$E_\theta(k) = C_O \langle \epsilon_\theta \rangle \langle \epsilon \rangle^{-1/3} k^{-5/3}, \quad \eta \ll r \ll l. \quad (1.5)$$

For $n > 3$ we observe an anomalous scaling since there are no closed-form expressions for higher order moments. This is due to related anisotropy present at multiple scales (Biferale and Procaccia, 2005; Carter and Coletti, 2017) and intrinsic internal intermittency which is responsible for slower than linear increase of exponent scaling of structure functions (Warhaft, 2000; Shraiman and Siggia, 2000; Falkovich and Sreenivasan, 2006). An intriguing aspect is that scalar intermittency is present even though it is not observed in velocity field (which can be purely Gaussian) as long as there is a multiplicity of scales giving a clear evidence of scalar and velocity fields decoupling (Kraichnan, 1994; Holzer and Siggia, 1994; Chen and Kraichnan, 1998). Recent numerical works (Iyer et al., 2018, 2020; Buaria and Sreenivasan, 2023) proved though a distinct exponent scaling that saturates with respect to n for moments order of about 12.

1.2.2 Scalar spectra regimes

The following scalar regimes discussion is given for 3D systems in terms of Sc and assuming that scalar field does not change the flow dynamically. In literature, for $Sc \approx 1$ the inertial-convective range (see Fig. 1.5) is defined with $k^{-5/3}$ spectrum scaling, usually referred as Corrsin-Obukhov (OC). In this regime scalar fluctuations injected at rate θ' are introduced at scale l_θ , which may differ from l , and the mean flux Π_θ transfers the energy to dissipative scale of η . As the wavenumber increase both viscosity and diffusivity are getting more significant and the spectrum is being truncated. This regime is poorly understood and only recent works (Khurshid et al., 2018; Buaria and Sreenivasan, 2020) explore $E(k)$ as the superposition of two exponentials. Authors note that as the Re increases there is an intermittent transfer of energy towards small scales observed, potentially from larger scales. So far no scalar spectrum research was reported in this regime.

When $Sc \gg 1$ the viscous-convective range is observed where the viscosity prevails over diffusivity (it becomes effective at much smaller scales) and exhibit small-scale rate-of-strain. The spectrum was derived by Batchelor (1959) and has the form

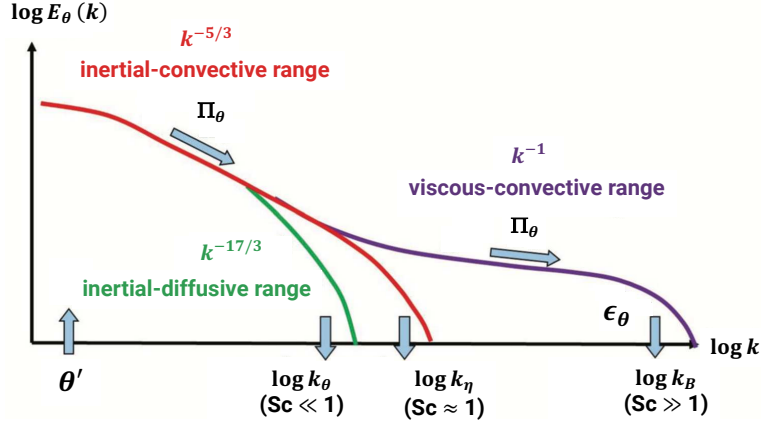


Figure 1.5: Schematic of passive scalar spectrum depending of Sc regime. Scalar fluctuations injected at rate θ' at low wavenumbers are transferred with the mean flux, Π_θ , to high wavenumbers and dissipated by the molecular diffusivity at the rate ϵ_θ . The remaining notation is $k_\eta = 1/\eta$, $k_B = 1/\eta_B$, and $k_\theta = 1/\eta_\theta$. Figure from [Gotoh and Yeung \(2012\)](#) with minor modifications.

$$E_\theta(k) = C_B(\nu/\langle\epsilon\rangle)^{1/2}\langle\epsilon_\theta\rangle k^{-1}, \quad \eta_B \ll r \ll \eta,$$

where $\eta_B = \eta Sc^{-1/2}$ and C_B is the Batchelor constant ([Yakhot and Orszag, 1987](#); [Antonia and Orlandi, 2003](#); [Dutta and Nandy, 2011](#); [Ni and Xia, 2013](#)). Batchelor's assumption on non-fluctuating strain turned out to be unrealistic but [Kraichnan \(1968\)](#) provided a better formulation with rapid velocity field changes and also got -1 scaling with a milder spectrum decay. Over the time there were no clear evidence for such regime however recent years brought a significant change ([Jullien et al., 2000](#); [Clay, 2017](#); [Iwano et al., 2021](#)) with a disclaimer that the viscous-diffusion range (the roll-off part of the spectrum) is affected by dramatic thermal noise renormalization ([Eyink and Jafari, 2022](#); [Bandak et al., 2022](#); [McMullen et al., 2023](#)).

The last regime, inertial-diffusive range, describe scales small enough that the diffusivity becomes important. In the limit of extremely low Sc and in the vicinity of $\eta_\theta = \eta/Sc^{-3/4}$. It is reflected as the Π_θ transfers from inertial range towards the high wavenumbers (see Fig. 1.5). The theory behind was first proposed by [Batchelor et al. \(1959\)](#), later explored by [Kraichnan \(1968\)](#) gave the scalar spectrum

$$E_\theta(k) = (C_K/3)\alpha^{-3}\langle\epsilon\rangle^{2/3}\langle\epsilon_\theta\rangle k^{-17/3}, \quad \eta \ll r \ll \eta_\theta,$$

No experimental data confirming this scaling was published due to difficulties in obtaining high Re keeping low Sc simultaneously. Notwithstanding, both numerical and analytical analysis confirmed the existence of such regime (Yeung and Sreenivasan, 2013, 2014; Hill, 2017; Jolly and Wirosotisno, 2020).

1.2.3 Cascade picture

In the previous discussion, different regimes of the energy and correlated scalar spectra were explored without addressing the mechanisms and directions of energy transfer between scales. The problem of energy cascades in turbulent flows is highly complex, and only a few idealized cases of homogeneous flows have been sufficiently described, allowing for the prediction of energy transfer directions. Recent reviews on this topic can be found in Alexakis and Biferale (2018) and Pouquet et al. (2019). Here, I will briefly highlight a few key aspects relevant to this work. A qualitative sketch of energy transfer in a scale-separated system is shown in Fig. 1.6. It demonstrates how injected energy can be transferred to both large and small scales, accounting for its dissipation due to the effects of drag and viscosity, respectively.

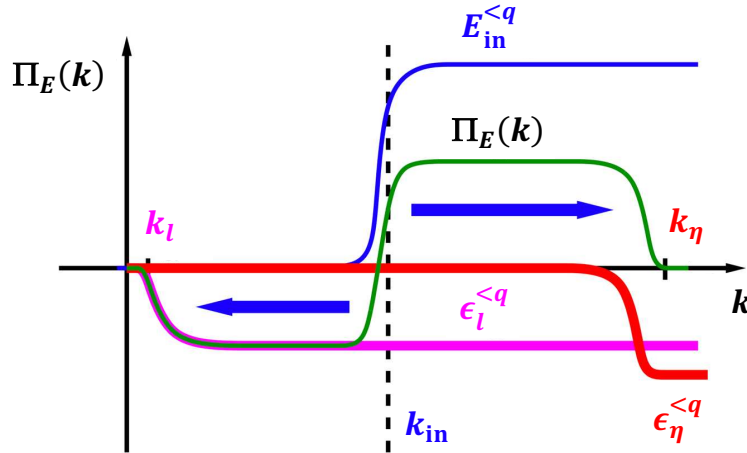


Figure 1.6: Qualitative sketch of the stationary energy transfer inside a sphere of radius q under assumption of scale separation. The net energy balance is of a form $\Pi_E(k) = -\epsilon_\eta^{<q} - \epsilon_l^{<q} + E_{in}^{<q}$ where the mean energy flux Π_E is driven by energy $E_{in}^{<q}$ being injected at k_{in} and dissipated through large-scale due to the drag $\epsilon_l^{<q}$ at scales k_l and due to viscosity $\epsilon_\eta^{<q}$ at k_η . Figure from Alexakis and Biferale (2018) with minor modifications.

Flow invariants—energy, enstrophy, and helicity—play a crucial role in shaping the energy cascade spectrum across various scale regimes. These quantities can dominate different ranges of scales, leading to phenomena like dual cascades, where

different cascading processes occur simultaneously. In some cases, the transfer of these invariants may coexist within the same regime, creating ambiguity as to whether the resulting energy spectrum is governed by a single cascading process or represents a superposition of power-law scalings. Additionally, it is not always clear whether the cascades follow the same directional flow. Another scenario involves split cascades, where an invariant is transferred simultaneously to both large and small scales. There is also the possibility of a bi-directional cascade, in which direct and inverse cascades of the same invariant coexist within the same regime (e.g., when energy is injected at multiple scales). These dynamics become even more complex in systems with varying flow configurations, making energy transfer predictions difficult, except in highly idealized cases of homogeneous turbulence.

In 3D turbulence, the classic scenario involves a direct energy cascade. However, in the presence of helicity injection, the direction of cascades depends on the definition of helicity sign within the respective regimes. Helicity, an invariant related to the topological structure of vortices, is not sign-definite and can be introduced to the system by large-scale stirring mechanisms. Studies show that under large-scale helical forcing, a dual forward cascade of energy and helicity can emerge. These studies demonstrate that the energy spectrum follows the KO scaling with sub-leading corrections from helicity (Eidelman et al., 2014; Sahoo et al., 2017; Alexakis, 2017; Yan et al., 2020). However, when considering the same sign of helicity in interacting triads, a counter-directional dual cascade can occur, with energy transferring toward larger scales. This behavior is observed in studies of homochiral turbulence, where the alignment of helicity signs plays a key role (Biferale et al., 2013; Plunian et al., 2020). The precise influence of helicity on energy transfer mechanisms remains an active area of research, with ongoing investigations into the details of this process (Chen et al., 2003; Yao and Hussain, 2022).

In contrast, reverse energy cascades are expected in 2D flows, as predicted by early works (Kraichnan, 1967; Leith, 1968; Batchelor, 1969; Kraichnan, 1971). Comprehensive reviews of 2D turbulence and quasi-two-dimensional flows can be found in Boffetta and Ecke (2012) and Alexakis (2023). The key invariant in 2D systems is enstrophy—a sign-definite measure of vorticity magnitude—which is closely related to energy in 2D flows, unlike helicity in 3D turbulence. The simultaneous conservation of energy and enstrophy leads to a dual counter-directional cascade, with enstrophy transferring forward to smaller scales and energy cascading inversely. The resulting energy spectrum follows KO scaling towards large scales and k^{-3} when transferring to smaller scales. Since the enstrophy is re-

lated with energy spectrum as $k^2 E(k)$, its cascade decays as k^{-1} . In this case, the enstrophy can be regarded as a passively advected field which differs from the viscous-convective regime for large Sc numbers. In quasi-two-dimensional systems, where strong reduction of the vertical component occurs, anisotropic distribution of Fourier modes can lead to scenarios where the flow behaves as 2D at some scales and 3D at others (Musacchio and Boffetta, 2019; de Wit et al., 2022).

Stratification adds another layer of complexity when discussing energy cascades and spectrum scaling. The direction of energy transfer is highly related to system dimensionality and can follow one of the previously mentioned scenarios (2D or 3D turbulence). To better describe the properties of stably stratified flows, it is useful to introduce the Froude number, $Fr = u/NL$, where N is the Brunt–Väisälä frequency defined as $N = \sqrt{-g\sigma/\rho}$, with the mean stratification parameter $\sigma = \partial\rho/\partial z$. When $Fr \ll 1$, strongly stratified, anisotropic, buoyancy-dominated flows occur, such as those in the Earth’s atmosphere, which exhibit complex dynamics. Turbulence in the $Fr \gg 1$ regime corresponds to weak stratification, where scalar fluctuations behave like a passive scalar and follow OC scaling. The $Fr \approx 1$ regime represents moderate buoyancy turbulence, for which Bolgiano-Obukhov (BO) phenomenology applies (Bolgiano Jr., 1959; Obukhov, 1959). This theory predicts dual scaling in the inertial range, with BO scaling ($k^{-11/5}$ for velocity fields and $k^{-7/5}$ for scalar fields) for $k < k_B$, and KO/OC scaling for $k > k_B$. The Bolgiano wavenumber k_B (Monin and Yaglom, 1975) splits the subranges of buoyancy-driven turbulence, where kinetic energy is converted to potential energy, and an inertial-dominated regime where buoyancy becomes weak. Numerical studies show that the simultaneous presence of both regimes requires very high Re (Alam et al., 2019). Unstable stratification, where density increases with height, is common in scenarios such as RBC and Rayleigh-Taylor instability (Boffetta and Mazzino, 2017; Livescu, 2020; Verma, 2021). It remains unclear to what extent BO scaling holds for thermal convection, as most 3D studies align with Kolmogorov’s prediction (Lohse and Xia, 2010; Verma et al., 2017; Lindborg, 2023; Lohse and Shishkina, 2024), while BO scaling is usually observed in 2D systems (Xie and Huang, 2022; Samuel and Verma, 2024; Zhang and Zhou, 2024). A key factor here is the difference in energy fluxes between thermal convection and stably stratified turbulence (Verma, 2021).

In recent years, increasing attention has been given to the problem of coherent thermal structures, such as plumes (Zhou et al., 2016a; Xie and Xia, 2017; De et al., 2018; Wang et al., 2022) and vortices (Yano and Morrison, 2024), which transfer energy across both large and small scales. As thermals form and develop, they actively mix with the surrounding environment, leading to entrainment processes—

an extremely complex issue that remains not fully understood (a summary can be found in (van Reeuwijk and Craske, 2015)). A significant series of numerical studies (large-eddy simulations) on thermal plumes has been recently published by Chen and Bhaganagar (Chen and Bhaganagar, 2021, 2023, 2024). The authors showed strong anisotropy near the heated surface and a gradual development of isotropy during the mixing stage. They observed scalar spectra scaling as $k^{-2.7}$ for both density and temperature fields, which were strongly correlated with velocity spectrum. The axial heat and mass fluxes exhibited a k^{-3} spectrum, the same scaling as obtained for the axial component of the turbulent kinetic energy (TKE) spectra. The 2D and 3D TKE spectra, along with helicity spectra, consistently showed $k^{-5/3}$ and k^{-3} scaling. Their flux analysis revealed inverse TKE and helicity cascades toward large structures and forward cascades of these invariants for the small scales. Furthermore, velocity-based longitudinal structure functions study found that the scaling exponents of the 2nd, 3rd, and 4th moments fell between the theoretical predictions for 2D and 3D systems suggesting a complex phenomena involved in the energy transfer.

1.2.4 Active scalars

In thermal convection processes, the temperature field cannot be assumed to be dynamically inactive, as it couples with the velocity field, resulting in energy exchange and strong scalar variability. There is a limited amount of literature that delves into the complexity of active scalars, as no generic phenomenology fully describes them, and most concepts are drawn from passive scalar theories. Although both passive and active scalars are governed by the same advection-diffusion equation (1.2), the presence of feedback between the scalar and the vector field introduces a strong non-linearity to the problem. This coupling leads to simultaneous vector and scalar fluctuations, which contribute to turbulence production. The magnitude of correlation between these fields can vary across systems, making the problem highly intricate. As a result, our understanding of active fields remains limited. Convection experiments designed to compare passive and active inputs suggest that temperature exhibits a higher level of intermittency compared to other scalar quantities (e.g., density), and that the active field shows anisotropic behavior (Celani et al., 2002; Zhou and Xia, 2008; Mazzitelli and Lanotte, 2012).

An extended discussion on the active scalar problem in given the context of RBC (see Subsec. 1.1.4). A review in this matter is provided by Lohse and Xia (2010). The temperature difference driving the convective motions establishes

the LSC, which is sustained by small-scale thermal plumes (De et al., 2018). However, the LSC structure locally disintegrates into smaller vortices, cascading energy toward smaller scales. The question about scalar characteristics in such situation is very relevant and have been investigated. Belmonte and Libchaber (1996) proposed four scenarios for passive and active scalars based on the product of two skewness factors: one derived from temperature time series and the other from its time derivative. They observed that near a hot plate, both skewness factors were positive, revealing cliff-ramp structures associated with thermal plumes. Conversely, when analyzing a mildly heated plate, the product was negative, and the scalar exhibited ramp-cliff forms. An alternative perspective was presented by Zhou and Xia (2002), who employed so-called *plus* and *minus* temperature increments to identify mixing zone dynamics. Their results demonstrated that as the Ra increased, mixing zones contracted. Using this methodology, regions dominated by thermal plumes were identified. More recently, He and Xia (2019) showed that such regions could also be determined using logarithmic root mean square temperature profiles. Additionally, Zhou and Xia (2008) conducted a comparative study of passive (fluorescent dye concentration) and active (temperature) scalars in a water-filled cell under thermally driven convection. They found distinct small-scale characteristics for each scalar when advected by the same flow. Temperature, as an active scalar, exhibited greater intermittency above the Bolgiano timescale (τ_B) but behaved like a passive scalar below it. Further differences emerged in the probability density functions (PDFs) comparison, while the normalized distributions of concentration increments remained non-Gaussian across scales, temperature increments transitioned from non-Gaussian at small scales to nearly Gaussian at larger ones.

1.3 Temperature dissipation rate

Turbulent mixing is a ubiquitous phenomenon in the atmosphere that unfolds in two stages. The first stage involves the progressive entanglement of air masses undergoing mixing, resulting in an increase in inhomogeneities (filamentation). The second stage is the smoothing of these structures due to molecular diffusion across the filament boundaries. In classical theory, temperature is treated as a passive scalar (see Sec. 1.2.2). However, in clouds, during condensation and evaporation, the assumption of passivity does not hold. The latent heat released or absorbed during the phase transformation of vapor to liquid water and vice versa can affect temperature fluctuations at the smallest scales, suggesting that the statistical properties of temperature gradients should differ from those when

temperature is regarded purely as a passive quantity.

In the previous section, the general scalar problem has been outlined, however, in many cases, temperature is the primary quantity of interest. Its dissipation rate, ϵ_T , is particularly significant in turbulence modeling, where any higher-order closure model requires solving a prognostic equation or a diagnostic parameterization for ϵ_T (Wyngaard, 2010). Improved estimates of temperature dissipation may also enhance our understanding of heat fluxes and spectral regimes. Historically, ϵ_T has gained attention as it is easier to evaluate than energy dissipation, involving only three components instead of the nine in ϵ . Its formula is given below in Eq. 1.6

$$\epsilon_T = \kappa \left\langle \left(\sum_i \partial_i T \right)^2 \right\rangle \quad (1.6)$$

where the subscript denotes the i -th component. Over the years, experimental studies have explored various aspects of temperature dissipation, such as deviations of the average ϵ_T from a log-normal distribution (Sreenivasan et al., 1977; Antonia and Sreenivasan, 1977; Ching and Kwok, 2000; Zhou and Jiang, 2016; Zhang et al., 2017b; Xu et al., 2023; Guo et al., 2024), following the so-called third Kolmogorov hypothesis (Kolmogorov, 1962; Oboukhov, 1962). Other studies have investigated temperature dissipation statistics in wind tunnels (Krishnamoorthy and Antonia, 1987), channel flows (Zhu and Antonia, 1993), turbulent round jets (Antonia and Mi, 1993), quasi-periodic Kármán vortices in turbulent near wakes (Antonia and Browne, 1986; Chen et al., 2020), convective surface layers (Kiely et al., 1996), and stably stratified flows (Basu et al., 2021) giving strong evidence for ϵ_T spatio-temporal intermittency (often higher than in ϵ), anisotropy, anomalous scaling, and non-Gaussian distributions of temperature fluctuations.

Special attention has been given to the correlation between ϵ and ϵ_T . Early work showed that this correlation depends on Re, measurement wire separation, and flow type (Antonia and Van Atta, 1975; Antonia and Chambers, 1980; Antonia et al., 2001), examining the relationship between these quantities and vorticity (Zhou and Antonia, 2000; Hao et al., 2008) and highlighting the potential role of organized structures in enhancing small-scale mixing (Abe et al., 2009). Scaling attempts have also been made for the normalized mean values of ϵ and ϵ_T (Abe and Antonia, 2011), as well as for the respective spectra (Lee et al., 2012). Eventually, a spectral chart method was developed to estimate both mean ϵ and ϵ_T directly from the temperature frequency spectrum (Lemay et al., 2020). This technique is applicable to slightly heated turbulent flows where temperature acts as a passive scalar and the Prandtl number is on the order of unity.

The RBC systems (see Subsec. 1.1.4) are currently one of the most active area of temperature dissipation research (He et al., 2011, 2014b; Zhang et al., 2017b; He et al., 2018; Bhattacharya et al., 2019; Xu et al., 2019; Christopher and Llewellyn Smith, 2021; Xu et al., 2023; Guo et al., 2024; Lohse and Shishkina, 2024). The statistics of local fluctuations, the total heat flux transported through the convective cell, and global turbulence are strongly influenced by the dissipation field properties. The heat flux is directly related to ϵ_T via the Nusselt number (Nu), another dimensionless quantity characterizing the ratio of convective to conductive heat transfer, which, in thermal convection, is defined in terms of Ra and Pr. The precise relationship depends on the regime and the convective cell’s aspect ratio and is explained by the Grossmann & Lohse theory (Lohse and Shishkina, 2024). This theory assumes a decomposition of both dissipation fields into boundary layer and bulk contributions, each with different scaling behaviors depending on Ra and Pr. The recent picture is as follows: the temperature dissipation ratio is higher in the boundary layer than in the bulk region (Xu et al., 2019; Vishnu et al., 2022a; Guo et al., 2024; Lohse and Shishkina, 2024). Both ϵ_T and ϵ distributions deviate from a log-normal distribution—the PDF tails become broader for the higher Ra and the lower Pr, indicating an increasing degree of small-scale intermittency with rising Reynolds numbers (Zhang et al., 2017b) (similar deviations are observed in Rayleigh–Taylor turbulence (Zhou and Jiang, 2016)). The work by He et al. (2018) links the exponential tails in the temperature fluctuation PDF to a convolution of dynamic modes conditioned on constant local temperature dissipation. The authors argue that thermal plume structures are responsible for such behavior, as the PDF conditioned on ϵ_T retrieves Gaussian statistics in the temperature time series.

To the best author’s knowledge there have been no studies delving into temperature dissipation rates in real clouds. The findings from laboratory studies and from lower boundary layer experiments could significantly differ from what could be observed under shallow convective conditions and in clouds interiors.

1.4 Scope of work

Although recent years have brought significant progress in understanding convection processes, cloud evolution, and general turbulent mixing, a more rigorous understanding of small-scale fluctuations in atmospheric flows is still lacking. In this work, I present measurements performed using high-resolution UltraFast Temperature sensors in various atmospheric and laboratory conditions. Chapter 2 introduces the instruments used, the two experimental facilities—the LACIS-T

wind tunnel and the Π Chamber—where the measurements were conducted, and provides an overview of the EUREC⁴A campaign, with an emphasis on the airborne operations of the Twin Otter aircraft. Each section also describes the experimental strategy and discusses the collected temperature datasets, with the final section outlining the general data processing methodology. Chapter 3 presents a detailed analysis of the time series obtained from laboratory facilities, where measurements were conducted under controlled and repeatable conditions. I describe the fundamental thermal characteristics of these two facilities and provide an extensive discussion on temperature spectra, employing different analytical approaches. In contrast, Chapter 4 focuses on field measurements in the real atmosphere, distinguishing three types of atmospheric segments and exploring the variability of the normalized temperature dissipation rate across these regions. Finally, in Chapter 5, I summarize the results and initiate a discussion on their broader implications, both for future experiments and for the general interpretation of atmospheric physics.

Measurements

2.1 UltraFast Thermometers

As outlined in the previous chapter, reliable in-situ temperature measurements in the real atmosphere remain challenging (e.g., [Siebert and Shaw \(2017\)](#); [Siebert et al. \(2021\)](#)). These difficulties primarily arise from the high velocities of airborne platforms, aerosol contamination, and collisions with water droplets that lead to sensor wetting. Laboratory experiments mitigate the issue of moving platforms and offer greater measurement flexibility; however, other challenges persist. The current state-of-the-art in temperature measurement techniques and instrumentation is comprehensively reviewed in the second edition of *Measurements in Fluid Mechanics* ([Tavoularis and Nedić, 2024](#)). Of particular relevance to this work are cold-wire sensors, which enable high-frequency temperature measurements due to their small dimensions, making them well-suited for studying small-scale turbulent structures. Despite their advantages, cold wires are highly sensitive to environmental conditions and may suffer from increasing temporal attenuation if the length-to-diameter aspect ratio is below 1000 ([Xia et al., 2022](#); [Houra and Tagawa, 2023](#)).

One representative of this group is UltraFast Thermometer family which were used for all the measurements described later in this chapter. The history of this instrumentation began with its prototype, a novel airborne thermometer designed for in-cloud measurements, known as VTU-1 ([Haman, 1992](#)). Its core featured a 50 μm thick thermocouple mounted on a frame, with a sensing element characterized by a time constant of around 0.1 s and an accuracy of 0.2 K. Back in time, there was a significant demand for precise and high-resolution sensors for temperature measurements to study the small-scale structure of clouds. At the Institute of Geophysics, University of Warsaw, a group led by Krzysztof Haman attempted to bridge this gap. The foundation of a new instrument began with fine wire measurements in the convective surface layer, incorporating the use of

fractal techniques to study turbulence (Malinowski and Leclerc, 1994). A few years later, the first UltraFast Thermometer (UFT) was developed and detailed in Haman et al. (1997). The main modification involved replacing the sensing element with a resistive platinum-coated tungsten wire, $2.5\text{ }\mu\text{m}$ thick, 5 mm long, and approximately $50\text{ }\Omega$ at room temperature. This change significantly improved the time constant to 10^{-4} s , enabling temperature measurements in clouds with a resolution of a few centimeters, depending on aircraft velocity (initially up to 40 m s^{-1}). Subsequent years witnessed the development of new versions of UFT tailored for specific airborne platforms and applications, particularly for airspeed up to 100 m s^{-1} (Haman et al., 2001), allowing for spatial resolutions as small as 1 cm (Haman et al., 2007). Unfortunately, technical issues persisted, such as electromagnetic interference with avionic systems and high vulnerability to relatively minimal displacements of shielding elements and cables from their optimal position. Consequently, only 10–20% of the data were of sufficient quality for further processing.



Figure 2.1: UFT-2A (left) and UFT-2B (right) head sensors. Both are topped with a tungsten wires ($2.5\text{ }\mu\text{m}$ thick, 3 mm long) spanned on an miniature industry standard wire probes by DANTEC®.

This challenge prompted another technological leap and redesign, minimizing the deficiencies of previous versions and making UFT a more reliable sensor (Kumala et al., 2013). Its efficiency was demonstrated during the POST campaign, providing valuable UFT results from 15 out of 17 research flights, aiding in establishing the stratocumulus-top region division into layers (Malinowski et al., 2013). However, one issue remained unresolved: the instrument’s construction included moving parts, such as a wind vane, making it challenging to pass through aircraft

certification procedures. The solution came in the form of a new generation, UFT-2.0, introduced just before the ACORES campaign (Nowak et al., 2018; Siebert et al., 2021). The reduced dimensions of the instrument limited spatial averaging and facilitated easier mounting on platforms. The pencil-sized design was complemented by a new construction of the signal amplifier, which was relocated to a special housing and shielded with a copper foil.

The current versions of UFT, UFT-2A and UFT-2B (see Fig. 2.1), brought some minor improvements. Two wires from UFT-2.0 were replaced by one, $2.5\text{ }\mu\text{m}$ thick, 3 mm long wire spanned on an industry miniature wire probe by DANTEC® (straight (55P11) for UFT-2A and right angle, parallel (55P13) for UFT-2B) which allowed for easy exchange of the sensing head in field conditions. The head sensors are usually accompanied by the straight, 4 mm DANTEC® probe support.

2.2 LACIS-T

2.2.1 Facility

The Turbulent Leipzig Aerosol Cloud Interaction Simulator (LACIS-T), located at Leibniz Institute for Tropospheric Research (TROPOS), Germany, is a relatively new facility among currently operational aerosol–cloud research chambers. It is a closed loop wind tunnel which enables turbulent and isobaric mixing of two humidified, aerosol-free air streams of separately adjusted, controllable and repeatable thermodynamic conditions. Its primary objective is to study interactions between turbulence and cloud microphysical processes in a wide range of conditions, including warm, mixed-phase and cold clouds. It operates in a temperature range of $-40\text{ }^{\circ}\text{C}$ to $25\text{ }^{\circ}\text{C}$ creating favorable conditions for local supersaturation with respect to liquid water and/or ice. The continuous-flow design, with both streams velocities varying between 0.5 and 2 m s^{-1} , allows for detailed studies in small temporal and spatial scales and with a Lagrangian framework. The field of study is 80 cm deep, 20 cm wide, and 2 m long measurement section (see Fig. 2.2) with an aerosol inlet and turbulence grid located at its top. All the technical aspects of the system, a list of the equipped instrumentation, and basic thermodynamic characteristics can be found in Niedermeier et al. (2020). Nowak et al. (2022) extended the studies on humidity field fluctuations scanning the tunnel in both transverse orientations (see Fig. 2.2) with the high temporal resolution ($\sim 2\text{ kHz}$) contactless infrared hygrometer. One of the interesting observations were wave-like features in the central part ($x = 0\text{ cm}$) of the tunnel where the mixing is the most intensified. The spatial extent of this inhomogeneity

was reported ≤ 4 cm at the characteristic frequency of 14 Hz.

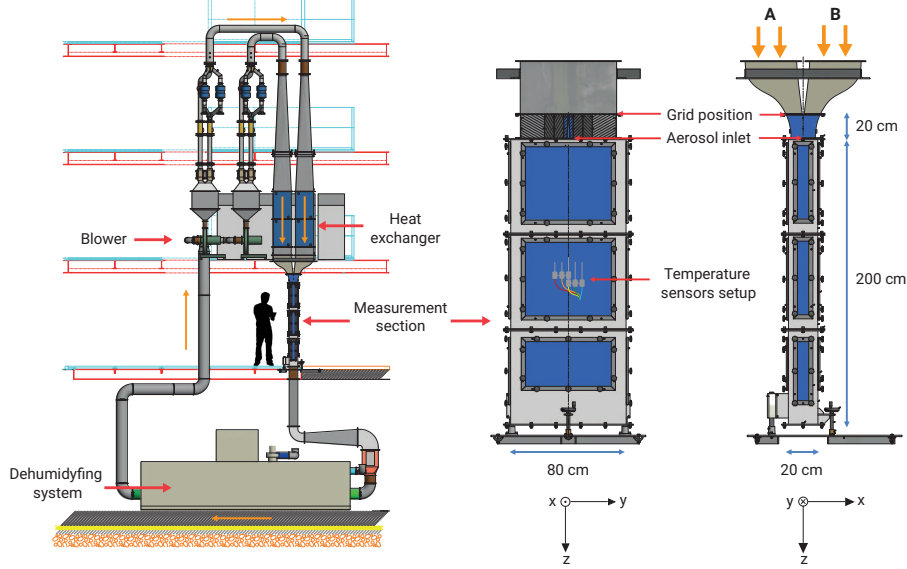


Figure 2.2: LACIS-T measurement section sketch. The orange arrows shows the location of „A” and „B” streams and the red arrow marks the position where aerosol can be injected. Turbulence is generated through a passive square-mesh grids showed on the right. The section is designed so that it provides flexibility for instrumentation mounting due to replacable windows which can be changed with the adjusted panels. The picture includes also information on tunnel dimensions and coordinate system orientation with $z = 0$ cm located at the aerosol inlet tip. Adapted from [Niedermeier et al. \(2020\)](#).

Due to its design solutions the tunnel allows for very unique experiments like e.g. simulating the processes in the interface of clouds and their surroundings i.e. entrainment and detrainment ([Frey et al., 2022](#)), or studies in humidity fluctuating environment to investigate hygroscopic aerosol properties ([Niedermeier et al., 2025](#)) and droplet generation induced by acoustic waves ([Roudini et al., 2020](#)). LACIS-T is then a suitable research field for mixed-phase clouds both in simulations and experiments ([Gouharianmohammadi et al., 2023](#)).

2.2.2 Experimental strategy & data

The data used in the following analyses comprises two experiments, named D-1-MIX and D-2-MIX, that involved tunnel scanning along the x direction (see Fig. 2.2) with the UFT-2A (see Fig. 2.1). The collected temperature time series were part of a bigger measurement campaign which aimed at comparing different temperature sensors (including 2A and 2B versions) in terms of their sensitivity and usability under changing humidity fluctuations and angle of attack between

the flow and the sensing element.

Table 2.1: List of the LACIS-T experiments with the corresponding measurement details. Symbol explanation: T_A and T_B denote temperatures of two air streams, F_A and F_B are corresponding flow rates, t is the measurement time at each position x .

Experiment	T_A [°C]	F_A [m ³ min ⁻¹]	T_B [°C]	F_B [m ³ min ⁻¹]	x [cm]	t [min]
D-1-MIX	0	6.1	25	4.5	-7 to 7	10
D-2-MIX	4	4.5	20	4.5	-7 to 7	5

The experimental strategy was straightforward and consisted of the measurement section's volume scans along the x -axis with a variable step and after the thermodynamic conditions in the tunnel had stabilized. Both selected experiments cover only dry and clean conditions (humidification system was turned off and no additional aerosol flow was injected) and 0 degree angle with respect to the flow. All the remaining conditions are summarized in Table 2.1, along with the data processing methodology outlined in Sec. 2.5.

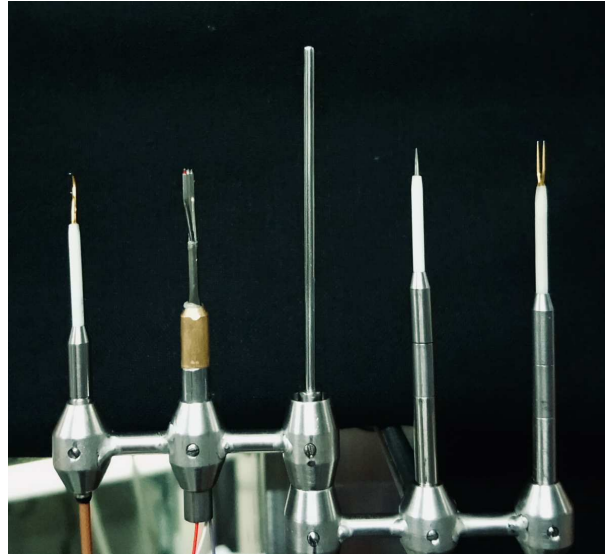


Figure 2.3: Temperature sensors setup used in LACIS-T. From left: UFT-2B, UFT-M, Pt100, cold wire (DANTEC®), and UFT-2A spaced with 2 cm from each other. The set was then placed inside the measurement section of the tunnel, parallel to the longer edge (along the y -axis), and moved along the shorter edge (along the x -axis) during the measurements. Horizontal distance of the setup center to the narrow window was 36 cm whereas the top of Pt100 was located at $z = 62$ cm.

The choice of UFT-2A comes from the fact that the sensing wire was placed perpendicular to the flow which could reduce the potential disturbance of bended rod of the UFT-2B. However, comparative analysis of the results obtained with the both sensors indicated overall small differences (not presented in this work).

2.3 Π Chamber

2.3.1 Facility

There are very few convection facilities similar to the Π Chamber (see Subsec. 1.1.4), making it an exceptional apparatus among other currently operational aerosol-cloud research chambers (see Tab. 1 in [Shaw et al. \(2020\)](#)). The chamber is a turbulent RBC cell, where the lower surface is set to a higher temperature than the upper surface, creating a temperature difference ΔT (see Fig. 2.4). This setup promotes turbulent mixing due to the buoyancy forces generated between the warm and cool air masses. A technical description, along with basic thermodynamic characteristics, can be found in the overview by [Chang et al. \(2016\)](#).

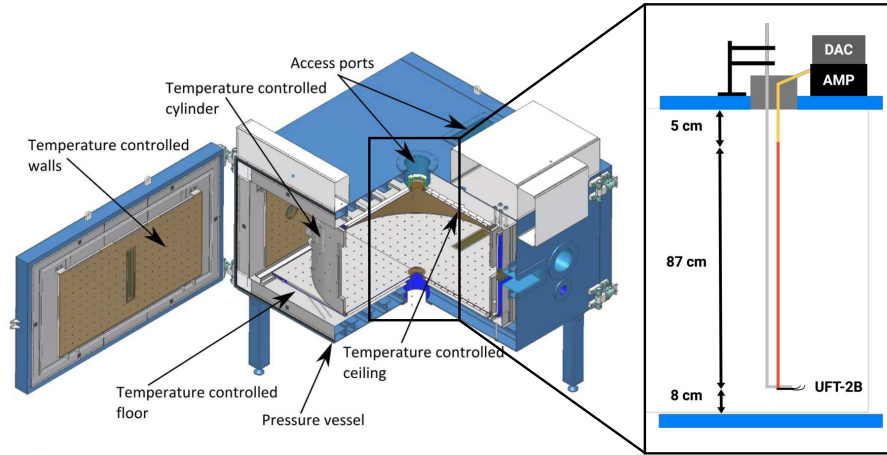


Figure 2.4: Schematic of the Π Chamber along with the experimental setup used during the experiments. The operations center, located at the top, housed most of the equipment and cabling, including a BNC cable (yellow), a UFT amplifier (AMP), a digital-to-analog converter (DAC), and a PC running DAC software. Inside the chamber, a vertical rod with a curved end (gray) supported a UFT-2B sensor (brown), which was mounted using a DANTEC[®] probe support (red). Measurements were conducted from approximately 8 cm above the bottom to about 5 cm below the top plate. For clarity, only a cutout of the cylindrical insert is shown, although it was present during the experiments. The left graphics is from Michigan Tech’s [website](#) (access: Feb. 28, 2025), while the right scheme is adapted from [Grosz et al. \(2024\)](#).

The primary objective of the chamber is to study small-scale aerosol-cloud interactions under varying environmental conditions, ranging from dry and clean to highly polluted and moist. As a result, the chamber is used in a wide variety of studies, including water vapor supersaturation fluctuations and their effects on cloud droplet growth (e.g., (Prabhakaran et al., 2020a; Anderson et al., 2024)), turbulent mixing of air masses with different properties (e.g., (Yeom et al., 2023, 2025)), and numerical research supporting the interpretation of laboratory experiments (e.g., (Chandrakar et al., 2022, 2023; Salesky et al., 2024)). There is also room for more unconventional experiments, such as exploring cloud formation purely through ionization (Chandrakar et al., 2024a).

2.3.2 Experimental strategy & data

The measurements were conducted along the vertical axis of the chamber for three temperature differences (10 K, 15 K, and 20 K), corresponding to a Ra of approximately 10^9 and Pr of 0.7. These experiments utilized the UFT-2B (see Fig. 2.1), which was mounted on a 1.5 m long rod with a 90 degree bend at the end (see Fig. 2.4).

Table 2.2: List of experiments along with the corresponding Π Chamber and UFT settings, including Rayleigh numbers. The symbol t denotes the measurement duration at a given height h above the bottom. Experiment names follow the convention: type of measurement („V” for vertical), ΔT , boundary type („S” for smooth, „R” for rough), and measurement duration („L” for 19 min, or unmarked for 3 min). An extended version of this table is available in Grosz et al. (2024).

Experiment	Boundaries type	ΔT [K]	h [cm]	t [min]	Ra [$\times 10^9$]
V10-S-L	smooth	10	irregular	19	1.1
V10-S	smooth	10	8–95	3	1.1
V15-S-L	smooth	15	irregular	19	1.6
V15-S	smooth	15	8–95	3	1.6
V20-S-L	smooth	20	irregular	19	2.1
V20-S	smooth	20	8–95	3	2.1
V20-R	rough	20	8–95	3	2.1

The irregular positions are: 8, 14, 26, 35, 50, 65, 74, 86, 95 [cm].

This setup allowed for manual control of the probe while ensuring minimal vertical

disturbances, enabling temperature profiling from 8 cm above the floor to 5 cm below the ceiling. The UFT-2B, with its sensing element aligned parallel to the mean flow of the LSC, recorded time series of two durations: 19 min and 3 min. While these recording lengths are shorter than those typically used in RBC experiments, analysis based on the framework by [Lenschow et al. \(1994\)](#) confirmed that both time series converged. The experimental conditions are summarized in Table 2.2. For a more detailed description of the measurements, refer to [Grosz et al. \(2024\)](#), along with the data processing methodology outlined in Sec. 2.5.

This study aimed to enhance the understanding of small-scale temperature fluctuations in thermally-driven convection within the chamber, with a particular focus on the regions near the bottom and top boundaries. It looked for valuable insights that could inform future experiments and contribute to the study of microphysical processes relevant to the real atmosphere, such as supersaturation fluctuations.

A secondary aspect of the study examined the role of surface topography. One experimental configuration featured rough boundaries, created by placing aluminum bars on the floor and ceiling to form longitudinal stripes. Subsequent UFT deployments were performed after removing these bars to compare temperature fluctuation properties between smooth and rough boundary conditions. However, due to excessive battery drainage, part of the dataset was lost, leaving only one rough boundary case available for analysis in this study.

2.4 EUREC⁴A

2.4.1 Campaign overview

The term EUREC⁴A stands for *ElUcidating the RolE of Cloud–Circulation Coupling in ClimAte* and describes a 2020 research field campaign in the trade-wind region of northwestern tropical Atlantic Ocean east of Barbados. This campaign investigated the interplay between shallow cumulus clouds, convection, and circulation, along with other components of the Earth system, such as upper-ocean processes and the life cycle of particulate matter. The primary focus was to assess how these elements of the climate system would respond to warming. The extensive scale of the study area, the large number of researchers involved, and particularly the high degree of coordination across 59 mobile platforms were uncommon compared to other similar programs. This complexity necessitated a lengthy preparation period to enhance the accuracy of cloud measurements in the trade-wind region ([Stevens et al., 2016, 2019](#)). By developing new measurement methods to

constrain large-scale mean motions and by deepening the understanding of cloud patterns, the research was able to overcome limitations that had hindered previous studies (e.g., GATE Greenfield and Fein (1979), ASTEX Albrecht et al. (1995), and RICO Rauber et al. (2007)).

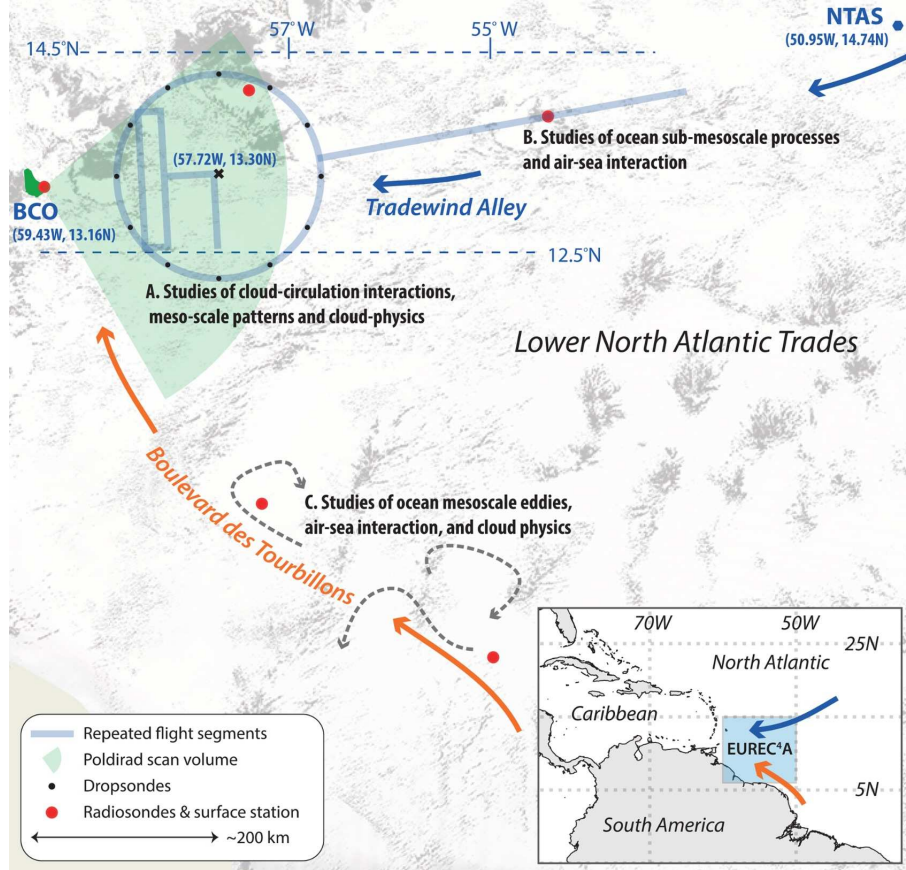


Figure 2.5: The EUREC⁴A campaign research field in the Lower North Atlantic Trades with three study areas marked (A, B, and C). The Tradewind Alley (areas A and B) extends between the Northwest Tropical Atlantic Station (NTAS) and the Barbados Cloud Observatory (BCO, radar range marked light green). The TO operated within the circle (marked A), sampling clouds at various altitudes. The Boulevard des Tourbillons (area C) represents a region influenced by the North Brazil Current, which could feature a different large-scale environment due to large freshwater filaments advected from the South American coast. Figure from Stevens et al. (2021).

EUREC⁴A addressed several key scientific objectives, including testing hypothesized clouds-feedback mechanisms related to climate sensitivity, which potentially explain discrepancies in climate modeling, establishing benchmark measurements for a new generation of models and satellite observations (Bony et al., 2017), studying air-sea interactions and cloud formation, and quantifying the factors influencing the sub-cloud layer, such as mass, energy, and momentum budgets.

The study areas of EUREC⁴A are illustrated in Fig. 2.5. A more comprehensive overview of the campaign’s objectives, activities, measurement platforms, and collected data is provided in [Stevens et al. \(2021\)](#).

2.4.2 Experimental strategy & data

EUREC⁴A focused on quantifying the diurnal variability of cloudiness and its surrounding environment, which required the use of four heavily instrumented aircraft: the High Altitude and Long Range Research Aircraft (HALO), the ATR, the WP-3D Orion (P3), and the British Antarctic Survey (BAS) Twin Otter (TO).

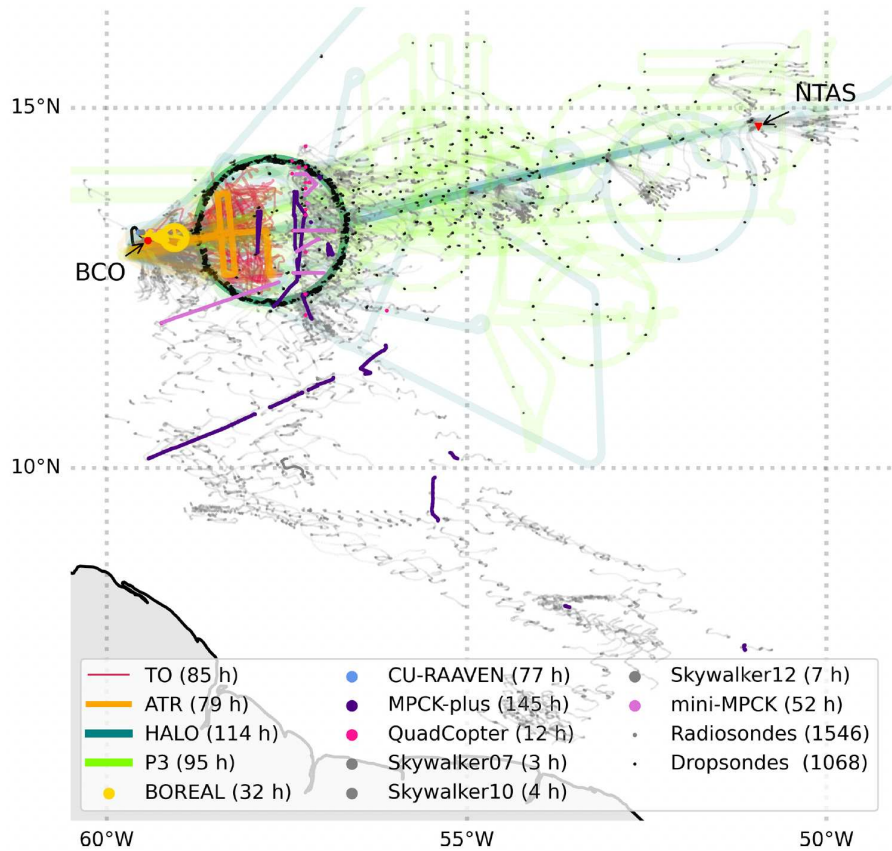


Figure 2.6: Map of airborne operations during the EUREC⁴A campaign. In addition to aircraft missions, uncrewed aerial systems (UASs) were used such as BOREAL, CU-RAAVEN, Skywalkers, and instrument boxes (MPCK-plus and mini-MPCK) flown with CloudKites attached to research vessels. Total flight time or number of soundings are indicated in parentheses. Figure from [Stevens et al. \(2021\)](#).

The TO’s objective was to perform daily, repeated penetrations of cumulus cloud shells and sub-cloud layers at various altitudes within the lower atmospheric

boundary layer. As indicated in Fig. 2.6, flights were mostly conducted in the western region of the EUREC⁴A-Circle. These operations totaled 85 h, reaching altitudes of up to approximately 5 km, with most measurements concentrated around 1.5 km. The aircraft was equipped with the UFT-2B, which was attached to the Best Air Turbulence (BAT) probe, separated by approximately 10 cm (see Fig. 2.7), allowing for undisturbed data collection in variable environmental conditions. In addition to the UFT, the TO was equipped with the Meteorological Airborne Science INstrumentation (MASIN) system, which provided 1 and 50 Hz data on GPS position, pressure, temperature, H₂O molar ratio, and 3D velocity components from the BAT probe. There were also two cloud spectrometers collecting data on cloud microphysics. Both instruments were located under the wings and separated by approximately 5 m. One was the Fast-Forward Scattering Spectrometer Probe (FFSSP), which operated at a 50 Hz resolution, and the other was the Cloud Droplet Probe (CDP), sampling data at 1 Hz. Unfortunately, due to technical issues some flights were covered only by CDP resulting in lower LWC data resolution.



Figure 2.7: UFT-2B mounted on the BAT probe on TO. Pictures taken by M. Posyniak.

Overall, UFT-2B provided data from 7 TO flights, resulting in 150 cloud (CL) segments (using an LWC threshold of $\geq 10^{-3} \text{ g m}^{-3}$ and temperature observations), 13 boundary layer (BL) segments ($p \geq 1010 \text{ hPa}$), and 24 free atmosphere (FA) segments (without cloud cover and with $p < 1010 \text{ hPa}$). Additional criteria required that selected segments only include horizontal flights lasting a minimum of 1 s, which, given the typical TO speed of 65 m s^{-1} , corresponds to a minimum

distance of 65 m. Moreover, the velocity fluctuations were of the order of a few m/s this is why the frozen flow hypothesis is applicable. The further data methodology is described in Sec. 2.5 along with the summary of the collected dataset in Table 2.3.

Table 2.3: List of the TO flights with the corresponding measurement details.

Flight	Date	CL segments	BL segments	FA segments	Spectrometer
F1	Jan. 24	13	0	1	FFSSP
F2	Jan. 24	6	0	1	FFSSP
F3	Jan. 26	0	3	3	—
F4	Jan. 28	84	5	8	CDP
F5	Jan. 28	15	0	1	CDP
F6	Jan. 30	32	4	7	CDP
F7	Feb. 2	0	1	3	—
		150	13	24	

For an extensive description of the atmospheric soundings from between 8 January and 19 February 2020, see [Stephan et al. \(2021\)](#). Here, I summarize only the aspects relevant to this work, specifically, the synoptic conditions provided by radiosondes launched from the research vessel Meteor and Barbados Cloud Observatory (BCO) which operated closest to the TO flights. According to the data, the lifting condensation level (LCL) was approximately constant through the given period of time and was located at about 670 m, corresponding with ~ 900 hPa. The depth of the trade-wind cumulus layer is characterized by the hydrolapse, defined as the mean height where mean relative humidity on a centered running 500 m range first drops below 30%. It exhibits a moderate variability during the first three flights reaching almost 4.9 km (~ 600 hPa) in the BCO data but remained relatively constant in the following days yielding about 2.37 km which translates into ~ 800 hPa. Both observations and ceilometer measurements (installed on the vessel) indicated that the dominant low-level clouds during the campaign were cumulus and stratocumulus. The reported technical codes, specified by the World Meteorological Organization (WMO) Cloud Atlas, were $C_L = 8$ and $C_L = 2^1$ which suggests the cumulus clouds were of „moderate

¹these symbols comes from the WMO [cloud classification aid](#) (access: Feb. 28, 2025)

or strong vertical extent, generally with protuberances in the form of domes or towers”² and stratocumulus bases were usually located above cumulus structures. For more details please refer to Sec. 3.2 as well as Fig. 8 and 9 in [Stephan et al. \(2021\)](#).

To date, no overview paper has been published on the results obtained with TO instrumentation, except for [Król et al. \(2024\)](#). The authors, using the same dataset, presented a novel approach for interpreting airborne turbulence measurements through recurrence quantification analysis, particularly to extract information about the dynamical boundaries of the clouds.

2.5 General data methodology

The UFT data was sampled at different frequencies depending on the research: 20 kHz for the II Chamber and TO experiments, and 3 kHz for the LACIS-T wind tunnel measurements. The collected time series underwent a standardized processing procedure consisting of several steps. First, voltage fluctuations recorded by the UFT were converted into temperature using a reference sensor and simple linear regression. The instrumentation varied by experiment: a 1 Hz thermocouple for the II Chamber, a 3 Hz Pt100 sensor for LACIS-T, and a 0.7 Hz non-deiced Goodrich Rosemount Probe (102E4AL) for airborne TO operations. Next, electronic artifacts were identified and removed through detailed time series analysis (e.g. filtering out recorded pilot conversations during EUREC⁴A flights). A Butterworth filter (10th order) was then applied, with cutoff frequencies set at 2 kHz for the II Chamber and EUREC⁴A data, and 1.5 kHz for LACIS-T measurements. Finally, the data was averaged to 2 kHz and 1.5 kHz, respectively.

Temperature measurement uncertainty is neglected in this study because the sensors have high accuracy ([Haman et al., 1997](#); [Kumala et al., 2013](#)), and the influence of environmental variability and flow conditions is difficult to estimate in airborne measurements ([Wendisch and Brenguier, 2013](#)).

Further methodological details are provided in the following sections.

²citation from the WMO [website](#) (access: Feb. 28, 2025)

Laboratory experiments

3.1 LACIS-T

3.1.1 Basic thermal characterization

As mentioned in Subsec. 2.2.1, the basic thermodynamic description of the tunnel has been provided in Niedermeier et al. (2020) and Nowak et al. (2022). However, no high-resolution temperature measurements have been performed to study scalar field fluctuations. Due to the facility design and the given stream settings (see Table 2.1), large temperature differences can be expected over short time scales, particularly at $x = 0$ cm, where mixing is most intense. This is why two experiments with changing conditions have been designed as described in Subsec. 2.2.2 and in Tab. 2.1.

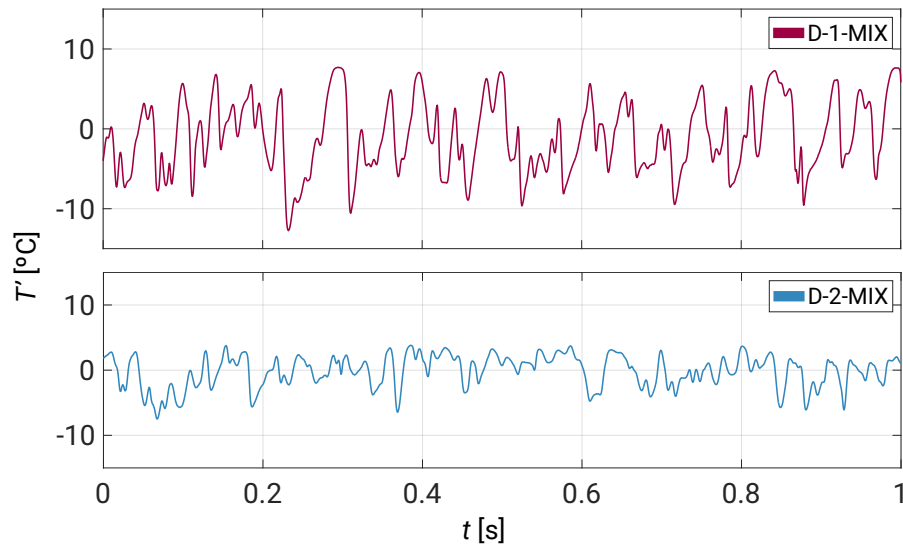


Figure 3.1: One second temperature fluctuations T' series at $x = 0$ cm.

Selectively chosen one-second temperature fluctuations recorded at $x = 0$ cm with the UFT-2A are presented in Fig. 3.1. The mean values have been removed for

clarity, i.e., $T' = T - \langle T \rangle$. The upper panel, showing the D-1-MIX case, exhibits higher temperature variability, with peak-to-peak amplitude reaching nearly 20 °C within ~ 0.06 s, compared to the D-2-MIX case, where a change of about 10 °C occur within ~ 0.01 s.

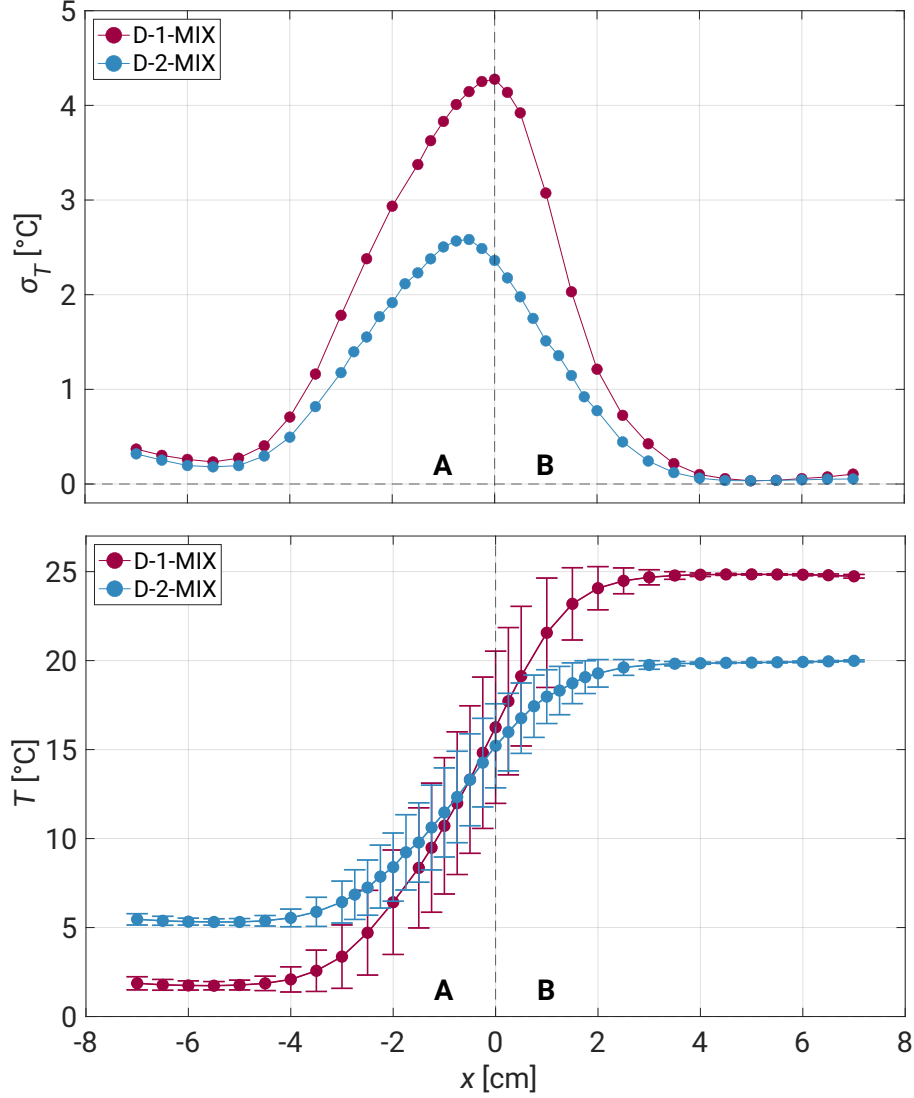


Figure 3.2: Standard deviation σ_T (top) and the overall T distribution in the measurement section (bottom), both plotted as a function of x . Error bars indicate σ_T , and the regions corresponding to the streams are marked as „A” and „B” at the bottom of each panel.

To better understand these temperature profiles, basic statistical tools have been employed. Top panel of Fig. 3.2 presents the standard deviation σ_T distribution for both cases, confirming the previous observations: in the central region, σ_T exceeds 4 °C in the D-1-MIX case, while for D-2-MIX, it reaches about 2.5 °C. The magnitude of the standard deviation gradually decreases as the sensor moves

toward the windows. Two interesting observations are worth mentioning. The first is a slight shift in the σ_T peak for D-2-MIX toward the A stream and a steeper right slope in the D-1-MIX σ_T distribution. The physics behind this behavior remains unclear due to the lack of additional data (e.g., velocity profiles), but it is presumably related to differences in the mixing dynamics of both cases. The second observation concerns the non-flat tails of both distributions near the left window. As mentioned in [Niedermeier et al. \(2020\)](#), the measurement section is not heat-insulated, and the small influence of outside conditions can be observed in the vicinity of the glass windows, particularly when the temperature difference between the lab and the air streams is significant (the lab temperature typically oscillates around 20 °C). For better context, the bottom panel of Fig. 3.2 presents the general T distribution within the measurement section.

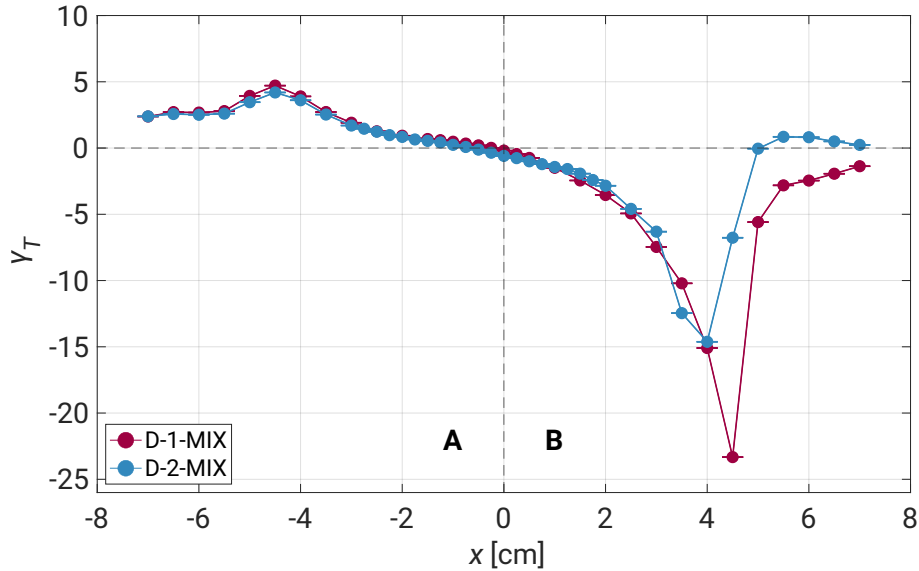


Figure 3.3: Skewness γ_T distribution in x . Uncertainties were calculated using formula $\lambda_{\gamma_T} = \sqrt{\frac{6M(M-1)}{(M-2)(M+1)(M+3)}}$ where M denotes the number of samples. At the bottom of the graph streams' regions are marked with „A” and „B”.

The third statistical moment, shown in Fig. 3.3, provides further insight into the temperature profile within the tunnel. The scalar distributions are nearly symmetrical in the central region but become increasingly skewed toward the windows, with two maxima at $x \approx -4.5$ cm and $x \approx 4.5$ cm, exhibiting opposite signs. In regions with lower stream temperatures, the positive maxima approach $\gamma_T \approx 5$, whereas for the warmer streams, the negative peaks do not overlap, reaching $\gamma_T \approx -15$ for D-2-MIX and $\gamma_T \approx -23$ for D-1-MIX. This strong asymmetry is not easy to explain. If external conditions were responsible, both sides of the tunnel would likely exhibit similar behavior. These two positions are equidistant

from both the most intense mixing region and the measurement section windows, meaning these regions could be affected by either thermal filaments from the central mixing or from the outside conditions. On the other hand, the magnitude of the „B” stream skewness might indicate the presence of an obstacle (e.g. other instrumentation) that could have slightly modified the flow near the UFT sensing element. However, verifying this hypothesis is extremely difficult, as the measurements were taken almost 6 years ago, and no such details were recorded in the experiment notes. It remains possible that both factors contributed to the observed measurements. The influence of external conditions is evident though near the windows. On the left side, temperature distributions remain positively skewed, with a constant value of $\gamma_T \approx 2.5$, whereas on the right side, they become more symmetrical as they approach the window.

3.1.2 Spectral analysis

In the next step, the signals were decomposed into discrete frequencies using Power Spectral Density (PSD) analysis with the Welch algorithm (window length of approximately 1/13 of the total segment and 50% overlap). Results from both experiments are presented in Fig. 3.4. The spectra for D-1-MIX and D-2-MIX exhibit a similar structure, with maximum PSDs characterizing the central mixing zone and a gradual shift toward lower spectral densities as the measurements approach the windows. While the overall PSD structure is comparable, in the middle of the tunnel, the spectral lines for D-1-MIX are an order of magnitude larger due to the stronger temperature difference between the two streams (25 K versus 16 K). Moreover, Nowak et al. (2022) reported a peak in humidity spectra at $f \approx 14$ Hz in the mixing zone, which the authors attributed to wave-like features arising from an inhomogeneous velocity profile in the central part of the tunnel (see Sec. 4.1 in Niedermeier et al. (2020)). No such effects are observed in the temperature spectra, most likely due to the difference between the UFT point measurements and the path-averaged humidity data. However, for the series corresponding to the $x \approx 0$ cm measurements, $P(f)$ maxima appear in the range of 12 to 16 Hz.

The averaged spectra over this frequency range are shown in Fig. 3.5. As expected, both distributions are relatively symmetrical around $x = 0$ cm, but this symmetry breaks at approximately ± 5 cm from the center, where local minima are observed, followed by an increase in PSDs. This observation aligns with the results in Fig. 3.3, suggesting that these regions experience least intensified dynamics events. Fig. 3.5 also provides additional evidence of the influence of external

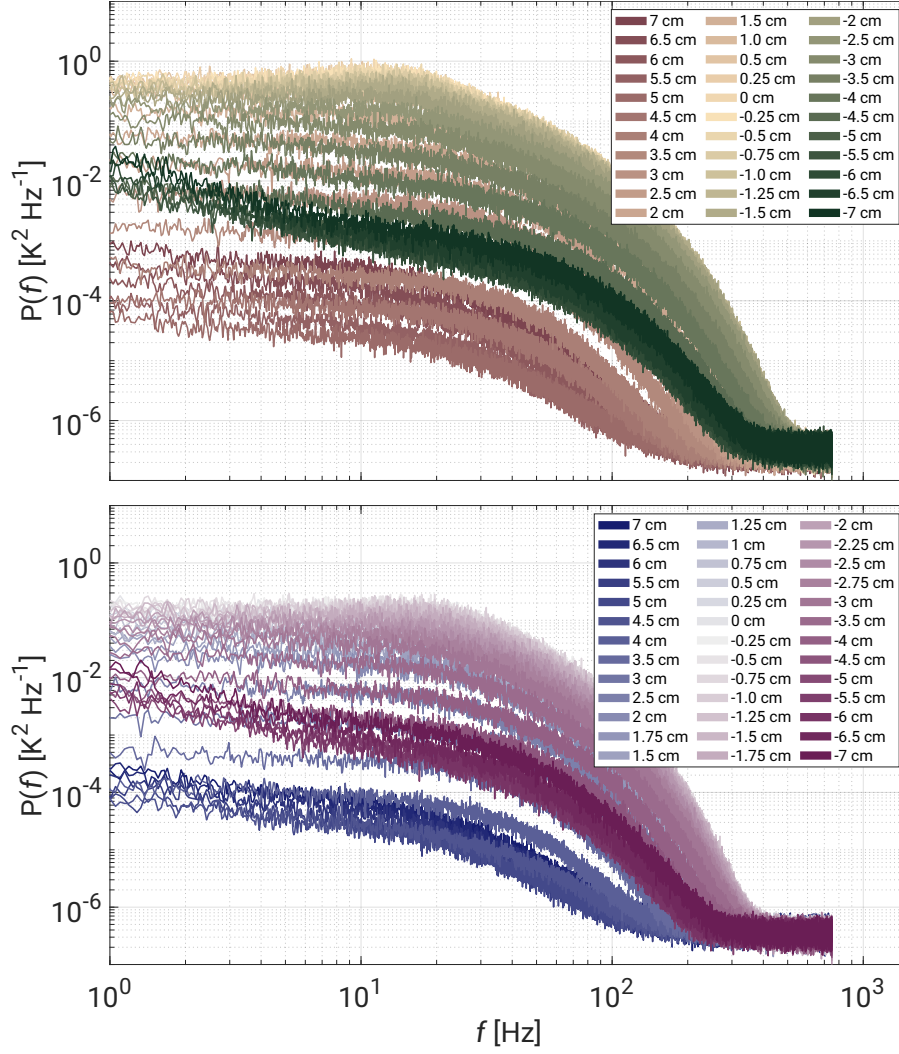


Figure 3.4: Frequency domain spectrum for D-1-MIX (top) and D-2-MIX (bottom). Color gradient represents horizontal scan along x -axis.

conditions within the measurement section, as the extrema differ by almost two orders of magnitude.

To normalize the spectral curves across different x positions, the scaling method proposed by [Zhou and Xia \(2001\)](#) was applied. This method employs the $f^2 P(f)$ function to determine peak frequencies f_p , around which the PSDs collapse into universal functions. Fig. 3.6 presents sample graphs for selected data from Fig. 3.5. To estimate the maxima, raw spectra were averaged over equidistant logarithmic frequency bins, yielding twenty three bins per decade, following the methodology described in [Siebert et al. \(2006b\)](#) and [Nowak et al. \(2021\)](#). For D-1-MIX, f_p oscillates around two frequencies, 47 Hz and 72 Hz, whereas for D-2-MIX, most peaks occur near 50 Hz. Notably, some $f^2 P(f)$ curves, especially near the „B” stream window, exhibit very weak extrema.

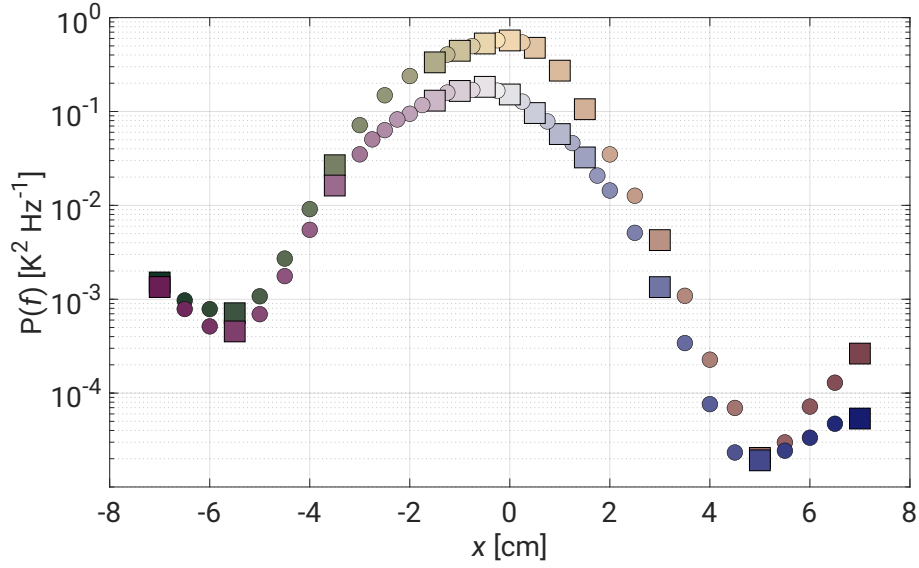


Figure 3.5: Spectrum from Fig. 3.4 averaged in a range of 12-16 Hz. Squares correspond with the data used in the following analysis.

The collapsed and non-dimensionalized form of selected curves from Fig. 3.4 is presented in Fig. 3.7. The first notable observation is that noise levels in both cases increase gradually, with lower noise magnitudes for data at $x \approx 0$ cm and significantly higher noise levels near the windows. Additionally, spectra from positions $x > 3$ cm exhibit reduced magnitudes with relatively flat slopes. To identify the corresponding spectral regimes, a linearity criterion was applied using the log-log Pearson correlation coefficient for resampled points. The sampled results for $x = 0$ cm are provided in Fig. 3.8, with the corresponding regime boundaries in the non-dimensionalized domain: 0.2, 0.5, 1.5, 4, and either 8 or 11, depending on the experiment (see Fig. 3.8). Assuming a mean vertical flow of $w = 1.3 \text{ m, s}^{-1}$ and $f_p = 50 \text{ Hz}$, these limits translate to approximate spatial scales of 13.0, 5.2, 1.7, 0.7, and either 0.3 or 0.2 cm, respectively. All the fitted power-law slopes are summarized in Fig. 3.9 along with the Pearson coefficients.

The first regime (13.0–5.2 cm) corresponds to tunnel dimensions and should thus be associated with the facility-affected range, with power-law slopes oscillating around -0.8 (D-1-MIX) and -0.5 (D-2-MIX). This is also the only range which is characterized by the Pearson coefficients higher than -0.9 since the remaining regimes are described mostly by near -1 values. Then we have relatively narrow inertial range between 5.2 and 1.7 cm with slopes of $\sim -5/3$. This observation aligns with Niedermeier et al. (2020) results which also reported not fully evolved inertial range in the TKE spectra basing on their experiments with uniform, dry conditions. The authors related this feature with a small Taylor-Reynolds number

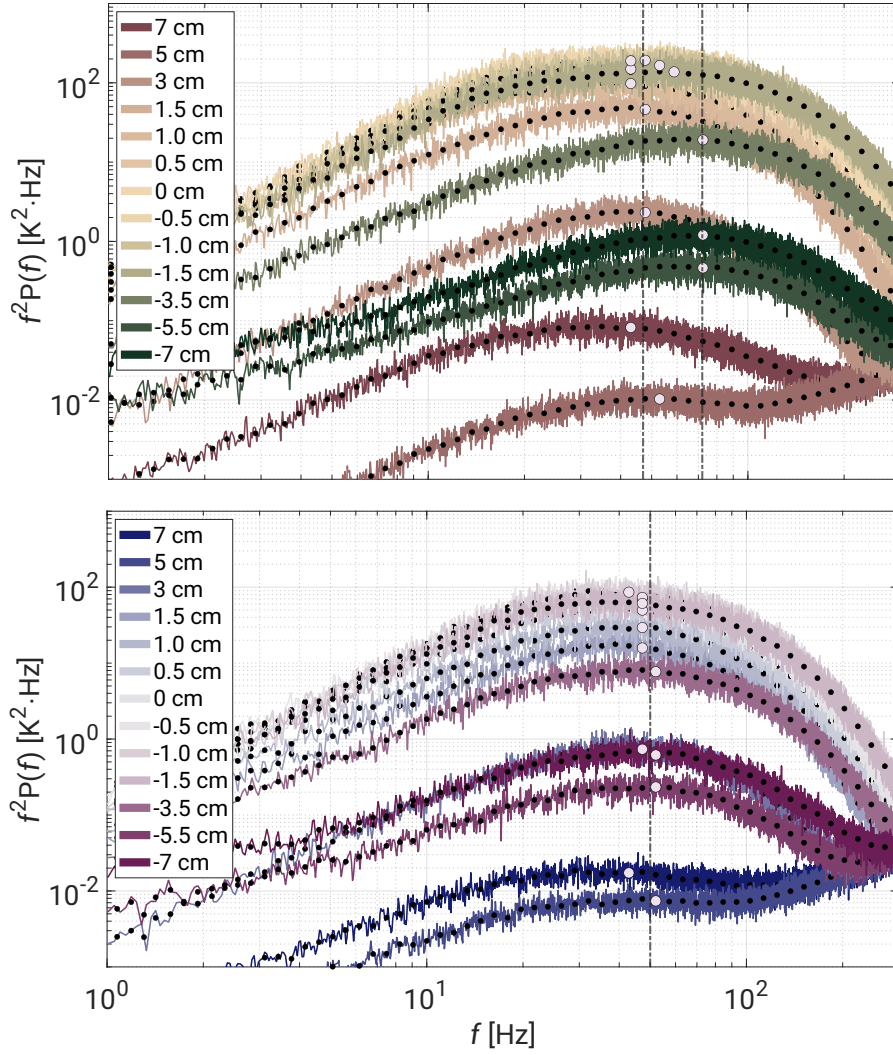


Figure 3.6: Scaled spectrum of $f^2 P(f)$ with marked mean f_p values for D-1-MIX (top) and D-2-MIX (bottom).

of $Re_\lambda = 30$ generated in the LACIS-T.

The dissipative regime is localized between 1.7 and 0.7 cm and is characterized by most diverse slopes (see Fig. 3.9). In the central positions they oscillate around -4 (D-1-MIX) and -5.5 (D-2-MIX) but the regions outside the mixing zone exhibit different behavior. The positions within the „B” stream have relatively similar slopes of ~ -4.5 despite the changing conditions. However, it seems that the region on the other side almost lacks the developed dissipative range since there are no significant differences with the inertial range slopes. Again at $x = 5$ cm the minimum is observed.

The last distinguishable regime lays between 0.7 and 0.3 or 0.2 cm and occurs merely in the mixing zone. These dimensions correspond with the size of the

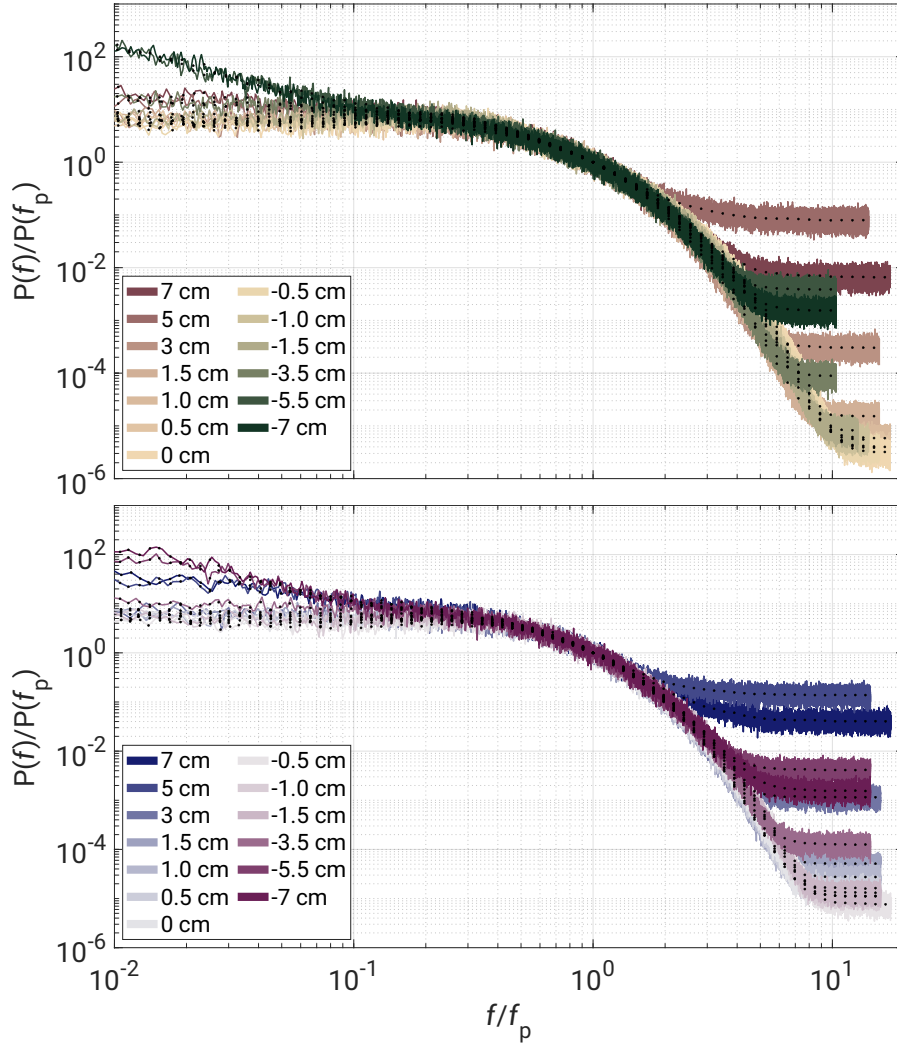


Figure 3.7: Scaled spectrum of $P(f)/P(f_p)$ versus $f/(f_p)$ for D-1-MIX (top) and D-2-MIX (bottom).

sensing element in the UFT which relates the observed range with instrument-affected regime. The instrument averages signals over its length, this is why the effect on the scales comparable to its sizes are then induced by its own action. The corresponding slopes are about -8.5 .

So far the scalar spectrum discussion focused on the power-law relations due to the fit simplicity and close to -1 values of the Pearson correlation coefficients. However, as noted in Pope (2000) to analytically study energy spectrum Eq. 1.4 can be supplemented with the non-dimensional functions f_l and f_η as follows

$$E(k) = C_K \langle \epsilon \rangle^{2/3} k^{-5/3} f_S(kS) f_\eta(k\eta). \quad (3.1)$$

The function f_S determines the shape of energy-containing range and tends to

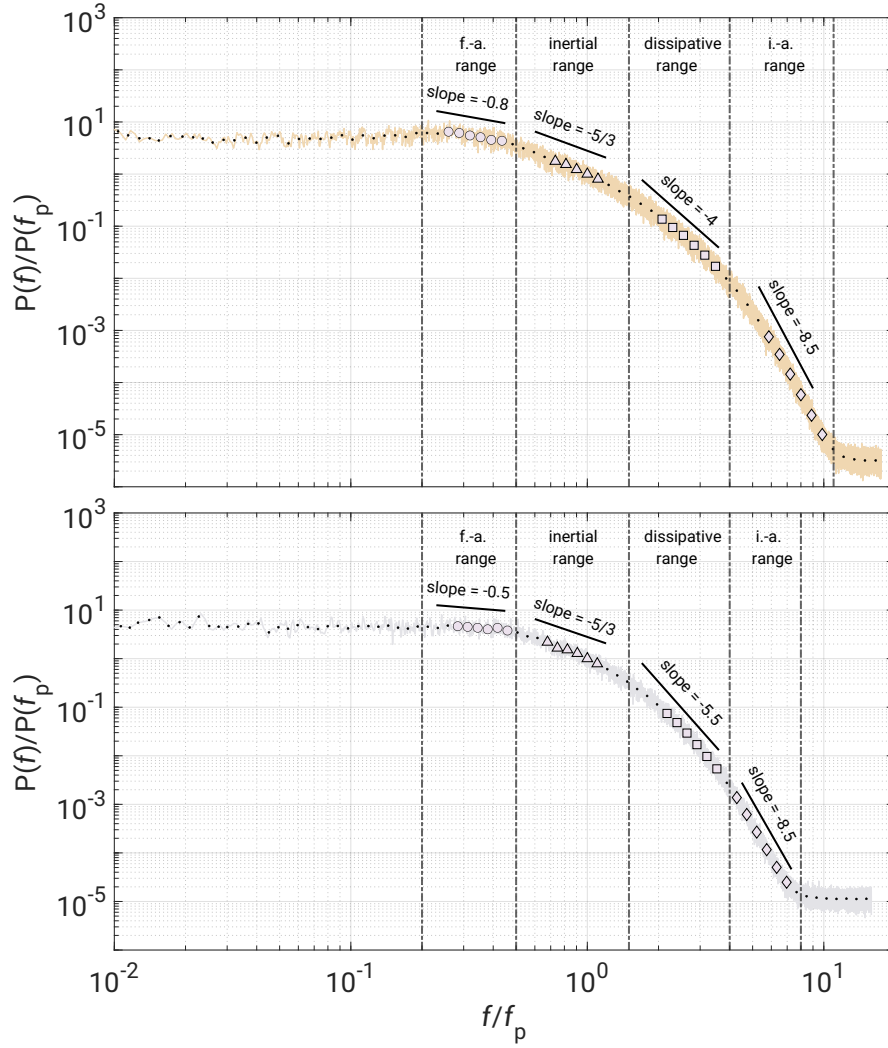


Figure 3.8: Scaled spectrum at $x = 0$ cm from Fig. 3.7. The regimes' limits are 0.2, 0.5, 1.5, 4, and 8 or 11 (depending on the experiment) which assuming the constant mean flow of 1.3 m s^{-1} and $f_p = 50 \text{ Hz}$ corresponds with the rounded spatial lengths of 13.0, 5.2, 1.7, 0.7, and 0.3 or 0.2 [cm] respectively. The top chart represents D-1-MIX and the bottom D-2-MIX.

unity for large kS . S here is a lengthscale defined as $K^{\frac{3}{2}}/\epsilon$ where K is the TKE. On the contrary, f_η describes the dissipative regime of a spectrum converging to unity for small $k\eta$. Both functions vanishes in the inertial range reducing Eq. 3.1 to the well known form of Eq. 1.4. There are three main f_η variants which can be used to characterize small-scale part of the energy spectrum. The most general is so-called Pope spectrum of a form

$$f_\eta(k\eta) = \exp(\beta\{[(k\eta)^4 + c_\eta^4]^{1/4} - c_\eta\}), \quad (3.2)$$

where following Pope (2000) $\beta = -5.2$ and $c_\eta = 0.4$. For $c_\eta = 0$ the above reduces

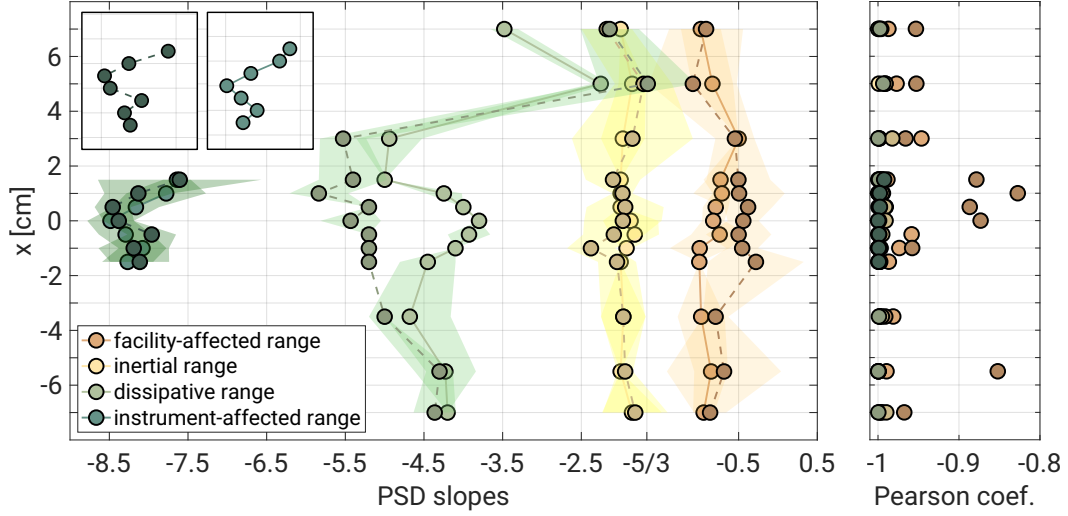


Figure 3.9: Scaled spectrum fit coefficients (left) and the Pearson correlation coefficients (right). The lighter color shades characterize D-1-MIX experiment whereas the darker color shades are assigned for D-2-MIX series. The zoomed instrument-affected range slopes are located in the upper left insets. The slopes are accompanied by 95% confidence bounds except in a few cases where the slopes were manually fixed due to fitting difficulties.

to simple exponential spectrum

$$f_{\eta}(k\eta) = \exp(\beta k\eta) \quad (3.3)$$

with $\beta = -2.1$. An alternative version of the spectrum is the Pao spectrum defined as

$$f_{\eta}(k\eta) = \exp(\beta \{k\eta\}^{4/3}). \quad (3.4)$$

In this case literature suggests that $\beta = -2.25$. Recently [Akinlabi et al. \(2019\)](#) showed with the DNS velocity spectra from stratocumulus cloud-top mixing layer that Eq. 3.2 provides a better fit. A similar approach, investigating the application of Eq. 3.2 in passive scalar spectra, was explored in the numerical study by [Wang et al. \(1999\)](#), where the authors obtained coefficients very similar to those reported in [Pope \(2000\)](#). However, to the best of the author's knowledge, no experimental verification has been conducted yet. Consequently, Eq. 1.5 transforms as follows:

$$E_{\theta}(k) = C_O \langle \epsilon_{\theta} \rangle \langle \epsilon \rangle^{-1/3} k^{-5/3} f_{\eta}(k\eta). \quad (3.5)$$

To employ this methodology the spectra need to be translated from frequency to wavenumber domain utilizing the following transformations:

$$k \approx \tilde{f} = 2\pi f/w,$$

$$P(k) \approx P(\tilde{f}) = P(f)w/2\pi.$$

where $P(\tilde{f})$ and \tilde{f} represent the scaled frequency spectrum and the scaled frequency respectively. The usual way of presenting such spectra includes the Kolmogorov length scale, defined as $\eta = (2\pi)/k_\phi$, with k_ϕ being the wavenumber noise level. Then the scaled $P(k\eta)$ spectrum was adapted to repeat the methodology of equidistant bin separation and the procedure of [Zhou and Xia \(2001\)](#). Fig. 3.10 presents the estimation of $k_p\eta$, what is a direct analogy to f_p in the scaled $k\eta^2 P(k\eta)$ spectra.

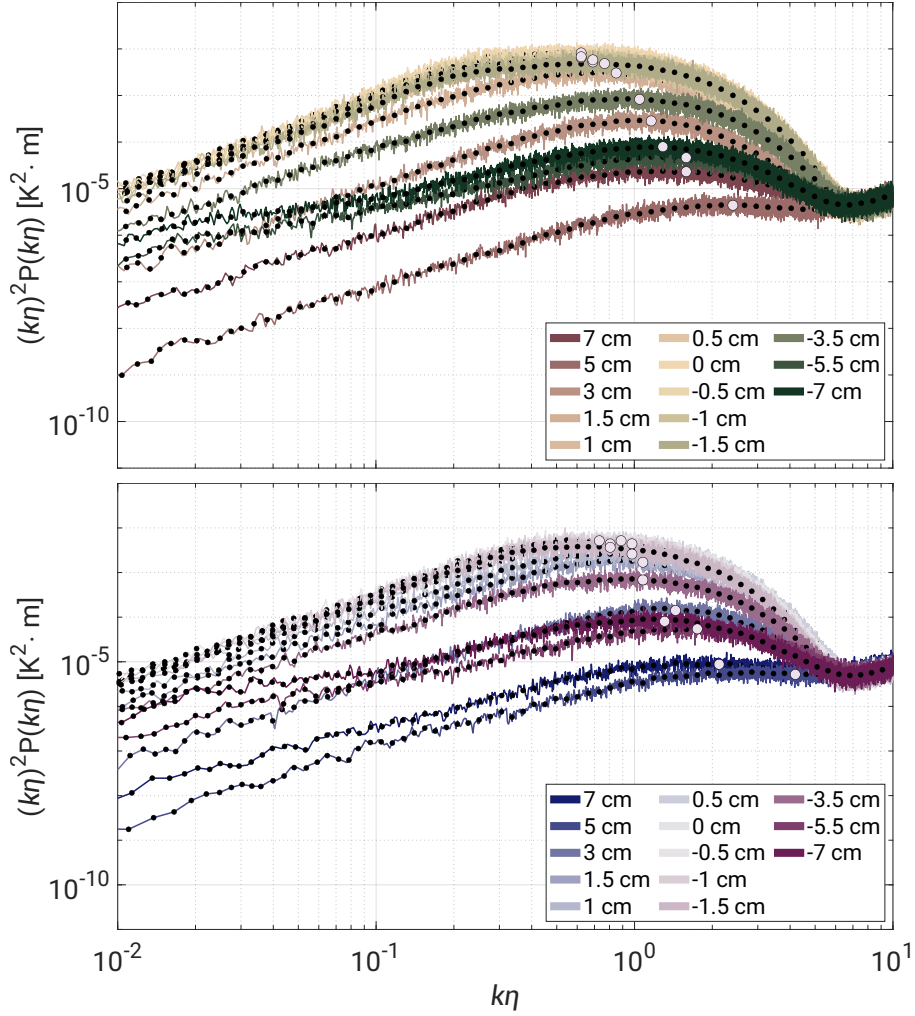


Figure 3.10: Analogical to Fig. 3.6 scaled spectra of $k\eta^2 P(k\eta)$ versus $k\eta$ for D-1-MIX (top) and D-2-MIX (bottom) cases.

Unlike the corresponding plot in the frequency domain (see Fig. 3.6), $k_p\eta$ variables do not oscillate around one value. Here, a gradual increase in $k_p\eta$ values towards

the windows regions is observed, spanning the $k\eta^2 P(k\eta)$ values between ~ 0.6 to ~ 4 . Note that the curves representing the $x > 3$ cm positions have relatively flat curvature in area where the maxima are expected which corresponds with the observations from Fig. 3.6.

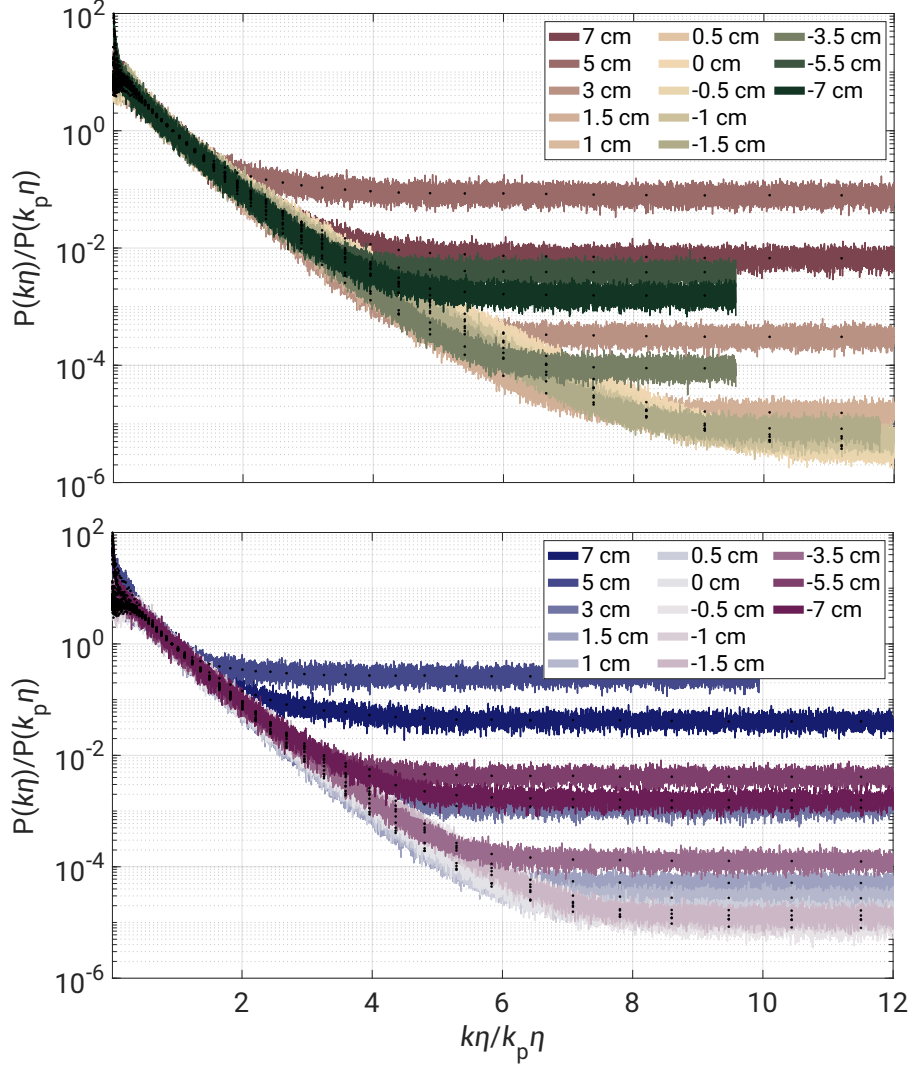


Figure 3.11: Dissipative branch of the spectra scaled in wavenumber domain for D-1-MIX (top) and D-2-MIX (bottom) cases.

Fig. 3.11 shows $P(k\eta)/P(k_p\eta)$ versus $k\eta/k_p\eta$ dissipative branches of the spectra from Fig. 3.7 in logarithmic-linear picture. Conclusions can be made similar to those raised before, the noise level is significantly lower in the positions near the center where the turbulence is more developed, and the near windows regions have very short dissipative branches which is especially evident on the „B” side.

The last step involved fitting the curves from Eq. 3.2, 3.3, and 3.4 in the dissipative regime marked in Fig. 3.8. The results for $x = 0$ cm cases are presented

in Fig. 3.12. In the given range all functions are accurate mostly overlapping each other. However, outside the limits and further at even smaller scales the Pao spectrum outlines the data suggesting that the Pope and exponential formulas might be a better choice. Worth noting here is also the fact that D-2-MIX curve has shorter scaled spectrum reaching the noise level at $k\eta/k_p\eta \approx 7$ whereas for D-1-MIX it happens at $k\eta/k_p\eta \approx 11$. Similarly, the noise level itself is located lower for the case of higher temperature difference between the streams which clearly indicate more intensified and more developed turbulence presence in D-1-MIX experiment.

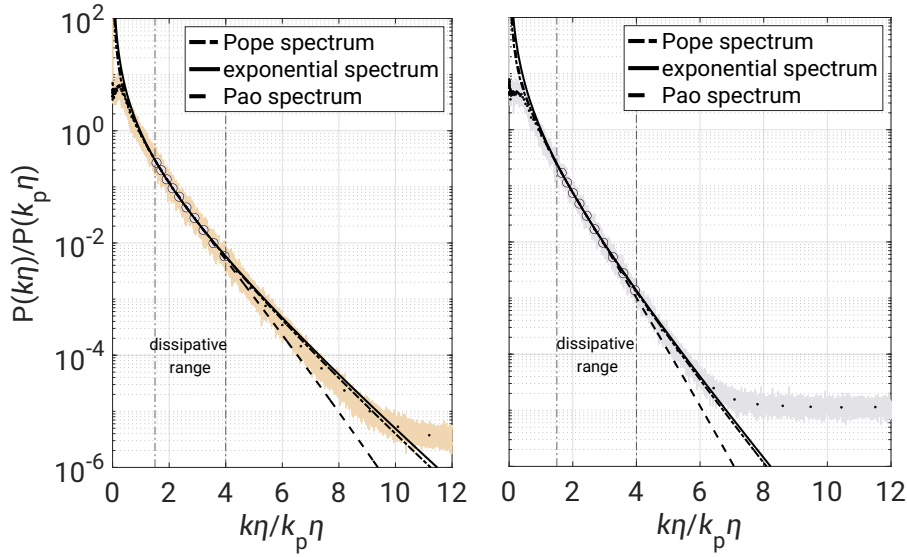


Figure 3.12: Dissipative branch of the spectra scaled in wavenumber domain at $x = 0$ cm. The fitted curves represent Eq. 3.2, 3.3, and 3.4. Graphs show D-1-MIX (left) and D-2-MIX (right) cases.

Fig. 3.12 shows the fittings characterizing only the central position but the same procedure has been performed in the remaining locations along x . The spectra exhibit no evidence of additional regime but rather gradual decrease up to the noise level suggesting that the sensor itself had minimal effect on the spectra shapes. Ultimately, the results are coherent proving that the Pope and exponential equations describe the dissipative regime in the LACIS-T better. This is why the summary graph in Fig. 3.13 provides merely the coefficients from these two formulas along with the Pearson correlation coefficients excluding also some the data from $x > 3$ cm due to the lack of developed dissipative branches in the data from these regions.

In general, the differences between β coefficients among the both formulas are minor suggesting that even the simplest exponential fit from Eq. 3.3 can characterize the spectra with satisfactory effectiveness. The β coefficients are in

a range from ~ -1 to ~ -2 which only approach the reported values in Pope (2000) but it is understandable considering small Taylor-Reynolds number. The corresponding c_η coefficients span between 0 and ~ 1.5 with most nonzero values localized in the central area of the tunnel demonstrating that the turbulence there is complex.

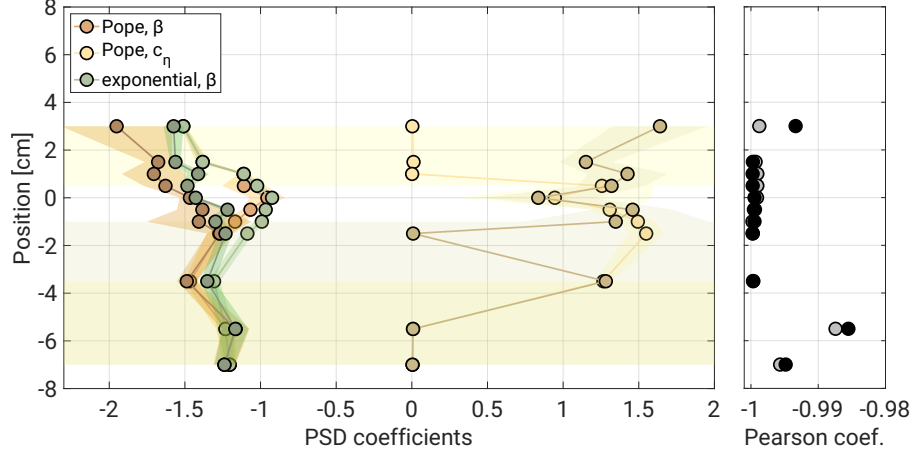


Figure 3.13: Fit coefficients for the scaled spectrum in wavenumber domain (left) and the Pearson correlation coefficients (right). The lighter color shades characterize D-1-MIX experiment whereas the darker color shades are assigned for D-2-MIX series. The coefficients are accompanied by 95% confidence bounds.

The near-zero c_η coefficients are accompanied by large 95% confidence bounds, which might result from numerical calculations. On the other hand, the spectra coefficients of the „A” stream show much simpler characteristics with mostly insignificant differences between both formulas.

The dissipative branch data in the „B” stream exhibits the opposite properties though revealing some form of a trend in the β coefficient leading to smaller values with respect to $x \approx 0$ cm spectra. It remains unclear whether it is directly related with the effect discussed before. The corresponding Pearson coefficients are close to negative unity confirming the proper dissipative range distinction.

3.2 II Chamber

A detailed description of the experiments conducted in the II Chamber along with the extensive analyses can be found in the preprint Grosz et al. (2024) whereas its accepted version is added in Appendix C. In the given section only major results will be presented.

Small-scale temperature profiling revealed significant variations in the distribution of temperature fluctuations near the top and bottom surfaces. In particular,

both the standard deviation (see Fig. C.5) and skewness (see Fig. C.6) showed noticeable changes. Although measurements taken over 19 min and 3 min were generally consistent, the shorter records exhibited higher variability in both moments. These variations were attributed to the dynamics of local thermal plumes and their interaction with the LSC. Data analysis suggested that topographic effects did not introduce major differences, likely due to the limited length of the time series (see last paragraph of Sec. C.3.1). However, recent numerical studies in the chamber suggest that rough boundaries can enhance thermal plumes and amplify temperature fluctuations, while varying bar heights may cause LSC reorientation and changes in thermal stratification (Zanganeh et al., 2024).

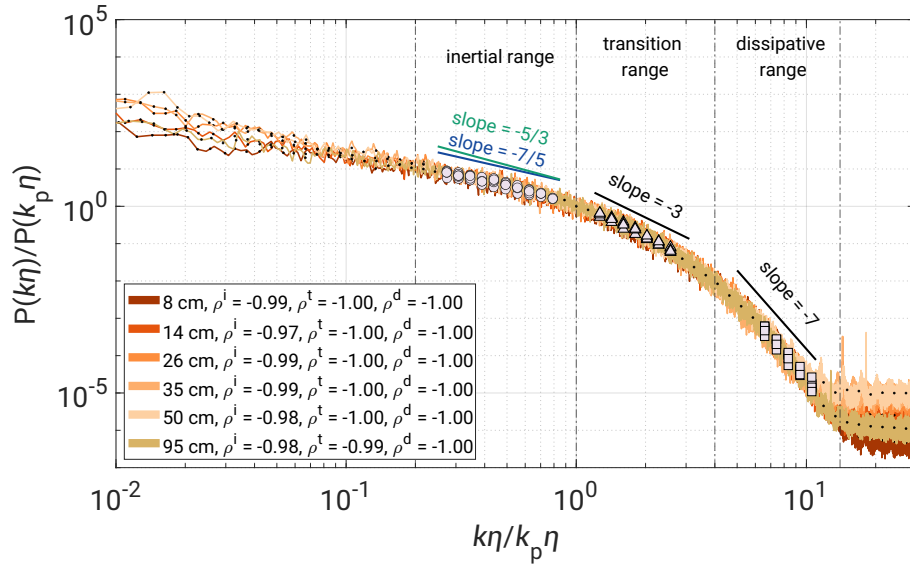


Figure 3.14: Scaled spectra for V20-S-L case in wavenumber domain with three defined regimes: inertial range (circles, $0.2 \leq k\eta/k_p\eta \leq 1$), transition range (triangles, $1 \leq k\eta/k_p\eta \leq 4$), and dissipative range (squares, $4 \leq k\eta/k_p\eta \leq 20$). Legend includes the Pearson correlation coefficients denoted as p . Figure from Grosz et al. (2024).

Further insights were gained through the PSD analysis, which revealed a periodicity in the LSC that varied with the temperature difference (see Fig. C.7). The observed periodicity was modeled by the power-law formula $\tau^e = 21.3 + 282.4 \cdot \Delta T^{-0.7}$, which was consistent with previous results by Anderson et al. (2021). Three distinct dynamic regimes were identified (see Fig. 3.14): an inertial range (slope $\sim -7/5$), a transition range (slope ~ -3), and a dissipative range (slope ~ -7). While it was unclear whether the spectra followed BO or OC scaling, the slopes were too close to be easily distinguished. However, they were slightly biased toward $\sim -7/5$, which is characteristic of thermal convection (see Subsec. 1.2.3). The scale break between the inertial and transition ranges

was attributed to a dynamic shift from an LSC-dominated regime to a thermal plume regime. The complementary discussion in the paper noted that a similar temperature spectra scaling of -2.7 was reported in the works of Chen and Bhaganagar (see Subsec. 1.2.3). In the II Chamber experiments, temperature acted as an active scalar, potentially coupling the vector and scalar fields and introducing nonlinear effects into the system. Additionally, variations in spectral scaling were observed near the surface, while turbulence in the chamber’s center resembled homogeneous, isotropic turbulence (see Fig. C.10). These differences were also attributed to the behavior of local thermal plumes and their interaction with the LSC (see the extended discussion in Sec. C.3.2).

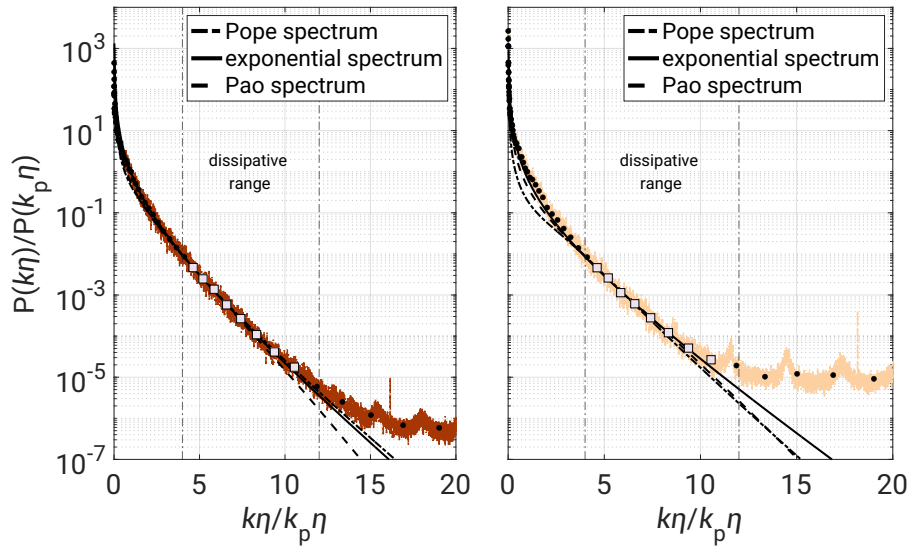


Figure 3.15: Dissipative branch of the spectra scaled in wavenumber domain at $h = 8$ cm (left) and $h = 50$ cm (right). The fitted curves represent Eq. 3.2, 3.3, and 3.4. Graphs made for the V20-S-L case.

To study the dissipative regime in more detail, the analysis related to Fig. 3.12 was repeated using the temperature time series from the II Chamber. The limits defining this regime were slightly adjusted, shifting the upper bounds toward smaller values for a better fit. Ultimately, three formulas—Eq. 3.2, 3.3, and 3.4—were fitted to the data, showing good agreement. The results for two distinct vertical locations are presented in Fig. 3.15. As before, there were minor differences between the fitted curves, with slight indications that the Pope and exponential spectra provided better fits. A notable distinction between the graphs is the change in noise levels, which is also observable in Fig. 3.14. When comparing both facilities in terms of dissipative regimes, it is worth to compare the dimensional limits. In the case of the wind tunnel, these were 1.7 cm to 0.7 cm, constrained by the presence of an instrument-affected regime at smaller scales.

In the RBC chamber data, the dimensional limits ranged between 6.3 mm and 2.1 mm (assuming $f_p = 4$ Hz and a mean flow of 0.1 m s^{-1}), suggesting that the regime could also be influenced by instrument properties.

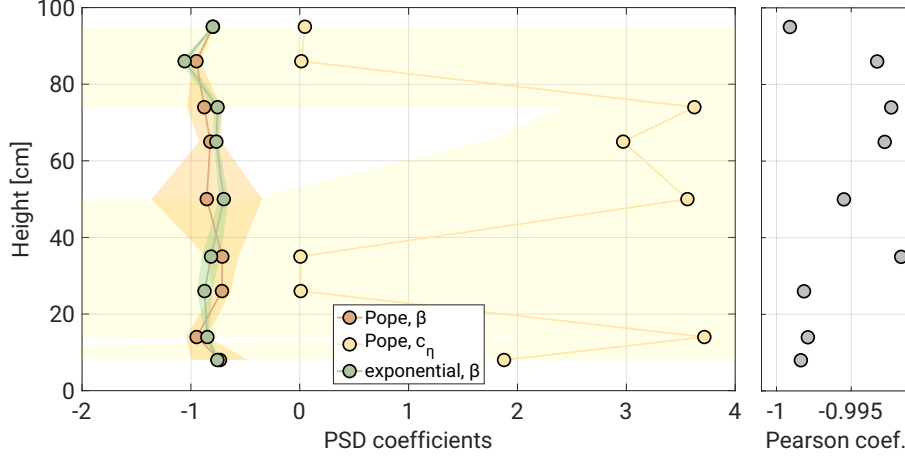


Figure 3.16: Fit coefficients for the scaled spectrum in wavenumber domain (left) and the Pearson correlation coefficients (right). Graphs made for the V20-S-L case. The coefficients are accompanied by 95% confidence bounds.

However, as Fig. 3.16 indicates, the β coefficients for both the Pope and exponential spectra are uniform across the volume and resemble those observed in the center of the wind tunnel ($\beta \approx -1$), arguing that the UFT itself had a minimal impact on small-scale scaling in the II Chamber study. This implies also that events at smallest scales are independent of large-scale processes, resulting in more universal scalar scaling in the dissipative regime. Again, the near-zero c_η coefficients are accompanied by large 95% confidence bounds, which might result from numerical calculations.

Finally, the experimental results from the II Chamber experiments showed convincing agreement with the DNS conducted under similar thermodynamic conditions, a rare comparative analysis in this field (see Sec. C.3.3 along with Fig. C.11 and C.12). Velocity profiles further supported the interpretation of thermal plume dynamics, and a method for converting spectra from the frequency to the wavenumber domain (see Fig. 3.14).

Field experiments

4.1 Cloud boundaries

One of the objectives of the EUREC⁴A campaign was to study convective cloud formation using four heavily instrumented research aircraft (see Subsec. 2.4.1). Among them, the BAS Twin Otter conducted seven flights equipped with the fine-scale temperature sensor UFT, sampling cumulus cloud shells and sub-cloud layers at various altitudes. The atmospheric conditions and measurement strategy are described in Subsec. 2.4.2. Figure 4.1 presents a sample temperature and pressure time series from Flight F4, which is considered the most representative due to its rich cloud segment statistics (84 segments in total) observed between 950 and 800 hPa.

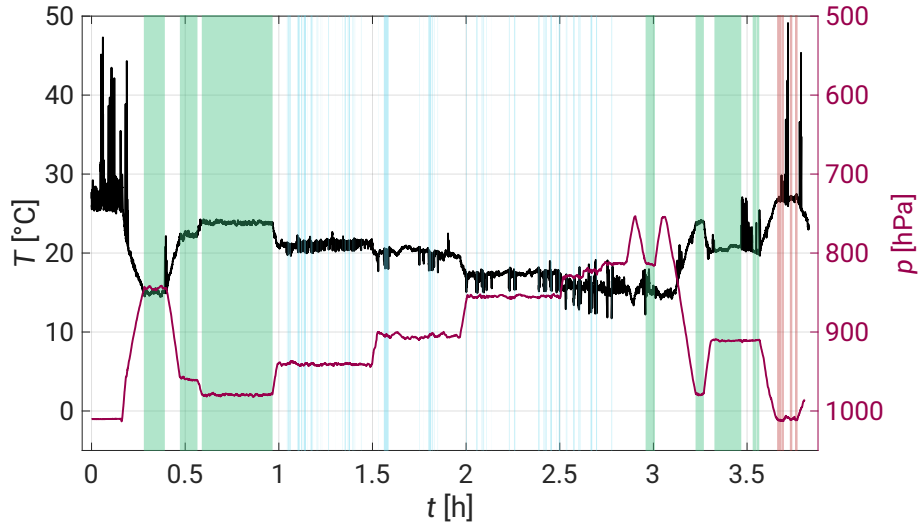


Figure 4.1: Temperature and pressure time series from the F4 flight, with cloud segments (blue), boundary layer segments (red), and free atmosphere segments (green) highlighted

This flight will be used to highlight key thermal properties in the following dis-

cussion, while temperature time series from the remaining flights are provided in Appendix A.

As discussed in Subsec. 1.1.3, cloud boundaries should be defined in terms of thermodynamic and microphysical properties. The top panel in Fig. 4.2 presents sample 8 min cloud segments from Fig. 4.1, accompanied by LWC time series. Notably, the segments satisfying the LWC threshold ($\text{LWC} \geq 10^{-3} \text{ g m}^{-3}$), used to identify cloud masks, coincide with significant temperature variability. Following this, in the present study, cloud positions are identified using LWC data, while the edges are recognized based on strong temperature fluctuations, relying on high-resolution UFT-2B measurements.

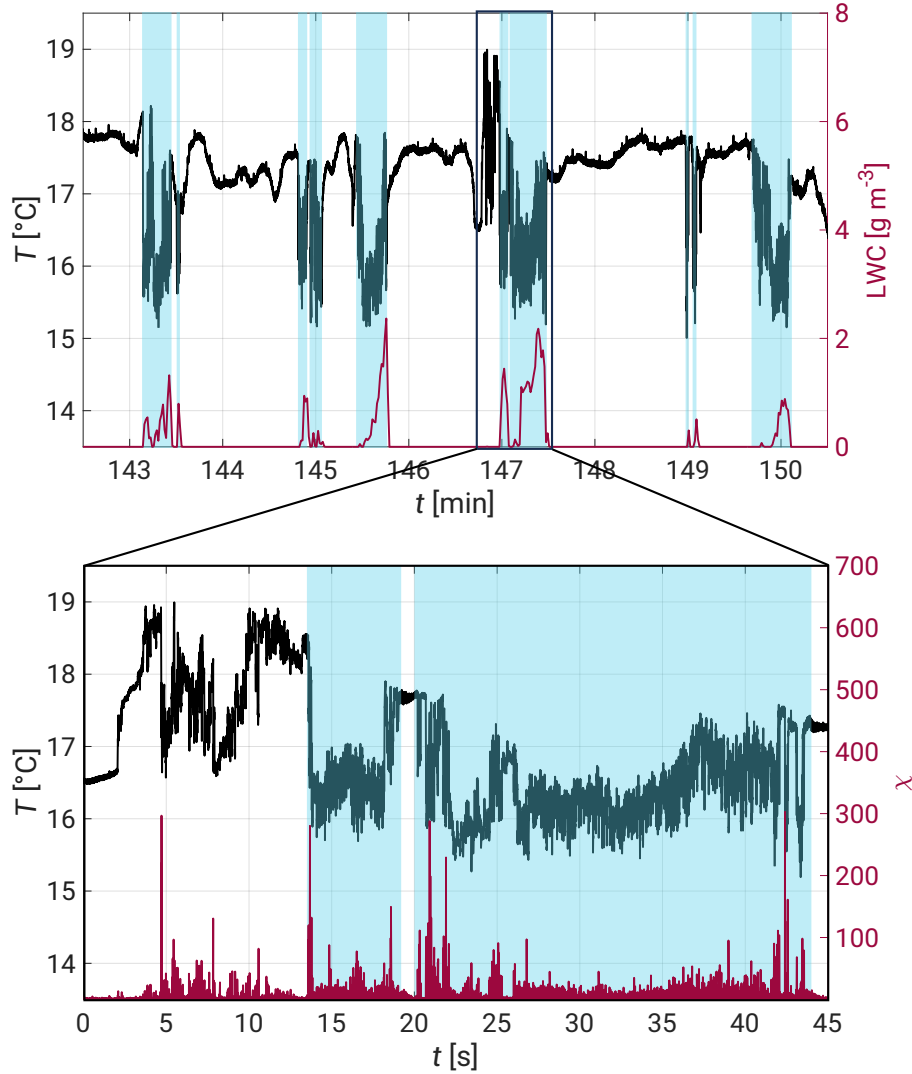


Figure 4.2: Sample cloud region from Fig. 4.1 versus LWC data (top) and a zoomed-in cloud with the χ series (bottom).

In this example, temperature decreases by approximately 2 °C at the clouds

boundaries and exhibits strong fluctuations within the cloud interiors. The bottom panel of Fig. 4.2 provides a zoomed-in view of two segments. Initially, the temperature remains stable but rises by about 2 °C after ~ 2 s, fluctuating strongly just before cloud penetration which may be associated with a detrained air masses forming a downdraft descending along the cloud boundary. Such flow can eventually create a subsiding shell around the cloud (see Subsec. 1.1.3). A subsequent sharp temperature drop (~ 2 °C) coincides with an increase in LWC, indicating that the aircraft crossed the cloud’s dynamic boundary. The following fluctuations suggest the presence of complex processes within the cloud volume, including turbulent mixing and phase transition. After exiting the cloud, the temperature rises and stabilizes for about a second before dropping again, marking another cloud penetration.

The clouds in Fig. 4.2 observed on Jan. 28 and at approximately 850 hPa, were penetrated by the aircraft at mid-height and exhibited lower temperatures compared to their surroundings. This phenomenon may be attributed to the environmental conditions during the early stage of convection, which were influenced by the ocean (water vapor supply). The air masses likely experienced substantial positive buoyancy forcing, contributing to humidity variations (Nowak et al., 2025), ultimately leading to the observed temperature gradient in the cloud segments during EUREC⁴A.

4.2 Temperature dissipation in atmosphere

Sec. 1.3, and more precisely Eq. 1.6, gives a canonical formula to estimate temperature dissipation rate in flows. However, for this study a normalized version was developed in which the actual dissipation rate is divided by the norm of the averaged dissipation estimated over a given segment. Assuming validity of Taylor frozen hypothesis, the partial derivative can be substituted by $\partial_i = -\frac{1}{U}\partial_t$ (where U represent the mean velocity $U = \sqrt{u^2 + v^2 + w^2}$) and then translated into the discrete domain. As a result, the obtained normalized dissipation formula yields

$$\chi = \frac{\delta T^2}{\langle \delta T \rangle^2}, \quad (4.1)$$

where δT represents here temperature differences between the consecutive time series records. The bottom panel of Fig. 4.2 shows sample χ series in just before the cloud penetration began and its variability inside the cloud volume. Notably, the highest value spikes are within approximately the cloud margins on both sides of the horizontal passage reaching about 300 whereas the regions of significant

temperature fluctuations within the cloud cores generally correspond with values below 50. The χ variability just before the cloud boundary exhibits relatively similar characteristics which indicate some cloud related dynamic effects.

During the EUREC⁴A aircraft operations, not only were clouds studied, but also the general mechanisms of convection to better address key scientific questions (see Subsec. 2.4.1). To achieve this, the Twin Otter conducted horizontal flights at different altitudes—below, between, and above clouds. In the first case, the aircraft typically flew at an altitude corresponding to the nearby BCO station. Figure 4.3 presents a 10 min sample temperature series from the lower boundary layer, along with a zoomed-in segment and χ fluctuations.

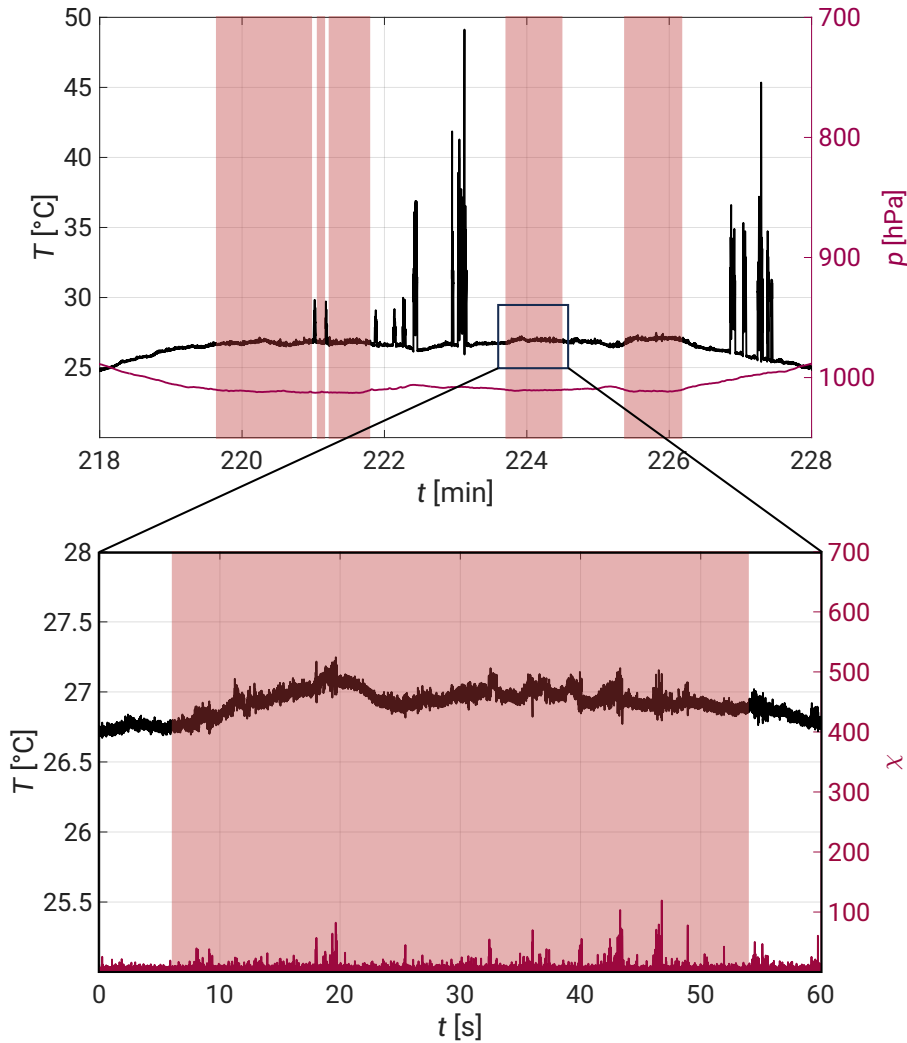


Figure 4.3: Sample boundary layer region from Fig. 4.1 (top) and a zoomed-in segment with the χ series (bottom).

The graph illustrates a relatively weak temperature dissipation rate, with values typically below 30, corresponding to a stable temperature level with an amplitude

not exceeding 1 °C. The spikes visible in the top panel of the figure are electronic artifacts caused by aircraft pilot conversations. These artifacts were excluded from the analysis through selective masking, as evident in the figure.

Similarly, the top panel of Fig. 4.4 presents analogous results from a selected free atmosphere region. It covers a 50 min segment measured at different altitudes, with a zoomed-in fragment shown in the bottom panel. This segment corresponds to a typical cloud height but lacks an LWC signature above the adopted threshold.

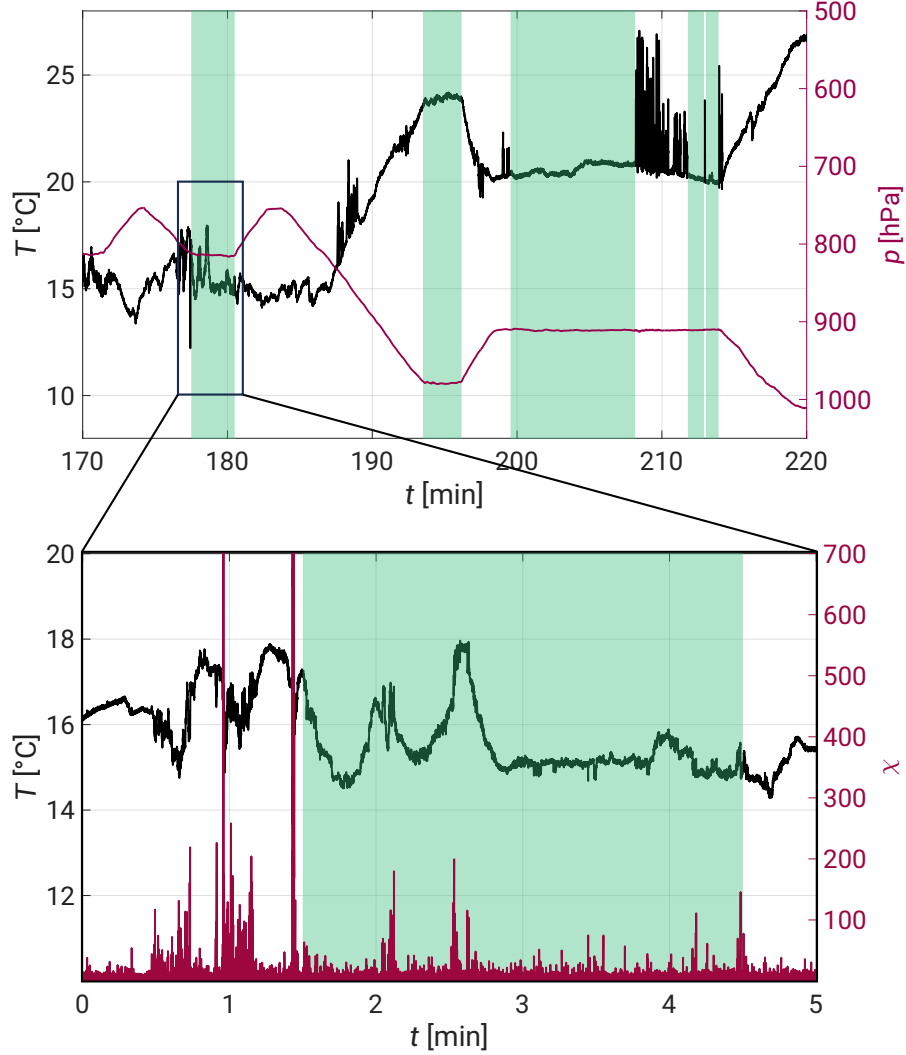


Figure 4.4: Sample free atmosphere region from Fig. 4.1 (top) and a zoomed-in segment with the χ series (bottom).

The plot is accompanied by the χ distribution, revealing interesting observations. The region marked in green exhibited temperature variability of a comparable magnitude to that observed in typical clouds during this experiment; however, the timescale of these changes differs. Based on the average aircraft velocity, the ~ 2.5 °C rise and drop occurred over a distance of nearly 2 km. This temperature

change could be attributed to local warm convective air masses, for example. Similarly, the variability observed just before the green-marked region may result from analogous processes. Additionally, it is important to note that during this time, the aircraft was changing its altitude, which could have further intensified the observed variations. The cause of the large χ events remains unclear, as they exceed the referential maximum scalar fluctuations typically associated with the identified clouds. These events cannot be attributed to electronic artifacts or sensor wetting and are characterized by a timescale of less than a second.

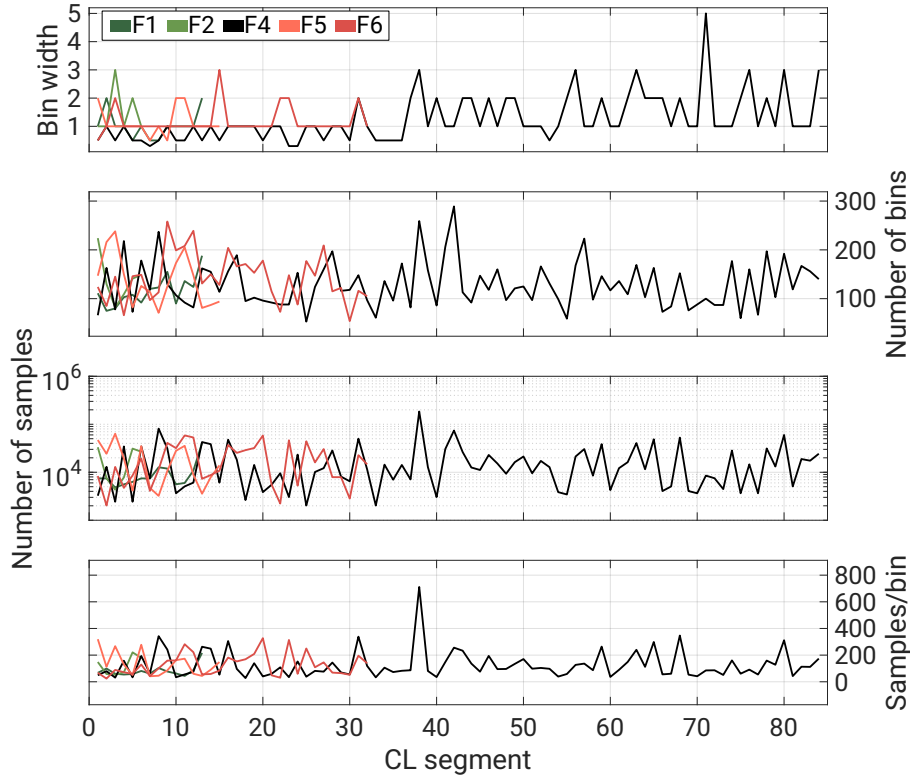


Figure 4.5: Temperature dissipation rate distribution statistics charts with respect to all identified clouds segments from 5 flights. The data is presented in the order of the flight timeline.

So far, the discussion has focused on analyzing specific flight segments to highlight different temperature features observed during the airborne experiments. To provide a broader perspective on temperature dissipation rates in clouds, Fig. 4.5 presents extended χ distribution statistics. The top panel shows bin width characteristics for each identified cloud segment. The binning method follows the Freedman-Diaconis rule, which is less sensitive to data outliers in heavy-tailed distributions. The resulting bin widths range from 0.3 to 5. In F4 data, bin widths increase in the latter part of the flight, likely due to higher temperature variability in these clouds (see Fig. 4.1). The subsequent panels display the

distribution of the number of bins (typically between 50 and 300), the number of samples (ranging from 10^3 to 10^5 , with a logarithmic scale), and the average number of samples per bin (between 20 and 800).

The corresponding statistics for boundary layer and free atmosphere segments are provided in Appendix B.

It should now be determined whether significant differences exist between the analyzed segment types and, if so, to what extent. Sample χ histograms are shown in Fig. 4.6, where each point represents the apex and center of a bin, normalized through the probability density function. To facilitate visual comparison, the distributions were further normalized by dividing the number of counts per bin (N_b) by $N_b(\chi = 6)$. The resulting histograms exhibit a relatively similar behavior, with most data characterized by low temperature dissipation rates, while the highest χ values occur least frequently, both contributing to elongated distribution tails. On the other hand, the mid-range values display a quasi-exponential spread this is why simple power laws in a form $N_b = A \cdot \chi^B$ have been fitted.

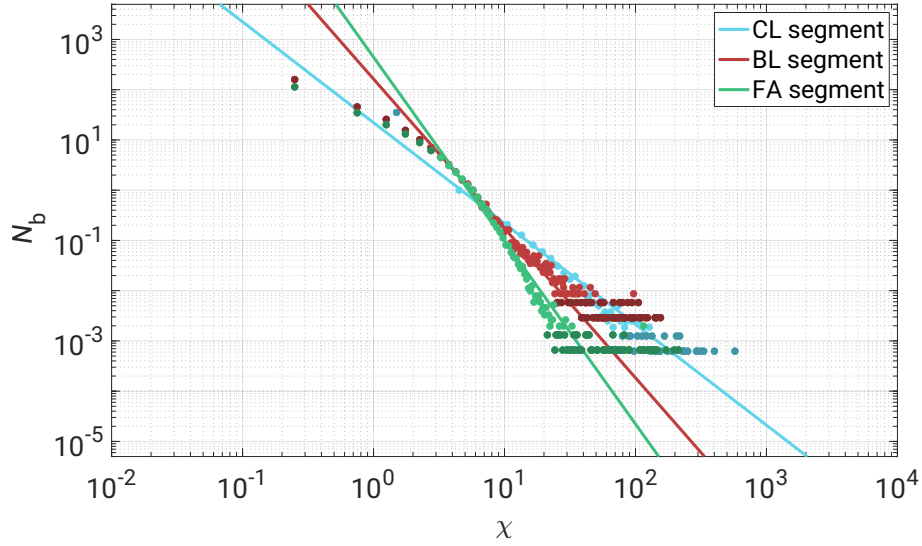


Figure 4.6: Sample normalized χ histograms representing the three discussed segment types: cloud (blue), boundary layer (red), and free atmosphere (green). N_b stands for the normalized number of counts per bin. The fitted power-law curves refer to light-colored points.

Typically, free atmosphere segments exhibit steeper slopes compared to boundary layer and cloud regions, with longer χ tails characteristic of high dissipation rates. This may result from a more uniform temperature structure, occasionally disrupted by strong fluctuations, such as the previously discussed downdrafts and detrained air masses at cloud-forming altitudes. In contrast, boundary layer and cloud segments display a more gradual incline, suggesting that higher tempera-

ture variability is more frequent in these structures. No clear distinctions between these two segment types have been observed.

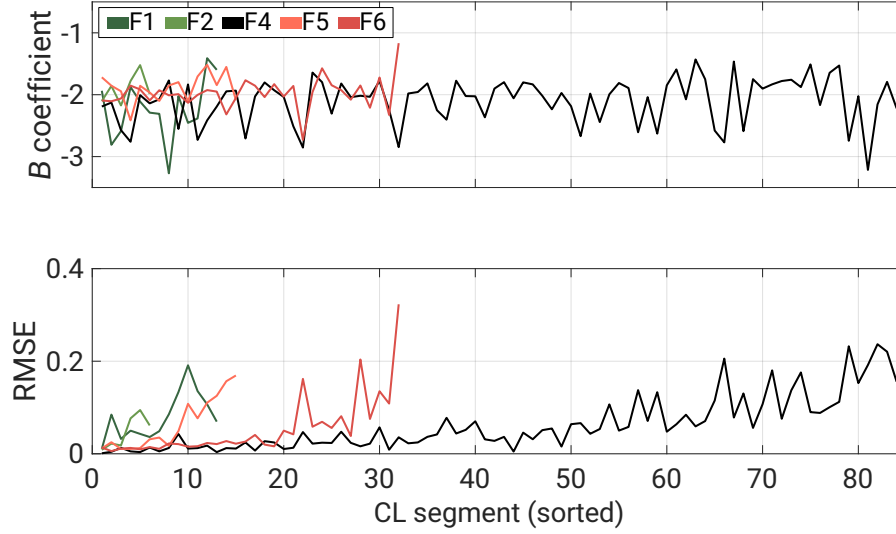


Figure 4.7: Power-law slopes for all identified cloud segments (top) with the corresponding RMSE (bottom).

Fig. 4.7 presents the fitted B coefficients along with root mean square errors (RMSE) for all identified cloud segments. The values are sorted in ascending order based on the average number of samples per bin, as shown in Fig. 4.5. The resulting slopes predominantly fall within the range of -3 to -2.5 , with no apparent trend or correlation with the sorting methodology. However, the corresponding RMSE distribution exhibits an increase as the data volume grows. This pattern is observed across all flights, albeit with varying magnitudes, and its origin remains unclear. According to [Stephan et al. \(2021\)](#), only during the F1 and F2 experiments was the deepening of the moist layer correlated with an increase in both cloud-top height and trade-wind inversion height (see Subsection 2.4.2). However, no additional thermodynamic variability was reported that could have significantly influenced the temperature structure of the selected segments. A possible explanation for the RMSE increase with data volume could be related to limitations in power-law applicability or more complex temperature profiles within the segments. Nevertheless, considering the analyzed data and the average RMSE magnitude, the applied methodology yields satisfactory results with good efficiency.

Fig. 4.8 presents analogous statistics to Fig. 4.7, this time characterizing BL segments. The fitted B coefficients fall within a similar range and do not exhibit any discernible trend. The corresponding RMSE series show no clear correlation with the average number of samples per bin, except for the F4 dataset, which

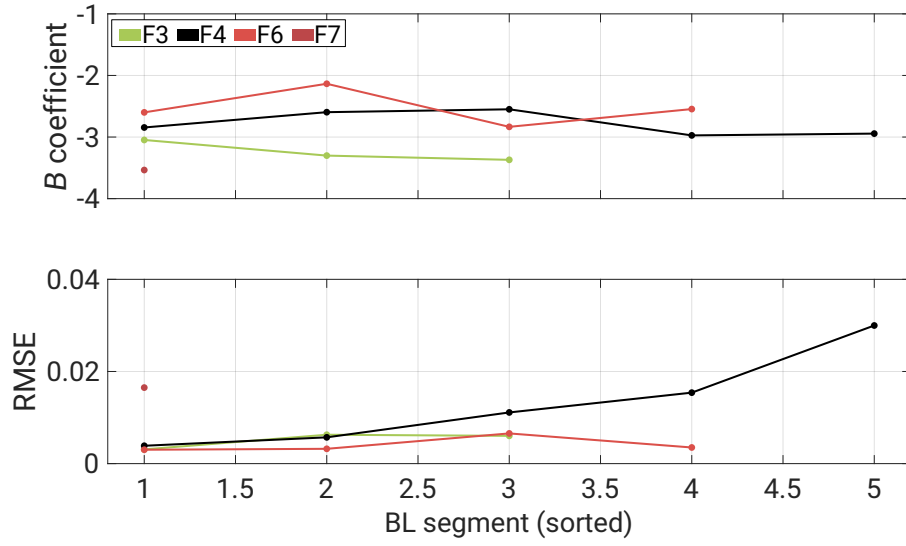


Figure 4.8: Power-law slopes for all identified boundary layer segments (top) with the corresponding RMSE (bottom).

reveals a systematic increase. Please note, that RMSE values for BL segments are an order of magnitude lower than those for CL segments discussed previously.

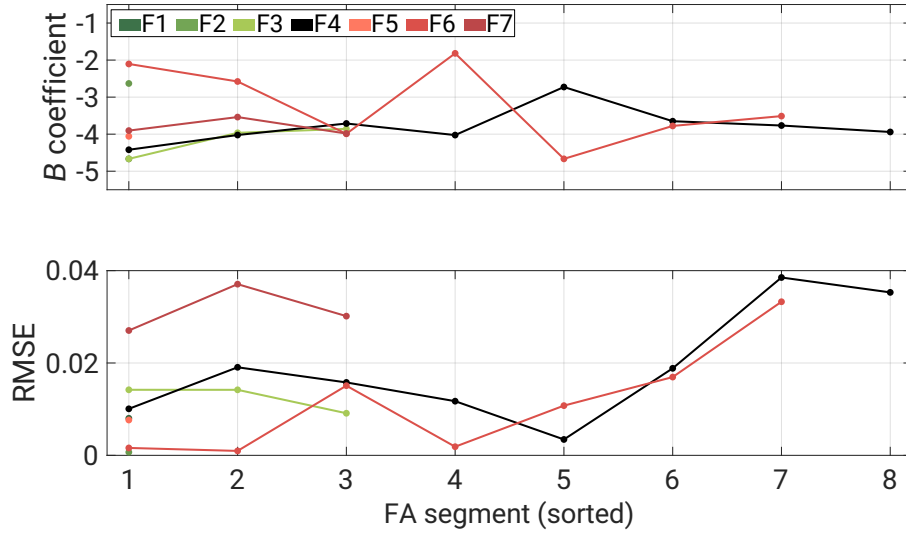


Figure 4.9: Power-law slopes for all identified free atmosphere segments (top) with the corresponding RMSE (bottom).

Similarly, Fig. 4.9 presents statistics for free atmosphere (FA) segments. The fitted B coefficients exhibit a slight shift toward steeper slopes. The figure also includes the corresponding RMSE values, but once again, no definitive correlation with the average number of samples per bin can be established. The RMSE limits remain consistent with those observed in Fig. 4.8.

Given the use of a simple power-law methodology to describe the normalized

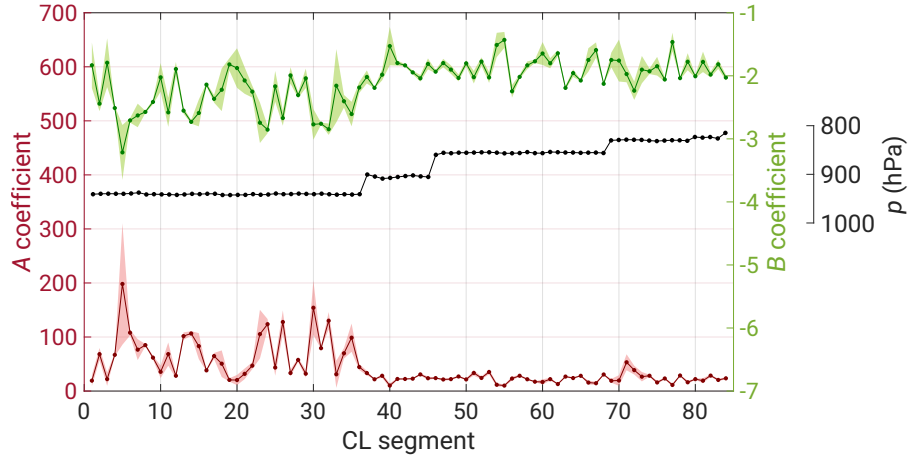


Figure 4.10: Relation between A and B coefficients for all cloud segments from the F4 experiment, including 95% confidence bounds and pressure dependence. The data is presented in the order of the flight timeline.

temperature dissipation rate spectrum, the analysis was extended to examine whether the A and B coefficients are independent or exhibit a relationship. Fig. 4.10 presents these coefficients for the F4 flight, revealing characteristic peaks and local monotonicity in a mirrored pattern. Notably, after segment number 40, the A factors stabilize around 30, while the corresponding B coefficients oscillate around -2 with slightly reduced fluctuations. Since the datasets follow the flight timeline, the chart is supplemented with a pressure time series. The observed change aligns with an altitude shift, where the aircraft transitions from approximately 930 hPa before segment 40 to a gradual increase up to 820 hPa afterward. However, establishing a direct link between flight altitude and slope coefficient variability is based on a single flight and the remaining flights do not provide sufficient data. Therefore, this observation should be considered an exploratory finding rather than a definitive conclusion.

The analysis of the relationship between the two power-law coefficients has been extended to all flights and segments. The results, where coefficient B is plotted against A , are presented in Fig. 4.11. In a lin-log representation, the data points exhibit a quasi-linear arrangement and follow the fitted logarithmic relationships

$$\text{CL segments: } B = -0.53 \cdot \log(A) - 0.21, \quad (4.2)$$

$$\text{BL segments: } B = -0.51 \cdot \log(A) - 0.37, \quad (4.3)$$

$$\text{FA segments: } B = -0.51 \cdot \log(A) - 0.48. \quad (4.4)$$

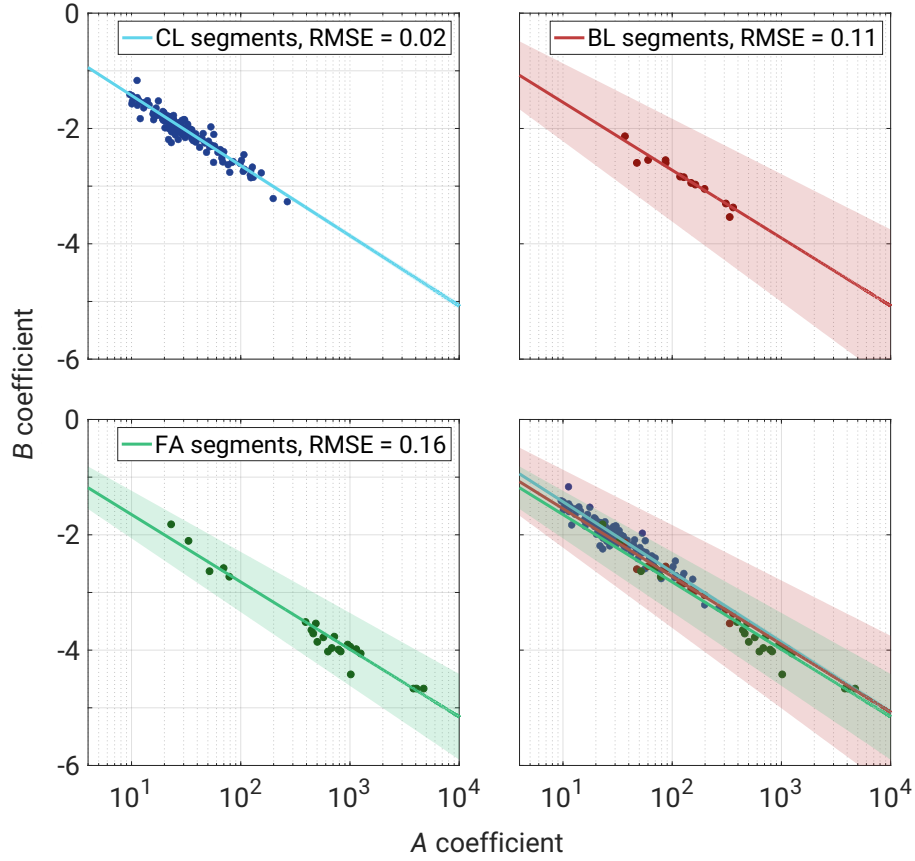


Figure 4.11: B versus A coefficients showed for all the identified cloud segments (left top), boundary layer segments (right top), and free atmosphere segments (bottom left) from 7 flights. The fitted curves are accompanied by 95% confidence bounds with RMSE placed in the legends. The bottom-right chart presents all data combined, along with the three fitted curves.

The above discussion, along with the formulas from Eqs. 4.2, 4.3, and 4.4, leads to two key conclusions. First, the temperature dissipation rate spectrum can be effectively described by a power law, where the coefficients are related by a logarithmic relationship. Second, this relationship appears to be universal across the studied atmospheric flows.

4.3 Temperature dissipation in laboratory

Given the high-resolution laboratory datasets, Fig. 4.12 presents the normalized temperature dissipation rate distributions from the D-1-MIX, D-2-MIX,

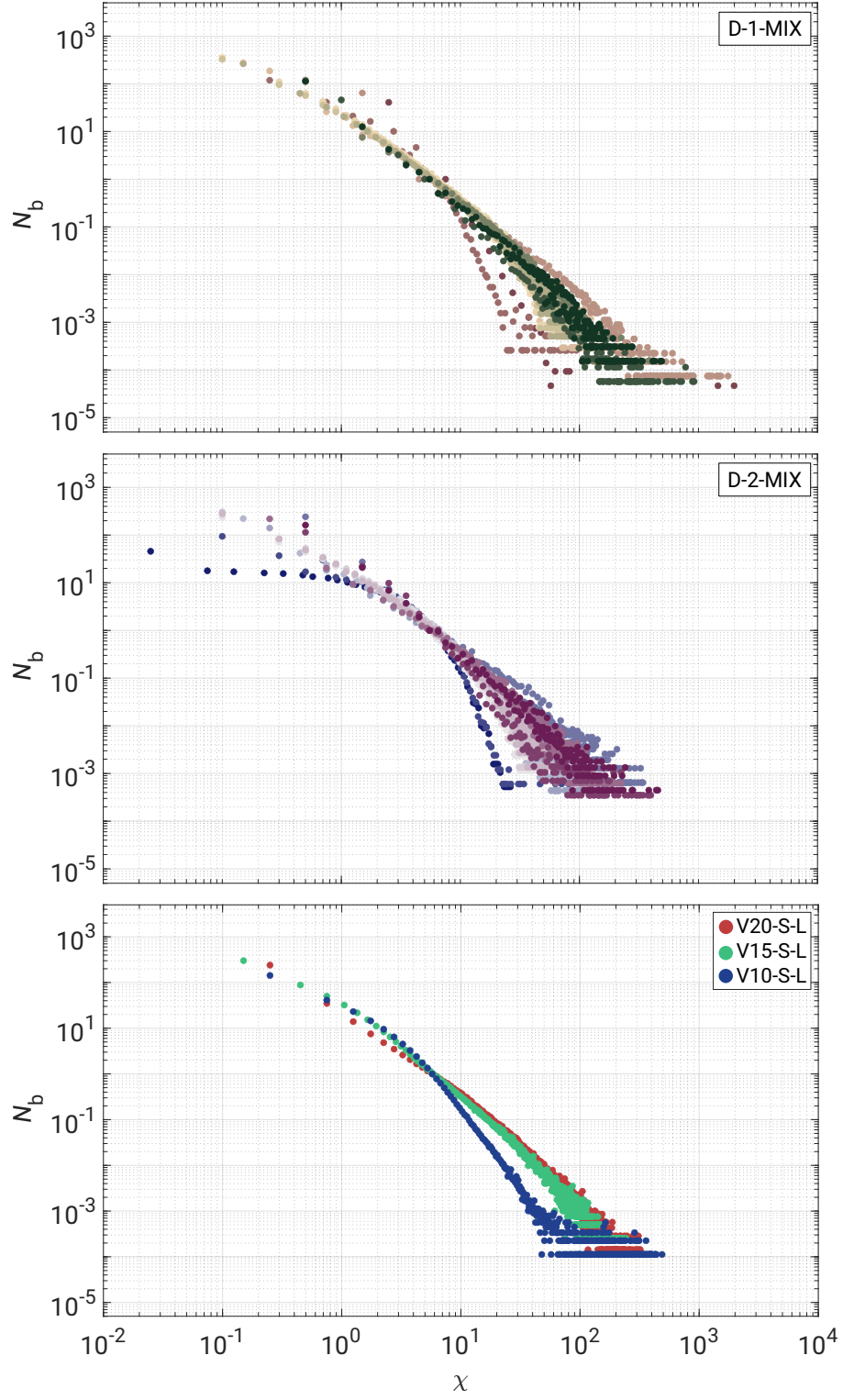


Figure 4.12: Histograms of χ for two LACIS-T experiments: D-1-MIX (top) and D-2-MIX (middle), as well as three Π Chamber experiments performed at $h = 8$ cm above the floor (bottom). The color scheme for the LACIS-T datasets matches that in Fig. 3.6.

and V20-S-L experiments, analogous to Fig. 4.6 for EUREC⁴A. The laboratory data were processed using the same methodology as the atmospheric temperature series.

The top and middle panels of Fig. 4.12, corresponding to LACIS-T experiments, exhibit χ distributions similar to those in atmospheric segments. The data points form quasi-linear arrangements with elongated tails on both sides, and most datasets overlap within the observed χ range. However, a few outlier series are shifted left, particularly near the tunnel edge, indicating inhomogeneities as discussed in Sec. 3.1. The primary difference between the two panels is in the N_b and χ ranges: D-1-MIX shows a broader χ spectrum due to a larger temperature difference between the flows. Compared to D-2-MIX, its lower N_b limit shifts by an order of magnitude, while the upper χ limit is about four times higher.

For the II Chamber experiments, the χ series at $h = 8$ cm above the floor show more convergent distributions than those in LACIS-T. The V20-S-L and V15-S-L cases largely overlap, both exhibiting quasi-linear arrangements. In contrast, the V10-S-L dataset features smaller temperature fluctuations, shifting the lower branch of the χ distribution left. Despite this, high scalar fluctuations persist, and all three cases share a similar upper χ limit. This behavior may result from thermal plumes passing the sensor Grosz et al. (2024), where localized temperature jumps contribute to the observed χ tail. The N_b lower limits are comparable across the three cases, falling between those of D-1-MIX and D-2-MIX.

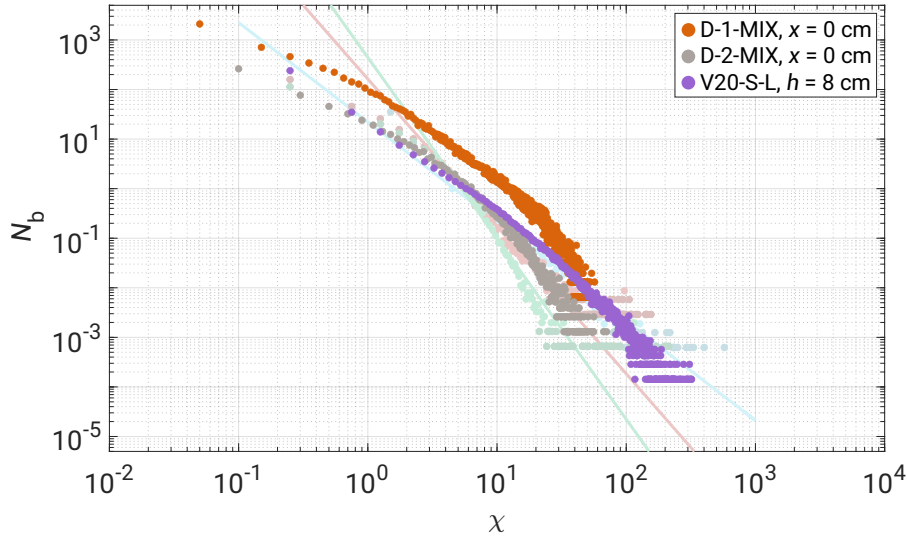


Figure 4.13: Overlapped χ histograms for the D-1-MIX and D-2-MIX experiments at $x = 0$ cm, along with the V20-S-L experiment performed at $h = 8$ cm above the floor. The background datasets correspond to Fig. 4.6, which presents sample χ series characteristics for different atmospheric regions during EUREC⁴A.

To summarize this part, Fig. 4.13 compares normalized temperature dissipation rate distributions across different flow types. Faded background series represent Fig. 4.6, with one series from each LACIS-T experiments at $x = 0$ cm and the V20-S-L II Chamber dataset at $h = 8$ cm superimposed. The latter closely resembles atmospheric distributions, while LACIS-T results at $x = 0$ cm lack comparably high χ values. This suggests that the highest dissipation rates are more frequent outside the tunnel center, potentially due to external influences (see Subsec. 3.1.1).

Summary and discussion

The presented study addresses the problem of small-scale temperature fluctuations in different flow regimes. Temperature time series were collected both in laboratory facilities, such as the LACIS-T wind tunnel and the II Chamber under dry and clean conditions, as well as in the real atmosphere during the airborne branch of the EUREC⁴A campaign. To the best of the author’s knowledge, most of the obtained results are among the very first of their kind. This enabled a full thermal characterization of both facilities across the entire range of scales, which may be crucial for future experiments in laboratory environments. It also provides a methodology and outlines possible future directions for achieving more precise estimates of scalar field dissipation, suggesting that certain features of turbulent flows may be more universal and not restricted to specific flow regimes. The significance of the performed research is discussed in detail in the following three points.

- **Basic facilities characteristics:** The controlled and undisturbed conditions in both facilities allowed for precise, high-resolution scans along axes with the highest thermodynamic variability. In the wind tunnel, two experiments were performed under temperature differences of 25 K and 16 K, respectively. The second statistical moment revealed two key features of the facility: (i) **the influence of outside conditions on streams mixing**, evidenced by an increase in σ_T on the „A” side, where the temperature difference between the measurement section and the laboratory was significant, and (ii) **changes in mixing dynamics between the two experiments**, indicated by shifts in σ_T peaks and asymmetric distribution slopes. The latter feature may be related to wave-like structures in the tunnel center, as reported in [Nowak et al. \(2022\)](#). Skewness analysis supported these observations, confirming the impact of limited thermal insulation and revealing **two scalar field inhomogeneities at $x \approx \{-5, 5\}$ [cm]**. These could result from overlapping from both strong mixing in the tunnel center and

boundary-layer effects near the windows. However, the enhanced skewness on the „B” side may also be due to the presence of an obstacle (another sensor), though this cannot be confirmed at present. These were the first high-resolution measurements conducted in the tunnel, providing deeper insights into the thermodynamic properties of the measurement section and highlighting the importance of careful instrumentation placement. According to private discussions with Dr. Dennis Niedermeier, who manages LACIS-T, the facility has undergone modifications, including a turbulence grid replacement, which could slightly alter flow mixing properties. Repeating the measurements and analyses would help better address the current research questions. A natural continuation of this work would be to conduct experiments under moist conditions with supersaturation, as temperature fluctuations and statistical moments are expected to exhibit greater variability in the presence of phase changes. Additionally, future measurements at different heights would be beneficial, as this study focused solely on $z = 62$ cm. Such experiments are crucial for understanding mixing in flows with varying properties, such as cloud margins and entrainment/detrainment processes.

The thermal characteristics of the II Chamber have been summarized in Sec. C.4, the accepted version of the preprint [Grosz et al. \(2024\)](#). Similar to LACIS-T, future small-scale experiments should also investigate moist conditions and regions closer to the lateral boundaries. As suggested in Sec. 1.1.4, heat fluxes, LSC, and thermal plumes exhibit strong variability in these areas. Moreover, the present measurements were conducted without the horizontal traverse arm, which is typically used to mount instrumentation. This helped minimize the influence of cabling and other sensors on the turbulent structure of the upper flow region. For comparative studies, it would be valuable to assess the extent to which the presence of the traverse affects small-scale events.

- **Power Spectral Densities:** Studies on spectra **aimed to distinguish regimes across the full range of scales, assess the applicability of energy spectral approaches to scalar spectra, and develop a robust methodology.** In the case of LACIS-T, the collected data allowed for the observation of dynamic changes as the sensor moved along the x -axis. As anticipated, the region with the most intense turbulence mixing exhibited the highest PSD values, which gradually decreased toward the windows, reaching minima at approximately $x \approx \{-5, 5\}$ [cm]. The spectra then increased again as the UFT moved closer to the boundaries, confirm-

ing through PSD analysis that external conditions influence events inside the tunnel. No wave-like features were observed, likely due to the point nature of the measurements. However, the PSD maxima appeared within a frequency range of 12–16 Hz, aligning with the 14 Hz peak observed in humidity spectra reported by Nowak et al. (2022). The method proposed by Zhou and Xia (2001) enabled spectral curve collapse, facilitating a more straightforward comparison and indicating a gradual reduction in noise levels, with the lowest values observed in the central region. The adopted methodology of equidistant logarithmic binning, inspired by Siebert et al. (2006a) and Nowak et al. (2021), provided a clear means to distinguish dynamical regimes. Using the linearity criterion of the Pearson correlation coefficient, **four spectral ranges were identified: facility-affected, inertial, dissipative, and instrument-affected.** The facility-affected regime corresponded to large-scale events comparable to the measurement section dimensions. This, along with wave-like features, should be considered in future experiments, as such effects inevitably overlap with other physical processes. **In the inertial regime, a $-5/3$ scaling was observed,** though only over a narrow range, as discussed in Niedermeier et al. (2020). The subsequent **dissipative power-law scalings at $x = 0$ cm were -4 and -5.5 , depending on the experiment,** with no direct equivalents in the literature. However, the underlying physical principles of LACIS-T differ significantly from previously studied cases. Here, two air streams with different properties are mechanically mixed within a relatively small volume, potentially leading to non-canonical effects. To better understand this regime, an analytical approach proposed by Pope (2000) was applied. Despite originating in energy spectral analysis, this method was successfully used to describe the dissipative regime in the scalar field. The best fit was provided by a simple exponential spectrum, with the resulting central-region scaling oscillating around $\beta = -1$. Finally, the regime associated with the sensor’s wire dimensions, referred here as **the instrument-affected range,** was characterized by slopes of approximately -8.5 .

On the other hand, applying the same spectral analysis to the II Chamber identified **three regimes: inertial, transition, and dissipative, with respective slopes of approximately $-7/5$, -3 , and -7 .** An extended discussion of these results is provided in Sec. C.4. The corresponding analysis of the dissipative regime, not included in Grosz et al. (2024), revealed that all resulting slopes were consistent with previous findings, oscillating around $\beta = -1$. This further suggests that the exponential spectrum ef-

fectively describes the dissipative regime. Additionally, **the comparative analysis indicates that small-scale turbulence in the scalar field is independent of large-scale events, which can vary significantly between different systems.** While this result has been anticipated, to the best of the author’s knowledge, this study provides the first qualitative confirmation in experiment. For future studies, it would be beneficial to conduct similar small-scale point measurements incorporating both temperature and velocity fields. This would enable a direct comparison of regimes and scalings, complementing the current findings and enhancing their interpretation, particularly for active scalars, since temperature data alone do not provide a complete picture.

From a technical perspective, careful spectral observations in the dissipative range also indicated that **the sensor itself did not significantly influence the measurements at scales comparable to its dimensions.** This was confirmed by the absence of noticeable differences in monotonicity across experiments in both facilities.

- **Temperature dissipation rate:** The final part of the thesis explores the problem of normalized temperature dissipation rate, which slightly deviates from the commonly used analytical formulation. To conduct the analysis, **airborne temperature time series collected over the subtropical Atlantic Ocean were categorized into three data groups: clouds, the boundary layer, and the free atmosphere.** Preliminary results indicated that cloud edges could be identified through sharp temperature fluctuations (around 2 °C), making this approach a valuable tool for more precise cloud detection. The standard method relies on LWC observations, but in turbulence studies, this can significantly reduce the available information on cloud dynamics. Therefore, **in this work, clouds were identified using LWC data, while their edges were determined based on high-resolution UFT records.**

Histograms of the selected segments revealed that, in addition to elongated tails on both sides of the distributions, **a quasi-linear range appears in a log-log representation, which can be described by a simple power law.** The corresponding slopes fell within the range $(-5, -1)$, showing a gradual increase: moderate in clouds and steepest in the free atmosphere. When compiling statistics across all identified segments, **the two resulting power-law coefficients were found to be depended following a logarithmic relation across all three groups, yielding a very consistent**

fit. This result is not straightforward to interpret, as it represents what appears to be the first observation of its kind. More broadly, it suggests that **such a temperature structure could be a more universal feature of atmospheric flows**—an insight further supported by the II Chamber data. On the other hand, the time series from LACIS-T displayed slightly different monotonicity, possibly due to the mixing mechanisms at play in the tunnel’s center. The presented results could potentially improve the formulation of the relationship between refractive index fluctuations in the atmosphere and temperature fluctuations, possibly contributing to better instrumentation performance (see, e.g., [Friehe et al. \(1975\)](#); [Wesely \(1976\)](#); [Wyngaard and LeMone \(1980\)](#)). Moreover, as discussed in Subsec. 1.1.3, recent studies suggest that supersaturation fluctuations play a crucial role in understanding cloud droplet formation processes, making small-scale temperature variability one of the key parameters in more accurate subgrid models parametrization.

Sec. 1.3 refers to recent work by [Lemay et al. \(2020\)](#), which presents a methodology for estimating temperature and energy dissipation rates directly from the dissipative range of the temperature spectrum in „slightly heated flows”. According to the authors, the method is limited to passive scalars and Prandtl numbers close to unity. To assess its applicability to the datasets analyzed in this thesis, I conducted a similar study using the II Chamber temperature spectrum for a temperature difference of 10 K at a height of $h = 50$ cm. This choice was based on the corresponding ϵ and ϵ_T estimates reported by [Niedermeier et al. \(2018\)](#) ($\epsilon \approx 6.5 \cdot 10^{-4} \text{ m}^2 \text{ s}^{-3}$ and $\epsilon_T \approx 3.5 \cdot 10^{-3} \text{ K}^2 \text{ s}^{-1}$). A slightly modified version of the formula proposed by [Lemay et al. \(2020\)](#) was used,

$$E_T(k) = C_O k^{-5/3} \exp(-\beta k \eta) \epsilon_T \epsilon^{-3/4} \nu^{5/4}, \quad (5.1)$$

following the discussion in Subsec. 3.1.2, which supports the use of a simplified exponential spectrum instead of its full form (see Eq. 3.2). Note that the prefactor C_O used here differs from those in Sec. 3.2 and Subsec. 3.1.2. The analysis also incorporated the spectral collapse technique from [Zhou and Xia \(2001\)](#) and equidistant logarithmic binning, as described by [Siebert et al. \(2006a\)](#) and [Nowak et al. \(2021\)](#). As this is preliminary research, the dissipation rates were estimated graphically, following the approach of [Lemay et al. \(2020\)](#). Eq. 5.1 was first fitted in the dissipative range with C_O and β as free parameters, using the reference values of ϵ_T and ϵ from

Niedermeier et al. (2018). Once estimates for C_O and β were obtained, these values were held fixed, and ϵ_T and ϵ were varied to fit the spectrum, following the approach in Fig. 5 of Lemay et al. (2020). Linear arrays of eight elements were created for both ϵ_T and ϵ , spanning from 0.5 to 1.5 times the reference values. The resulting eight spectral curves, along with the one providing the best fit, are shown in Fig. 5.1. Lemay et al. (2020) reported expected uncertainties of $\pm 8\%$ for ϵ_T and $\pm 12\%$ for ϵ . The best fit in this study was obtained for $\epsilon_T = 3.2 \cdot 10^{-3} \text{ K}^2 \text{ s}^{-1}$ and $\epsilon = 7.0 \cdot 10^{-4} \text{ m}^2 \text{ s}^{-3}$, yielding errors of approximately $\pm 7\%$, which aligns well with the reported uncertainty margins.

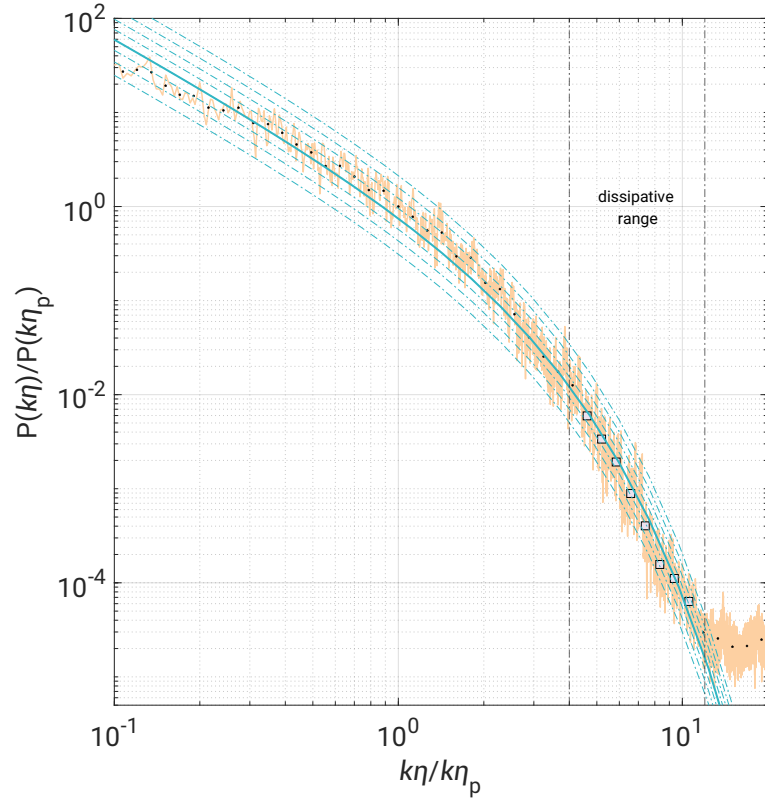


Figure 5.1: One-dimensional temperature spectrum of V10-L-S with the methodology of Lemay et al. (2020) applied to graphically estimate ϵ_T and ϵ . Dashed-dotted curves represent eight different combinations of ϵ_T and ϵ values, with the bold line indicating the best visual fit.

The results are promising, particularly considering the simplicity of the method and the fact that the analyzed temperature spectrum originates from an active scalar—beyond the stated limitations of the approach. Moreover, the estimation relied solely on graphical fitting, which could be further improved through numerical regression techniques. Future work should aim

to refine the methodology, for instance by reducing the number of free parameters and estimating ϵ_T directly from its definition (see Eq. 1.6). This could enable more accurate estimation of ϵ based solely on temperature spectra obtained from the UFT sensors.

Two key limitations of this part of the study should be acknowledged, particularly concerning the airborne datasets. The first relates to the statistical representation of selected segments in terms of time duration, which ranged from a few seconds for clouds to several minutes for boundary layer and free atmosphere segments. While this variation reflects natural atmospheric variability, ideally, the analysis should be performed on more comparable datasets. The second limitation arises from the study's primary focus on temperature profiles, which constrains the understanding of segment dynamics. While the results suggest a potentially universal temperature structure in atmospheric flows, further research is needed to deepen our understanding of the underlying processes driving atmospheric variability.

This study offers a foundation and a compelling introduction to further research in this area. As is often the case with exploratory studies, it raises many questions but also sparks numerous ideas for future development, particularly concerning scalar fields and their intricate ties—both direct and indirect—with vector fields.

Temperature time series from EUREC⁴A

The following plots illustrate the temperature and pressure time series collected during the EUREC⁴A campaign, except for Flight F4, which is presented in Fig. 4.1. Sections 4.1 and 4.2 provide further interpretations of various observable features in the data.

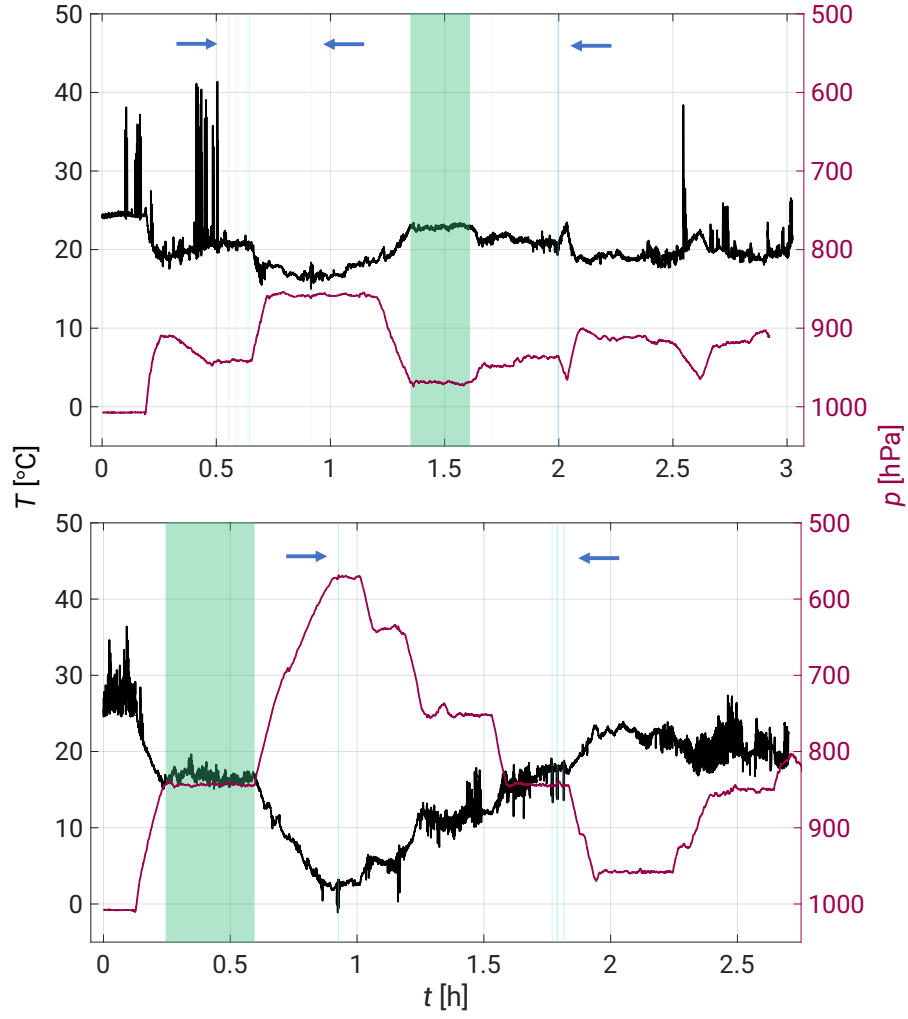


Figure A.1: Temperature and pressure time series from the F1 (top) and F2 (bottom) flights, with cloud segments (blue), boundary layer segments (red), and free atmosphere segments (green) highlighted. Arrows indicate cloud regions for clarity.

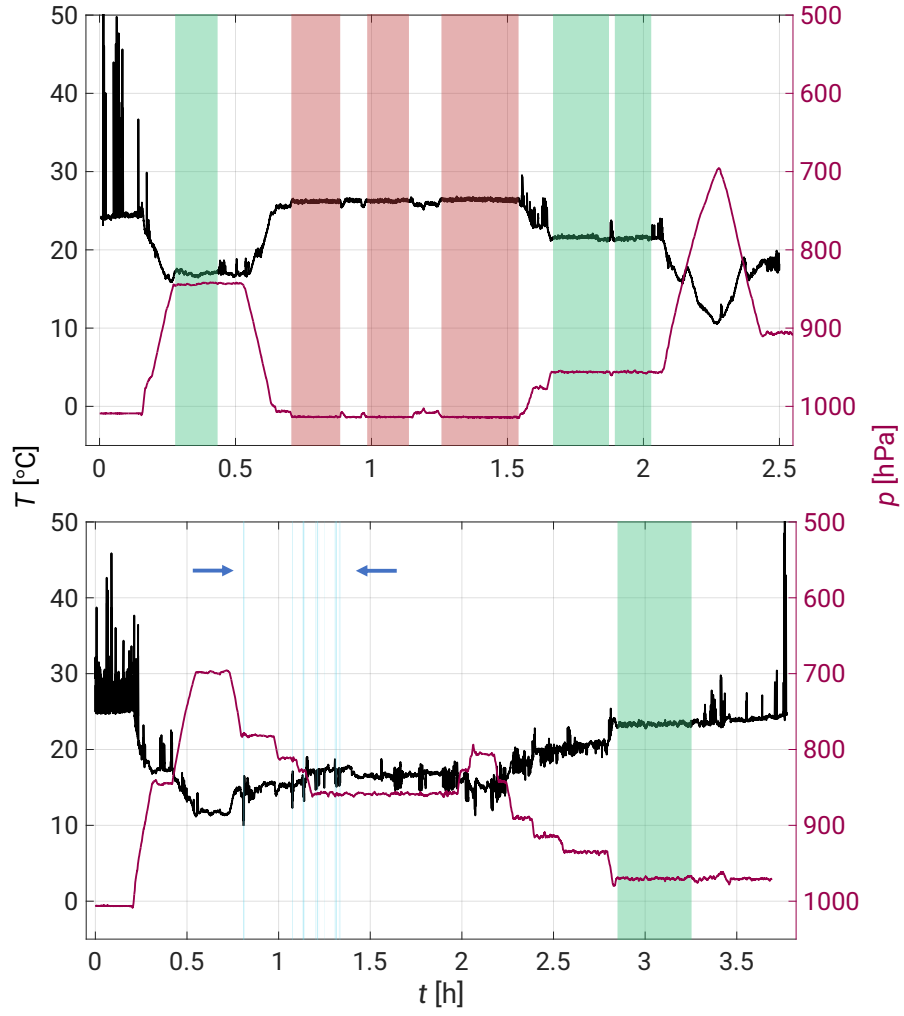


Figure A.2: Temperature and pressure time series from the F3 (top) and F5 (bottom) flights, with cloud segments (blue), boundary layer segments (red), and free atmosphere segments (green) highlighted. Arrows indicate cloud regions for clarity.

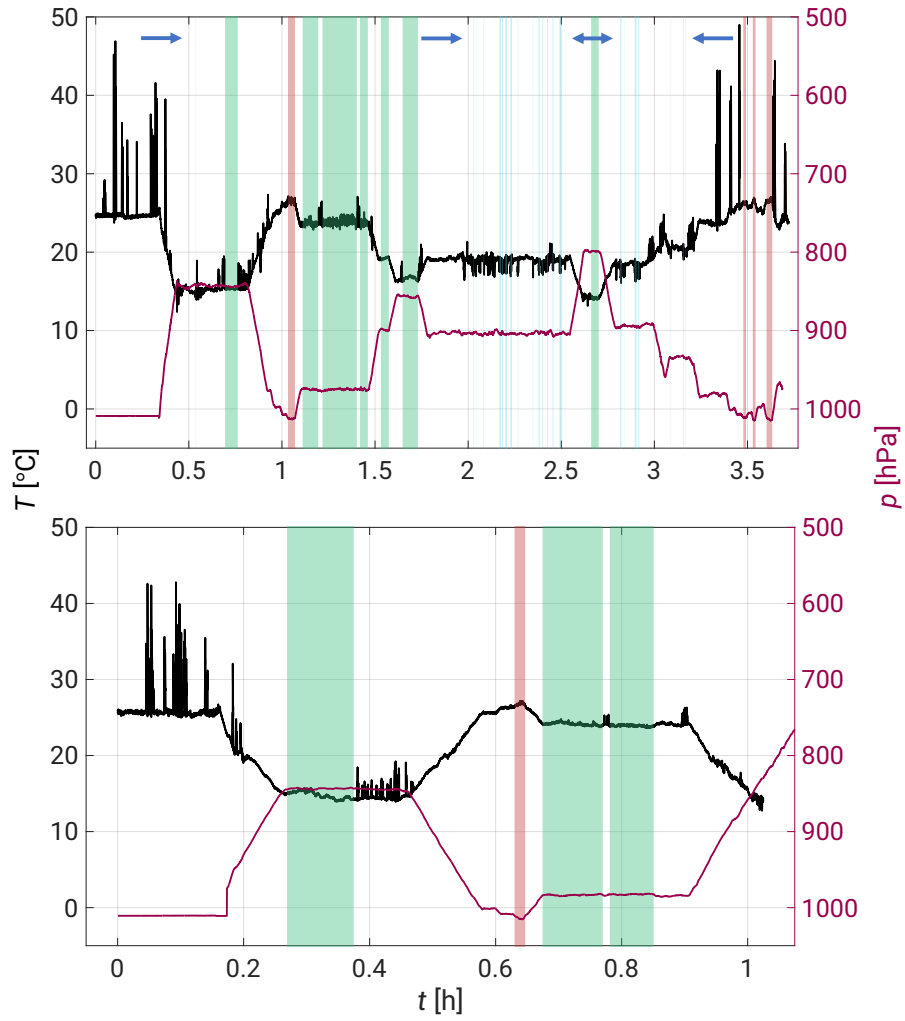


Figure A.3: Temperature and pressure time series from the F6 (top) and F7 (bottom) flights, with cloud segments (blue), boundary layer segments (red), and free atmosphere segments (green) highlighted. Arrows indicate cloud regions for clarity.

Additional χ statistics from EUREC⁴A

This section provides additional statistics on boundary layer and free atmosphere segments, complementing the discussion in Sec. 4.2 and corresponding to the statistics presented in Fig. 4.5.

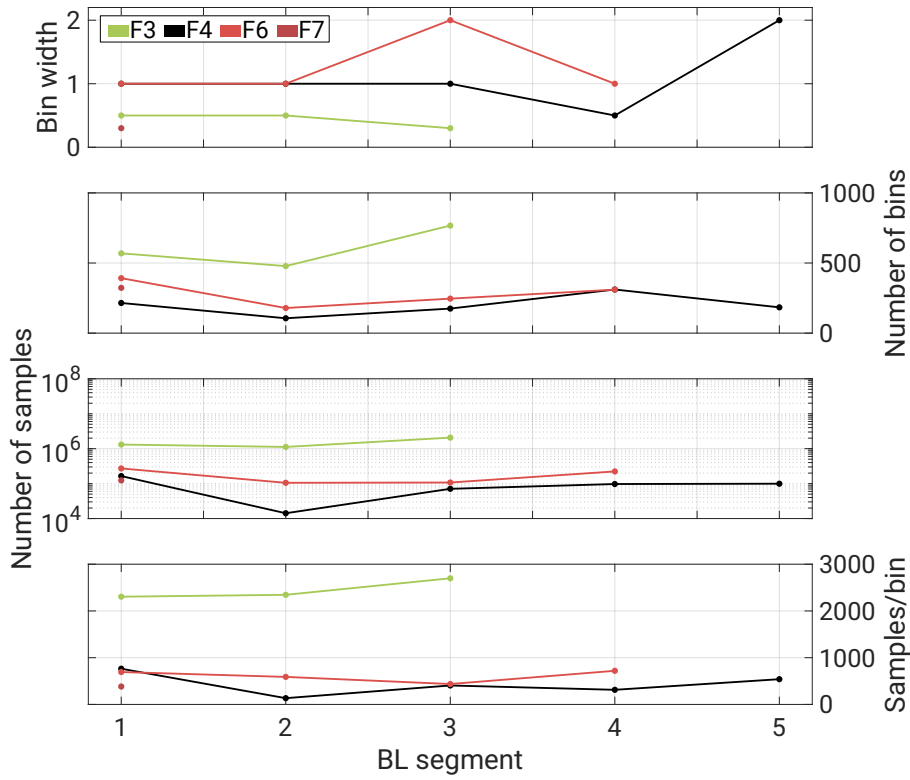


Figure B.1: Temperature dissipation rate distribution statistics charts with respect to all identified boundary layer segments from 4 flights. The data is presented in the order of the flight timeline.

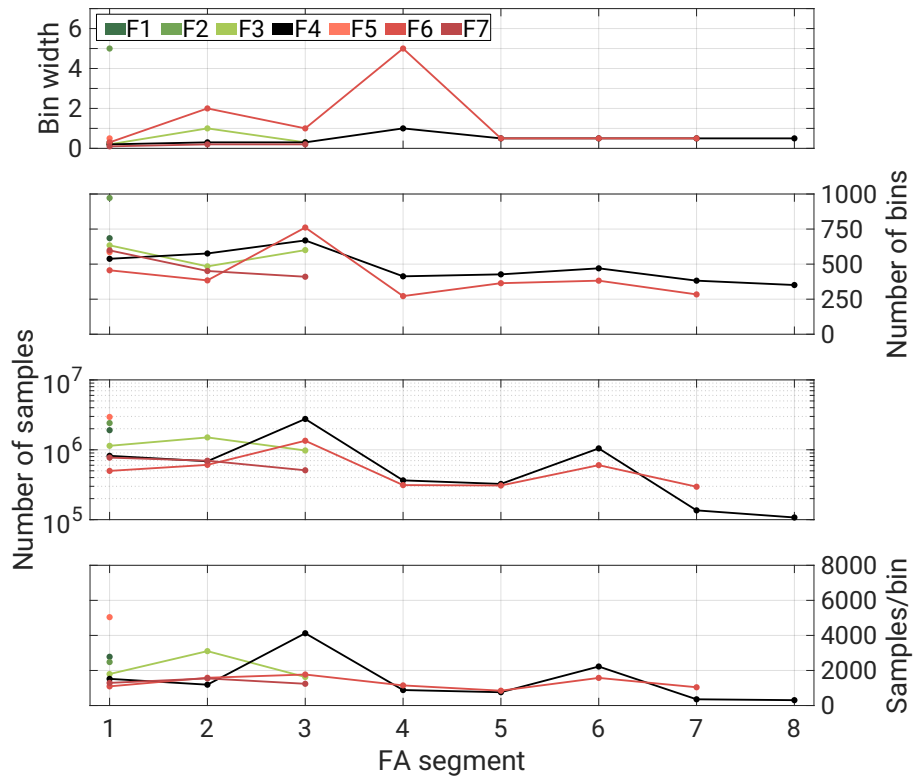


Figure B.2: Temperature dissipation rate distribution statistics charts with respect to all identified free atmosphere segments from 7 flights. The data is presented in the order of the flight timeline.

Accepted manuscript version

At the time of this thesis submission, only a preprint is available online (see [Grosz et al. \(2024\)](#)). That manuscript does not include the most recent revisions made for the accepted version. Therefore, for the reader's convenience, the accepted version is provided below.

High-resolution temperature profiling in the Π Chamber: variability of statistical properties of temperature fluctuations

Robert Grosz¹, Kamal Kant Chandrakar², Raymond A. Shaw³, Jesse C. Anderson³, Will Cantrell³, and Szymon P. Malinowski¹

¹Institute of Geophysics, Faculty of Physics, University of Warsaw, Pasteura 5, 02-293 Warsaw, Poland

²Mesoscale & Microscale Meteorology Laboratory, NSF National Center for Atmospheric Research, 3090 Center Green Drive, Boulder, CO 80301, USA

³Department of Physics, Michigan Technological University, 1400 Townsend Drive, Houghton, MI 49931, USA

Abstract

This study delves into the small-scale temperature structure inside the turbulent convection Π Chamber under three temperature differences (10 K, 15 K, and 20 K) at Rayleigh number $Ra \sim 10^9$ and Prandtl number $Pr \approx 0.7$. We performed high frequency measurements (2 kHz) with the UltraFast Thermometer (UFT) at selected points along the vertical axis. The miniaturized design of the sensor featured with a resistive platinum-coated tungsten wire, 2.5 μm thick and

3 mm long, mounted on a miniature wire probe allowed for vertically undisturbed temperature profiling through the chamber’s depth spanning from 8 cm above the bottom to 5 cm below the top. The collected data, consisting of 19 min and 3 min time series, were used to investigate the variability of the temperature field within the chamber, aiming to better address scientific questions related to its primary objective: understanding small-scale aerosol-cloud interactions. The analyses reveal substantial variability in both variance and skewness of temperature distributions near the top and bottom plates and in the bulk (central) region, which were linked to local thermal plume dynamics. We also identified three spectral regimes termed inertial range (slopes of $\sim -7/5$), transition range (slopes of ~ -3) and dissipative range, characterized by slopes varying ~ -7 . Furthermore, the analysis showed a power law relationship between the periodicity of large-scale circulation (LSC) and the temperature difference. Notably, experimental results are in good agreement with Direct Numerical Simulations (DNS) conducted under similar thermodynamic conditions, illustrating a comparative analysis of this nature.

C.1 Introduction

The convection-cloud chamber, officially named the II Chamber, represents one of the most advanced facilities for controlled experiments on cloud microphysics (Chang et al., 2016). Its design allows for reproducible and controlled measurements across a wide range of temporal scales, from minutes to days, while maintaining stationary thermodynamic forcing. It operates in two modes. The first mode utilizes static pressure reduction to simulate updrafts in the atmosphere. In the second mode, it induces Rayleigh-Bénard convection (RBC), where air in the chamber is heated from below and cooled from above. In the present study we investigate temperature fluctuations in full spectrum of scales in the chamber operating in the second mode. We focus on small-scale temperature fluctuations in a course of turbulent mixing inside the chamber, since the facility is designed for research on aerosol-cloud interactions in turbulent environment (Chandrakar et al., 2018a,b; Desai et al., 2018, 2019; Chandrakar et al., 2020c; Prabhakaran et al., 2020b; MacMillan et al., 2022). Unlike typical RBC experiments, the chamber includes side windows and various mounting points for microphysical instrumentation, which introduce asymmetries between the upper and lower plates. Thus the detailed (e.g. thermal) characterization of the chamber is required to evaluate how closely the flow resembles classic RBC flows. It is important to note that this study does not aim to extend beyond conventional RBC research, which often

involves day-long averaging.

Atmospheric phenomena undergo non-stationary and unstable processes, making them difficult to study in real atmosphere conditions. The RBC setup used in this study provides more controllable environment than the real atmosphere but we do not push to reach the level of convergence recognized in the RB community. Nonetheless, we report statistics which can be compared to previous highly-resolved measurements within the RBC systems (du Puits et al., 2013; du Puits, 2022; du Puits, 2024).

Our work primarily focuses on understanding the small-scale and short-term variability of thermal conditions within the facility, emphasizing the importance of absolute temperature. This aspect is crucial for more comprehensive studies on aerosol interactions with water vapor and droplet growth/evaporation in a turbulent environment. However, a few selected results are presented in a non-dimensional form (see Appendix C.6). One recent study of particular relevance to small-scale variability is the paper by Salesky et al. (2024) on the subgrid scale scalar variance modeled in large eddy simulations over the range $Ra \sim 10^8 - 10^9$. Our approach was to collect high resolution (2 kHz) temperature time series using the UltraFast Thermometer (UFT) at selected locations in a vertical profile near the axis of the chamber and to perform statistical and spectral analysis investigating small-scale structure of RBC under laboratory conditions.

UltraFast Thermometers (UFTs) have been specifically designed for airborne in-cloud measurements. They resolve scales down to or even below 1 cm, effectively reaching the dissipation range. Successive models of the UFT family (Haman et al., 1997, 2001; Kumala et al., 2013) have utilized similar sensing element—a resistive platinum-coated tungsten wire, 2.5 μm thick and 5 mm long, mounted on a small vane to adapt to local airflow. In the next sensor versions (Nowak et al., 2018; Siebert et al., 2021), the vane has been removed, leading to further miniaturization of the instrument’s dimensions and the implementation of a custom-built electronic system. The current iteration (UFT-2B) has undergone testing i.e. during the recent EUREC⁴A campaign (Stevens et al., 2021). The 3 mm long sensing wire is spanned on an industry-standard miniature wire probe, allowing for easy exchange of the sensing head (see Fig. C.1).

Not only small-scale fluctuations are important in their own sake, but also for understanding of changes in the LSC on distributions of mixing ratio, temperature, and supersaturation inside the cell. The established LSC period in the II Chamber at the temperature difference of 12 K, was estimated to be $\tau_{12} \approx 72$ s (moist convection characterized by a mixing ratio of 7.55 g kg^{-1}) (Anderson et al., 2021). In this paper we investigate LSC for three temperature differences (ΔT): 10 K,



Figure C.1: UFT-2B head sensor. A parallel to the mean flow, tungsten wire ($2.5\ \mu\text{m}$ thick, 3 mm long) spanned on miniature industry-standard wire probe by DANTEC[®].

15 K, and 20 K showing a variability of periodicity which can be described by the power law function.

To place our measurements in a broader context, we discuss the results from canonical RBC systems that have been conducted over the years. For comprehensive overviews of recent advancements in RBC, see the works by [Fan et al. \(2021\)](#) and [Lohse and Shishkina \(2024\)](#), along with their references. A more detailed analyses of statistical properties of the temperature field in RBC has been explored in recent experimental ([He et al., 2018](#); [Wang et al., 2019, 2022](#)), theoretical ([Shishkina et al., 2017](#); [Olsthoorn, 2023](#)), and numerical ([Xu et al., 2021b](#)) studies where the authors characterized boundary layer and mixing zone of convective flows. Some investigations aimed at describing buoyant thermal plumes departing from the thermal boundary layer, contributing to the overall heat flux through LSC in a wide range of Rayleigh numbers (Ra ranging from 10^7 to 10^{14}) ([Liu and Ecke, 2011](#); [van der Poel et al., 2015](#); [Zhu et al., 2018](#); [Blass et al., 2021](#); [Reiter et al., 2021](#); [Vishnu et al., 2022b](#); [Wang et al., 2022](#)). Large-scale convective structures have been further explored through DNS, revealing relatively fewer plumes near the sidewalls carrying large heat fluxes, contrasted with more numerous plumes near the cell axis but with weaker heat fluxes, highlighting strong intermittency in this region ([Lakkaraju et al., 2012](#); [Chillà and Schumacher, 2012](#); [Stevens et al., 2018](#); [Pandey et al., 2018](#); [Krug et al., 2020](#); [Moller et al., 2021](#)).

The simulations also demonstrated the persistence of discrete thermal structures in RBC (Sakievich et al., 2016).

The studies also examined the effects of cell dimensions, revealing the variable nature of the LSC depending on the cell’s aspect ratio ($\Gamma = \text{width}/\text{height}$) (Shishkina, 2021). The aspect ratio characterizing the facility (width = 2 m, height = 1 m, $\Gamma = 2$) corresponds to a single roll with a fixed orientation and pronounced oscillations about the mean position, a result of asymmetries inside the chamber (Anderson et al., 2021) (see Fig. C.2). In cases where $\Gamma \gtrsim 4$, a three-dimensional, multi-roll structure has been observed (Bailon-Cuba et al., 2010; Ahlers et al., 2022). Another aspect is the stability of the LSC as numerous analysis have proved its random reorientation and reversal in both cylindrical setups (Brown and Ahlers, 2007; Mishra et al., 2011; Wei, 2021; Xu et al., 2021a) and rectangular cells (Vasiliev et al., 2016; Foroozani et al., 2017; Wang et al., 2018; Vishnu et al., 2020), without clearly indicating a superior choice.

Natural convection plays a crucial role in heat and mass transfer within the atmosphere. Despite its fundamental importance, several aspects of this phenomenon remain poorly understood even on a simplified level of controlled RBC conditions and require further investigation. One such example is the scaling of scalar fields, recently discussed by Kumar and Verma (2018). The authors examined the validity of the Taylor frozen hypothesis in the context of thermally driven turbulence in RBC systems, concluding that the hypothesis holds true only when a steady LSC is present in the flow. They also raised doubts about the suitability of the temperature field for determining whether the Bolgiano-Obukhov (BO, $-7/5$) or Obukhov-Corrsin (OC, $-5/3$) scaling applies to turbulent convection. This uncertainty stems from the ambiguous power law behavior of temperature spectra and the challenges in comparing the associated scaling factors. Similar concerns are highlighted in Lohse and Xia (2010), where the authors reviewed structure functions in RBC and suggested that the limited scale separation between the Bolgiano and outer length scales could be the main problem in obtaining BO scaling. In RBC systems, temperature serves as the primary driver of the convective mechanism rather than behaving as a passive scalar, leading to temperature spectra that may deviate from predictions based on passive scalar theories which are often applied in atmospheric analyses. Additionally, He and Xia (2019) demonstrated that a single RBC system can exhibit distinct local dynamics due to the coexistence of different types of force balances. Consequently, applying a single physical mechanism to describe the entire convection cell may oversimplify its complex dynamics.

From a microphysical perspective, which is the primary application of the

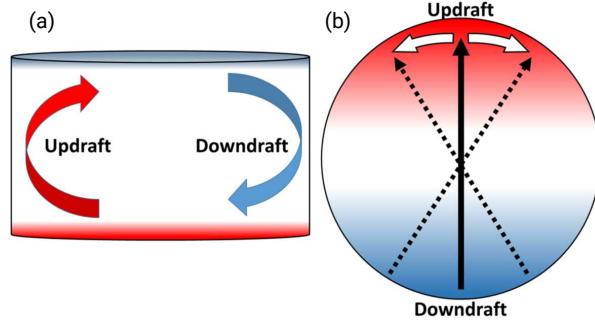


Figure C.2: Schematic of the II Chamber (a) and its plan view (b) with the marked LSC. (a) The arrows represent the mean direction of the warm updraft (red) and the cool downdraft (blue). (b). The dotted and white arrows show the azimuthal oscillations in the circulation. Figure from [Anderson et al. \(2021\)](#).

chamber, understanding the spatial variability of scalar fluctuations within the chamber, including the properties of the LSC, is crucial. This understanding impacts not only the positioning of instruments inside the chamber but also the strategies for measurements, such as the lengths of measurement time series. Only with insight into the physics involved can different phenomena be effectively linked together. This is why analyses aimed at addressing the full spectrum of scales are the focus of the present study.

C.2 Methods

C.2.1 Setup and experimental strategy

In our measurements, we utilized the most recent version of the UFT, namely UFT-2B, as outlined in Section C.1. The schematic representation of the complete UFT setup can be observed in Fig. C.3. The sensor head was affixed to a 1 m probe support and linked to a specially designed 1 mA bridge/amplifier (AMP) using an approximately 1 m standard BNC cable. This amplifier was powered by four AA batteries. Subsequently, the analog signal was acquired by a 16-bit resolution digital-to-analog converter (DAC) from Measurement Computing Corporation (MCC). The DAC had a sampling rate of up to 100 kS s^{-1} (S stands for samples) and utilized the dedicated MCC software DAQami. Despite the time constant allowing for about 10 kHz data collection, we opted for an over-sampling rate of 20 kHz to facilitate post-processing and filter out artifacts from other lab systems. Using two head sensors during this study, each possessing an approximate resistance of $30 \, \Omega$, we attained a UFT sensitivity of approximately

75 mV K⁻¹ after calibrating with a standard thermocouple.

For vertical profiling, the UFT was attached to a 6 mm diameter, 1.5 m long rod with a 90 degree bend at the end. The rod was marked in 3 cm increments to facilitate easy UFT positioning. A sturdy metal stand with two adjustable clamps was used to secure the rod in a stable, vertical position while allowing for the user to manually move the UFT to the desired location (see Fig. C.3). To minimize potential movements of the UFT cabling and sensor head, both were affixed to the rod using simple adhesive, maintaining the wire in an upward and parallel orientation to the floor.

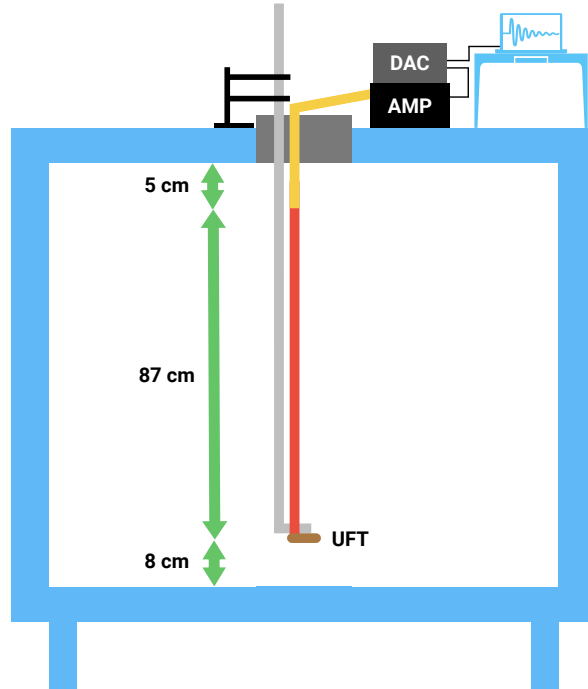


Figure C.3: Schematic of the setup used during the measurements (diagram not to scale). At the top there was an operations center housing with most of the devices and cabling, including a BNC cable (yellow), an UFT amplifier (AMP), digital-to-analog converter (DAC), and a PC with a DAC software. Inside the Π Chamber, a vertical rod with a curved end (gray) and a UFT sensor (brown) with DANTEC® probe support (red) attached to that end was deployed. The profiling limits were about 8 cm above the bottom and around 5 cm below the top layer. Note that, for clarity, the schematic does not include the cylindrical thermal panel which was installed during the measurements.

We studied the small-scale temperature structure within the convection environment across three temperature differences between the chamber's floor and ceiling: 10 K, 15 K, and 20 K, as detailed in Table C.1. The measurement setup included the cylindrical thermal panel (1 m high, 2 m diameter), which is not

shown in Fig. C.3. For a more detailed schematic, please refer to Chang et al. (2016). The Rayleigh number was on the order of $\sim 10^9$ for the set boundary conditions and the chamber height of 1 m. We performed our calculations based on the formula suggested by Niedermeier et al. (2018), assuming dry convection with an estimated Prandtl number of 0.72.

Our primary focus was on examining scalar fluctuations throughout the entire vertical dimension, with a particular emphasis on regions near the floor and the ceiling. To achieve this, the UFT deployments featured irregular measurement positions (see Table C.1) increasing slightly the spatial resolution of measurements near the both plates. Another consideration was the variable measurement time t , ranging from 3 min to 19 min. Such choice was dictated by the chamber’s operational schedule, which constrained both the number of sampled points and the range of explored conditions. To quantify whether the measurements are converged, we employed the framework provided by Lenschow et al. (1994). According to the results presented by the authors, when the ratio of the measurement time t to the large eddy correlation time t_c ratio gives $t/t_c \approx 10$, the data is within approximately 10% of the *true* value. Considering the turbulent properties, we link t_c with the large eddy correlation time for the turbulence flow, which is estimated to be on the order of several seconds, 10 s in calculations, assuming a mean flow velocity of tens of centimeters per second. In this case, the averaging time of 3 min corresponds to approximately $18t_c$, whereas for 19 min time series it gives $114t_c$ indicating satisfactory convergence for atmospheric applications.

A less emphasized aspect was the surface topography. One configuration involved the presence of rough boundaries, consisting of aluminum bars (4 cm wide and 1.4 cm high) positioned on the floor and ceiling forming longitudinal stripes separated by 17 cm intervals. The bars themselves were at a slightly different temperature compared to the rest of both panels (approximately 0.4 K). Subsequent UFT deployments were conducted after removing the bars, aiming to compare temperature fluctuation properties between the two cases. Unfortunately, a portion of the dataset is invalid due to high battery drainage, resulting in coverage of only one rough boundary case in this study.

As the surfaces inside the chamber reached steady temperatures (refer to Tab. C.1), the UFT sensor was initially positioned 8 cm above the floor, near the axis of the cell. Due to the rod’s length inside the chamber corresponding to its height, we had to wait for some time to allow the vibrations of the head sensor to dampen. This was really important after each position (h) change but played a crucial role especially in profiling the lower half of the measurement volume. The chamber’s flange was covered with a thick foam layer, effectively reducing most

mixing events near the opening. Although not an ideal solution, it seemed the most reasonable choice considering the ease of checking the UFT position, as well as the insulating and damping properties of the foam (when coating the rod).

After completing the measurements, the dataset underwent several basic preparations. These included the removal of electronic artifacts, signal despiking, Butterworth filtering (10th order, 2 kHz cutoff frequency), 2 kHz averaging, and the translation of values from voltage to temperature units. Additionally, each time series was consequently normalized by subtracting mean temperature value in the given position (see e.g., Fig. C.4).

C.2.2 DNS methodology

Cloud Model 1 (CM1) (Bryan and Fritsch, 2002) in DNS configuration is used for these simulations. The model and setup are described in detail in Chandrakar et al. (2022, 2023). The computational domain size for DNS is $960 \times 960 \times 500$ grid cells with a homogeneously 2.083 mm grid spacing in horizontal and stretched grid in vertical (finer near the top and bottom boundaries). Note the computation domain represents a rectangular parallelepiped system rather than a cylindrical setup used during the experiments. CM1 solves the conservation equation set with the Boussinesq approximation and a prognostic pressure equation using a three-step Runge–Kutta time integration method with a fifth-order advection scheme. The Klemp–Wilhelmson time-split steps are used for the acoustic terms in the compressible solver. The time integration of the governing equations uses an adaptive time step with a maximum Courant–Friedrichs–Lewy (CFL) number of 0.8. A no-slip boundary condition for all walls is applied, and the temperature boundary conditions (constant temperatures) are the same as the experimental setup. The simulations use molecular viscosity and thermal diffusivity values at the mean temperature (Prandtl number = 0.72). DNS is performed for the three experimental cases, V20-S, V15-S, and V10-S, listed in Tab. C.1. Outputs from a steady-state period after the initial spin-up are used for the analysis. Consistent with the experiments, the Eulerian temperature time series are outputted at 0.0012–0.0015 s intervals from a region near the center of the domain (95–105 cm from sidewalls) at multiple heights from the bottom surface.

Table C.1: List of experiments together with the corresponding Π Chamber and UFT settings, and the Rayleigh numbers. Symbols explanation: T_F , T_C , T_W represent floor, ceiling, and walls temperature respectively, t stands for the measurement time at a given height h above the floor. Names of the experiments are made as follows: type of the measurement ("V" for vertical), ΔT , type of boundaries (S for smooth or R for rough), and time spent at a single position (L for 19 min or no marking for 3 min).

Experiment	rough/smooth boundaries	T_F [°C / K]	T_C [°C / K]	T_W [°C / K]	h [cm]	t [min]	Ra [$\times 10^9$]
V10-S-L	smooth	25 / 298	15 / 288	20 / 293	irregular	19	1.1
V10-S	smooth	25 / 298	15 / 288	20 / 293	8-95	3	1.1
V15-S-L	smooth	27.5 / 300.5	12.5 / 285.5	20 / 293	irregular	19	1.6
V15-S	smooth	27.5 / 300.5	12.5 / 285.5	20 / 293	8-95	3	1.6
V20-S-L	smooth	30 / 303	10 / 283	20 / 293	irregular	19	2.1
V20-S	smooth	30 / 303	10 / 283	20 / 293	8-95	3	2.1
V20-R	rough	30 / 303	10 / 283	20 / 293	8-95	3	2.1

The irregular positions are: 8, 14, 26, 35, 50, 65, 74, 86, 95 [cm].

C.3 Results

C.3.1 Determination of basic characteristics of temperature profile

The top panel of Fig. C.4 provides a sample of temperature fluctuations T' ($T' = T_h - \bar{T}_h$, where T_h represents the temperature series at a given height h , and overline denotes the mean) from the vertical scan of the measurement volume near the axis of the chamber. The skewed fluctuations observed in the closest proximity to the plates serve as expected temperature evidence of thermal plumes characteristic for RBC. We can observe a smooth transition involving gradual suppression of fluctuations or rather gradual decrease in occurring thermal plumes as the sensor moved towards the mid-height plane. The reverse symmetry is present in the upper half of the cell. The nature of these fluctuations aligns with the numerical results of heat fluxes in the bulk region obtained by Lakkaraju et al. (2012), temperature time series reported in He and Xia (2019) and Wang et al. (2022), and experimental data provided by Anderson et al. (2021). However, it is noteworthy that all these works primarily focused on specific regions of the cells, lacking a more detailed insight into the temperature characteristics, especially considering the limited temporal resolution of the used instrumentation.

The most substantial temperature fluctuations are observed near the floor region. In cases with a flat surface (experiments summary in Tab. C.1), peaks oscillate around 4 K, while rough boundaries scan exhibit fluctuations exceeding 5 K. As the sensor approaches the mid-high plane, the differences between $\Delta T = 20$ K cases become negligible. Similarly, no distinctions are apparent near the upper plate, with a maximal amplitude at the level of -4 K for both V20-S and V20-R.

In the bottom panel of Fig. C.4, two vertical layouts are presented, each illustrating 10 min series near both plates positions and segregating T' based on the given ΔT . The evident reverse symmetry is notable; however, it is important to highlight that there are varying amplitudes of fluctuations in each corresponding pair of graphs (same ΔT but distinct h). This variation may result from weaker thermal plumes departing from the top plate, as well as from the not perfectly insulated chamber's flange (mentioned in C.2.1), which could lead to minor mixing in the vicinity of the sensor deployment spot. For a more in-depth examination of the temperature fluctuations near both plates, refer to Appendix C.5.

The temperature fluctuations also manifest oscillations, particularly noticeable in the case of $\Delta T = 20$ K near the plates. However, these oscillations gradually

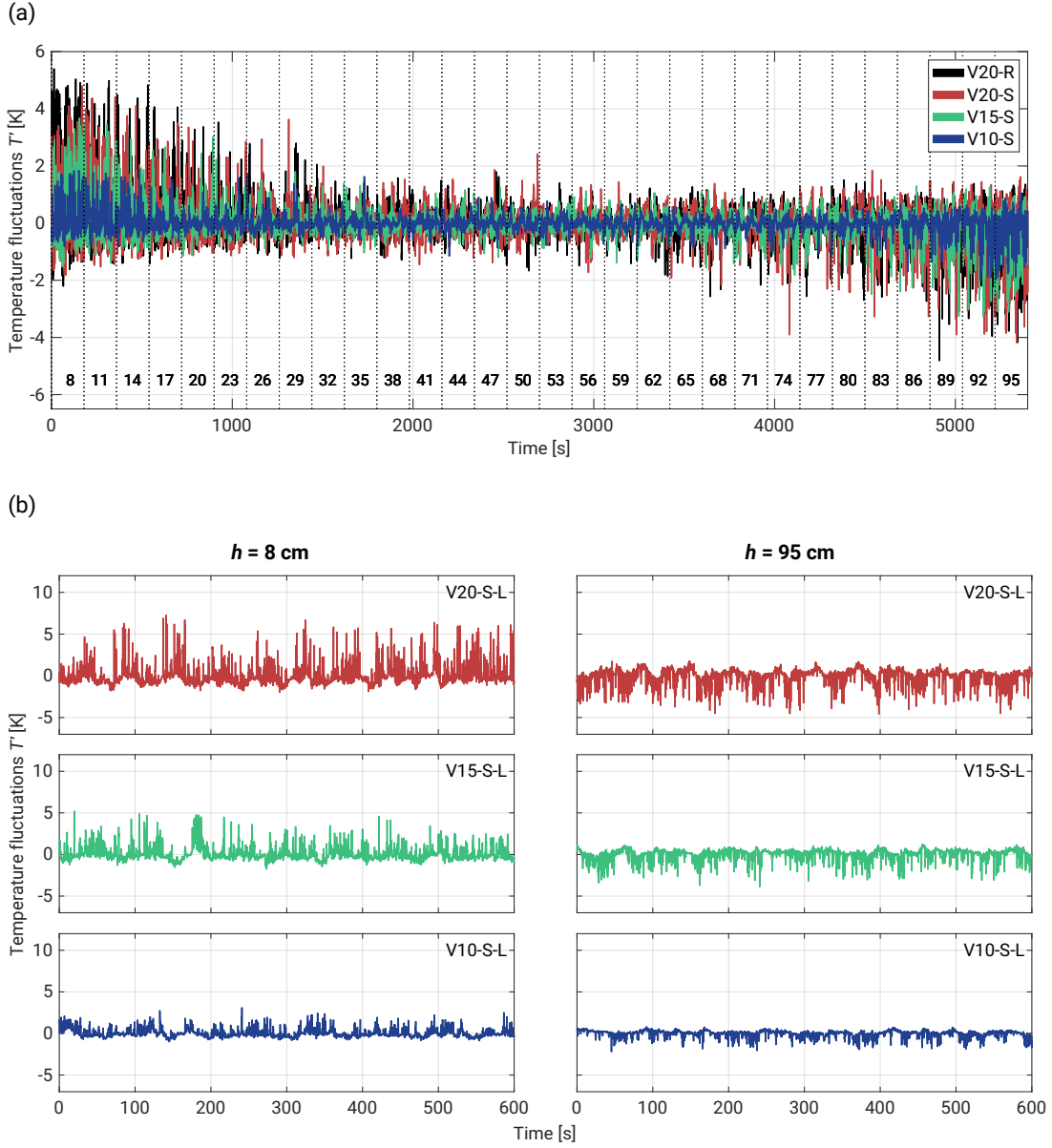


Figure C.4: Temperature fluctuations T' time series corresponding to different ΔT that are described in Tab. C.1. Top panel (a) shows time series collected during full vertical scans with the consecutive changes of the sensor positions across the chamber. The horizontal row of numbers denote the heights in centimeters above the lower plate. The chart includes 3 min series. Lower panels (b) represents 10 min measurements near the floor ($h = 8$ cm), and just below the ceiling ($h = 95$ cm, 5 cm below the top plate).

diminish as the temperature difference decreases and as the sensor moves toward the center of the cell. Analyzing V20-S-L at both heights, the periodicity appears irregular but is of a same order of magnitude as observed by [Anderson et al. \(2021\)](#) and therefore corresponds to the LSC. Previous studies have highlighted that the

LSC can exhibit various modes around its mean position, leading to phenomena such as out-of-phase oscillations at the top and bottom of the chamber (torsional mode, see [Funfschilling et al. \(2008\)](#)), as well as side-to-side oscillations (sloshing mode, see [Xi et al. \(2009\)](#); [Brown and Ahlers \(2009\)](#)). Cells with very high symmetry might be also characterized by spontaneously cease and reorientation of the LSC to different angular position ([Brown and Ahlers, 2009](#)). All these effects are beyond the scope of this investigation but the raw measurements give clear evidence of temperature oscillations near both plates.

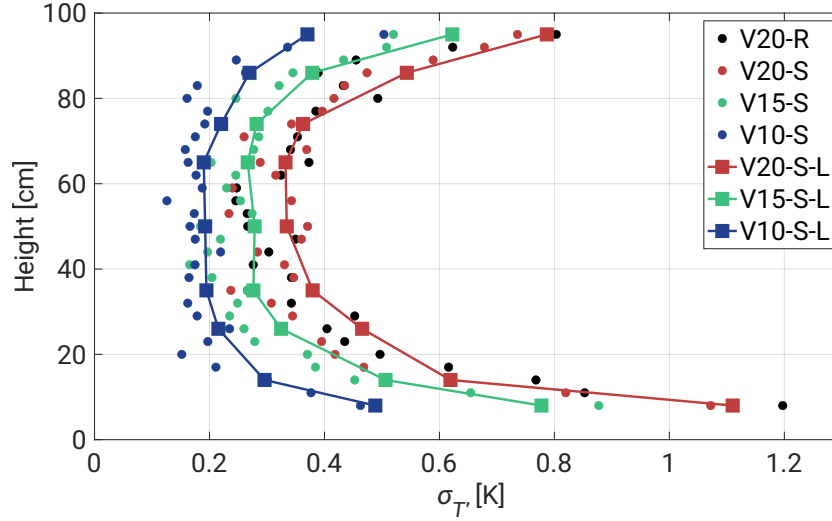


Figure C.5: Standard deviation $\sigma_{T'}$ with respect to the position of the sensor. Short time series (3 min) are denoted by circles, squares represent longer measurements (19 min). Decreasing ΔT shifts left $\sigma_{T'}$ values reducing the temperature fluctuations at all positions.

In Fig. C.5, the standard deviation $\sigma_{T'}$ is presented in relation to the sensor position within the chamber and illustrates the dependence of the fluctuation level, corresponding to the top panel of Fig. C.4. The highest $\sigma_{T'}$ values are observed near both plates with the maximum at the bottom. This asymmetry diminishes as ΔT decreases, starting with an approximate 0.4 K disparity in V20-R and concluding with about a 0.1 K shift in V10-S-L. It's noteworthy that extended measurements yield slightly different values, reflecting a more robust convergence as opposed to 3 min cases. The bulk region exhibits relatively constant values with comparatively small deviations. Additionally, this region experiences the smallest differences between corresponding ΔT values. Decreasing ΔT shifts left $\sigma_{T'}$ values and damps T' in the whole volume. In Fig. C.15a we provide non-dimensionalized form of standard deviation.

The surface topography contributes to slightly higher $\sigma_{T'}$ values, primarily in the closest vicinity of the plates. This effect may be attributed to the elevated

surface level, potentially leading to varied stages of thermal plume development at the same measurement position. However, these thermal structures are getting mixed with the surroundings, producing approximately equivalent results just a few centimeters higher. As previously mentioned, [He and Xia \(2019\)](#) emphasized that each region of the RBC can exhibit its local dynamics, a consequence of overlapping mechanisms that act as drivers for each other. In this specific case, the LSC induces mixing of all thermal structures originating from the surface. It can also turbulently propel thermal plumes due to irregular topography. The resulting mixing and stronger turbulence in this region might be responsible for the thermal peaks observed in the top panel of Fig. C.4.

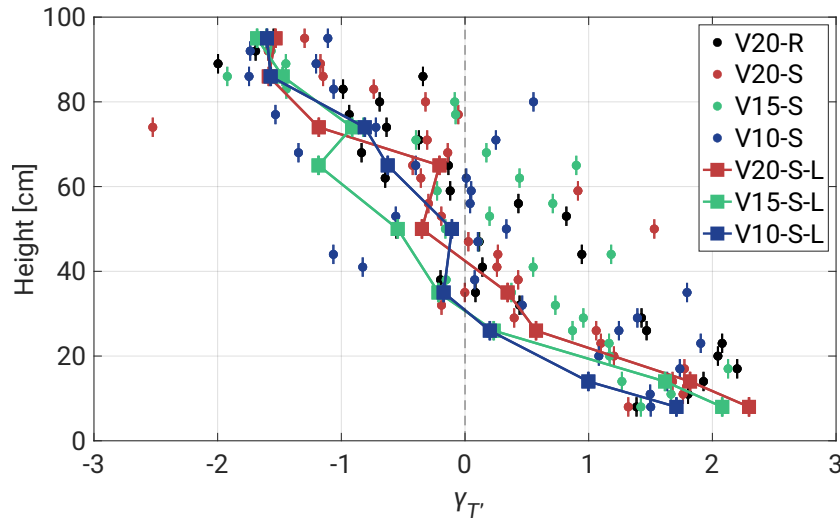


Figure C.6: Skewness $\gamma_{T'}$ with respect to the position of the sensor. Short time series (3 min) are denoted by circles, squares represent longer measurements (19 min). Uncertainties were calculated using formula $\delta_{\gamma_{T'}} = \sqrt{\frac{6N(N-1)}{(N-2)(N+1)(N+3)}}$ where N denotes the number of samples.

In Fig. C.6, the skewness of T' , denoted as $\gamma_{T'}$, is analyzed with respect to the vertical positions within the chamber. We use adjusted Fisher–Pearson standardized third moment, expressed as $\gamma_{T'} = \frac{N^2}{(N-1)(N-2)} \frac{\overline{T'^3}}{\sigma_{T'}^3}$, where N represents the number of samples. The findings confirm previous observations, showing positive skewness (associated with warm plumes) near the floor and negative skewness (indicative of cold plumes) just below the ceiling. The third moment is notably influenced by rare events, leading to significant fluctuations in the 3 min dataset but mostly averaged out in longer segments, resulting in more consistent curves.

The regions near both plates demonstrate data convergence of $\gamma_{T'}$ values with minimal deviations. An interesting observation is noted at a distance of 8 cm above the floor, where the 3 min records initially exhibit a skewness of about

1.4. This area likely experiences a higher frequency of intense thermal plumes, resulting in a broader range of temperature fluctuations (refer to Fig. C.5). It has been shown in previous studies that thermal plume detachment introduces large fluctuations in temperature and velocity boundary layer thickness (Wagner et al., 2012; Shi et al., 2012; De et al., 2018; Shevkar et al., 2022). Similar effects might be responsible for what we observe. As the plume structures develop, $\gamma_{T'}$ increases to approximately 2. Then, at the 20 cm level, there is a subtle indication of possible change in the thermal dynamics of the system. This change may be associated with specific transitions in convective flow patterns and more intense interaction of thermal plumes with the LSC in the ring layer around the walls and plates (see Fig. C.2a). Moving further away from the heated floor, the LSC is likely dominating the existing structures, increasing the dissipation of thermal energy and leading to a decrease in skewness. This results in thermal structures becoming more dispersed, leading to a narrower and less extreme distribution of temperature fluctuations.

However, not all thermal plumes could be fully averaged out, especially as the flow around the cell decreases towards more central regions. This might allow some remaining plume structures to reach the central region between 40–70 cm and mix which could result in positive skewness (bottom plumes carry higher energy). Similar behavior might be also observed in longer records, manifesting as fluctuations in $\gamma_{T'}$ within the 50–70 cm segment. Importantly, the positions of these shifts do not appear to be directly dependent on ΔT .

A comprehensive understanding of the thermal dynamics requires additional information on the small-scale temperature field around the axis, its velocity field, and a detailed description of the LSC time evolution. From the perspective of microphysical processes in future moist experiments, the Lagrangian histories of droplets or aerosols carried by thermal plumes—or alternatively located in the volumes between them—can theoretically lead to different droplet sizes (Chandrakar et al., 2018b, 2023). The local variability of $\sigma_{T'}$ and $\gamma_{T'}$ indicates that, over short timescales, droplets present in a given volume of the chamber may develop differing growth habits.

Upon comparing the topographic effect, we did not observe any major differences and concluded that 3 min records might be insufficient to investigate the impact caused by the presence of roughness. However, recent numerical work by Zhang et al. (2018) (for $10^7 \leq Ra \leq 10^{11}$ and fixed $Pr = 0.7$) indicates that there is a critical roughness height h_c below which the presence of roughness reduces heat transfer in RBC. The authors link this phenomenon with fluid being trapped and accumulated inside the cavity regions between the rough boundaries. Our ap-

proximate calculations for the II Chamber setup indicate the h_c of approximately 7 mm, compared to the 1.4 cm height of the tiles.

C.3.2 Power Spectral Densities

Power Spectral Density (PSD) of T' was computed using the Welch algorithm. Initial analyses were primarily directed towards estimating the LSC periods τ for the given ΔT and with respect to the measurement position (see Fig. C.7a). This involved utilizing 19 min datasets with window lengths approximately equal to the size of the collected segments. Employing a 50% overlap between segments and incorporating a high number of discrete Fourier transforms (eight times the window length), we derived estimates of the LSC periods along with their associated standard deviations. For $\Delta T = 10$ K a modest convergence of data points is observed, particularly notable within the 60–80 cm region. This resulted in relatively elevated standard deviation (grey areas denote $\pm 1\sigma_\tau$), yielding a period of approximately $\tau_{10} \approx 79$ s. Subsequent ΔT demonstrated a more uniform distribution across all levels, accompanied by a gradual reduction in the LSC period to approximately $\tau_{15} \approx 65$ s and $\tau_{20} \approx 57$ s.

The relationship between τ and ΔT , modeled by the power law function τ^e , is illustrated in Fig. C.7b. The fit exhibits narrow 95% prediction bounds in the fitted region but significantly large bounds outside. The model was constructed using a sparse dataset consisting of only four data points, including the result obtained by [Anderson et al. \(2021\)](#) at $\Delta T = 12$ K. Consequently, this limited dataset may not fully capture the true relationship, particularly at lower ($\Delta T < 10$ K) and higher ($\Delta T > 20$ K) temperature differences. The potential discrepancies could be attributed to a stronger diffusion dominance over convection at lower ΔT or more pronounced overlapping thermal plumes at higher temperatures, respectively.

In subsequent PSD analyses, we continued using only 19 min records, as shorter measurements exhibit too much variability in spectra due to their duration being comparable with the LSC periods. This time-modified window length, approximately 1/9 of the total segment with windows overlapping by half of their length, resulted in 17 individual PSDs that were averaged. This approach enhances chart readability while maintaining fidelity to the spectral slopes. To collapse the curves representing measurements from different positions, we followed the scaling method proposed by [Zhou and Xia \(2001\)](#). Fig. C.8a plots the scaled $f^2 P(f)$ spectrum for the V20-S-L case, enabling determination of the peak frequency f_p , around which the PSDs become universal functions. In this case, f_p oscillates around $f = 4$ Hz, exhibiting high convergence across all curves.

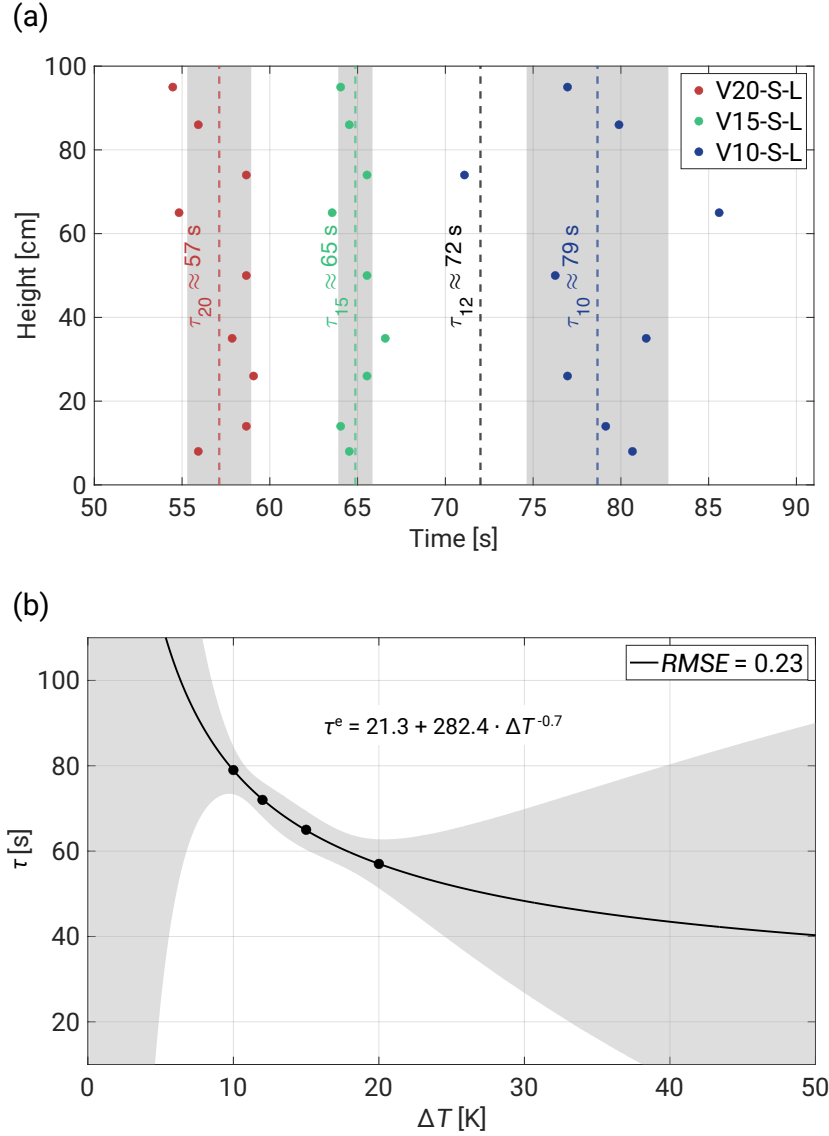
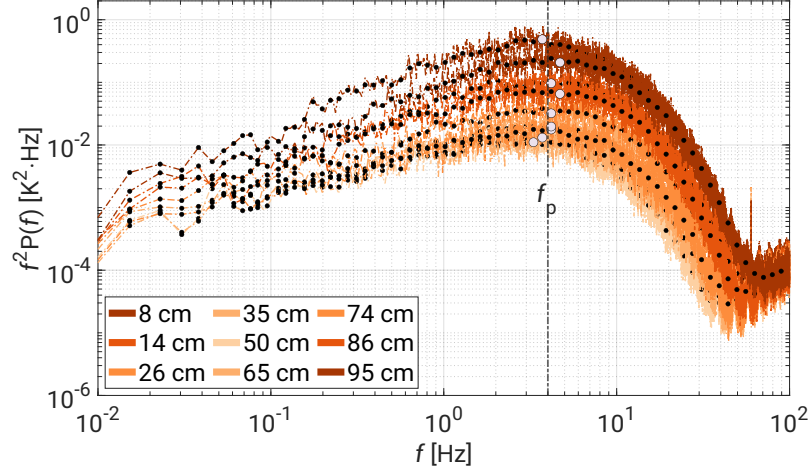


Figure C.7: Measured LSC periods with respect to ΔT and vertical position of the sensor. **(a)** Grey regions describe $\pm 1\sigma_\tau$ and the black dashed line denotes the result obtained by [Anderson et al. \(2021\)](#) for $\Delta T = 12$ K. **(b)** The relationship between τ and ΔT modeled by the power law (τ^e) function. The plot includes 95% simultaneous functional bounds, fitted equation, and root mean squared error ($RMSE$).

In Fig. C.8b, we provide a sample of scaled PSD $P(f)/P(f_p)$ versus f/f_p in the lower half of the chamber and define three spectrum regimes. Based on the scaling method proposed by [Kumar and Verma \(2018\)](#) and [Zhou and Xia \(2001\)](#), we conducted also a similar analysis in the wavenumber domain. For more details, please refer to Appendix C.7. To estimate the slopes, we employed a methodology outlined in [Siebert et al. \(2006b\)](#) and [Nowak et al. \(2021\)](#), averaging raw spectra

(a)



(b)

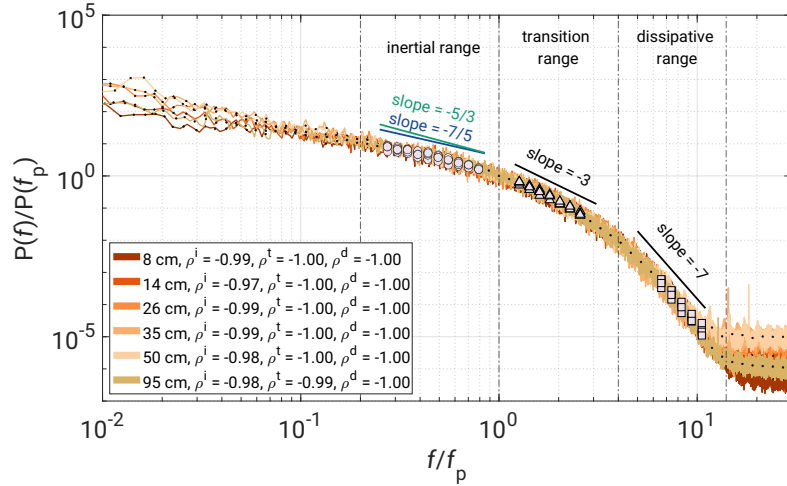


Figure C.8: Scaled V20-S-L PSD with respect to the UFT positions (color gradients) in the chamber. **(a)** Scaled spectrum of $f^2 P(f)$ across the chamber volume and with marked mean f_p value, $f_p \approx 4$ Hz. **(b)** PSD $P(f)/P(f_p)$ versus $f/(f_p)$ with three defined regimes: inertial range (circles, $0.2 \leq f/f_p \leq 1$), transition range (triangles, $1 \leq f/f_p \leq 4$), and dissipative range (squares, $4 \leq f/f_p \leq 20$). Each regime is denoted by different markers with an approximate slope value added above curves. The Pearson correlation coefficients p have upper indices to indicate the regimes. Please note that the results presented in the bottom panel cover positions from the lower half of the chamber as well as the top position.

over equidistant logarithmic frequency bins (twenty bins per decade in our case) and then fitting power law functions. To obtain the best possibly fit we selected spectra regions based on the highest log-log linearity criteria using the Pearson correlation coefficient p for the resampled points.

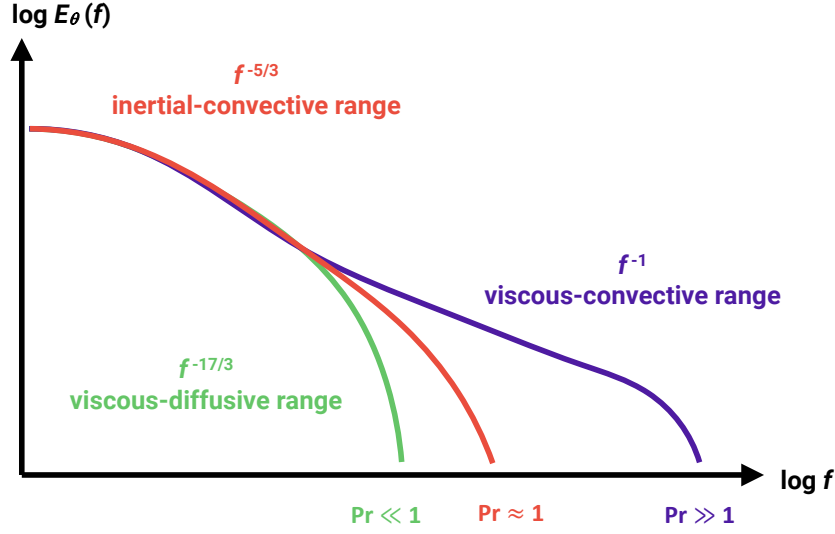


Figure C.9: Schematic of passive scalar spectrum depending of Pr regime. Figure based on the graph from [Gotoh and Yeung \(2012\)](#) with minor modifications.

Extended discussions on passive scalar spectra scaling can be found in works such as [Gotoh and Yeung \(2012\)](#) and [Sreenivasan \(2019\)](#). We adapted the graph from the former study for Fig. C.9, which illustrates possible spectral slopes as a function of the Pr number. For our experimental conditions, the results are expected to align with the scaling for $Pr \approx 1$. In the following paragraphs, we aim to contextualize our findings within the broader scope of the literature and address potential explanations for observations that have not yet been described.

In Fig. C.10a, the regime $0.2 \leq f/f_p \leq 1$, marked by circles, in the literature is referred to as the inertial-convective regime which is associated with OC scaling, where the temperature field (acting as a passive scalar) does not influence the flow dynamics ([Castaing, 1990](#); [Cioni et al., 1995](#); [He et al., 2014a](#)). However, in thermally-driven convection, the flow is actively driven by temperature-induced buoyancy differences. This range is therefore redefined as the inertial-buoyancy range, where the temperature spectrum follows BO scaling ([Chillá et al., 1993](#); [Ashkenazi and Steinberg, 1999](#); [Zhou and Xia, 2001](#)). Our analysis provides no definitive answer, as the slopes oscillate between OC and BO scaling, with a slight bias toward $-7/5$. However, as previously noted, the two slopes are too close to be easily distinguished (see Fig. C.8b). Thus, we classify this range simply as the inertial range without committing to a specific scaling profile. Interestingly, [Niemela et al. \(2000\)](#) ($10^6 \leq Ra \leq 10^7$) and [Pawar and Arakeri \(2016\)](#) (axially homogeneous buoyancy-driven turbulent flow, $10^4 \leq Ra \leq 10^9$) observed both scaling behaviors in their experiments. The latter study raised the question of whether these results indicate dual scaling or a gradual steepening of the spectrum.

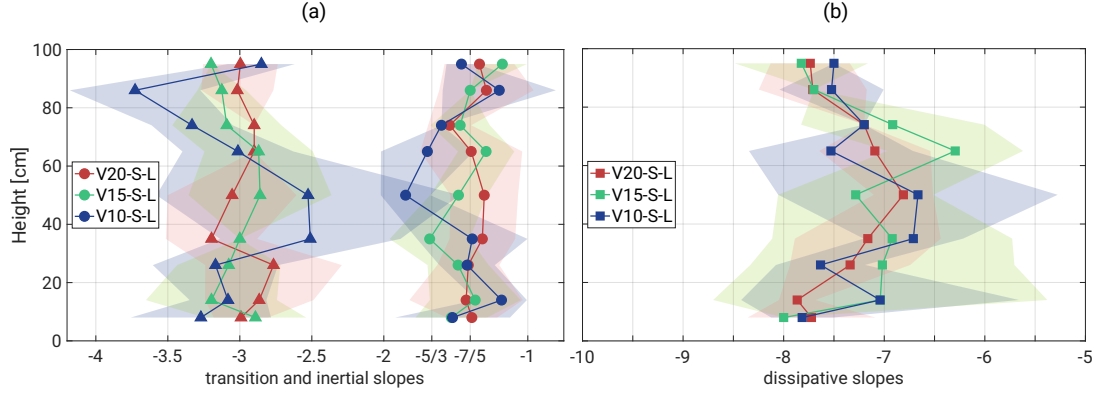


Figure C.10: Panel of fitted slopes. **(a)** corresponds to transition and inertial ranges respectively whereas **(b)** describes dissipative regime. The slopes are accompanied by 95% confidence bounds except in a few cases where the slopes were manually fixed due to fitting difficulties.

No direct references in the literature address the subsequent regime scalings (~ -3 and ~ -7) or the roll-off region of the scalar spectrum (see Fig. C.9). Recent investigations of the dissipation range in the energy spectrum only began exploring this regime suggesting a superposition of two exponential forms (Khurshid et al., 2018; Buaria and Sreenivasan, 2020). Therefore, our further discussion will explore potential connections between our and other results in convective flow research.

The -3 scaling might simply represent a crossover into the following dissipative range but the mid-range scales in the system could also be subjected to more subtle phenomena. RBC dynamics span a wide range of scales, including thermal plumes, vortices, and the LSC, with complex interactions between these structures (Fernando and Smith IV, 2001; Xi et al., 2004; Zhou et al., 2016b; Guo et al., 2017; Chen et al., 2018; Pandey et al., 2018; De et al., 2018; Dabbagh et al., 2020; Wang et al., 2022; Yano, 2023; Yano and Morrison, 2024). These overlapping processes likely influence the observed spectra. Recent LES studies on thermal plumes have revealed additional insights into scalar spectral scaling (Chen and Bhaganagar, 2021, 2023, 2024). Using a heated surface experiment, the authors reported density and temperature spectra scaling as -2.7 , strongly correlated with the velocity spectrum. Furthermore, vertical heat and mass fluxes exhibited a -3 scaling, matching the vertical component of the turbulent kinetic energy (TKE) spectrum. This corresponds with the regime $1 \leq f/f_p \leq 4$ marked by triangles in Fig. C.10a, which is characterized by slopes oscillating around -3 , with slightly greater variability observed for the V10-S-L case.

Moreover, in the papers by Chen and Bhaganagar both spectra of 2D TKE, horizontal structures of 3D TKE, as well as helicity, consistently exhibited slopes

of $-5/3$ and -3 respectively. Their flux analysis revealed inverse TKE and helicity cascades toward large structures and forward cascades of these invariants for the small scales. Further studies on velocity-based longitudinal structure functions (2nd, 3rd, and 4th moments) showed that the scaling exponents fell between theoretical predictions for 2D and 3D systems. For example, strong vertical confinement or anisotropic Fourier mode distributions can mimic 2D dynamics in certain ranges (Musacchio and Boffetta, 2019; de Wit et al., 2022; Alexakis, 2023). Consequently, energy cascades and their directions are highly scale-dependent, influenced by invariants such as enstrophy and helicity, potentially resulting in the coexistence of multiple cascades and the superposition of power law spectra. Detailed discussions on cascades and transitions in turbulence are provided by Alexakis and Biferale (2018). However, in the II Chamber we do not recognize strong anisotropy and only regions near the top and bottom plates could potentially exhibit such quasi 2D, effects whereas similar spectra slopes are observed in the whole volume of the chamber. On the other hand, in 3D turbulence, large-scale stirring can introduce helicity, modifying cascade directions and contributing sub-leading corrections depending on the helicity’s sign (Eidelman et al., 2014; Yan et al., 2020; Plunian et al., 2020). The exact role of helicity in energy transfer mechanisms remains unclear and is an active area of research (Yao and Hussain, 2022).

Given this complexity, it is reasonable to question whether theoretical assumptions such as isotropy, homogeneity, stationarity, and self-similarity are sufficient to capture the full physical reality. Anisotropy and non-stationary coherent structures likely play significant roles, potentially causing deviations from predicted spectral scaling. In the RBC, temperature forcing drives both large- and small-scale structures, complicating the universality of passive and active scalar theories. Alexakis and Biferale (2018) emphasize that strong assumptions about cascades and their directions are not feasible for active scalars, particularly when velocity and scalar fields are strongly coupled. This leaves open questions about preferential sampling effects of forcing along Lagrangian trajectories of the active scalar field. In the given full spectrum analysis, the nature of the spectral break observed near $f/f_p \approx 1$ may be linked to a transition between LSC-dominated scales, characterized by large coherent structures, and smaller-scale thermal plumes and vortices. These overlapping power laws could ultimately shape the observed spectra. Consequently, we interpret the -3 regime as a transition range between buoyancy-scale processes and molecular dissipative scales. Additional analysis presented in Appendix C.8 estimates the dominance of thermal plumes near the chamber center. Following He and Xia (2019), we demonstrate a logarithmic dependence of

$\sigma_{T'}$ on chamber height, reflecting a balance between buoyancy and inertial forces.

Finally, our high-frequency measurements indicate that the dissipative regime slopes are approximately -7 (see Fig. C.10b). The slope distribution with respect to chamber height is symmetrical, reaching the steepest values near the plates (~ -8) and the smallest in the bulk region (~ -7). According to Sreenivasan (2019), no scalar spectrum description exists for the dissipative regime. While the energy spectrum in this range can be represented by an exponential form, our findings suggest that for the scalar field, even a single power law is sufficient. Corresponding characteristics are visible in Niemela et al. (2000) and Zhou and Xia (2001), although these studies provide limited discussion on the observed slopes.

Worth noting is also the variability of the noise level (starting around $f/f_p \approx 12$) with respect to the chamber height, with its highest values linked to the bulk region and the lowest (10 times magnitude difference) representing regions near the plates (see Fig. C.16 in Appendix C.7). This phenomenon is attributed to the mean velocity field and its strong reduction in the central areas of the cell causing the noise to rise.

C.3.3 DNS versus experimental data

Another goal of the presented study was to compare the experimental results obtained with the UFT and the corresponding DNS data. The essential details on the DNS methodology and properties of the series can be found in Sec. C.2.2. Our approach was to repeat the analysis and to retrieve both basic characteristics of temperature profile and information on PSD at different cell's levels. Sample series can be seen in Fig. C.13 and Fig. C.14.

Fig. C.11 present analogous to Fig. C.5 study but with the DNS data covering exactly same thermodynamic conditions in the cell. Since the vertical grid size spans from about 1 mm near the plates to about 2.3 mm at the center, the available range significantly improves comprehensiveness of boundary layers. The limit regions exhibit maximum deviation of $\sigma_{T'} \approx 2$ K with a bias in the vicinity of the upper plate. Also the shape of the curves is more bumped up in the center and slightly shifted left what might be an analogy to 3 min records in the Fig. C.5. The numerical data provide more stable monotonicity but represents equivalent periods of time. In Fig. C.15b there is non-dimensionalized form of this figure.

Similar conclusions can be made in terms of skewness profiles in Fig C.12a. The DNS data exhibits much smaller fluctuations than corresponding 3 min UFT segments but preserve the general tendency near the floor and in the central region.

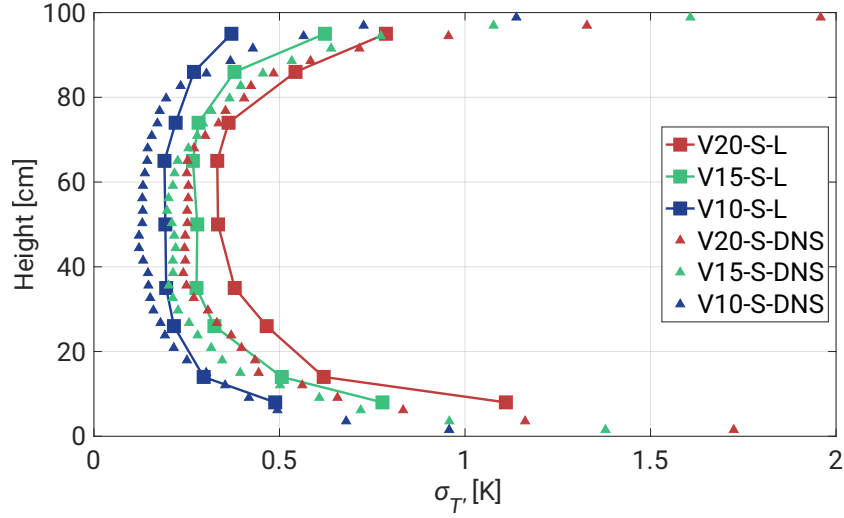


Figure C.11: Standard deviation σ_T with respect to the height of the chamber. The chart analogical to Fig. C.5 but including only 19 min segments (squares) and the DNS (triangles).

The characteristic jump in $\gamma_{T'}$ is observed not around 20 cm but in half way. On the other side, a symmetrical jump is also observed near the ceiling what was not revealed in the UFT measurements likely due to a very shallow layer of thermal plume regime (the UFT measurements ended about 5 cm below the ceiling). Also the mixing region between 40–70 cm is reestablished resulting in higher deviations for lower ΔT . The skewness distribution contributes to the mean vertical profile in the cell (see Fig. C.12b). The presence of both positive (~ 40 cm) and negative (~ 80 cm) velocity jumps drives dynamics in the bulk region, facilitating the mixing of cold and warm plumes. The horizontal components of the flow follow the LSC directions giving mean values of 15 cm/s near the plates. A more comprehensive discussion on the dynamics of the thermal plumes can be found in Sec. C.3.1. Note that the plots in Fig. C.11 and C.12 represent single-column data (not the horizontal average), meaning perfect symmetry is not expected, in particular for the period of the LSC circulation.

C.4 Summary

We conducted a small-scale study on the temperature structure of RBC in the II Chamber using three temperature differences (10 K, 15 K, and 20 K) at Ra of approximately 10^9 and Pr of 0.7. The objective was to improve our understanding of thermally-driven convection by analyzing small-scale variations along the chamber's axis. Measurements were performed using a miniaturized Ultra-

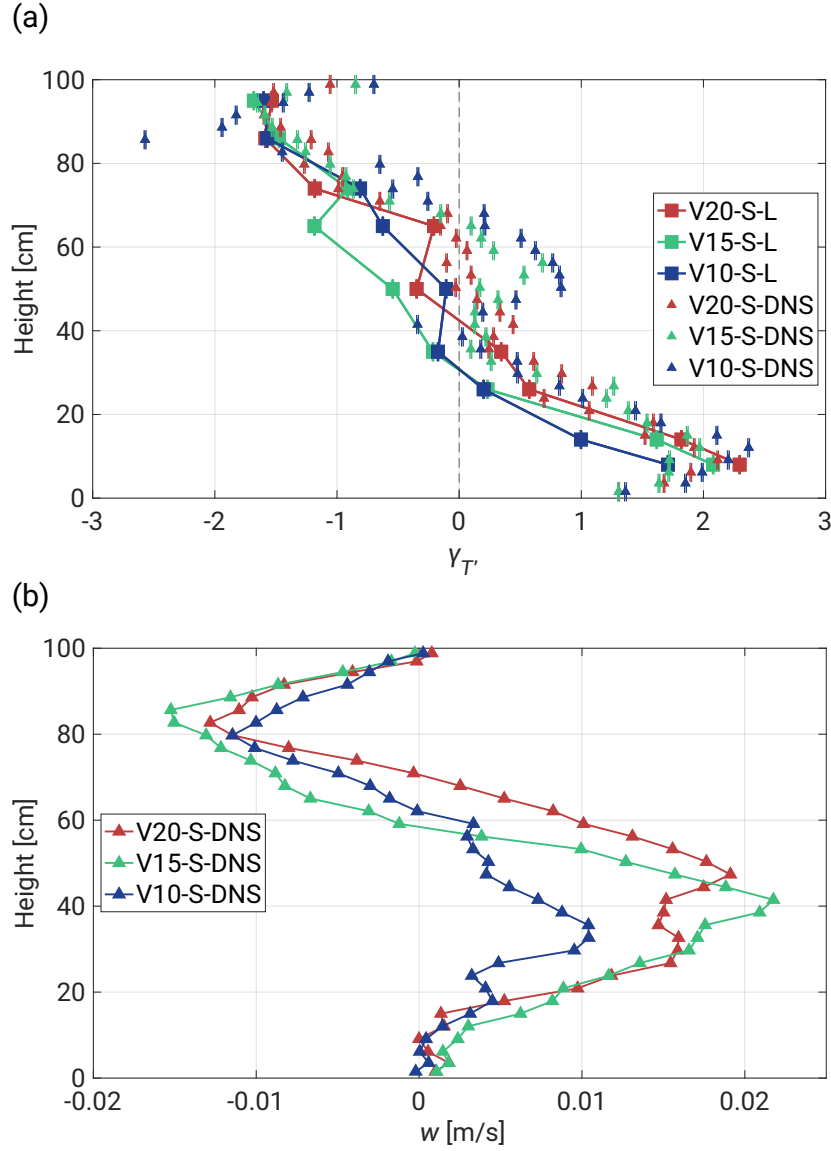


Figure C.12: **(a)** Skewness, $\gamma_{T'}$, as a function of height within the chamber supported by the 3 min DNS data. The chart analogical to Fig. C.6 but including only 19 min segments (squares) and the numerical time series (triangles). **(b)** Mean vertical flow profile provided by the DNS.

Fast Thermometer operating at 2 kHz, enabling undisturbed vertical temperature profiling from 8 cm above the floor to 5 cm below the ceiling. Unlike classical RBC studies, this research is characterized by relatively short measurement durations of 19 min and 3 min, which fall below the typical record lengths for such experiments. Nevertheless, the primary goal was to link this work with other experiments conducted in the II Chamber. Its main objective is to investigate microphysical processes relevant to the real atmosphere, such as supersaturation fluctuations crucial for cloud formation and development. Small-scale temper-

ature profiling under varying conditions, as typically observed in the chamber, provides valuable insights that could inform future experiments and address related scientific questions. The key findings of this study are summarized below.

- Basic Characteristics:** We observed significant changes in the standard deviation and skewness of the distribution of temperature fluctuations near the top and bottom surfaces. Additionally, we see variations in the spectra scaling in these near-surface regions. The turbulence in the center of the chamber exhibited characteristics more akin to homogeneous, isotropic turbulence. These observed variations were attributed to the dynamics of local thermal plumes and their interaction with the large-scale circulation (LSC). Both 19 min and 3 min measurements were consistent, although the shorter records showed higher variability in standard deviation and skewness distribution. The statistical properties of the temperature field obtained in the II Chamber may offer insights into thermal structures development in the atmospheric surface layer, thereby enhancing our understanding of surface-air temperature fluctuations characteristics with respect to the thermal conditions (Kukharets and Nalbandyan, 2006). Furthermore, the analysis of large-scale coherent structures in RBC provides a framework for broader perspective on thermal circulations, as well as the distribution of temperature and moisture, both in cloud chambers (Anderson et al., 2021) and by analogy in the lower atmosphere (Zhou and Xia, 2013; Moller et al., 2021). The chamber is not designed for idealized RBC experiments. Its structure solutions (e.g. windows on sides, atypical side-wall boundary conditions) aimed at cloud microphysics research is revealed in asymmetries of the profiles of temperature fluctuations statistics.
- Topographic Effects:** No major differences were observed corresponding to topographic effects, likely due to insufficient time series. However, numerical work by Zhang et al. (2018) shed light on the necessary roughness height for robust heat transfer in RBC. Below the critical point, the authors observed trapped and accumulated heat inside the cavity regions between the rough boundaries.
- Dynamic Regimes:** PSD analysis revealed periodicity of LSC with respect to the temperature differences, characterized by the power law formula consistent with previous findings (Anderson et al., 2021). We identified three distinct dynamic regimes: an inertial range (with slopes of $\sim -7/5$), a transition range (slopes of ~ -3), and a dissipative range (slopes of ~ -7). The

scale break between the inertial and transition ranges was attributed to a dynamic transition from the LSC-dominated regime to the thermal plume regime. Appendix C.8 demonstrated that this transition is also observable in the spatial domain. Our findings are consistent with other studies not directly related to RBC though. For example, a similar scale break between inertial and transition ranges was observed in temperature fluctuation measurements near the surface of Jezero Crater on Mars (de la Torre Juárez et al., 2023), whereas slopes of $-17/3$ and -3 have been reported in power spectra of solar surface intensity variance field, attributed to buoyancy-driven turbulent dynamics in a strongly thermally diffusive regime (Rieutord et al., 2010).

- **Experiment Versus DNS:** Experimental findings showed convincing agreement with DNS conducted under similar thermodynamic conditions, marking a rare comparative analysis in this field. Velocity profiles supported the argument for the nature of thermal plumes, and a method to convert spectra from the frequency domain to the wavenumber domain was detailed (see Appendix C.7). Despite the presence of imperfect boundaries such as window flanges, sampling ports, and instrumentation, idealized DNS provided a reasonable representation of the actual II Chamber flow, indicating that DNS adequately resolves surface layer fluxes. These results are valuable for improving and validating numerical research, such as sub-grid Large-Eddy Simulation models (Salesky et al., 2024), as well as heat transport models (Goluskin, 2015).

C.5 Quicklooks of temperature fluctuations

The figures illustrate two realizations of temperature fluctuations at the sensor’s position under similar conditions (from the experiment and DNS). The presence of filaments or coherent structures, with temperatures close to that of the nearby plate, is clearly visible. It is important to note that this is not a one-to-one comparison of the same flow but rather an illustration of the maximal scalar fluctuations observed in both the simulation and the experiment. Despite differences in time resolution, both curves in each case exhibit similar magnitudes. The subsequent zoomed-in segments further emphasize the variability within these realizations.

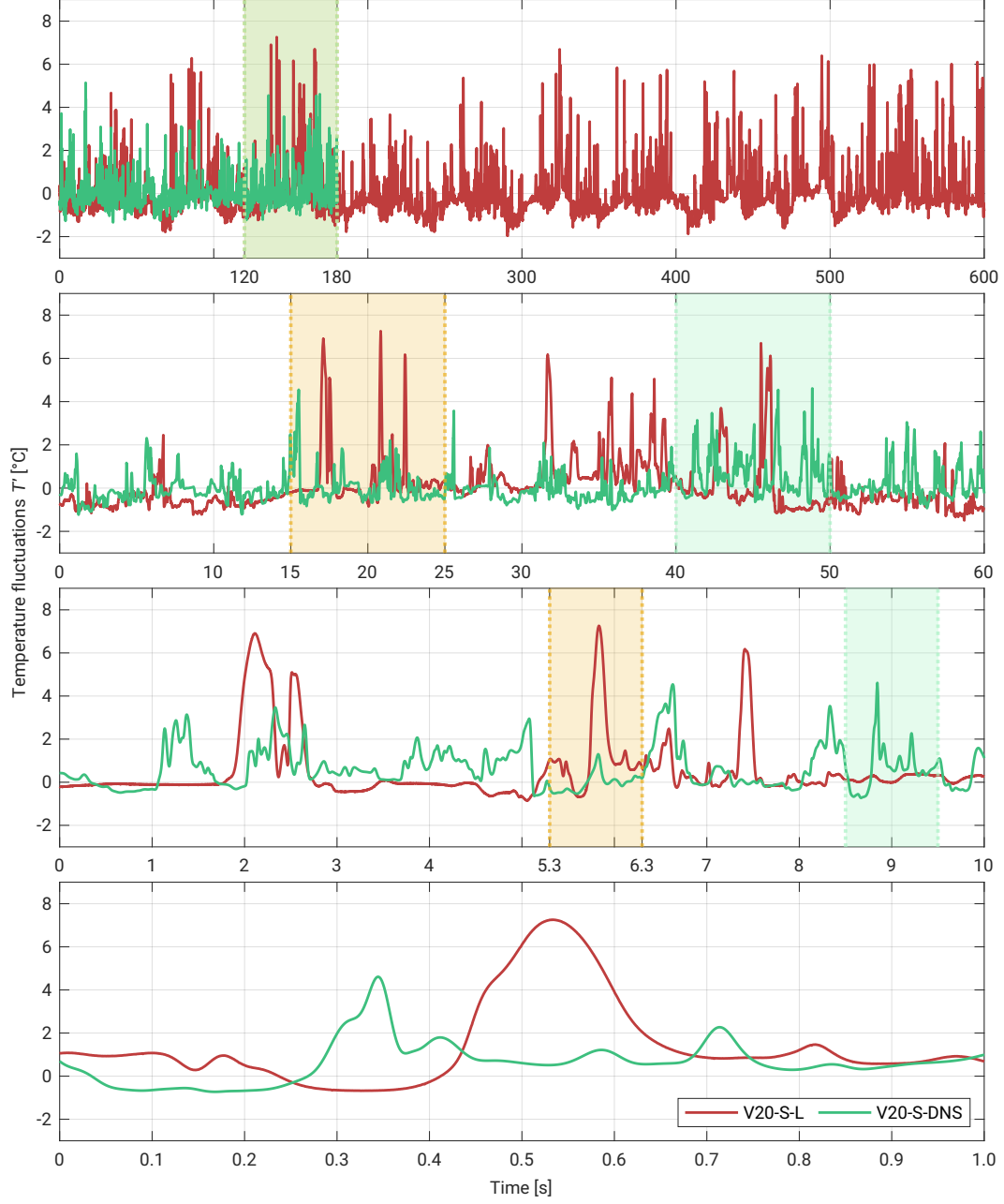


Figure C.13: Experimental versus DNS T' series ~ 8 cm above the floor showed in the following zoomed in time segments: 600 s, 60 s, 10 s, and 1 s. The used dataset covers $\Delta T = 20$ K case. Please note that the time series from the experiment and the DNS simulation do not correspond to each other.

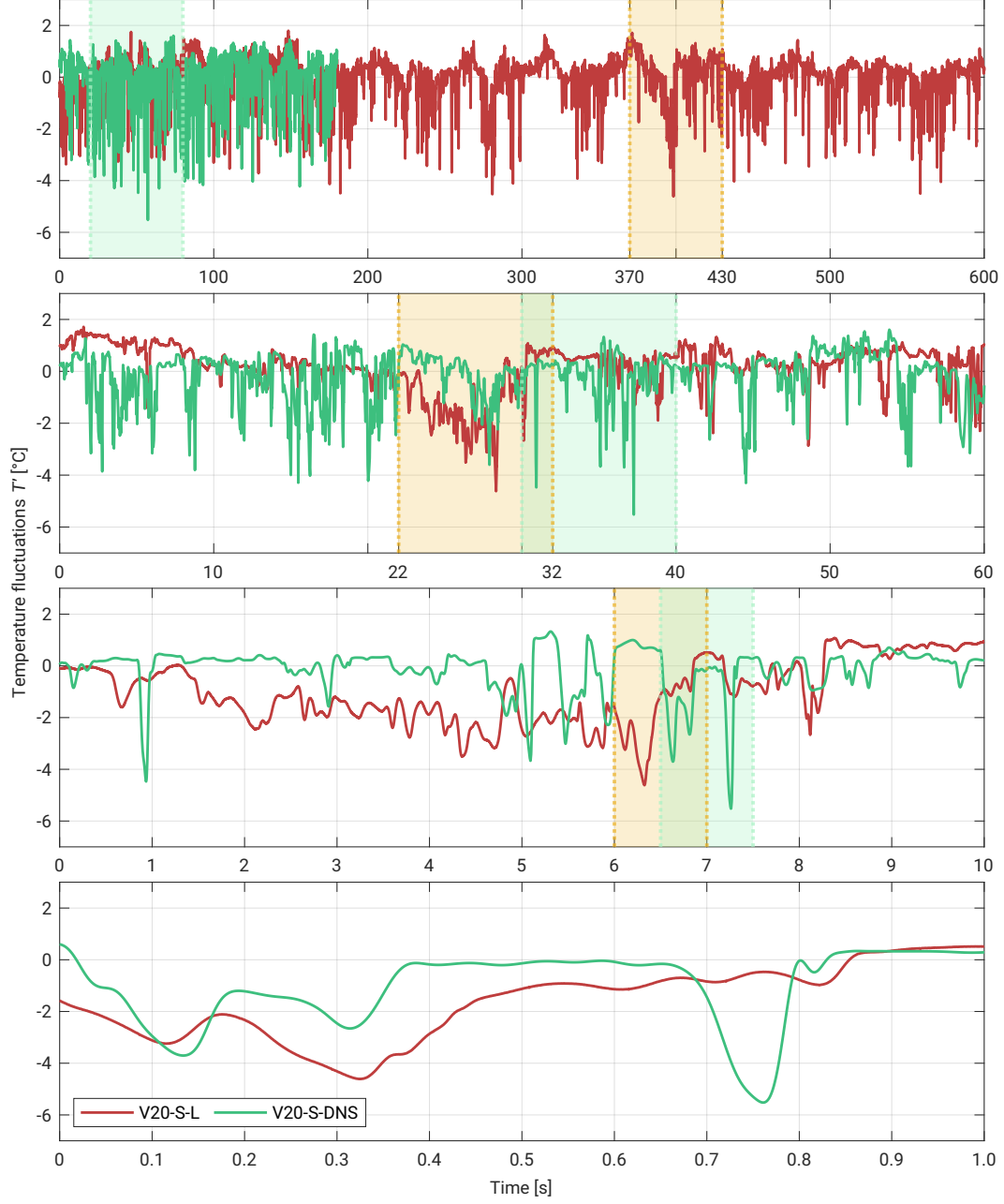


Figure C.14: Experimental versus DNS T' series ~ 5 cm below the ceiling showed in the following zoomed in time segments: 600 s, 60 s, 10 s, and 1 s. The used dataset covers $\Delta T = 20$ K case. Please note that the time series from the experiment and the DNS simulation do not correspond to each other.

C.6 Non-dimensional representation of standard deviations

Non-dimensionalized profiles of the standard deviation show stronger convergence in longer records compared to their dimensional representation.

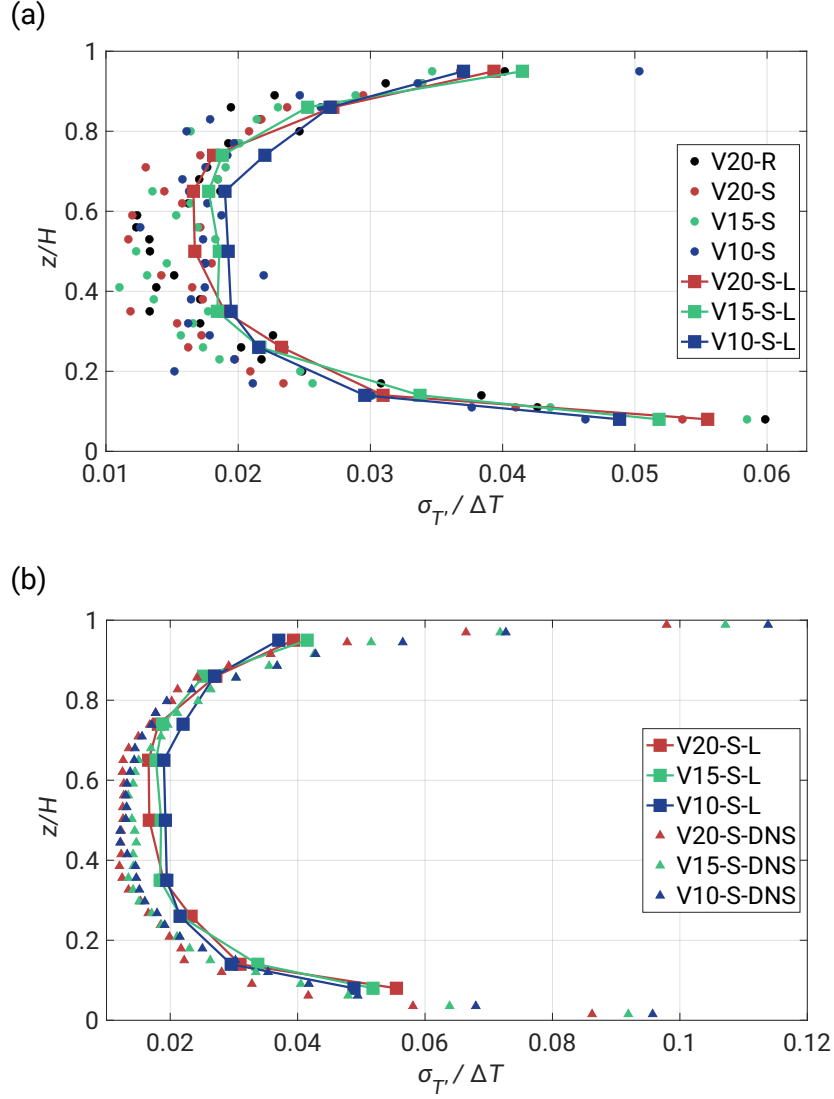


Figure C.15: Non-dimensionalized standard deviation scaled by corresponding ΔT . In the figure z/H represents vertical distance z measured from the bottom plate being normalized by the cell height $H = 1$ m. (a) Analogy of Fig. C.5. (b) Analogy of Fig. C.11.

C.7 Power Spectral Density in wavenumber space

In the atmospheric community, PSD is typically presented in either the frequency or wavenumber domain, depending on preferences or scientific goals. As demonstrated in Section C.3.2, the collapsed spectral curves in the frequency domain exhibit three dynamic regimes that characterize thermal convection in the Π Chamber. However, by following the scaling method proposed by Kumar and Verma (2018) and the generalized approach of Zhou and Xia (2001), one can obtain analogous PSD in the wavenumber domain.

The first step of the scaling procedure involves the following transformations:

$$k \approx \tilde{f} = f(2\pi)/U,$$

$$P(k) \approx P(\tilde{f}) = P(f)U/2\pi.$$

where $P(\tilde{f})$ and \tilde{f} represent the scaled frequency spectrum and scaled frequency, respectively. The DNS data revealed a symmetrical profile of the mean velocity U near the axis (see Fig. C.16). It gradually decreases towards the bulk region, reaching about 0.02 m/s, and maintains approximately equal values near both plates. The resulting wavenumber spectral curves are rescaled with U and shifted accordingly. To collapse them, we found the Kolmogorov length scale, defined as $\eta = (2\pi)/k_n$, where k_n is the wavenumber noise level, and performed another scaling to obtain the $P(k\eta)$ spectrum. The last step follows the adopted procedure of Zhou and Xia (2001).

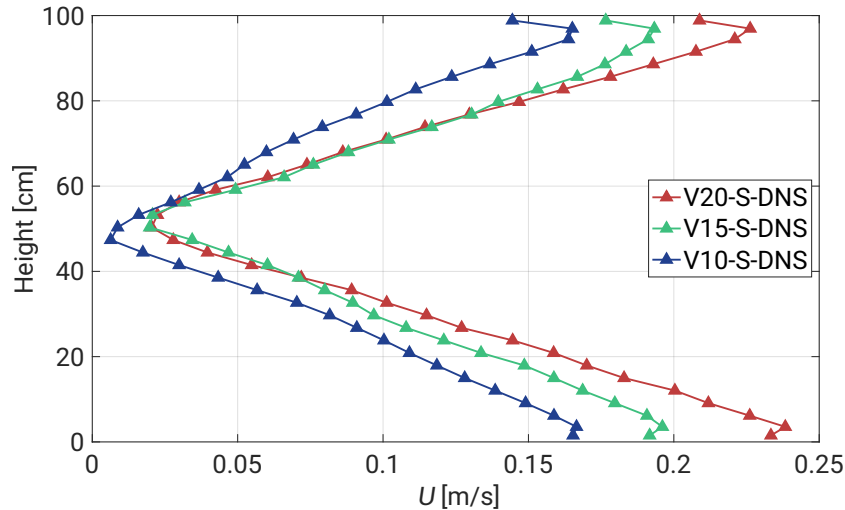


Figure C.16: Magnitude of the mean velocity U profile near the axis of the chamber with respect to its height. Each curve represent different ΔT .

In Fig. C.17a, we present the estimation of $k_p\eta$, what is a direct analogy to

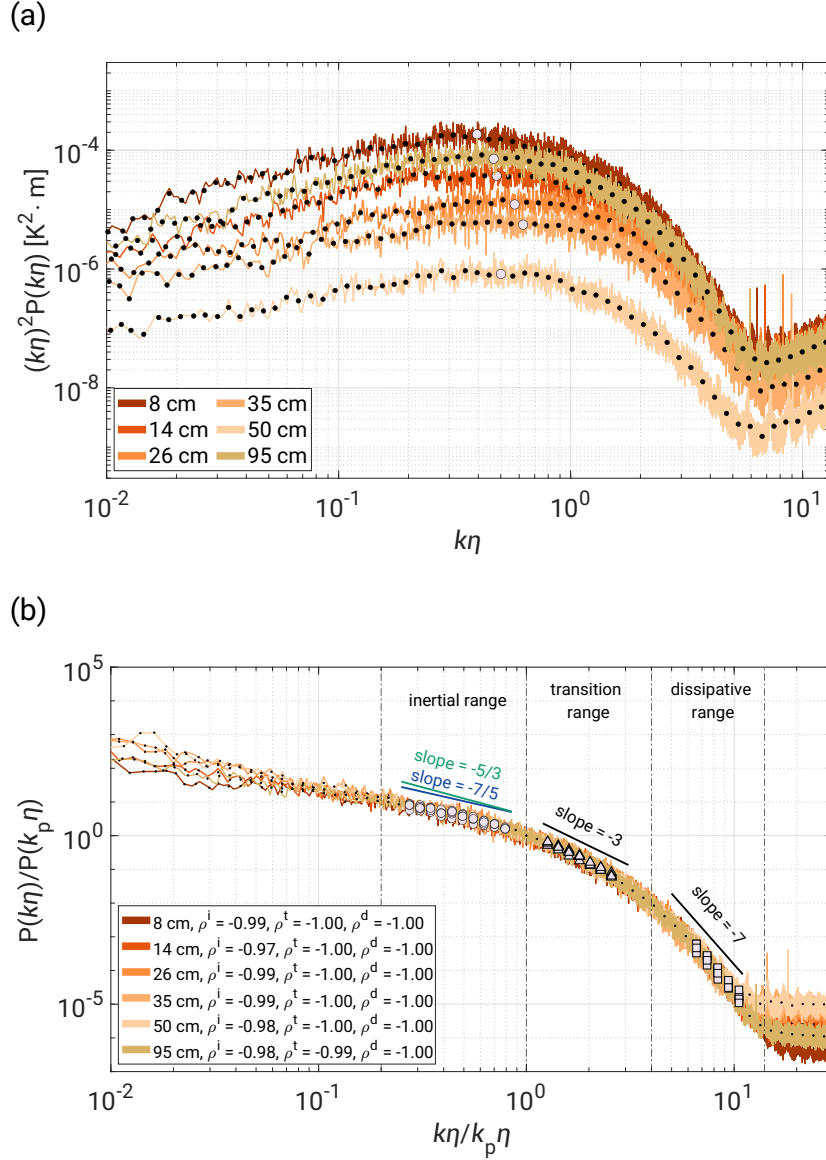


Figure C.17: Analogical to Fig. C.8 spectra of V20-S-L case but in wavenumber domain. (a) Scaled spectrum of $k\eta^2 P(k\eta)$. (b) PSD $P(k\eta)/P(k_p\eta)$ versus $k\eta/k_p\eta$ with three defined regimes: inertial range (circles, $0.2 \leq k\eta/k_p\eta \leq 1$), transition range (triangles, $1 \leq k\eta/k_p\eta \leq 4$), and dissipative range (squares, $4 \leq k\eta/k_p\eta \leq 20$). Legend includes the Pearson correlation coefficients p .

f_p in Subsection C.3.2, for the V20-S-L case in the scaled $k\eta^2 P(k\eta)$ spectrum. Unlike the corresponding plot in the frequency domain (see Fig. C.8a), $k_p\eta$ does not oscillate around one value. Here, we observe a gradual increase in $k_p\eta$ values towards the bulk region, with the $k\eta^2 P(k\eta)$ maximum occurring around $k_p\eta \approx 0.5$. Fig. C.17b provides the final result of the frequency to wavenumber scaling. Both the slopes and dynamic ranges are conserved, providing a clear analogy to Fig. C.8.

C.8 Standard deviation scaling

To verify if and where we can observe thermal plume dominance in the chamber, we followed the methodology outlined by [He and Xia \(2019\)](#).

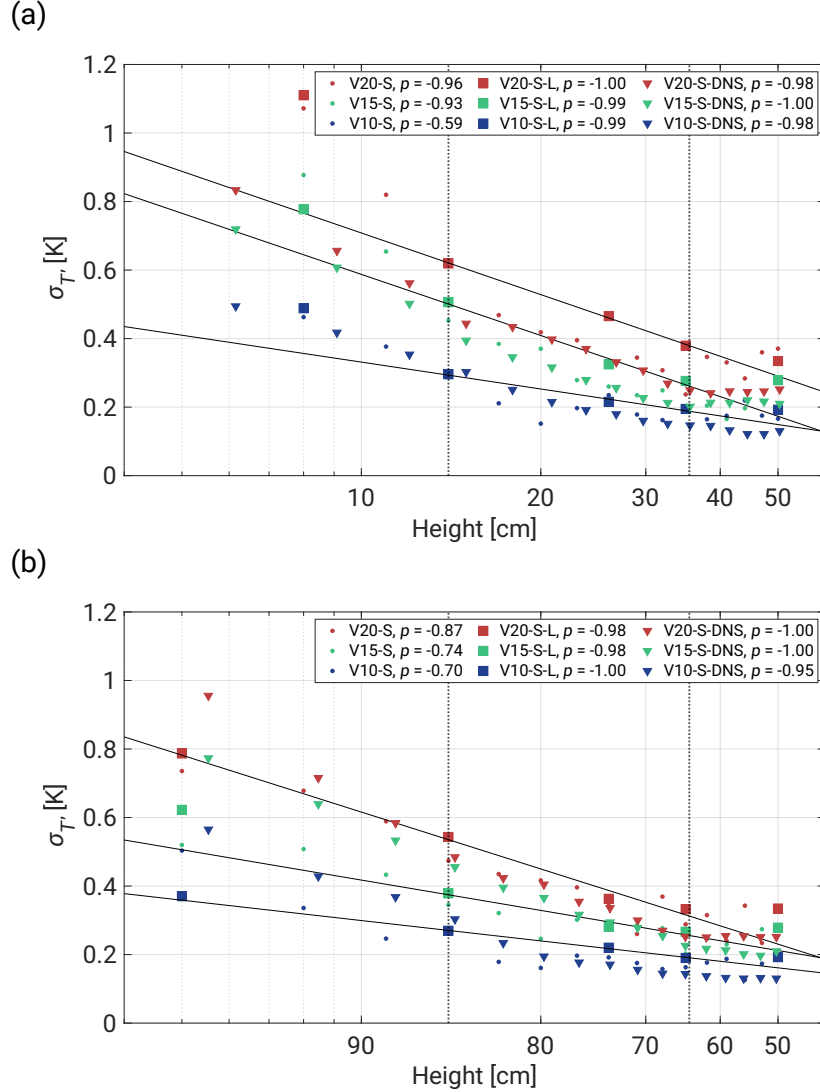


Figure C.18: Standard deviation $\sigma_{T'}$ distribution of both 19 min, 3 min and DNS dataset in semi-log domain near the floor **(a)** and close to the ceiling **(b)**. Both legends include Pearson correlation coefficients. Note that the fitted curves correspond only with 19 min measurements.

They demonstrated a strong connection between plumes and the logarithmic root mean square temperature profile using a different setup, which consisted of water as a working fluid ($Pr = 4.34$), a rectangular-shaped container with $\Gamma = 4.2$, and Ra varied from 3.2×10^7 to 2×10^8 . For our purposes, we analyzed the standard deviation $\sigma_{T'}$ distribution of both the 19 min, 3 min, and DNS datasets.

Fig. C.18 presents the results for two regions in the semi-log domain— $\sim 15\text{--}35$ cm near the floor (Fig. C.18a) and $\sim 65\text{--}95$ cm near the ceiling (Fig. C.18b). In the both regimes we provided the respective Pearson correlation coefficients and fitted the curves for 19 min time series. Each profile in the lower half of the chamber exhibits significant linearity correlation in the given region, including the 3 min experimental dataset. Only the V10-S case notably differs from the remaining results, dropping down to $p = -0.59$. The corresponding area in the upper half gives similarly high indications of the p values, excluding shorter measurements, providing evidence of weaker thermal plume response. This observation is reasonable considering the previous discussion in Sec. C.3.1 on differences between both regions of the cell.

It is worth mentioning that the zones outside the selected profiles are clearly dominated by different types of forces, resulting in very local dynamics in the RBC.

List of Symbols

The following lists provide definitions of the symbols used throughout this thesis, categorized into Latin and Greek letters. Each symbol is accompanied by its description.

Latin

A	power-law prefactor
B	power-law slope
C_B	Batchelor constant
C_K	Kolmogorov constant
C_n	n -th constant in structure functions
C_O	scalar spectrum constant
D	diameter of a cylindrical system in RBC
E	energy spectrum
E_θ	scalar spectrum
$E_{\text{in}}^{<q}$	energy injection rate inside a sphere of radius q
F_A	„A“-stream flow rate
F_B	„B“-stream flow rate
H	height of a system in RBC
K	turbulent kinetic energy (TKE)
L	characteristic length
M	number of samples

N	Brunt–Väisälä frequency
N_b	number of counts per bin
Nu	Nusselt number
P	power spectrum density
Pr	Prandtl number
Ra	Rayleigh number
Re	Reynolds number
Re_λ	Taylor-Reynolds number
S	lengthscale ($K^{\frac{3}{2}}/\epsilon$)
S_n	n -th order vector structure function
S_n^θ	n -th order scalar structure function
Sc	Schmidt number
T	temperature
T_0	ambient temperature
T_A	„A”-stream temperature
T_B	„B”-stream temperature
T'	temperature fluctuations, i.e. $T' = T - \langle T \rangle$
U	mean velocity, i.e. $U = \sqrt{(u^2 + v^2 + w^2)}$
c_η	coefficient in f_η
f	frequency
\tilde{f}	scaled frequency
f_p	peak frequency
f_η	non-dimensional function determining dissipative range
f_l	non-dimensional function determining energy-containing range
g	gravitational acceleration

h	measurement height
k	wavenumber
k_l	energy dissipation wavenumber due to drag
k_{in}	energy injection wavenumber
k_B	Batchelor wavenumber, i.e. $1/\eta_B$
k_η	Kolmogorov wavenumber, i.e. $1/\eta$
k_ϕ	wavenumber noise level
k_θ	scalar spectrum wavenumber limit for low Sc
k_p	peak wavenumber
l	integral scale
l_θ	integral scale for scalar
p	pressure
q	sphere radius
r	separation distance
t	time
u'_{rms}	root mean square of velocity fluctuations
\mathbf{U}	3D velocity vector $\mathbf{U} = (u, v, w)$
\mathbf{f}	abstract forcing vector
\mathbf{r}	3D displacement vector $\mathbf{r} = (x, y, z)$

Greek

Δ	large-scale variability, e.g. temperature contrasts between air streams
Γ	aspect ratio in RBC
Π_θ	mean scalar flux

Π_E	mean energy flux
α	molecular diffusivity
β	coefficient in f_η
γ_T	skewness in temperature series
δ	small-scale variability, e.g. temperature fluctuations between consecutive data record
ϵ	turbulent kinetic energy dissipation rate
ϵ_θ	turbulent scalar dissipation rate
$\epsilon_\eta^{<q}$	energy dissipation due to viscosity
$\epsilon_l^{<q}$	energy dissipation due to drag
η	Kolmogorov length scale
η_B	Batchelor length
η_T	temperature dissipation rate
η_θ	scalar spectrum length scale limit for extremely low Sc
θ	generic scalar field in advection/diffusion equation
θ'	generic scalar fluctuations rate
κ	thermal diffusivity
λ	Taylor microscale
ν	kinematic viscosity
ξ	generic coefficient in advection/diffusion equation
ψ	thermal expansion coefficient
ρ	density
σ	stratification parameter
σ_T	standard deviation in temperature series
τ_B	Bolgiano timescale
τ^e	LSC periodicity formula

χ normalized temperature dissipation rate

Bibliography

- Abe, H. and Antonia, R. A., Scaling of normalized mean energy and scalar dissipation rates in a turbulent channel flow, *Physics of Fluids*, **23**(5), 055104, ISSN: 1070-6631, doi:[10.1063/1.3584124](https://doi.org/10.1063/1.3584124) (2011).
- Abe, H., Antonia, R. A., and Kawamura, H., Correlation between small-scale velocity and scalar fluctuations in a turbulent channel flow, *Journal of Fluid Mechanics*, **627**, 1–32, doi:[10.1017/S0022112008005569](https://doi.org/10.1017/S0022112008005569) (2009).
- Ahlers, G., Bodenschatz, E., Hartmann, R., He, X., Lohse, D., Reiter, P., Stevens, R. J. A. M., Verzicco, R., Wedi, M., Weiss, S., Zhang, X., Zwirner, L., and Shishkina, O., Aspect ratio dependence of heat transfer in a cylindrical rayleigh-bénard cell, *Phys. Rev. Lett.*, **128**, 084501, doi:[10.1103/PhysRevLett.128.084501](https://doi.org/10.1103/PhysRevLett.128.084501) (2022).
- Ahlers, G., Funfschilling, D., and Bodenschatz, E., Transitions in heat transport by turbulent convection at Rayleigh numbers up to 10^{15} , *New Journal of Physics*, **11**(12), 123001, doi:[10.1088/1367-2630/11/12/123001](https://doi.org/10.1088/1367-2630/11/12/123001) (2009).
- Akhmedagaev, R., Zikanov, O., Krasnov, D., and Schumacher, J., Turbulent Rayleigh–Bénard convection in a strong vertical magnetic field, *Journal of Fluid Mechanics*, **895**, R4, doi:[DOI: 10.1017/jfm.2020.336](https://doi.org/10.1017/jfm.2020.336) (2020).
- Akinlabi, E. O., Waclawczyk, M., Mellado, J. P., and Malinowski, S. P., Estimating Turbulence Kinetic Energy Dissipation Rates in the Numerically Simulated Stratocumulus Cloud-Top Mixing Layer: Evaluation of Different Methods, *Journal of the Atmospheric Sciences*, **76**(5), 1471–1488, doi:<https://doi.org/10.1175/JAS-D-18-0146.1> (2019).
- Alam, S., Guha, A., and Verma, M. K., Revisiting Bolgiano–Obukhov scaling for moderately stably stratified turbulence, *Journal of Fluid Mechanics*, **875**, 961–973, doi:[10.1017/jfm.2019.529](https://doi.org/10.1017/jfm.2019.529) (2019).

- Albrecht, B. A., Bretherton, C. S., Johnson, D., Scubert, W. H., and Frisch, A. S., The Atlantic Stratocumulus Transition Experiment—ASTEX, *Bulletin of the American Meteorological Society*, **76**(6), 889–904, doi:[https://doi.org/10.1175/1520-0477\(1995\)076<0889:TASTE>2.0.CO;2](https://doi.org/10.1175/1520-0477(1995)076<0889:TASTE>2.0.CO;2) (1995).
- Alexakis, A., Helically decomposed turbulence, *Journal of Fluid Mechanics*, **812**, 752–770, doi:[10.1017/jfm.2016.831](https://doi.org/10.1017/jfm.2016.831) (2017).
- Alexakis, A., Quasi-two-dimensional turbulence, *Reviews of Modern Plasma Physics*, **7**(1), 31, doi:[10.1007/s41614-023-00134-3](https://doi.org/10.1007/s41614-023-00134-3) (2023).
- Alexakis, A. and Biferale, L., Cascades and transitions in turbulent flows, *Physics Reports*, **767-769**, 1–101, ISSN: 0370-1573, doi:[10.1016/j.physrep.2018.08.001](https://doi.org/10.1016/j.physrep.2018.08.001) (2018).
- Allan, R. P., Barlow, M., Byrne, M. P., Cherchi, A., Douville, H., Fowler, H. J., Gan, T. Y., Pendergrass, A. G., Rosenfeld, D., Swann, A. L. S., Wilcox, L. J., and Zolina, O., Advances in understanding large-scale responses of the water cycle to climate change, *Annals of the New York Academy of Sciences*, **1472**(1), 49–75, doi:<https://doi.org/10.1111/nyas.14337> (2020).
- Anderson, J. C., Beeler, P., Ovchinnikov, M., Cantrell, W., Krueger, S., Shaw, R. A., Yang, F., and Fierce, L., Enhancements in cloud condensation nuclei activity from turbulent fluctuations in supersaturation, *Geophysical Research Letters*, **50**(17), e2022GL102635, doi:<https://doi.org/10.1029/2022GL102635> (2023).
- Anderson, J. C., Helman, I., Shaw, R. A., and Cantrell, W., Droplet Growth or Evaporation Does Not Buffer the Variability in Supersaturation in Clean Clouds, *Journal of the Atmospheric Sciences*, **81**(1), 225–233, doi:<https://doi.org/10.1175/JAS-D-23-0104.1> (2024).
- Anderson, J. C., Thomas, S., Prabhakaran, P., Shaw, R. A., and Cantrell, W., Effects of the large-scale circulation on temperature and water vapor distributions in the II Chamber, *Atmospheric Measurement Techniques*, **14**(8), 5473–5485, doi:[10.5194/AMT-14-5473-2021](https://doi.org/10.5194/AMT-14-5473-2021) (2021).
- Angulo-Umana, P. and Kim, D., Mesoscale convective clustering enhances tropical precipitation, *Science Advances*, **9**(2), eabo5317, doi:[10.1126/sciadv.abo5317](https://doi.org/10.1126/sciadv.abo5317) (2023).

- Antonia, R., Zhou, T., and Xu, G., Correlation between energy and temperature dissipation rates in turbulent flows, in *IUTAM Symposium on Geometry and Statistics of Turbulence: Proceedings of the IUTAM Symposium held at the Shonan International Village Center, Hayama (Kanagawa-ken), Japan, November 1–5, 1999*, 185–190, Springer (2001).
- Antonia, R. A. and Browne, L. W. B., Anisotropy of the temperature dissipation in a turbulent wake, *Journal of Fluid Mechanics*, **163**, 393–403, doi:[10.1017/S0022112086002343](https://doi.org/10.1017/S0022112086002343) (1986).
- Antonia, R. A. and Chambers, A. J., On the correlation between turbulent velocity and temperature derivatives in the atmospheric surface layer, *Boundary-Layer Meteorology*, **18**(4), 399–410, doi:[10.1007/BF00119496](https://doi.org/10.1007/BF00119496) (1980).
- Antonia, R. A. and Mi, J., Temperature dissipation in a turbulent round jet, *Journal of Fluid Mechanics*, **250**, 531–551, doi:[10.1017/S0022112093001557](https://doi.org/10.1017/S0022112093001557) (1993).
- Antonia, R. A. and Orlandi, P., On the Batchelor constant in decaying isotropic turbulence, *Physics of Fluids*, **15**(7), 2084–2086, ISSN: 1070-6631, doi:[10.1063/1.1577346](https://doi.org/10.1063/1.1577346) (2003).
- Antonia, R. A. and Sreenivasan, K. R., Log-normality of temperature dissipation in a turbulent boundary layer, *The Physics of Fluids*, **20**(11), 1800–1804, ISSN: 0031-9171, doi:[10.1063/1.861795](https://doi.org/10.1063/1.861795) (1977).
- Antonia, R. A. and Van Atta, C. W., On the correlation between temperature and velocity dissipation fields in a heated turbulent jet, *Journal of Fluid Mechanics*, **67**(2), 273–288, doi:[10.1017/S0022112075000304](https://doi.org/10.1017/S0022112075000304) (1975).
- Ashkenazi, S. and Steinberg, V., Spectra and statistics of velocity and temperature fluctuations in turbulent convection, *Phys. Rev. Lett.*, **83**, 4760–4763, doi:[10.1103/PhysRevLett.83.4760](https://doi.org/10.1103/PhysRevLett.83.4760) (1999).
- Aumann, H. H., Behrangi, A., and Wang, Y., Increased frequency of extreme tropical deep convection: Airs observations and climate model predictions, *Geophysical Research Letters*, **45**(24), 13,530–13,537, doi:[https://doi.org/10.1029/2018GL079423](https://doi.org/https://doi.org/10.1029/2018GL079423) (2018).
- Aurnou, J. M. and Olson, P. L., Experiments on Rayleigh–Bénard convection, magnetoconvection and rotating magnetoconvection in liquid gallium, *Journal of Fluid Mechanics*, **430**, 283–307, doi:[DOI: 10.1017/S0022112000002950](https://doi.org/DOI:10.1017/S0022112000002950) (2001).

- Bailon-Cuba, J., Emran, M. S., and Schumacher, J., Aspect ratio dependence of heat transfer and large-scale flow in turbulent convection, *Journal of Fluid Mechanics*, **655**, 152–173, doi:[10.1017/S0022112010000820](https://doi.org/10.1017/S0022112010000820) (2010).
- Bandak, D., Goldenfeld, N., Mailybaev, A. A., and Eyink, G., Dissipation-range fluid turbulence and thermal noise, *Phys. Rev. E*, **105**, 065113, doi:[10.1103/PhysRevE.105.065113](https://doi.org/10.1103/PhysRevE.105.065113) (2022).
- Basu, S., DeMarco, A. W., and He, P., On the dissipation rate of temperature fluctuations in stably stratified flows, *Environmental Fluid Mechanics*, **21**(1), 63–82, doi:[10.1007/s10652-020-09761-7](https://doi.org/10.1007/s10652-020-09761-7) (2021).
- Batchelor, G. K., Small-scale variation of convected quantities like temperature in turbulent fluid part 1. general discussion and the case of small conductivity, *Journal of Fluid Mechanics*, **5**(1), 113–133, doi:[10.1017/S002211205900009X](https://doi.org/10.1017/S002211205900009X) (1959).
- Batchelor, G. K., Computation of the Energy Spectrum in Homogeneous Two-Dimensional Turbulence, *The Physics of Fluids*, **12**(12), II–233–II–239, ISSN: 0031-9171, doi:[10.1063/1.1692443](https://doi.org/10.1063/1.1692443) (1969).
- Batchelor, G. K., Howells, I. D., and Townsend, A. A., Small-scale variation of convected quantities like temperature in turbulent fluid part 2. the case of large conductivity, *Journal of Fluid Mechanics*, **5**(1), 134–139, doi:[10.1017/S0022112059000106](https://doi.org/10.1017/S0022112059000106) (1959).
- Belmonte, A. and Libchaber, A., Thermal signature of plumes in turbulent convection: The skewness of the derivative, *Phys. Rev. E*, **53**, 4893–4898, doi:[10.1103/PhysRevE.53.4893](https://doi.org/10.1103/PhysRevE.53.4893) (1996).
- Bénard, H., Les tourbillons cellulaires dans une nappe liquide, *Revue Générale des Sciences Pures et Appliquées*, **11**, 1261–1271, 1309–1328 (1900).
- Benzi, R. and Toschi, F., Lectures on turbulence, *Physics Reports*, **1021**, 1–106, ISSN: 0370-1573, doi:[10.1016/j.physrep.2023.05.001](https://doi.org/10.1016/j.physrep.2023.05.001) (2023).
- Bhattacharya, S., Samtaney, R., and Verma, M. K., Scaling and spatial intermittency of thermal dissipation in turbulent convection, *Physics of Fluids*, **31**(7), 075104, ISSN: 1070-6631, doi:[10.1063/1.5098073](https://doi.org/10.1063/1.5098073) (2019).
- Biagioli, G. and Tompkins, A. M., Measuring Convective Organization, *Journal of the Atmospheric Sciences*, **80**(12), 2769–2789, doi:<https://doi.org/10.1175/JAS-D-23-0103.1> (2023).

- Biferale, L., Musacchio, S., and Toschi, F., Split energy–helicity cascades in three-dimensional homogeneous and isotropic turbulence, *Journal of Fluid Mechanics*, **730**, 309–327, doi:[10.1017/jfm.2013.349](https://doi.org/10.1017/jfm.2013.349) (2013).
- Biferale, L. and Procaccia, I., Anisotropy in turbulent flows and in turbulent transport, *Physics Reports*, **414**(2), 43–164, ISSN: 0370-1573, doi:[10.1016/j.physrep.2005.04.001](https://doi.org/10.1016/j.physrep.2005.04.001) (2005).
- Blass, A., Verzicco, R., Lohse, D., Stevens, R. J. A. M., and Krug, D., Flow organisation in laterally unconfined rayleigh–bénard turbulence, *Journal of Fluid Mechanics*, **906**, A26, doi:[10.1017/jfm.2020.797](https://doi.org/10.1017/jfm.2020.797) (2021).
- Bodenschatz, E., Malinowski, S. P., Shaw, R. A., and Stratmann, F., Can We Understand Clouds Without Turbulence?, *Science*, **327**(5968), 970–971, doi:[10.1126/science.1185138](https://doi.org/10.1126/science.1185138) (2010).
- Boffetta, G. and Ecke, R. E., Two-Dimensional Turbulence, *Annual Review of Fluid Mechanics*, **44**, 427–451, ISSN: 1545-4479, doi:[10.1146/annurev-fluid-120710-101240](https://doi.org/10.1146/annurev-fluid-120710-101240) (2012).
- Boffetta, G. and Mazzino, A., Incompressible rayleigh–taylor turbulence, *Annual Review of Fluid Mechanics*, **49**, 119–143, ISSN: 1545-4479, doi:[10.1146/annurev-fluid-010816-060111](https://doi.org/10.1146/annurev-fluid-010816-060111) (2017).
- Bolgiano Jr., R., Turbulent spectra in a stably stratified atmosphere, *Journal of Geophysical Research (1896-1977)*, **64**(12), 2226–2229, doi:[10.1029/JZ064i012p02226](https://doi.org/10.1029/JZ064i012p02226) (1959).
- Bony, S., Schulz, H., Vial, J., and Stevens, B., Sugar, Gravel, Fish, and Flowers: Dependence of Mesoscale Patterns of Trade-Wind Clouds on Environmental Conditions, *Geophysical Research Letters*, **47**(7), e2019GL085988, doi:<https://doi.org/10.1029/2019GL085988> (2020a).
- Bony, S., Semie, A., Kramer, R. J., Soden, B., Tompkins, A. M., and Emanuel, K. A., Observed modulation of the tropical radiation budget by deep convective organization and lower-tropospheric stability, *AGU Advances*, **1**(3), e2019AV000155, doi:<https://doi.org/10.1029/2019AV000155> (2020b).
- Bony, S., Stevens, B., Ament, F., Bigorre, S., Chazette, P., Crewell, S., Delanoë, J., Emanuel, K., Farrell, D., Flamant, C., Gross, S., Hirsch, L., Karstensen, J., Mayer, B., Nuijens, L., Ruppert, J. H., Sandu, I., Siebesma, P., Speich, S., Szczap, F., Totems, J., Vogel, R., Wendisch, M., and Wirth, M., EUREC4A: A

- Field Campaign to Elucidate the Couplings Between Clouds, Convection and Circulation, *Surveys in Geophysics*, **38**(6), 1529–1568, doi:[10.1007/s10712-017-9428-0](https://doi.org/10.1007/s10712-017-9428-0) (2017).
- Boussinesq, J., *Essai sur la Théorie des Eaux Courantes*, Mémoires Présentés par Divers Savants à l’Académie des Sciences, Académie des Sciences (1877).
- Brown, E. and Ahlers, G., Large-scale circulation model for turbulent rayleigh–bénard convection, *Phys. Rev. Lett.*, **98**, 134501, doi:[10.1103/PhysRevLett.98.134501](https://doi.org/10.1103/PhysRevLett.98.134501) (2007).
- Brown, E. and Ahlers, G., The origin of oscillations of the large-scale circulation of turbulent rayleigh–bénard convection, *Journal of Fluid Mechanics*, **638**, 383–400, doi:[10.1017/S0022112009991224](https://doi.org/10.1017/S0022112009991224) (2009).
- Bryan, G. H. and Fritsch, J. M., A benchmark simulation for moist nonhydrostatic numerical models, *Monthly Weather Review*, **130**(12), 2917–2928 (2002).
- Buaria, D. and Sreenivasan, K. R., Dissipation range of the energy spectrum in high Reynolds number turbulence, *Phys. Rev. Fluids*, **5**, 092601, doi:[10.1103/PhysRevFluids.5.092601](https://doi.org/10.1103/PhysRevFluids.5.092601) (2020).
- Buaria, D. and Sreenivasan, K. R., Saturation and multifractality of lagrangian and eulerian scaling exponents in three-dimensional turbulence, *Phys. Rev. Lett.*, **131**, 204001, doi:[10.1103/PhysRevLett.131.204001](https://doi.org/10.1103/PhysRevLett.131.204001) (2023).
- Burr, U. and Müller, U., Rayleigh–Bénard convection in liquid metal layers under the influence of a horizontal magnetic field, *Journal of Fluid Mechanics*, **453**, 345–369, doi:[DOI: 10.1017/S002211200100698X](https://doi.org/10.1017/S002211200100698X) (2002).
- Burr, U. and Müller, U., Rayleigh–Bénard convection in liquid metal layers under the influence of a vertical magnetic field, *Physics of Fluids*, **13**(11), 3247–3257, ISSN: 1070-6631, doi:[10.1063/1.1404385](https://doi.org/10.1063/1.1404385) (2001).
- Busse, F. H., *Bénard Convection and Geophysical Applications*, 103–125, Springer New York, New York, NY, ISBN: 978-0-387-25111-0, doi:[10.1007/978-0-387-25111-0_6](https://doi.org/10.1007/978-0-387-25111-0_6) (2006).
- Carter, D. W. and Coletti, F., Scale-to-scale anisotropy in homogeneous turbulence, *Journal of Fluid Mechanics*, **827**, 250–284, doi:[10.1017/jfm.2017.496](https://doi.org/10.1017/jfm.2017.496) (2017).

- Castaing, B., Scaling of turbulent spectra, *Phys. Rev. Lett.*, **65**, 3209–3209, doi:[10.1103/PhysRevLett.65.3209](https://doi.org/10.1103/PhysRevLett.65.3209) (1990).
- Celani, A., Cencini, M., Mazzino, A., and Vergassola, M., Active versus passive scalar turbulence, *Phys. Rev. Lett.*, **89**, 234502, doi:[10.1103/PhysRevLett.89.234502](https://doi.org/10.1103/PhysRevLett.89.234502) (2002).
- Celani, A., Cencini, M., Mazzino, A., and Vergassola, M., Active and passive fields face to face, *New Journal of Physics*, **6**(1), 72, doi:[10.1088/1367-2630/6/1/072](https://doi.org/10.1088/1367-2630/6/1/072) (2004).
- Ceppi, P. and Nowack, P., Observational evidence that cloud feedback amplifies global warming, *Proceedings of the National Academy of Sciences*, **118**(30), e2026290118, doi:[10.1073/pnas.2026290118](https://doi.org/10.1073/pnas.2026290118) (2021).
- Chakraborty, S., Sullivan, S. C., and Feng, Z., *An Overview of Mesoscale Convective Systems: Global Climatology, Satellite Observations, and Modeling Strategies*, chapter 9, 195–221, American Geophysical Union (AGU), ISBN: 9781119700357, doi:<https://doi.org/10.1002/9781119700357.ch9> (2023).
- Chandrakar, K. K., Cantrell, W., Ciochetto, D., Karki, S., Kinney, G., and Shaw, R. A., Aerosol removal and cloud collapse accelerated by supersaturation fluctuations in turbulence, *Geophysical Research Letters*, **44**(9), 4359–4367, doi:<https://doi.org/10.1002/2017GL072762> (2017).
- Chandrakar, K. K., Cantrell, W., Kostinski, A. B., and Shaw, R. A., Dispersion aerosol indirect effect in turbulent clouds: Laboratory measurements of effective radius, *Geophysical Research Letters*, **45**(19), 10,738–10,745, doi:[10.1029/2018GL079194](https://doi.org/10.1029/2018GL079194) (2018a).
- Chandrakar, K. K., Cantrell, W., Krueger, S., Shaw, R. A., and Wunsch, S., Supersaturation fluctuations in moist turbulent Rayleigh–Bénard convection: a two-scalar transport problem, *Journal of Fluid Mechanics*, **884**, A19, doi:[DOI: 10.1017/jfm.2019.895](https://doi.org/10.1017/jfm.2019.895) (2020a).
- Chandrakar, K. K., Cantrell, W., Krueger, S., Shaw, R. A., and Wunsch, S., Supersaturation fluctuations in moist turbulent Rayleigh–Bénard convection: a two-scalar transport problem, *Journal of Fluid Mechanics*, **884**, A19, doi:[DOI: 10.1017/jfm.2019.895](https://doi.org/10.1017/jfm.2019.895) (2020b).
- Chandrakar, K. K., Cantrell, W., and Shaw, R. A., Influence of Turbulent Fluctuations on Cloud Droplet Size Dispersion and Aerosol Indirect Effects,

- Journal of the Atmospheric Sciences*, **75**(9), 3191–3209, ISSN: 0022-4928, doi:[10.1175/JAS-D-18-0006.1](https://doi.org/10.1175/JAS-D-18-0006.1) (2018b).
- Chandrakar, K. K., Cantrell, W., and Shaw, R. A., Ion-induced cloud modulation through new particle formation and runaway cloud condensation nuclei production, *Oxford Open Climate Change*, **4**(1), ISSN: 2634-4068, doi:[10.1093/oxfclm/kgae018](https://doi.org/10.1093/oxfclm/kgae018) (2024a).
- Chandrakar, K. K., Grabowski, W. W., Morrison, H., and Bryan, G. H., Impact of Entrainment Mixing and Turbulent Fluctuations on Droplet Size Distributions in a Cumulus Cloud: An Investigation Using Lagrangian Microphysics with a Subgrid-Scale Model, *Journal of the Atmospheric Sciences*, **78**(9), 2983–3005, doi:<https://doi.org/10.1175/JAS-D-20-0281.1> (2021).
- Chandrakar, K. K., Morrison, H., Grabowski, W. W., Bryan, G. H., and Shaw, R. A., Supersaturation variability from scalar mixing: Evaluation of a new subgrid-scale model using direct numerical simulations of turbulent rayleigh–bénard convection, *Journal of the Atmospheric Sciences*, **79**(4), 1191–1210 (2022).
- Chandrakar, K. K., Morrison, H., Grabowski, W. W., and Lawson, R. P., Are turbulence effects on droplet collision–coalescence a key to understanding observed rain formation in clouds?, *Proceedings of the National Academy of Sciences*, **121**(27), e2319664121, doi:[10.1073/pnas.2319664121](https://doi.org/10.1073/pnas.2319664121) (2024b).
- Chandrakar, K. K., Morrison, H., and Shaw, R. A., Lagrangian and eulerian supersaturation statistics in turbulent cloudy rayleigh–bénard convection: applications for les subgrid modeling, *Journal of the Atmospheric Sciences*, **80**(9), 2261–2285 (2023).
- Chandrakar, K. K., Saito, I., Yang, F., Cantrell, W., Gotoh, T., and Shaw, R. A., Droplet size distributions in turbulent clouds: experimental evaluation of theoretical distributions, *Quarterly Journal of the Royal Meteorological Society*, **146**(726), 483–504, doi:<https://doi.org/10.1002/qj.3692> (2020c).
- Chang, K., Bench, J., Brege, M., Cantrell, W., Chandrakar, K., Ciochetto, D., Mazzoleni, C., Mazzoleni, L. R., Niedermeier, D., and Shaw, R. A., A Laboratory Facility to Study Gas–Aerosol–Cloud Interactions in a Turbulent Environment: The II Chamber, *Bulletin of the American Meteorological Society*, **97**(12), 2343–2358, ISSN: 0003-0007, doi:[10.1175/BAMS-D-15-00203.1](https://doi.org/10.1175/BAMS-D-15-00203.1) (2016).

- Chen, C. H. and Bhaganagar, K., New findings in vorticity dynamics of turbulent buoyant plumes, *Physics of Fluids*, **33**(11), 115104, ISSN: 1070-6631, doi:[10.1063/5.0065322](https://doi.org/10.1063/5.0065322) (2021).
- Chen, C. H. and Bhaganagar, K., Energetics of buoyancy-generated turbulent flows with active scalar: pure buoyant plume, *Journal of Fluid Mechanics*, **954**, A23, doi:[10.1017/jfm.2022.1011](https://doi.org/10.1017/jfm.2022.1011) (2023).
- Chen, C. H. and Bhaganagar, K., Turbulent cascading in buoyant plumes, *Environmental Fluid Mechanics*, doi:[10.1007/s10652-023-09963-9](https://doi.org/10.1007/s10652-023-09963-9) (2024).
- Chen, J., Antonia, R., Zhou, Y., and Zhou, T., Characteristics of temperature dissipation rate in a turbulent near wake, *Experimental Thermal and Fluid Science*, **114**, 110050, ISSN: 0894-1777, doi:<https://doi.org/10.1016/j.expthermflusci.2020.110050> (2020).
- Chen, J., Yin, Z.-X., and Zou, H.-Y., Visualization of thermal structures in turbulent rayleigh-bnard convection, in *Proceedings 18th International Symposium on Flow Visualization*, ETH Zurich (2018).
- Chen, Q., Chen, S., and Eyink, G. L., The joint cascade of energy and helicity in three-dimensional turbulence, *Physics of Fluids*, **15**(2), 361–374, ISSN: 1070-6631, doi:[10.1063/1.1533070](https://doi.org/10.1063/1.1533070) (2003).
- Chen, S. and Kraichnan, R. H., Simulations of a randomly advected passive scalar field, *Physics of Fluids*, **10**(11), 2867–2884, ISSN: 1070-6631, doi:[10.1063/1.869808](https://doi.org/10.1063/1.869808) (1998).
- Chillà, F. and Schumacher, J., New perspectives in turbulent rayleigh-bénard convection, *The European Physical Journal E*, **35**(7), 58, doi:[10.1140/epje/i2012-12058-1](https://doi.org/10.1140/epje/i2012-12058-1) (2012).
- Chillà, F., Ciliberto, S., Innocenti, C., and Pampaloni, E., Boundary layer and scaling properties in turbulent thermal convection, *Il Nuovo Cimento D*, **15**(9), 1229–1249, doi:[10.1007/BF02451729](https://doi.org/10.1007/BF02451729) (1993).
- Ching, E. S. C. and Kwok, C. Y., Statistics of local temperature dissipation in high Rayleigh number convection, *Phys. Rev. E*, **62**, R7587–R7590, doi:[10.1103/PhysRevE.62.R7587](https://doi.org/10.1103/PhysRevE.62.R7587) (2000).
- Christopher, T. W. and Llewellyn Smith, S. G., Bounding temperature dissipation in time-modulated Rayleigh-Bénard convection, *Phys. Rev. Fluids*, **6**, L051501, doi:[10.1103/PhysRevFluids.6.L051501](https://doi.org/10.1103/PhysRevFluids.6.L051501) (2021).

- Cioni, S., Ciliberto, S., and Sommeria, J., Temperature structure functions in turbulent convection at low prandtl number, *Europhysics Letters*, **32**(5), 413, doi:[10.1209/0295-5075/32/5/006](https://doi.org/10.1209/0295-5075/32/5/006) (1995).
- Clay, M. P., *Strained turbulence and low-diffusivity turbulent mixing using high performance computing*, Ph.D. thesis, Georgia Institute of Technology (2017).
- Corrsin, S., On the Spectrum of Isotropic Temperature Fluctuations in an Isotropic Turbulence, *Journal of Applied Physics*, **22**(4), 469–473, ISSN: 0021-8979, doi:[10.1063/1.1699986](https://doi.org/10.1063/1.1699986) (1951).
- Dabbagh, F., Trias, F. X., Gorobets, A., and Oliva, A., Flow topology dynamics in a three-dimensional phase space for turbulent rayleigh-bénard convection, *Phys. Rev. Fluids*, **5**, 024603, doi:[10.1103/PhysRevFluids.5.024603](https://doi.org/10.1103/PhysRevFluids.5.024603) (2020).
- Davidson, P., *Turbulence: An Introduction for Scientists and Engineers*, Oxford University Press, ISBN: 9780198722588, doi:[10.1093/acprof:oso/9780198722588.001.0001](https://doi.org/10.1093/acprof:oso/9780198722588.001.0001) (2015).
- Davidson, P. A., Kaneda, Y., Moffatt, K., and Sreenivasan, K. R., *A Voyage Through Turbulence*, Cambridge University Press, ISBN: 9781139018241, doi:[10.1017/CBO9781139018241](https://doi.org/10.1017/CBO9781139018241) (2011).
- De, A. K., Eswaran, V., and Mishra, P. K., Dynamics of plumes in turbulent Rayleigh–Bénard convection, *European Journal of Mechanics - B/Fluids*, **72**, 164–178, doi:<https://doi.org/10.1016/j.euromechflu.2018.05.007> (2018).
- Denby, L., Discovering the importance of mesoscale cloud organization through unsupervised classification, *Geophysical Research Letters*, **47**(1), e2019GL085190, doi:<https://doi.org/10.1029/2019GL085190> (2020).
- Desai, N., Chandrakar, K. K., Chang, K., Cantrell, W., and Shaw, R. A., Influence of microphysical variability on stochastic condensation in a turbulent laboratory cloud, *Journal of the Atmospheric Sciences*, **75**(1), 189 – 201, doi:[10.1175/JAS-D-17-0158.1](https://doi.org/10.1175/JAS-D-17-0158.1) (2018).
- Desai, N., Chandrakar, K. K., Kinney, G., Cantrell, W., and Shaw, R. A., Aerosol-mediated glaciation of mixed-phase clouds: Steady-state laboratory measurements, *Geophysical Research Letters*, **46**(15), 9154–9162, doi:[10.1029/2019GL083503](https://doi.org/10.1029/2019GL083503) (2019).
- Descartes, R., *Discourse on the Method of Rightly Conducting One’s Reason and of Seeking Truth in the Sciences*, Leiden: Jan Maire (1637).

- Donzis, D. A. and Sreenivasan, K. R., The bottleneck effect and the Kolmogorov constant in isotropic turbulence, *Journal of Fluid Mechanics*, **657**, 171–188, doi:[10.1017/S0022112010001400](https://doi.org/10.1017/S0022112010001400) (2010).
- du Puits, R., Time-resolved measurements of the local wall heat flux in turbulent rayleigh–bénard convection, *International Journal of Heat and Mass Transfer*, **188**, 122649, ISSN: 0017-9310, doi:<https://doi.org/10.1016/j.ijheatmasstransfer.2022.122649> (2022).
- Dutta, K. and Nandy, M. K., Heisenberg approximation in passive scalar turbulence, *Phys. Rev. E*, **84**, 036315, doi:[10.1103/PhysRevE.84.036315](https://doi.org/10.1103/PhysRevE.84.036315) (2011).
- Ebert, A., Resagk, C., and Thess, A., Experimental study of temperature distribution and local heat flux for turbulent Rayleigh–Bénard convection of air in a long rectangular enclosure, *International Journal of Heat and Mass Transfer*, **51**(17), 4238–4248, doi:<https://doi.org/10.1016/j.ijheatmasstransfer.2008.01.017> (2008).
- Ecke, R. E. and Shishkina, O., Turbulent Rotating Rayleigh–Bénard Convection, *Annual Review of Fluid Mechanics*, **55**(Volume 55, 2023), 603–638, ISSN: 1545-4479, doi:<https://doi.org/10.1146/annurev-fluid-120720-020446> (2023).
- Eidelman, A., Elperin, T., Gluzman, I., and Golbraikh, E., Helicity of mean and turbulent flow with coherent structures in Rayleigh–Bénard convective cell, *Physics of Fluids*, **26**(6), 065103, ISSN: 1070-6631, doi:[10.1063/1.4881939](https://doi.org/10.1063/1.4881939) (2014).
- Emanuel, K. A., *Atmospheric Convection*, Oxford University Press, ISBN: 9780195066302 (1994).
- Eyink, G. and Jafari, A., High Schmidt-number turbulent advection and giant concentration fluctuations, *Phys. Rev. Res.*, **4**, 023246, doi:[10.1103/PhysRevResearch.4.023246](https://doi.org/10.1103/PhysRevResearch.4.023246) (2022).
- Falkovich, G. and Sreenivasan, K. R., Lessons from hydrodynamic turbulence, *Physics Today*, **59**(4), 43–49, ISSN: 0031-9228, doi:[10.1063/1.2207037](https://doi.org/10.1063/1.2207037) (2006).
- Fan, Y., Zhao, Y., Torres, J. F., Xu, F., Lei, C., Li, Y., and Carmeliet, J., Natural convection over vertical and horizontal heated flat surfaces: A review of recent progress focusing on underpinnings and implications for heat transfer and environmental applications, *Physics of Fluids*, **33**(10), 101301, ISSN: 1070-6631, doi:[10.1063/5.0065125](https://doi.org/10.1063/5.0065125) (2021).

- Fernando, H. and Smith IV, D., Vortex structures in geophysical convection, *European Journal of Mechanics - B/Fluids*, **20**(4), 437–470, ISSN: 0997-7546, doi:[10.1016/S0997-7546\(01\)01129-3](https://doi.org/10.1016/S0997-7546(01)01129-3) (2001).
- Foroozani, N., Niemela, J. J., Armenio, V., and Sreenivasan, K. R., Reorientations of the large-scale flow in turbulent convection in a cube, *Phys. Rev. E*, **95**, 033107, doi:[10.1103/PhysRevE.95.033107](https://doi.org/10.1103/PhysRevE.95.033107) (2017).
- Fossà, L., Abdunabiev, S., Golshan, M., and Tordella, D., Microphysical timescales and local supersaturation balance at a warm cloud top boundary, *Physics of Fluids*, **34**(6), 067103, ISSN: 1070-6631, doi:[10.1063/5.0090664](https://doi.org/10.1063/5.0090664) (2022).
- Frey, W., Schmalfuß, S., Stratmann, F., and Niedermeier, D., Which parameters govern the strength of entrainment?, *ESS Open Archive*, doi:[10.1002/essoar.10510020.1](https://doi.org/10.1002/essoar.10510020.1) (2022).
- Friehe, C. A., La Rue, J. C., Champagne, F. H., Gibson, C. H., and Dreyer, G. F., Effects of temperature and humidity fluctuations on the optical refractive index in the marine boundary layer, *Journal of the Optical Society of America*, **65**(12), 1502–1511, doi:[10.1364/JOSA.65.001502](https://doi.org/10.1364/JOSA.65.001502) (1975).
- Funfschilling, D., Brown, E., and Ahlers, G., Torsional oscillations of the large-scale circulation in turbulent rayleigh–bénard convection, *Journal of Fluid Mechanics*, **607**, 119–139, doi:[10.1017/S0022112008001882](https://doi.org/10.1017/S0022112008001882) (2008).
- George, G., Stevens, B., Bony, S., Vogel, R., and Naumann, A. K., Widespread shallow mesoscale circulations observed in the trades, *Nature Geoscience*, **16**(7), 584–589, doi:[10.1038/s41561-023-01215-1](https://doi.org/10.1038/s41561-023-01215-1) (2023).
- Goessling, H. F., Rackow, T., and Jung, T., Recent global temperature surge intensified by record-low planetary albedo, *Science*, **0**(0), doi:[10.1126/science.adq7280](https://doi.org/10.1126/science.adq7280) (2024).
- Goluskin, D., *Internally Heated Convection and Rayleigh-Bénard Convection*, SpringerBriefs in Applied Sciences and Technology, Springer International Publishing, ISBN: 9783319239415, doi:[10.1007/978-3-319-23941-5](https://doi.org/10.1007/978-3-319-23941-5) (2015).
- Gotoh, T. and Yeung, P., *Ten Chapters in Turbulence*, 87–131, Cambridge University Press, doi:[10.1017/CBO9781139032810](https://doi.org/10.1017/CBO9781139032810) (2012).

- Gouharianmohammadi, S., Niedermeier, D., Schmalfuß, S., Mellado, J.-P., Shaw, R., and Stratmann, F., Computational studies on the influence of turbulence on ice crystal formation and diffusional growth in mixed-phase clouds, in *XXVIII General Assembly of the International Union of Geodesy and Geophysics (IUGG)*, GFZ German Research Centre for Geosciences, Berlin, doi:[10.57757/IUGG23-2462](https://doi.org/10.57757/IUGG23-2462) (2023).
- Grabowski, W. W., Broadening of Cloud Droplet Spectra through Eddy Hopping: Why Did We All Have It Wrong?, *Journal of the Atmospheric Sciences*, **82**(2), 443–453, doi:<https://doi.org/10.1175/JAS-D-24-0082.1> (2025).
- Grabowski, W. W., Thomas, L., and Kumar, B., Impact of Cloud-Base Turbulence on CCN Activation: CCN Distribution, *Journal of the Atmospheric Sciences*, **79**(11), 2965–2981, doi:<https://doi.org/10.1175/JAS-D-22-0075.1> (2022).
- Greenfield, R. S. and Fein, J. S., The Global Atmospheric Research Programs’s Atlantic Tropical Experiment, *Reviews of Geophysics*, **17**(7), 1762–1772, doi:<https://doi.org/10.1029/RG017i007p01762> (1979).
- Grosz, R., Chandrakar, K. K., Shaw, R. A., Anderson, J. C., Cantrell, W., and Malinowski, S. P., High-resolution temperature profiling in the II Chamber: variability of statistical properties of temperature fluctuations, *EGUsphere*, **2024**, 1–31, doi:[10.5194/egusphere-2024-2051](https://doi.org/10.5194/egusphere-2024-2051) (2024).
- Guo, S.-X., Zhou, S.-Q., Qu, L., Cen, X.-R., and Lu, Y.-Z., Evolution and statistics of thermal plumes in tilted turbulent convection, *International Journal of Heat and Mass Transfer*, **111**, 933–942, ISSN: 0017-9310, doi:[10.1016/j.ijheatmasstransfer.2017.04.039](https://doi.org/10.1016/j.ijheatmasstransfer.2017.04.039) (2017).
- Guo, X., Qin, P., Wu, J., Wang, B., Chong, K. L., and Zhou, Q., Statistics of kinetic and thermal energy dissipation rates in two-dimensional thermal vibrational convection, *Physics of Fluids*, **36**(7), 075132, ISSN: 1070-6631, doi:[10.1063/5.0214369](https://doi.org/10.1063/5.0214369) (2024).
- Haerter, J. O. and Muller, C., *Mechanisms for the Self-Organization of Tropical Deep Convection*, chapter 8, 179–193, American Geophysical Union (AGU), ISBN: 9781119700357, doi:<https://doi.org/10.1002/9781119700357.ch8> (2023).
- Haman, K. E., A new thermometric instrument for airborne measurements in clouds, *Journal of Atmospheric & Oceanic Technology*, **9**(1), 86–90, ISSN: 0739-0572, doi:[10.1175/1520-0426\(1992\)009<0086:ANTIFA>2.0.CO;2](https://doi.org/10.1175/1520-0426(1992)009<0086:ANTIFA>2.0.CO;2) (1992).

- Haman, K. E., Makulski, A., Malinowski, S. P., and Busen, R., A new ultra-fast thermometer for airborne measurements in clouds, *Journal of Atmospheric and Oceanic Technology*, **14**(2), 217–227, ISSN: 07390572, doi:[10.1175/1520-0426\(1997\)014<0217:ANUTFA>2.0.CO;2](https://doi.org/10.1175/1520-0426(1997)014<0217:ANUTFA>2.0.CO;2) (1997).
- Haman, K. E., Malinowski, S. P., Kurowski, M. J., Gerber, H., and Brenguier, J.-L., Small scale mixing processes at the top of a marine stratocumulus—a case study, *Quarterly Journal of the Royal Meteorological Society*, **133**(622), 213–226, ISSN: 00359009, doi:[10.1002/qj.5](https://doi.org/10.1002/qj.5) (2007).
- Haman, K. E., Malinowski, S. P., and Struś, B. D., Two new types of ultrafast aircraft thermometer, *Journal of Atmospheric and Oceanic Technology*, **18**(2), 117–134, ISSN: 07390572, doi:[10.1175/1520-0426\(2001\)018<0117:TNTOUA>2.0.CO;2](https://doi.org/10.1175/1520-0426(2001)018<0117:TNTOUA>2.0.CO;2) (2001).
- Hao, Z., Zhou, T., Chua, L., and Yu, S., Approximations to energy and temperature dissipation rates in the far field of a cylinder wake, *Experimental Thermal and Fluid Science*, **32**(3), 791–799, ISSN: 0894-1777, doi:<https://doi.org/10.1016/j.expthermflusci.2005.08.008> (2008).
- He, X., Ching, E. S. C., and Tong, P., Locally averaged thermal dissipation rate in turbulent thermal convection: A decomposition into contributions from different temperature gradient components, *Physics of Fluids*, **23**(2), 025106, ISSN: 1070-6631, doi:[10.1063/1.3555637](https://doi.org/10.1063/1.3555637) (2011).
- He, X., van Gils, D. P. M., Bodenschatz, E., and Ahlers, G., Logarithmic spatial variations and universal f^{-1} power spectra of temperature fluctuations in turbulent rayleigh-bénard convection, *Phys. Rev. Lett.*, **112**, 174501, doi:[10.1103/PhysRevLett.112.174501](https://doi.org/10.1103/PhysRevLett.112.174501) (2014a).
- He, X., Shang, X.-d., and Tong, P., Test of the anomalous scaling of passive temperature fluctuations in turbulent Rayleigh–Bénard convection with spatial inhomogeneity, *Journal of Fluid Mechanics*, **753**, 104–130, doi:[10.1017/jfm.2014.325](https://doi.org/10.1017/jfm.2014.325) (2014b).
- He, X., Wang, Y., and Tong, P., Dynamic heterogeneity and conditional statistics of non-Gaussian temperature fluctuations in turbulent thermal convection, *Phys. Rev. Fluids*, **3**, 052401, doi:[10.1103/PhysRevFluids.3.052401](https://doi.org/10.1103/PhysRevFluids.3.052401) (2018).
- He, Y.-H. and Xia, K.-Q., Temperature fluctuation profiles in turbulent thermal convection: A logarithmic dependence versus a power-law dependence, *Phys. Rev. Lett.*, **122**, 014503, doi:[10.1103/PhysRevLett.122.014503](https://doi.org/10.1103/PhysRevLett.122.014503) (2019).

- Heinz, S., On the Kolmogorov constant in stochastic turbulence models, *Physics of Fluids*, **14**(11), 4095–4098, ISSN: 1070-6631, doi:[10.1063/1.1514217](https://doi.org/10.1063/1.1514217) (2002).
- Hill, R. J., Spectra of turbulently advected scalars that have small Schmidt number, *Phys. Rev. Fluids*, **2**, 094601, doi:[10.1103/PhysRevFluids.2.094601](https://doi.org/10.1103/PhysRevFluids.2.094601) (2017).
- Holland, J. Z. and Rasmusson, E. M., Measurements of the Atmospheric Mass, Energy, and Momentum Budgets Over a 500-Kilometer Square of Tropical Ocean, *Monthly Weather Review*, **101**(1), 44–55, doi:[https://doi.org/10.1175/1520-0493\(1973\)101<0044:MOTAME>2.3.CO;2](https://doi.org/10.1175/1520-0493(1973)101<0044:MOTAME>2.3.CO;2) (1973).
- Holzer, M. and Siggia, E. D., Turbulent mixing of a passive scalar, *Physics of Fluids*, **6**(5), 1820–1837, ISSN: 1070-6631, doi:[10.1063/1.868243](https://doi.org/10.1063/1.868243) (1994).
- Houra, T. and Tagawa, M., Highly reliable measurement of temperature fluctuation in near-wall turbulence by a sophisticated cold-wire technique for considering the frequency response and spatial resolution, *International Journal of Heat and Mass Transfer*, **208**, 124078, doi:<https://doi.org/10.1016/j.ijheatmasstransfer.2023.124078> (2023).
- Houze, R. A., 100 Years of Research on Mesoscale Convective Systems, *Meteorological Monographs*, **59**, doi:<https://doi.org/10.1175/AMSMONOGRAPHS-D-18-0001.1> (2018).
- Houze Jr, R. A., Wang, J., Fan, J., Brodzik, S., and Feng, Z., Extreme convective storms over high-latitude continental areas where maximum warming is occurring, *Geophysical Research Letters*, **46**(7), 4059–4065, doi:<https://doi.org/10.1029/2019GL082414> (2019).
- Hsiao, W.-T., Maloney, E. D., Leitmann-Niimi, N. M., and Kummerow, C. D., Observed relationships between sea surface temperature, vertical wind shear, tropical organized deep convection, and radiative effects, *Journal of Climate*, **37**(4), 1277–1293 (2024).
- Imomov, A. A. and Murtazaev, M. S., On the Kolmogorov constant explicit form in the theory of discrete-time stochastic branching systems, *Journal of Applied Probability*, **61**(3), 927–941, doi:[10.1017/jpr.2023.85](https://doi.org/10.1017/jpr.2023.85) (2024).
- IPCC, *Climate Change 2021: The Physical Science Basis. Contribution of Working Group I to the Sixth Assessment Report of the Intergovernmental Panel on Climate Change*, volume In Press, Cambridge University Press, Cambridge, United Kingdom and New York, NY, USA, doi:[10.1017/9781009157896](https://doi.org/10.1017/9781009157896) (2021).

- Iwano, K., Hosoi, J., Sakai, Y., and Ito, Y., Power spectrum of high Schmidt number scalar in a turbulent jet at a moderate Reynolds number, *Experiments in Fluids*, **62**(6), 129, doi:[10.1007/s00348-021-03216-5](https://doi.org/10.1007/s00348-021-03216-5) (2021).
- Iyer, K. P., Schumacher, J., Sreenivasan, K. R., and Yeung, P. K., Steep cliffs and saturated exponents in three-dimensional scalar turbulence, *Phys. Rev. Lett.*, **121**, 264501, doi:[10.1103/PhysRevLett.121.264501](https://doi.org/10.1103/PhysRevLett.121.264501) (2018).
- Iyer, K. P., Sreenivasan, K. R., and Yeung, P. K., Scaling exponents saturate in three-dimensional isotropic turbulence, *Phys. Rev. Fluids*, **5**, 054605, doi:[10.1103/PhysRevFluids.5.054605](https://doi.org/10.1103/PhysRevFluids.5.054605) (2020).
- Janssens, M., Vilà-Guerau de Arellano, J., Scheffer, M., Antonissen, C., Siebesma, A. P., and Glassmeier, F., Cloud Patterns in the Trades Have Four Interpretable Dimensions, *Geophysical Research Letters*, **48**(5), e2020GL091001, doi:<https://doi.org/10.1029/2020GL091001> (2021).
- Jeffreys, H., Some cases of instability in fluid motion, *Proceedings of the Royal Society of London. Series A, Containing Papers of a Mathematical and Physical Character*, **118**(779), 195–208, doi:[10.1098/rspa.1928.0045](https://doi.org/10.1098/rspa.1928.0045) (1928).
- Jen-La Plante, I., Ma, Y., Nurowska, K., Gerber, H., Khelif, D., Karpinska, K., Kopec, M. K., Kumala, W., and Malinowski, S. P., Physics of Stratocumulus Top (POST): Turbulence characteristics, *Atmospheric Chemistry and Physics*, **16**(15), 9711–9725, ISSN: 16807324, doi:[10.5194/acp-16-9711-2016](https://doi.org/10.5194/acp-16-9711-2016) (2016).
- Jensen, M. P., Petersen, W. A., Bansemer, A., Bharadwaj, N., Carey, L. D., Cecil, D. J., Collis, S. M., Del Genio, A. D., Dolan, B., Gerlach, J., Giangrande, S. E., Heymsfield, A., Heymsfield, G., Kollias, P., Lang, T. J., Nesbitt, S. W., Neumann, A., Poellot, M., Rutledge, S. A., Schwaller, M., Tokay, A., Williams, C. R., Wolff, D. B., Xie, S., and Zipser, E. J., The midlatitude continental convective clouds experiment (mc3e), *Bulletin of the American Meteorological Society*, **97**(9), 1667–1686, doi:<https://doi.org/10.1175/BAMS-D-14-00228.1> (2016).
- Jolly, M. S. and Wirosoetisno, D., Tracer Turbulence: The Batchelor–Howells–Townsend Spectrum Revisited, *Journal of Mathematical Fluid Mechanics*, **22**(2), 18, doi:[10.1007/s00021-019-0478-6](https://doi.org/10.1007/s00021-019-0478-6) (2020).
- Jullien, M.-C., Castiglione, P., and Tabeling, P., Experimental Observation of Batchelor Dispersion of Passive Tracers, *Phys. Rev. Lett.*, **85**, 3636–3639, doi:[10.1103/PhysRevLett.85.3636](https://doi.org/10.1103/PhysRevLett.85.3636) (2000).

- Katzwinkel, J., Siebert, H., Heus, T., and Shaw, R. A., Measurements of turbulent mixing and subsiding shells in trade wind cumuli, *Journal of the Atmospheric Sciences*, **71**(8), 2810–2822, doi:<https://doi.org/10.1175/JAS-D-13-0222.1> (2014).
- Kazil, J., Narenpitak, P., Yamaguchi, T., and Feingold, G., On Climate Change and Trade Cumulus Organization, *Journal of Advances in Modeling Earth Systems*, **16**(9), e2023MS004057, doi:<https://doi.org/10.1029/2023MS004057> (2024).
- Kendon, E. J., Prein, A. F., Senior, C. A., and Stirling, A., Challenges and outlook for convection-permitting climate modelling, *Philosophical Transactions of the Royal Society A: Mathematical, Physical and Engineering Sciences*, **379**(2195), 20190547, doi:[10.1098/rsta.2019.0547](https://doi.org/10.1098/rsta.2019.0547) (2021).
- Khurshid, S., Donzis, D. A., and Sreenivasan, K. R., Energy spectrum in the dissipation range, *Phys. Rev. Fluids*, **3**, 082601, doi:[10.1103/PhysRevFluids.3.082601](https://doi.org/10.1103/PhysRevFluids.3.082601) (2018).
- Kiely, G., Albertson, J. D., Parlance, M. B., and Eichinger, W. E., Convective scaling of the average dissipation rate of temperature variance in the atmospheric surface layer, *Boundary-Layer Meteorology*, **77**(3), 267–284, doi:[10.1007/BF00123528](https://doi.org/10.1007/BF00123528) (1996).
- Kogawa, T., Shoji, E., Okajima, J., Komiya, A., and Maruyama, S., Experimental evaluation of thermal radiation effects on natural convection with a Rayleigh number of 10^8 – 10^9 by using an interferometer, *International Journal of Heat and Mass Transfer*, **132**, 1239–1249, doi:<https://doi.org/10.1016/j.ijheatmasstransfer.2018.11.162> (2019).
- Kolmogorov, A. N., Dissipation of energy in locally isotropic turbulence, *Doklady Akademii Nauk SSSR*, **32**, 16–18, doi:[10.1098/rspa.1991.0076](https://doi.org/10.1098/rspa.1991.0076) (1941a), reprinted in *Proc. R. Soc. Lond. A*, **434**, 15–17 (1991).
- Kolmogorov, A. N., The local structure of turbulence in incompressible viscous fluid for very large reynolds numbers, *Doklady Akademii Nauk SSSR*, **30**, 301–305, doi:[10.1098/rspa.1991.0075](https://doi.org/10.1098/rspa.1991.0075) (1941b), reprinted in *Proc. R. Soc. Lond. A*, **434**, 9–13 (1991).
- Kolmogorov, A. N., On the degeneration (decay) of isotropic turbulence in an incompressible viscous liquid, *Doklady Akademii Nauk SSSR*, **31**, 319–323 (1941c).

- Kolmogorov, A. N., A refinement of previous hypotheses concerning the local structure of turbulence in a viscous incompressible fluid at high Reynolds number, *Journal of Fluid Mechanics*, **13**(1), 82–85, ISSN: 14697645, doi:[10.1017/S0022112062000518](https://doi.org/10.1017/S0022112062000518) (1962).
- Kraichnan, R. H., Inertial Ranges in Two-Dimensional Turbulence, *The Physics of Fluids*, **10**(7), 1417–1423, ISSN: 0031-9171, doi:[10.1063/1.1762301](https://doi.org/10.1063/1.1762301) (1967).
- Kraichnan, R. H., Small-Scale Structure of a Scalar Field Convected by Turbulence, *The Physics of Fluids*, **11**(5), 945–953, ISSN: 0031-9171, doi:[10.1063/1.1692063](https://doi.org/10.1063/1.1692063) (1968).
- Kraichnan, R. H., Inertial-range transfer in two- and three-dimensional turbulence, *Journal of Fluid Mechanics*, **47**(3), 525–535, doi:[10.1017/S0022112071001216](https://doi.org/10.1017/S0022112071001216) (1971).
- Kraichnan, R. H., Anomalous scaling of a randomly advected passive scalar, *Phys. Rev. Lett.*, **72**, 1016–1019, doi:[10.1103/PhysRevLett.72.1016](https://doi.org/10.1103/PhysRevLett.72.1016) (1994).
- Krishnamoorthy, L. V. and Antonia, R. A., Temperature-dissipation measurements in a turbulent boundary layer, *Journal of Fluid Mechanics*, **176**, 265–281, doi:[10.1017/S0022112087000661](https://doi.org/10.1017/S0022112087000661) (1987).
- Krug, D., Lohse, D., and Stevens, R. J. A. M., Coherence of temperature and velocity superstructures in turbulent rayleigh–bénard flow, *Journal of Fluid Mechanics*, **887**, A2, doi:[10.1017/jfm.2019.1054](https://doi.org/10.1017/jfm.2019.1054) (2020).
- Król, S., Blyth, A., Böing, S., Denby, L., Lachlan-Cope, T., and Malinowski, S. P., Can Recurrence Quantification Analysis Be Useful in the Interpretation of Airborne Turbulence Measurements?, *Geophysical Research Letters*, **51**(6), e2023GL105753, doi:<https://doi.org/10.1029/2023GL105753> (2024).
- Kukharets, V. P. and Nalbandyan, H. G., Temperature fluctuations in the atmospheric surface layer over the thermally inhomogeneous underlying surface, *Izvestiya, Atmospheric and Oceanic Physics*, **42**(4), 456–462, doi:[10.1134/S0001433806040050](https://doi.org/10.1134/S0001433806040050) (2006).
- Kumala, W., Haman, K. E., Kopec, M. K., Khelif, D., and Malinowski, S. P., Modified ultrafast thermometer UFT-M and temperature measurements during Physics of Stratocumulus Top (POST), *Atmospheric Measurement Techniques*, **6**(8), 2043–2054, ISSN: 1867-8548, doi:[10.5194/amt-6-2043-2013](https://doi.org/10.5194/amt-6-2043-2013) (2013).

- Kumar, A. and Verma, M. K., Applicability of Taylor's hypothesis in thermally driven turbulence, *Royal Society Open Science*, **5**(4), 172152, doi:[10.1098/rsos.172152](https://doi.org/10.1098/rsos.172152) (2018).
- von Kármán, T. and Howarth, L., On the statistical theory of isotropic turbulence, *Proceedings of the Royal Society of London. Series A - Mathematical and Physical Sciences*, **164**(917), 192–215, doi:[10.1098/rspa.1938.0013](https://doi.org/10.1098/rspa.1938.0013) (1938).
- Lafleur, L. J., Descartes, Father of Modern Meteorology, *Bulletin of the American Meteorological Society*, **31**(4), 138–140, ISSN: 15200477 (1950).
- Lakkaraju, R., Stevens, R. J. A. M., Verzicco, R., Grossmann, S., Prosperetti, A., Sun, C., and Lohse, D., Spatial distribution of heat flux and fluctuations in turbulent Rayleigh-Bénard convection, *Phys. Rev. E*, **86**, 056315, doi:[10.1103/PhysRevE.86.056315](https://doi.org/10.1103/PhysRevE.86.056315) (2012).
- Landau, L. D. and Lifshitz, E. M., *Fluid Mechanics*, volume 6 of *Course of Theoretical Physics*, Pergamon Press, Burlington, MA, 2nd edition (1987).
- Lee, S. K., Benaissa, A., Djenidi, L., Lavoie, P., and Antonia, R. A., Scaling range of velocity and passive scalar spectra in grid turbulence, *Physics of Fluids*, **24**(7), 075101, ISSN: 1070-6631, doi:[10.1063/1.4731295](https://doi.org/10.1063/1.4731295) (2012).
- Leith, C. E., Diffusion Approximation for Two-Dimensional Turbulence, *The Physics of Fluids*, **11**(3), 671–672, ISSN: 0031-9171, doi:[10.1063/1.1691968](https://doi.org/10.1063/1.1691968) (1968).
- Lemay, J., Djenidi, L., and Antonia, R., Estimation of mean turbulent kinetic energy and temperature variance dissipation rates using a spectral chart method, *Physics of Fluids*, **32**(5), 055109, ISSN: 1070-6631, doi:[10.1063/5.0006923](https://doi.org/10.1063/5.0006923) (2020).
- Lenschow, D. H., Mann, J., and Kristensen, L., How long is long enough when measuring fluxes and other turbulence statistics?, *Journal of Atmospheric and Oceanic Technology*, **11**(3), 661–673, doi:[10.1175/1520-0426\(1994\)011<0661:HLILEW>2.0.CO;2](https://doi.org/10.1175/1520-0426(1994)011<0661:HLILEW>2.0.CO;2) (1994).
- Li, X.-Y., Svensson, G., Brandenburg, A., and Haugen, N. E. L., Cloud-droplet growth due to supersaturation fluctuations in stratiform clouds, *Atmospheric Chemistry and Physics*, **19**(1), 639–648, doi:[10.5194/acp-19-639-2019](https://doi.org/10.5194/acp-19-639-2019) (2019).

- Li, Y.-R., Zhang, H., Zhang, L., and Wu, C.-M., Three-dimensional numerical simulation of double-diffusive Rayleigh–Bénard convection in a cylindrical enclosure of aspect ratio 2, *International Journal of Heat and Mass Transfer*, **98**, 472–483, doi:<https://doi.org/10.1016/j.ijheatmasstransfer.2016.03.026> (2016).
- Lin, J., Qian, T., Bechtold, P., Grell, G., Zhang, G. J., Zhu, P., Freitas, S. R., Barnes, H., and Han, J., Atmospheric convection, *Atmosphere-Ocean*, **60**(3-4), 422–476, doi:[10.1080/07055900.2022.2082915](https://doi.org/10.1080/07055900.2022.2082915) (2022).
- Lindborg, E., Scaling in Rayleigh–Bénard convection, *Journal of Fluid Mechanics*, **956**, A34, doi:[10.1017/jfm.2023.46](https://doi.org/10.1017/jfm.2023.46) (2023).
- Liu, S., Jiang, L., Chong, K. L., Zhu, X., Wan, Z.-H., Verzicco, R., Stevens, R. J. A. M., Lohse, D., and Sun, C., From Rayleigh–Bénard convection to porous-media convection: how porosity affects heat transfer and flow structure, *Journal of Fluid Mechanics*, **895**, A18, doi:DOI: [10.1017/jfm.2020.309](https://doi.org/10.1017/jfm.2020.309) (2020).
- Liu, Y. and Ecke, R. E., Local temperature measurements in turbulent rotating rayleigh-bénard convection, *Phys. Rev. E*, **84**, 016311, doi:[10.1103/PhysRevE.84.016311](https://doi.org/10.1103/PhysRevE.84.016311) (2011).
- Livescu, D., Turbulence with Large Thermal and Compositional Density Variations, *Annual Review of Fluid Mechanics*, **52**, 309–341, ISSN: 1545-4479, doi:[10.1146/annurev-fluid-010719-060114](https://doi.org/10.1146/annurev-fluid-010719-060114) (2020).
- Lohse, D. and Shishkina, O., Ultimate Rayleigh–Bénard turbulence, *Rev. Mod. Phys.*, **96**, 035001, doi:[10.1103/RevModPhys.96.035001](https://doi.org/10.1103/RevModPhys.96.035001) (2024).
- Lohse, D. and Xia, K.-Q., Small-scale properties of turbulent rayleigh-bénard convection, *Annual Review of Fluid Mechanics*, **42**(Volume 42, 2010), 335–364, ISSN: 1545-4479, doi:[10.1146/annurev.fluid.010908.165152](https://doi.org/10.1146/annurev.fluid.010908.165152) (2010).
- Lu, C.-L., Luo, K., Zhou, P.-C., and Yi, H.-L., Rayleigh–Bénard convection in a dielectric fluid under an external electric field with a melting boundary, *Phys. Rev. Fluids*, **6**, 063504, doi:[10.1103/PhysRevFluids.6.063504](https://doi.org/10.1103/PhysRevFluids.6.063504) (2021).
- Ma, Y., Cheng, W., Huang, S., Schmitt, F. G., Lin, X., and Huang, Y., Hidden turbulence in van Gogh’s *The Starry Night*, *Physics of Fluids*, **36**(9), 095140, ISSN: 1070-6631, doi:[10.1063/5.0213627](https://doi.org/10.1063/5.0213627) (2024).
- Ma, Y. F., Malinowski, S. P., Karpinska, K., Gerber, H. E., and Kumala, W., Scaling analysis of temperature and liquid water content in the marine boundary

- layer clouds during POST, *Journal of the Atmospheric Sciences*, **74**(12), 4075–4092, ISSN: 15200469, doi:[10.1175/JAS-D-17-0015.1](https://doi.org/10.1175/JAS-D-17-0015.1) (2017).
- MacMillan, T., Shaw, R. A., Cantrell, W. H., and Richter, D. H., Direct numerical simulation of turbulence and microphysics in the pi chamber, *Phys. Rev. Fluids*, **7**, 020501, doi:[10.1103/PhysRevFluids.7.020501](https://doi.org/10.1103/PhysRevFluids.7.020501) (2022).
- Malinowski, S. P., Gerber, H., Jen-La Plante, I., Kopec, M. K., Kumala, W., Nurowska, K., Chuang, P. Y., Khelif, D., and Haman, K. E., Physics of Stratocumulus Top (POST): Turbulent mixing across capping inversion, *Atmospheric Chemistry and Physics*, **13**(24), 12171–12186, ISSN: 16807316, doi:[10.5194/acp-13-12171-2013](https://doi.org/10.5194/acp-13-12171-2013) (2013).
- Malinowski, S. P. and Leclerc, M. Y., Fractal properties of temperature fluctuations in the convective surface layer, *Boundary-Layer Meteorology*, **71**(1-2), 169–187, ISSN: 00068314, doi:[10.1007/BF00709225](https://doi.org/10.1007/BF00709225) (1994).
- Mazzitelli, I. and Lanotte, A. S., Active and passive scalar intermittent statistics in turbulent atmospheric convection, *Physica D: Nonlinear Phenomena*, **241**(3), 251–259, ISSN: 0167-2789, doi:[10.1016/j.physd.2011.07.009](https://doi.org/10.1016/j.physd.2011.07.009) (2012).
- McMullen, R. M., Torczynski, J. R., and Gallis, M. A., Thermal-fluctuation effects on small-scale statistics in turbulent gas flow, *Physics of Fluids*, **35**(1), 011705, ISSN: 1070-6631, doi:[10.1063/5.0134870](https://doi.org/10.1063/5.0134870) (2023).
- Mishra, P. K., De, A. K., Verma, M. K., and Eswaran, V., Dynamics of reorientations and reversals of large-scale flow in rayleigh–bénard convection, *Journal of Fluid Mechanics*, **668**, 480–499, doi:[10.1017/S0022112010004830](https://doi.org/10.1017/S0022112010004830) (2011).
- Moller, S., Resagk, C., and Cierpka, C., Long-time experimental investigation of turbulent superstructures in rayleigh–bénard convection by noninvasive simultaneous measurements of temperature and velocity fields, *Experiments in Fluids*, **62**(4), 64, doi:[10.1007/s00348-020-03107-1](https://doi.org/10.1007/s00348-020-03107-1) (2021).
- Monin, A. and Yaglom, A., *Statistical Fluid Mechanics, Volume II: Mechanics of Turbulence*, The MIT Press (1975).
- Musacchio, S. and Boffetta, G., Condensate in quasi-two-dimensional turbulence, *Phys. Rev. Fluids*, **4**, 022602, doi:[10.1103/PhysRevFluids.4.022602](https://doi.org/10.1103/PhysRevFluids.4.022602) (2019).
- Myers, T. A., Scott, R. C., Zelinka, M. D., Klein, S. A., Norris, J. R., and Caldwell, P. M., Observational constraints on low cloud feedback reduce uncertainty of cli-

- mate sensitivity, *Nature Climate Change*, **11**(6), 501–507, doi:[10.1038/s41558-021-01039-0](https://doi.org/10.1038/s41558-021-01039-0) (2021).
- Ni, R. and Xia, K.-Q., Experimental investigation of pair dispersion with small initial separation in convective turbulent flows, *Phys. Rev. E*, **87**, 063006, doi:[10.1103/PhysRevE.87.063006](https://doi.org/10.1103/PhysRevE.87.063006) (2013).
- Niedermeier, D., Chang, K., Cantrell, W., Chandrakar, K. K., Ciochetto, D., and Shaw, R. A., Observation of a link between energy dissipation rate and oscillation frequency of the large-scale circulation in dry and moist Rayleigh-Bénard turbulence, *Phys. Rev. Fluids*, **3**, 083501, doi:[10.1103/PhysRevFluids.3.083501](https://doi.org/10.1103/PhysRevFluids.3.083501) (2018).
- Niedermeier, D., Hoffmann, R., Schmalfuss, S., Frey, W., Senf, F., Hellmuth, O., Pöhlker, M., and Stratmann, F., Particle deliquescence in a turbulent humidity field, *Aerosol Research Discussions*, **2025**, 1–19, doi:[10.5194/ar-2024-41](https://doi.org/10.5194/ar-2024-41) (2025).
- Niedermeier, D., Voigtländer, J., Schmalfuß, S., Busch, D., Schumacher, J., Shaw, R. A., and Stratmann, F., Characterization and first results from LACIS-T: A moist-air wind tunnel to study aerosol-cloud-turbulence interactions, *Atmospheric Measurement Techniques*, **13**(4), 2015–2033, doi:[10.5194/AMT-13-2015-2020](https://doi.org/10.5194/AMT-13-2015-2020) (2020).
- Niemela, J. J., Skrbek, L., Sreenivasan, K. R., and Donnelly, R. J., Turbulent convection at very high rayleigh numbers, *Nature*, **404**(6780), 837–840, doi:[10.1038/35009036](https://doi.org/10.1038/35009036) (2000).
- Nowak, J., Kumala, W., Kwiatkowski, A., Kwiatkowski, K., Czyżewska, D., Karpińska, K., and Malinowski, S., UltraFast Thermometer 2.0 - new temperature sensor for airborne applications and its performance during ACORES 2017, *Geophysical Research Abstracts*, doi:[10.13140/RG.2.2.12500.24967](https://doi.org/10.13140/RG.2.2.12500.24967) (2018).
- Nowak, J. L., Grosz, R., Frey, W., Niedermeier, D., Mijas, J., Malinowski, S. P., Ort, L., Schmalfuß, S., Stratmann, F., Voigtländer, J., and Stacewicz, T., Contactless optical hygrometry in LACIS-T, *Atmospheric Measurement Techniques*, **15**(13), 4075–4089, doi:[10.5194/amt-15-4075-2022](https://doi.org/10.5194/amt-15-4075-2022) (2022).
- Nowak, J. L., Siebert, H., Szodry, K.-E., and Malinowski, S. P., Coupled and decoupled stratocumulus-topped boundary layers: turbulence properties, *Atmospheric Chemistry and Physics Discussions*, **2021**, 1–41, doi:[10.5194/acp-2021-214](https://doi.org/10.5194/acp-2021-214) (2021).

- Nowak, J. L., Waclawczyk, M., Vassilicos, J. C., Król, S., and Malinowski, S. P., Scale-by-scale budget of turbulence kinetic energy in the convective atmospheric boundary layer: Analysis of structure functions, *Quarterly Journal of the Royal Meteorological Society*, 1–18, doi:<https://doi.org/10.1002/qj.4879> (2025).
- Oboukhov, A. M., Some specific features of atmospheric turbulence, *Journal of Fluid Mechanics*, **13**(1), 77–81, doi:[10.1017/S0022112062000506](https://doi.org/10.1017/S0022112062000506) (1962).
- Obukhov, A. M., The structure of the temperature field in a turbulent flow, *Doklady Akademii Nauk SSSR*, **67**(4), 643–646 (1949).
- Obukhov, A. M., On influence of buoyancy forces on the structure of temperature field in a turbulent flow, *Doklady Akademii Nauk SSSR*, **125**, 1246–1248 (1959).
- Olsthoorn, J., Accounting for surface temperature variations in rayleigh-bénard convection, *Phys. Rev. Fluids*, **8**, 033501, doi:[10.1103/PhysRevFluids.8.033501](https://doi.org/10.1103/PhysRevFluids.8.033501) (2023).
- Pandey, A., Scheel, J. D., and Schumacher, J., Turbulent superstructures in rayleigh-bénard convection, *Nature Communications*, **9**(1), 2118, doi:[10.1038/s41467-018-04478-0](https://doi.org/10.1038/s41467-018-04478-0) (2018).
- Pawar, S. S. and Arakeri, J. H., Kinetic energy and scalar spectra in high Rayleigh number axially homogeneous buoyancy driven turbulence, *Physics of Fluids*, **28**(6), 065103, ISSN: 1070-6631, doi:[10.1063/1.4953858](https://doi.org/10.1063/1.4953858) (2016).
- Peng, Y., Selvakumar, R. D., and Wu, J., Onset of Rayleigh-Bénard convection in dielectric liquids with electric conduction, *Phys. Rev. Fluids*, **9**, 013902, doi:[10.1103/PhysRevFluids.9.013902](https://doi.org/10.1103/PhysRevFluids.9.013902) (2024).
- Plunian, F., Teimurazov, A., Stepanov, R., and Verma, M. K., Inverse cascade of energy in helical turbulence, *Journal of Fluid Mechanics*, **895**, A13, doi:[10.1017/jfm.2020.307](https://doi.org/10.1017/jfm.2020.307) (2020).
- van der Poel, E. P., Ostilla-Mónico, R., Verzicco, R., Grossmann, S., and Lohse, D., Logarithmic mean temperature profiles and their connection to plume emissions in turbulent rayleigh-bénard convection, *Phys. Rev. Lett.*, **115**, 154501, doi:[10.1103/PhysRevLett.115.154501](https://doi.org/10.1103/PhysRevLett.115.154501) (2015).
- Pope, S. B., *Turbulent flows*, Cambridge University Press, Cambridge, ISBN: 9780521598866, doi:[10.1017/CBO9780511840531](https://doi.org/10.1017/CBO9780511840531) (2000).

- Pouquet, A., Rosenberg, D., Stawarz, J., and Marino, R., Helicity Dynamics, Inverse, and Bidirectional Cascades in Fluid and Magnetohydrodynamic Turbulence: A Brief Review, *Earth and Space Science*, **6**(3), 351–369, doi:[10.1029/2018EA000432](https://doi.org/10.1029/2018EA000432) (2019).
- Prabhakaran, P., Kinney, G., Cantrell, W., Shaw, R. A., and Bodenschatz, E., High Supersaturation in the Wake of Falling Hydrometeors: Implications for Cloud Invigoration and Ice Nucleation, *Geophysical Research Letters*, **47**(10), e2020GL088055, doi:<https://doi.org/10.1029/2020GL088055> (2020a).
- Prabhakaran, P., Shawon, A. S. M., Kinney, G., Thomas, S., Cantrell, W., and Shaw, R. A., The role of turbulent fluctuations in aerosol activation and cloud formation, *Proceedings of the National Academy of Sciences*, **117**(29), 16831–16838, doi:[10.1073/pnas.2006426117](https://doi.org/10.1073/pnas.2006426117) (2020b).
- Prabhakaran, P., Thomas, S., Cantrell, W., Shaw, R. A., and Yang, F., Sources of Stochasticity in the Growth of Cloud Droplets: Supersaturation Fluctuations versus Turbulent Transport, *Journal of the Atmospheric Sciences*, **79**(12), 3145–3162, doi:<https://doi.org/10.1175/JAS-D-22-0051.1> (2022).
- Prandtl, L., Bericht über untersuchungen zur ausgebildeten turbulenz, *Zeitschrift für Angewandte Mathematik und Mechanik*, **5**(2), 136–139, doi:[10.1002/zamm.19250050212](https://doi.org/10.1002/zamm.19250050212) (1925).
- du Puits, R., Thermal boundary layers in turbulent rayleigh-bénard convection with rough and smooth plates: A one-to-one comparison, *Phys. Rev. Fluids*, **9**, 023501, doi:[10.1103/PhysRevFluids.9.023501](https://doi.org/10.1103/PhysRevFluids.9.023501) (2024).
- du Puits, R., Resagk, C., and Thess, A., Thermal boundary layers in turbulent rayleigh-bénard convection at aspect ratios between 1 and 9, *New Journal of Physics*, **15**(1), 013040, doi:[10.1088/1367-2630/15/1/013040](https://doi.org/10.1088/1367-2630/15/1/013040) (2013).
- Quinn, P. K., Thompson, E. J., Coffman, D. J., Baidar, S., Bariteau, L., Bates, T. S., Bigorre, S., Brewer, A., de Boer, G., de Szoeke, S. P., Drushka, K., Foltz, G. R., Intrieri, J., Iyer, S., Fairall, C. W., Gaston, C. J., Jansen, F., Johnson, J. E., Krüger, O. O., Marchbanks, R. D., Moran, K. P., Noone, D., Pezoa, S., Pincus, R., Plueddemann, A. J., Pöhlker, M. L., Pöschl, U., Quinones Melendez, E., Royer, H. M., Szczodrak, M., Thomson, J., Upchurch, L. M., Zhang, C., Zhang, D., and Zuidema, P., Measurements from the RV *Ronald H. Brown* and related platforms as part of the Atlantic Tradewind Ocean-Atmosphere Mesoscale Interaction Campaign (ATOMIC), *Earth System Science Data*, **13**(4), 1759–1790, doi:[10.5194/essd-13-1759-2021](https://doi.org/10.5194/essd-13-1759-2021) (2021).

- Rauber, R. M., Stevens, B., Ochs, H. T., Knight, C., Albrecht, B. A., Blyth, A. M., Fairall, C. W., Jensen, J. B., Lasher-Trapp, S. G., Mayol-Bracero, O. L., Vali, G., Anderson, J. R., Baker, B. A., Bandy, A. R., Burnet, E., Brenguier, J. L., Brewer, W. A., Brown, P. R. A., Chuang, R., Cotton, W. R., Di Girolamo, L., Geerts, B., Gerber, H., Göke, S., Gomes, L., Heikes, B. G., Hudson, J. G., Kollias, P., Lawson, R. R., Krueger, S. K., Lenschow, D. H., Nuijens, L., O’Sullivan, D. W., Rilling, R. A., Rogers, D. C., Siebesma, A. P., Snodgrass, E., Stith, J. L., Thornton, D. C., Tucker, S., Twohy, C. H., and Zuidema, P., Rain in Shallow Cumulus Over the Ocean: The RICO Campaign, *Bulletin of the American Meteorological Society*, **88**(12), 1912–1928, doi:<https://doi.org/10.1175/BAMS-88-12-1912> (2007).
- Rayleigh, L., On the convective currents in a horizontal layer of fluid when the higher temperature is on the under side, *Philosophical Magazine*, **32**(192), 529–546 (1916).
- van Reeuwijk, M. and Craske, J., Energy-consistent entrainment relations for jets and plumes, *Journal of Fluid Mechanics*, **782**, 333–355, doi:[10.1017/jfm.2015.534](https://doi.org/10.1017/jfm.2015.534) (2015).
- Reid, W. H. and Harris, D. L., Some Further Results on the Bénard Problem, *The Physics of Fluids*, **1**(2), 102–110, ISSN: 0031-9171, doi:[10.1063/1.1705871](https://doi.org/10.1063/1.1705871) (1958).
- Reiter, P., Shishkina, O., Lohse, D., and Krug, D., Crossover of the relative heat transport contributions of plume ejecting and impacting zones in turbulent rayleigh-bénard convection(a), *Europhysics Letters*, **134**(3), 34002, doi:[10.1209/0295-5075/134/34002](https://doi.org/10.1209/0295-5075/134/34002) (2021).
- Richardson, L. F., *Weather Prediction by Numerical Process*, Cambridge University Press (1922).
- Richardson, L. F. and Walker, G. T., Atmospheric diffusion shown on a distance-neighbour graph, *Proceedings of the Royal Society of London. Series A, Containing Papers of a Mathematical and Physical Character*, **110**(756), 709–737, doi:[10.1098/rspa.1926.0043](https://doi.org/10.1098/rspa.1926.0043) (1926).
- Rieutord, M., Roudier, T., Rincon, F., Malherbe, J.-M., Meunier, N., Berger, T., and Frank, Z., On the power spectrum of solar surface flows, *A&A*, **512**, A4, doi:[10.1051/0004-6361/200913303](https://doi.org/10.1051/0004-6361/200913303) (2010).

- Roca, R. and Fiolleau, T., Extreme precipitation in the tropics is closely associated with long-lived convective systems, *Communications Earth & Environment*, **1**(1), 18, doi:[10.1038/s43247-020-00015-4](https://doi.org/10.1038/s43247-020-00015-4) (2020).
- Roca, R., Fiolleau, T., John, V. O., and Schulz, J., METEOSAT Long-Term Observations Reveal Changes in Convective Organization Over Tropical Africa and Atlantic Ocean, *Surveys in Geophysics*, doi:[10.1007/s10712-024-09862-8](https://doi.org/10.1007/s10712-024-09862-8) (2024).
- Roudini, M., Niedermeier, D., Stratmann, F., and Winkler, A., Droplet Generation in Standing-Surface-Acoustic-Wave Nebulization at Controlled Air Humidity, *Phys. Rev. Appl.*, **14**, 014071, doi:[10.1103/PhysRevApplied.14.014071](https://doi.org/10.1103/PhysRevApplied.14.014071) (2020).
- Sahoo, G., De Pietro, M., and Biferale, L., Helicity statistics in homogeneous and isotropic turbulence and turbulence models, *Phys. Rev. Fluids*, **2**, 024601, doi:[10.1103/PhysRevFluids.2.024601](https://doi.org/10.1103/PhysRevFluids.2.024601) (2017).
- Sakievich, P., Peet, Y., and Adrian, R., Large-scale thermal motions of turbulent rayleigh–bénard convection in a wide aspect-ratio cylindrical domain, *International Journal of Heat and Fluid Flow*, **61**, doi:[10.1016/j.ijheatfluidflow.2016.04.011](https://doi.org/10.1016/j.ijheatfluidflow.2016.04.011) (2016).
- Salesky, S. T., Gillis, K., Anderson, J., Helman, I., Cantrell, W., and Shaw, R. A., Modeling the subgrid scale scalar variance: a priori tests and application to supersaturation in cloud turbulence, *Journal of the Atmospheric Sciences*, doi:[10.1175/JAS-D-23-0163.1](https://doi.org/10.1175/JAS-D-23-0163.1) (2024).
- Samuel, R. and Verma, M. K., Bolgiano-Obukhov scaling in two-dimensional Rayleigh-Bénard convection at extreme Rayleigh numbers, *Phys. Rev. Fluids*, **9**, 023502, doi:[10.1103/PhysRevFluids.9.023502](https://doi.org/10.1103/PhysRevFluids.9.023502) (2024).
- Schulz, H., Eastman, R., and Stevens, B., Characterization and Evolution of Organized Shallow Convection in the Downstream North Atlantic Trades, *Journal of Geophysical Research: Atmospheres*, **126**(17), e2021JD034575, doi:<https://doi.org/10.1029/2021JD034575> (2021).
- Schumacher, R. S. and Rasmussen, K. L., The formation, character and changing nature of mesoscale convective systems, *Nature Reviews Earth & Environment*, **1**(6), 300–314, doi:[10.1038/s43017-020-0057-7](https://doi.org/10.1038/s43017-020-0057-7) (2020).
- Sharifi Ghazijahani, M., Kästner, C., Valori, V., Thieme, A., Täschner, K., Schumacher, J., and Cierpka, C., The SCALEX facility –an apparatus for

- scaled fluid dynamical experiments, *Technisches Messen*, **90**(5), 296–309, doi:[doi:10.1515/teme-2022-0121](https://doi.org/10.1515/teme-2022-0121) (2023).
- Shaw, R. A., Cantrell, W., Chen, S., Chuang, P., Donahue, N., Feingold, G., Kollias, P., Korolev, A., Kreidenweis, S., Krueger, S., Mellado, J. P., Niedermeier, D., and Xue, L., Cloud–Aerosol–Turbulence Interactions: Science Priorities and Concepts for a Large-Scale Laboratory Facility, *Bulletin of the American Meteorological Society*, **101**(7), E1026–E1035, doi:<https://doi.org/10.1175/BAMS-D-20-0009.1> (2020).
- Sherwood, S. C. and Forest, C. E., Opinion: Can uncertainty in climate sensitivity be narrowed further?, *Atmospheric Chemistry and Physics*, **24**(4), 2679–2686, doi:[doi:10.5194/acp-24-2679-2024](https://doi.org/10.5194/acp-24-2679-2024) (2024).
- Shevkar, P. P., Vishnu, R., Mohanan, S. K., Koothur, V., Mathur, M., and Puthenveetil, B. A., On separating plumes from boundary layers in turbulent convection, *Journal of Fluid Mechanics*, **941**, A5, doi:[DOI: 10.1017/jfm.2022.271](https://doi.org/10.1017/jfm.2022.271) (2022).
- Shi, N., Emran, M. S., and Schumacher, J., Boundary layer structure in turbulent Rayleigh–Bénard convection, *Journal of Fluid Mechanics*, **706**, 5–33, doi:[DOI: 10.1017/jfm.2012.207](https://doi.org/10.1017/jfm.2012.207) (2012).
- Shishkina, O., Rayleigh–bénard convection: The container shape matters, *Phys. Rev. Fluids*, **6**, 090502, doi:[10.1103/PhysRevFluids.6.090502](https://doi.org/10.1103/PhysRevFluids.6.090502) (2021).
- Shishkina, O., Horn, S., Emran, M. S., and Ching, E. S. C., Mean temperature profiles in turbulent thermal convection, *Phys. Rev. Fluids*, **2**, 113502, doi:[10.1103/PhysRevFluids.2.113502](https://doi.org/10.1103/PhysRevFluids.2.113502) (2017).
- Shraiman, B. I. and Siggia, E. D., Scalar turbulence, *Nature*, **405**(6787), 639–646, doi:[10.1038/35015000](https://doi.org/10.1038/35015000) (2000).
- Siebert, H., Franke, H., Lehmann, K., Maser, R., Saw, E. W., Schell, D., Shaw, R. A., and Wendisch, M., Probing Finescale Dynamics and Microphysics of Clouds with Helicopter-Borne Measurements, *Bulletin of the American Meteorological Society*, **87**(12), 1727–1738, ISSN: 0003-0007, doi:[10.1175/BAMS-87-12-1727](https://doi.org/10.1175/BAMS-87-12-1727) (2006a).
- Siebert, H., Lehmann, K., and Wendisch, M., Observations of small-scale turbulence and energy dissipation rates in the cloudy boundary layer, *Journal of the Atmospheric Sciences*, **63**(5), 1451–1466, ISSN: 00224928, doi:[10.1175/JAS3687.1](https://doi.org/10.1175/JAS3687.1) (2006b).

- Siebert, H. and Shaw, R. A., Supersaturation Fluctuations during the Early Stage of Cumulus Formation, *Journal of the Atmospheric Sciences*, **74**(4), 975–988, doi:<https://doi.org/10.1175/JAS-D-16-0115.1> (2017).
- Siebert, H., Szodry, K. E., Egerer, U., Wehner, B., Henning, S., Chevalier, K., Lückerath, J., Welz, O., Weinhold, K., Lauermann, F., Gottschalk, M., Ehrlich, A., Wendisch, M., Fialho, P., Roberts, G., Allwayin, N., Schum, S., Shaw, R. A., Mazzoleni, C., Mazzoleni, L., Nowak, J. L., Malinowski, S. P., Karpinska, K., Kumala, W., Czyzewska, D., Luke, E. P., Kollias, P., Wood, R., and Mellado, J. P., Observations of aerosol, cloud, turbulence, and radiation properties at the top of the Marine Boundary Layer over the Eastern North Atlantic Ocean: The ACORES Campaign, *Bulletin of the American Meteorological Society*, **102**(1), E123–E147, doi:[10.1175/BAMS-D-19-0191.1](https://doi.org/10.1175/BAMS-D-19-0191.1) (2021).
- Siebesma, A. P., Bony, S., Jakob, C., and Stevens, B., eds., *Clouds and Climate: Climate science’s greatest challenge*, Cambridge University Press, United Kingdom, ISBN: 9781107061071, doi:[10.1017/9781107447738](https://doi.org/10.1017/9781107447738) (2020).
- Sreenivasan, K. R., On the universality of the Kolmogorov constant, *Physics of Fluids*, **7**(11), 2778–2784, ISSN: 1070-6631, doi:[10.1063/1.868656](https://doi.org/10.1063/1.868656) (1995).
- Sreenivasan, K. R., The passive scalar spectrum and the Obukhov–Corrsin constant, *Physics of Fluids*, **8**(1), 189–196, ISSN: 1070-6631, doi:[10.1063/1.868826](https://doi.org/10.1063/1.868826) (1996).
- Sreenivasan, K. R., Turbulent mixing: A perspective, *Proceedings of the National Academy of Sciences*, **116**(37), 18175–18183, doi:[10.1073/pnas.1800463115](https://doi.org/10.1073/pnas.1800463115) (2019).
- Sreenivasan, K. R., Antonia, R. A., and Danh, H. Q., Temperature dissipation fluctuations in a turbulent boundary layer, *The Physics of Fluids*, **20**(8), 1238–1249, ISSN: 0031-9171, doi:[10.1063/1.862005](https://doi.org/10.1063/1.862005) (1977).
- Stephan, C. C., Schnitt, S., Schulz, H., Bellenger, H., de Szoeko, S. P., Acquistapace, C., Baier, K., Dauhut, T., Laxenaire, R., Morfa-Avalos, Y., Person, R., Quiñones Meléndez, E., Bagheri, G., Böck, T., Daley, A., Güttler, J., Helfer, K. C., Los, S. A., Neuberger, A., Röttenbacher, J., Raeke, A., Ringel, M., Ritschel, M., Sadoulet, P., Schirmacher, I., Stolla, M. K., Wright, E., Charpentier, B., Doerenbecher, A., Wilson, R., Jansen, F., Kinne, S., Reverdin, G., Speich, S., Bony, S., and Stevens, B., Ship- and island-based atmospheric soundings from the 2020 EUREC⁴A field campaign, *Earth System Science Data*, **13**(2), 491–514, doi:[10.5194/essd-13-491-2021](https://doi.org/10.5194/essd-13-491-2021) (2021).

Stevens, B., Ament, F., Bony, S., Crewell, S., Ewald, F., Gross, S., Hansen, A., Hirsch, L., Jacob, M., Kölling, T., Konow, H., Mayer, B., Wendisch, M., Wirth, M., Wolf, K., Bakan, S., Bauer-Pfundstein, M., Brueck, M., Delanoë, J., Ehrlich, A., Farrell, D., Forde, M., Gödde, F., Grob, H., Hagen, M., Jäkel, E., Jansen, F., Klepp, C., Klingebiel, M., Mech, M., Peters, G., Rapp, M., Wing, A. A., and Zinner, T., A High-Altitude Long-Range Aircraft Configured as a Cloud Observatory: The NARVAL Expeditions, *Bulletin of the American Meteorological Society*, **100**(6), 1061–1077, doi:<https://doi.org/10.1175/BAMS-D-18-0198.1> (2019).

Stevens, B., Bony, S., Brogniez, H., Hentgen, L., Hohenegger, C., Kiemle, C., L’Ecuyer, T. S., Naumann, A. K., Schulz, H., Siebesma, P. A., Vial, J., Winker, D. M., and Zuidema, P., Sugar, gravel, fish and flowers: Mesoscale cloud patterns in the trade winds, *Quarterly Journal of the Royal Meteorological Society*, **146**(726), 141–152, doi:<https://doi.org/10.1002/qj.3662> (2020).

Stevens, B., Bony, S., Farrell, D., Ament, F., Blyth, A., Fairall, C., Karstensen, J., Quinn, P. K., Speich, S., Acquistapace, C., Aemisegger, F., Albright, A. L., Bellenger, H., Bodenschatz, E., Caesar, K. A., Chewitt-Lucas, R., De Boer, G., Delanoë, J., Denby, L., Ewald, F., Fildier, B., Forde, M., George, G., Gross, S., Hagen, M., Hausold, A., Heywood, K. J., Hirsch, L., Jacob, M., Jansen, F., Kinne, S., Klocke, D., Kölling, T., Konow, H., Lothon, M., Mohr, W., Naumann, A. K., Nuijens, L., Olivier, L., Pincus, R., Pöhlker, M., Reverdin, G., Roberts, G., Schnitt, S., Schulz, H., Pier Siebesma, A., Stephan, C. C., Sullivan, P., Touzé-Peiffer, L., Vial, J., Vogel, R., Zuidema, P., Alexander, N., Alves, L., Arix, S., Asmath, H., Bagheri, G., Baier, K., Bailey, A., Baranowski, D., Baron, A., Barrau, S., Barrett, P. A., Batier, F., Behrendt, A., Bendinger, A., Beucher, F., Bigorre, S., Blades, E., Blossey, P., Bock, O., Böing, S., Bosser, P., Bourras, D., Bouruet-Aubertot, P., Bower, K., Branellec, P., Branger, H., Brennek, M., Brewer, A., Brilouet, P. E., Brüggmann, B., Buehler, S. A., Burke, E., Burton, R., Calmer, R., Canonici, J. C., Carton, X., Cato, G., Charles, J. A., Chazette, P., Chen, Y., Chilinski, M. T., Choularton, T., Chuang, P., Clarke, S., Coe, H., Cornet, C., Coutris, P., Couvreur, F., Crewell, S., Cronin, T., Cui, Z., Cuypers, Y., Daley, A., Damerell, G. M., Dauhut, T., Deneke, H., Desbios, J. P., Dörner, S., Donner, S., Douet, V., Drushka, K., Dütsch, M., Ehrlich, A., Emanuel, K., Emmanouilidis, A., Etienne, J. C., Etienne-Leblanc, S., Faure, G., Feingold, G., Ferrero, L., Fix, A., Flamant, C., Flatau, P. J., Foltz, G. R., Forster, L., Furtuna, I., Gadian, A., Galewsky, J., Gallagher, M., Gallimore, P., Gaston, C., Gentemann, C., Geyskens, N., Giez, A., Gol-

lop, J., Gouirand, I., Gourbeyre, C., De Graaf, D., De Groot, G. E., Grosz, R., Güttler, J., Gutleben, M., Hall, K., Harris, G., Helfer, K. C., Henze, D., Herbert, C., Holanda, B., Ibanez-Landeta, A., Intrieri, J., Iyer, S., Julien, F., Kalesse, H., Kazil, J., Kellman, A., Kidane, A. T., Kirchner, U., Klingebiel, M., Körner, M., Kremper, L. A., Kretzschmar, J., Krüger, O., Kumala, W., Kurz, A., L'Hégaret, P., Labaste, M., Lachlan-Cope, T., Laing, A., Landschützer, P., Lang, T., Lange, D., Lange, I., Laplace, C., Lavik, G., Laxenaire, R., LeBihan, C., Leandro, M., Lefevre, N., Lena, M., Lenschow, D., Li, Q., Lloyd, G., Los, S., Losi, N., Lovell, O., Luneau, C., Makuch, P., Malinowski, S., Manta, G., Marinou, E., Marsden, N., Masson, S., Maury, N., Mayer, B., Mayers-Als, M., Mazel, C., McGeary, W., McWilliams, J. C., Mech, M., Mehlmann, M., Meroni, A. N., Mieslinger, T., Minikin, A., Minnett, P., Möller, G., Avalos, Y. M., Muller, C., Musat, I., Napoli, A., Neuberger, A., Noisel, C., Noone, D., Nordsiek, F., Nowak, J. L., Oswald, L., Parker, D. J., Peck, C., Person, R., Philippi, M., Plueddemann, A., Pöhlker, C., Pörtge, V., Pöschl, U., Pologne, L., Posyniak, M., Prange, M., Meléndez, E. Q., Radtke, J., Ramage, K., Reimann, J., Renault, L., Reus, K., Reyes, A., Ribbe, J., Ringel, M., Ritschel, M., Rocha, C. B., Rochetin, N., Röttenbacher, J., Rollo, C., Royer, H., Sadoulet, P., Saffin, L., Sandiford, S., Sandu, I., Schäfer, M., Schemann, V., Schirmacher, I., Schlenczek, O., Schmidt, J., Schröder, M., Schwarzenboeck, A., Sealy, A., Senff, C. J., Serikov, I., Shohan, S., Siddle, E., Smirnov, A., Späth, F., Spooner, B., Katharina Stolla, M., Szkółka, W., De Szoeko, S. P., Tarot, S., Tetoni, E., Thompson, E., Thomson, J., Tomassini, L., Totems, J., Ubele, A. A., Villiger, L., Von Arx, J., Wagner, T., Walther, A., Webber, B., Wendisch, M., Whitehall, S., Wiltshire, A., Wing, A. A., Wirth, M., Wiskandt, J., Wolf, K., Worbes, L., Wright, E., Wulfmeyer, V., Young, S., Zhang, C., Zhang, D., Ziemann, F., Zinner, T., and Zöger, M., EUREC4A, *Earth System Science Data*, **13**(8), 4067–4119, ISSN: 18663516, doi:[10.5194/ESSD-13-4067-2021](https://doi.org/10.5194/ESSD-13-4067-2021) (2021).

Stevens, B., Farrell, D., Hirsch, L., Jansen, F., Nuijens, L., Serikov, I., Brüggemann, B., Forde, M., Linne, H., Lonitz, K., and Prospero, J. M., The Barbados Cloud Observatory: Anchoring Investigations of Clouds and Circulation on the Edge of the ITCZ, *Bulletin of the American Meteorological Society*, **97**(5), 787–801, doi:<https://doi.org/10.1175/BAMS-D-14-00247.1> (2016).

Stevens, R. J. A. M., Blass, A., Zhu, X., Verzicco, R., and Lohse, D., Turbulent thermal superstructures in rayleigh-bénard convection, *Phys. Rev. Fluids*, **3**, 041501, doi:[10.1103/PhysRevFluids.3.041501](https://doi.org/10.1103/PhysRevFluids.3.041501) (2018).

Tavoularis, S. and Nedić, J., eds., *Measurement of Temperature*, 541–570,

- Cambridge University Press, Cambridge, 2 edition, ISBN: 9781009343626, doi:[10.1017/9781009343657.017](https://doi.org/10.1017/9781009343657.017) (2024).
- Taylor, G. I., Statistical theory of turbulence, *Proceedings of the Royal Society of London. Series A - Mathematical and Physical Sciences*, **151**(873), 421–444, doi:[10.1098/rspa.1935.0158](https://doi.org/10.1098/rspa.1935.0158) (1935).
- Taylor, G. I., The spectrum of turbulence, *Proceedings of the Royal Society of London. Series A - Mathematical and Physical Sciences*, **164**(919), 476–490, doi:[10.1098/rspa.1938.0032](https://doi.org/10.1098/rspa.1938.0032) (1938).
- Thackeray, C. W., Hall, A., Norris, J., and Chen, D., Constraining the increased frequency of global precipitation extremes under warming, *Nature Climate Change*, **12**(5), 441–448, doi:[10.1038/s41558-022-01329-1](https://doi.org/10.1038/s41558-022-01329-1) (2022).
- de la Torre Juárez, M., Chavez, A., Tamppari, L. K., Munguira, A., Martínez, G., Hueso, R., Chide, B., Murdoch, N., Stott, A. E., Navarro, S., Sánchez-Lavega, A., Orton, G. S., Viúdez-Moreiras, D., Banfield, D. J., and Rodríguez-Manfredi, J. A., Diurnal cycle of rapid air temperature fluctuations at Jezero crater: Probability distributions, exponential tails, scaling, and intermittency, *Journal of Geophysical Research: Planets*, **128**(7), e2022JE007458, doi:[10.1029/2022JE007458](https://doi.org/10.1029/2022JE007458) (2023).
- Trapp, R. J., *Mesoscale-Convective Processes in the Atmosphere*, Cambridge University Press (2013).
- Vasiliev, A., Sukhanovskii, A., Frick, P., Budnikov, A., Fomichev, V., Bolshukhin, M., and Romanov, R., High rayleigh number convection in a cubic cell with adiabatic sidewalls, *International Journal of Heat and Mass Transfer*, **102**, 201–212, ISSN: 0017-9310, doi:[10.1016/j.ijheatmasstransfer.2016.06.015](https://doi.org/10.1016/j.ijheatmasstransfer.2016.06.015) (2016).
- Verma, M. K., Variable energy flux in turbulence, *Journal of Physics A: Mathematical and Theoretical*, **55**(1), 013002, doi:[10.1088/1751-8121/ac354e](https://doi.org/10.1088/1751-8121/ac354e) (2021).
- Verma, M. K., Kumar, A., and Pandey, A., Phenomenology of buoyancy-driven turbulence: recent results, *New Journal of Physics*, **19**(2), 025012, doi:[10.1088/1367-2630/aa5d63](https://doi.org/10.1088/1367-2630/aa5d63) (2017).
- Vishnu, V. T., De, A. K., and Mishra, P. K., Dynamics of large-scale circulation and energy transfer mechanism in turbulent Rayleigh–Bénard convection in a cubic cell, *Physics of Fluids*, **32**(9), 095115, ISSN: 1070-6631, doi:[10.1063/5.0021667](https://doi.org/10.1063/5.0021667) (2020).

- Vishnu, V. T., De, A. K., and Mishra, P. K., Statistics of thermal plumes and dissipation rates in turbulent Rayleigh-Bénard convection in a cubic cell, *International Journal of Heat and Mass Transfer*, **182**, 121995, doi:<https://doi.org/10.1016/j.ijheatmasstransfer.2021.121995> (2022a).
- Vishnu, V. T., De, A. K., and Mishra, P. K., Statistics of thermal plumes and dissipation rates in turbulent rayleigh-bénard convection in a cubic cell, *International Journal of Heat and Mass Transfer*, **182**, 121995, ISSN: 0017-9310, doi:<https://doi.org/10.1016/j.ijheatmasstransfer.2021.121995> (2022b).
- Vogel, R., Albright, A. L., Vial, J., George, G., Stevens, B., and Bony, S., Strong cloud-circulation coupling explains weak trade cumulus feedback, *Nature*, **612**(7941), 696–700, doi:[10.1038/s41586-022-05364-y](https://doi.org/10.1038/s41586-022-05364-y) (2022).
- Wagner, S., Shishkina, O., and Wagner, C., Boundary layers and wind in cylindrical Rayleigh-Bénard cells, *Journal of Fluid Mechanics*, **697**, 336–366 (2012).
- Wang, L.-P., Chen, S., and Brasseur, J. G., Examination of hypotheses in the Kolmogorov refined turbulence theory through high-resolution simulations. Part 2. Passive scalar field, *Journal of Fluid Mechanics*, **400**, 163–197, doi:[DOI: 10.1017/S0022112099006448](https://doi.org/10.1017/S0022112099006448) (1999).
- Wang, Q., Xia, S.-N., Wang, B.-F., Sun, D.-J., Zhou, Q., and Wan, Z.-H., Flow reversals in two-dimensional thermal convection in tilted cells, *Journal of Fluid Mechanics*, **849**, 355–372, doi:[10.1017/jfm.2018.451](https://doi.org/10.1017/jfm.2018.451) (2018).
- Wang, Y. and Geerts, B., Humidity variations across the edge of trade wind cumuli: Observations and dynamical implications, *Atmospheric Research*, **97**(1), 144–156, doi:<https://doi.org/10.1016/j.atmosres.2010.03.017> (2010).
- Wang, Y., Geerts, B., and French, J., Dynamics of the cumulus cloud margin: An observational study, *Journal of the Atmospheric Sciences*, **66**(12), 3660–3677, doi:<https://doi.org/10.1175/2009JAS3129.1> (2009).
- Wang, Y., He, X., and Tong, P., Turbulent temperature fluctuations in a closed rayleigh-bénard convection cell, *Journal of Fluid Mechanics*, **874**, 263–284, doi:[10.1017/jfm.2019.405](https://doi.org/10.1017/jfm.2019.405) (2019).
- Wang, Y., Wei, Y., Tong, P., and He, X., Collective effect of thermal plumes on temperature fluctuations in a closed Rayleigh-Bénard convection cell, *Journal of Fluid Mechanics*, **934**, A13, doi:[10.1017/jfm.2021.1107](https://doi.org/10.1017/jfm.2021.1107) (2022).

- Warhaft, Z., Passive scalars in turbulent flows, *Annual Review of Fluid Mechanics*, **32**, 203–240, ISSN: 1545-4479, doi:[10.1146/annurev.fluid.32.1.203](https://doi.org/10.1146/annurev.fluid.32.1.203) (2000).
- Watanabe, T. and Gotoh, T., Statistics of a passive scalar in homogeneous turbulence, *New Journal of Physics*, **6**(1), 40, doi:[10.1088/1367-2630/6/1/040](https://doi.org/10.1088/1367-2630/6/1/040) (2004).
- Wei, P., The persistence of large-scale circulation in rayleigh–bénard convection, *Journal of Fluid Mechanics*, **924**, A28, doi:[10.1017/jfm.2021.619](https://doi.org/10.1017/jfm.2021.619) (2021).
- Wendisch, M. and Brenguier, J. L., *Airborne Measurements for Environmental Research*, Wiley-VCH Verlag GmbH and Co. KGaA, Weinheim, Germany, ISBN: 9783527653218, doi:[10.1002/9783527653218](https://doi.org/10.1002/9783527653218) (2013).
- Wesely, M. L., The Combined Effect of Temperature and Humidity Fluctuations on Refractive Index, *Journal of Applied Meteorology (1962-1982)*, **15**(1), 43–49, ISSN: 00218952, 2163534X (1976).
- de Wit, X. M., van Kan, A., and Alexakis, A., Bistability of the large-scale dynamics in quasi-two-dimensional turbulence, *Journal of Fluid Mechanics*, **939**, R2, doi:[10.1017/jfm.2022.209](https://doi.org/10.1017/jfm.2022.209) (2022).
- Wulfmeyer, V., Behrendt, A., Kottmeier, C., Corsmeier, U., Barthlott, C., Craig, G. C., Hagen, M., Althausen, D., Aoshima, F., Arpagaus, M., Bauer, H.-S., Bennett, L., Blyth, A., Brandau, C., Champollion, C., Crewell, S., Dick, G., Di Girolamo, P., Dorninger, M., Dufournet, Y., Eigenmann, R., Engelmann, R., Flamant, C., Foken, T., Gorgas, T., Grzeschik, M., Handwerker, J., Hauck, C., Höller, H., Junkermann, W., Kalthoff, N., Kiemle, C., Klink, S., König, M., Krauss, L., Long, C. N., Madonna, F., Mobbs, S., Neininger, B., Pal, S., Peters, G., Pigeon, G., Richard, E., Rotach, M. W., Russchenberg, H., Schwitalla, T., Smith, V., Steinacker, R., Trentmann, J., Turner, D. D., van Baelen, J., Vogt, S., Volkert, H., Weckwerth, T., Wernli, H., Wieser, A., and Wirth, M., The convective and orographically-induced precipitation study (cops): the scientific strategy, the field phase, and research highlights, *Quarterly Journal of the Royal Meteorological Society*, **137**(S1), 3–30, doi:<https://doi.org/10.1002/qj.752> (2011).
- Wyngaard, J. C., *Turbulence in the Atmosphere*, Cambridge University Press (2010).
- Wyngaard, J. C. and LeMone, M. A., Behavior of the Refractive Index Structure Parameter in the Entraining Convective Boundary Layer, *Journal of*

- Atmospheric Sciences*, **37**(7), 1573–1585, doi:[https://doi.org/10.1175/1520-0469\(1980\)037<1573:BOTRIS>2.0.CO;2](https://doi.org/10.1175/1520-0469(1980)037<1573:BOTRIS>2.0.CO;2) (1980).
- Xi, H.-D., Lam, S., and Xia, K.-Q., From laminar plumes to organized flows: the onset of large-scale circulation in turbulent thermal convection, *Journal of Fluid Mechanics*, **503**, 47–56, doi:[10.1017/S0022112004008079](https://doi.org/10.1017/S0022112004008079) (2004).
- Xi, H.-D., Zhou, S.-Q., Zhou, Q., Chan, T.-S., and Xia, K.-Q., Origin of the temperature oscillation in turbulent thermal convection, *Phys. Rev. Lett.*, **102**, 044503, doi:[10.1103/PhysRevLett.102.044503](https://doi.org/10.1103/PhysRevLett.102.044503) (2009).
- Xia, Y., Abu Rowin, W., Jelly, T., Marusic, I., and Hutchins, N., Investigation of cold-wire spatial and temporal resolution issues in thermal turbulent boundary layers, *International Journal of Heat and Fluid Flow*, **94**, 108926, doi:<https://doi.org/10.1016/j.ijheatfluidflow.2022.108926> (2022).
- Xie, J.-H. and Huang, S.-D., Bolgiano–Obukhov scaling in two-dimensional isotropic convection, *Journal of Fluid Mechanics*, **942**, A19, doi:[DOI: 10.1017/jfm.2022.373](https://doi.org/10.1017/jfm.2022.373) (2022).
- Xie, Y.-C. and Xia, K.-Q., Turbulent thermal convection over rough plates with varying roughness geometries, *Journal of Fluid Mechanics*, **825**, 573–599, doi:[10.1017/jfm.2017.397](https://doi.org/10.1017/jfm.2017.397) (2017).
- Xu, A., Chen, X., and Xi, H.-D., Tristable flow states and reversal of the large-scale circulation in two-dimensional circular convection cells, *Journal of Fluid Mechanics*, **910**, A33, doi:[10.1017/jfm.2020.964](https://doi.org/10.1017/jfm.2020.964) (2021a).
- Xu, A., Shi, L., and Xi, H.-D., Statistics of temperature and thermal energy dissipation rate in low-Prandtl number turbulent thermal convection, *Physics of Fluids*, **31**(12), 125101, ISSN: 1070-6631, doi:[10.1063/1.5129818](https://doi.org/10.1063/1.5129818) (2019).
- Xu, A., Xu, B.-R., and Xi, H.-D., Pore-scale statistics of temperature and thermal energy dissipation rate in turbulent porous convection, *Phys. Rev. Fluids*, **8**, 093504, doi:[10.1103/PhysRevFluids.8.093504](https://doi.org/10.1103/PhysRevFluids.8.093504) (2023).
- Xu, W., Wang, Y., He, X., Wang, X., Schumacher, J., Huang, S.-D., and Tong, P., Mean velocity and temperature profiles in turbulent rayleigh–bénard convection at low prandtl numbers, *Journal of Fluid Mechanics*, **918**, A1, doi:[10.1017/jfm.2021.255](https://doi.org/10.1017/jfm.2021.255) (2021b).
- Yaglom, A. M., On the local structure of a temperature field in a turbulent flow, *Doklady Akademii Nauk SSSR*, **69**, 743–746 (1949).

- Yakhot, V. and Orszag, S. A., Relation between the Kolmogorov and Batchelor constants, *The Physics of Fluids*, **30**(1), 3–3, ISSN: 0031-9171, doi:[10.1063/1.866057](https://doi.org/10.1063/1.866057) (1987).
- Yan, Z., Li, X., and Yu, C., Scale locality of helicity cascade in physical space, *Physics of Fluids*, **32**(6), 061705, ISSN: 1070-6631, doi:[10.1063/5.0013009](https://doi.org/10.1063/5.0013009) (2020).
- Yang, J. C., Vogt, T., and Eckert, S., Transition from steady to oscillating convection rolls in Rayleigh-Bénard convection under the influence of a horizontal magnetic field, *Phys. Rev. Fluids*, **6**, 023502, doi:[10.1103/PhysRevFluids.6.023502](https://doi.org/10.1103/PhysRevFluids.6.023502) (2021).
- Yano, J., *Geophysical Convection Dynamics*, number t. 5 in Developments in Weather and Climate Science, Elsevier Science, ISBN: 9780323912136 (2023).
- Yano, J.-I. and Morrison, H., Thermal vortex ring: vortex-dynamics analysis of a high-resolution simulation, *Journal of Fluid Mechanics*, **991**, A18, doi:[10.1017/jfm.2024.485](https://doi.org/10.1017/jfm.2024.485) (2024).
- Yao, J. and Hussain, F., Vortex Reconnection and Turbulence Cascade, *Annual Review of Fluid Mechanics*, **54**, 317–347, ISSN: 1545-4479, doi:[10.1146/annurev-fluid-030121-125143](https://doi.org/10.1146/annurev-fluid-030121-125143) (2022).
- Yeom, J. M., Fahandezh Sadi, H., Anderson, J. C., Yang, F., Cantrell, W., and Shaw, R. A., Cloud microphysical response to entrainment of dry air containing aerosols, *npj Climate and Atmospheric Science*, **8**(1), 8, doi:[10.1038/s41612-024-00889-7](https://doi.org/10.1038/s41612-024-00889-7) (2025).
- Yeom, J. M., Helman, I., Prabhakaran, P., Anderson, J. C., Yang, F., Shaw, R. A., and Cantrell, W., Cloud microphysical response to entrainment and mixing is locally inhomogeneous and globally homogeneous: Evidence from the lab, *Proceedings of the National Academy of Sciences*, **120**(42), e2307354120, doi:[10.1073/pnas.2307354120](https://doi.org/10.1073/pnas.2307354120) (2023).
- Yeung, P. K. and Sreenivasan, K. R., Spectrum of passive scalars of high molecular diffusivity in turbulent mixing, *Journal of Fluid Mechanics*, **716**, R14, doi:[10.1017/jfm.2012.632](https://doi.org/10.1017/jfm.2012.632) (2013).
- Yeung, P. K. and Sreenivasan, K. R., Direct numerical simulation of turbulent mixing at very low Schmidt number with a uniform mean gradient, *Physics of Fluids*, **26**(1), 015107, ISSN: 1070-6631, doi:[10.1063/1.4861070](https://doi.org/10.1063/1.4861070) (2014).

- Yeung, P. K. and Zhou, Y., Universality of the Kolmogorov constant in numerical simulations of turbulence, *Phys. Rev. E*, **56**, 1746–1752, doi:[10.1103/PhysRevE.56.1746](https://doi.org/10.1103/PhysRevE.56.1746) (1997).
- Yoshikawa, H. N., Tadie Fogaing, M., Crumeyrolle, O., and Mutabazi, I., Dielectrophoretic Rayleigh–Bénard convection under microgravity conditions, *Phys. Rev. E*, **87**, 043003, doi:[10.1103/PhysRevE.87.043003](https://doi.org/10.1103/PhysRevE.87.043003) (2013).
- Zang, X., Zhong, J., and Sun, C., Heat transfer in porous media Rayleigh–Bénard convection at various Prandtl numbers, *Physics of Fluids*, **35**(7), 075124, ISSN: 1070-6631, doi:[10.1063/5.0157666](https://doi.org/10.1063/5.0157666) (2023).
- Zanganeh, H., Yang, F., Khairoutdinov, M., Shaw, R., Wang, A., and Choi, Y., Exploring the Impact of Surface Topography on Rayleigh–Bénard Convection in the Pi Chamber Using Openfoam: In Both Cylindrical and Rectangular Geometries, *SSRN*, doi:[10.2139/ssrn.4979686](https://doi.org/10.2139/ssrn.4979686) (2024).
- Zaveri, R. A., Wang, J., Fan, J., Zhang, Y., Shilling, J. E., Zelenyuk, A., Mei, F., Newsom, R., Pekour, M., Tomlinson, J., Comstock, J. M., Shrivastava, M., Fortner, E., Machado, L. A. T., Artaxo, P., and Martin, S. T., Rapid growth of anthropogenic organic nanoparticles greatly alters cloud life cycle in the amazon rainforest, *Science Advances*, **8**(2), eabj0329, doi:[10.1126/sciadv.abj0329](https://doi.org/10.1126/sciadv.abj0329) (2022).
- Zhang, C. and Yoneyama, K., *CINDY/DYNAMO Field Campaign: Advancing Our Understanding of MJO Initiation*, volume 9 of *World Scientific Series on Asia-Pacific Weather and Climate*, 339–348, World Scientific, ISBN: 978-981-320-090-6, doi:[doi:10.1142/9789813200913_0027](https://doi.org/10.1142/9789813200913_0027) (2016).
- Zhang, L., Li, Y.-R., and Zhang, H., Onset of double-diffusive Rayleigh–Bénard convection of a moderate Prandtl number binary mixture in cylindrical enclosures, *International Journal of Heat and Mass Transfer*, **107**, 500–509, doi:<https://doi.org/10.1016/j.ijheatmasstransfer.2016.11.054> (2017a).
- Zhang, Y. and Zhou, Q., Low-Prandtl-number effects on global and local statistics in two-dimensional Rayleigh–Bénard convection, *Physics of Fluids*, **36**(1), 015107, ISSN: 1070-6631, doi:[10.1063/5.0175011](https://doi.org/10.1063/5.0175011) (2024).
- Zhang, Y., Zhou, Q., and Sun, C., Statistics of kinetic and thermal energy dissipation rates in two-dimensional turbulent Rayleigh–Bénard convection, *Journal of Fluid Mechanics*, **814**, 165–184, doi:[10.1017/jfm.2017.19](https://doi.org/10.1017/jfm.2017.19) (2017b).

- Zhang, Y.-Z., Sun, C., Bao, Y., and Zhou, Q., How surface roughness reduces heat transport for small roughness heights in turbulent rayleigh–bénard convection, *Journal of Fluid Mechanics*, **836**, doi:[10.1017/jfm.2017.786](https://doi.org/10.1017/jfm.2017.786) (2018).
- Zhao, B., Donahue, N. M., Zhang, K., Mao, L., Shrivastava, M., Ma, P.-L., Shen, J., Wang, S., Sun, J., Gordon, H., Tang, S., Fast, J., Wang, M., Gao, Y., Yan, C., Singh, B., Li, Z., Huang, L., Lou, S., Lin, G., Wang, H., Jiang, J., Ding, A., Nie, W., Qi, X., Chi, X., and Wang, L., Global variability in atmospheric new particle formation mechanisms, *Nature*, **631**(8019), 98–105, doi:[10.1038/s41586-024-07547-1](https://doi.org/10.1038/s41586-024-07547-1) (2024).
- Zhou, Q. and Jiang, L.-F., Kinetic and thermal energy dissipation rates in two-dimensional Rayleigh-Taylor turbulence, *Physics of Fluids*, **28**(4), 045109, ISSN: 1070-6631, doi:[10.1063/1.4946799](https://doi.org/10.1063/1.4946799) (2016).
- Zhou, Q. and Xia, K.-Q., Comparative experimental study of local mixing of active and passive scalars in turbulent thermal convection, *Phys. Rev. E*, **77**, 056312, doi:[10.1103/PhysRevE.77.056312](https://doi.org/10.1103/PhysRevE.77.056312) (2008).
- Zhou, Q. and Xia, K.-Q., Thermal boundary layer structure in turbulent rayleigh–bénard convection in a rectangular cell, *Journal of Fluid Mechanics*, **721**, 199–224, doi:[10.1017/jfm.2013.73](https://doi.org/10.1017/jfm.2013.73) (2013).
- Zhou, S.-Q. and Xia, K.-Q., Scaling properties of the temperature field in convective turbulence, *Phys. Rev. Lett.*, **87**, 064501, doi:[10.1103/PhysRevLett.87.064501](https://doi.org/10.1103/PhysRevLett.87.064501) (2001).
- Zhou, S.-Q. and Xia, K.-Q., Plume statistics in thermal turbulence: Mixing of an active scalar, *Phys. Rev. Lett.*, **89**, 184502, doi:[10.1103/PhysRevLett.89.184502](https://doi.org/10.1103/PhysRevLett.89.184502) (2002).
- Zhou, S.-Q., Xie, Y.-C., Sun, C., and Xia, K.-Q., Statistical characterization of thermal plumes in turbulent thermal convection, *Phys. Rev. Fluids*, **1**, 054301, doi:[10.1103/PhysRevFluids.1.054301](https://doi.org/10.1103/PhysRevFluids.1.054301) (2016a).
- Zhou, S.-Q., Xie, Y.-C., Sun, C., and Xia, K.-Q., Statistical characterization of thermal plumes in turbulent thermal convection, *Phys. Rev. Fluids*, **1**, 054301, doi:[10.1103/PhysRevFluids.1.054301](https://doi.org/10.1103/PhysRevFluids.1.054301) (2016b).
- Zhou, T. and Antonia, R. A., Approximations for turbulent energy and temperature variance dissipation rates in grid turbulence, *Physics of Fluids*, **12**(2), 335–344, ISSN: 1070-6631, doi:[10.1063/1.870312](https://doi.org/10.1063/1.870312) (2000).

- Zhou, Y., Turbulence theories and statistical closure approaches, *Physics Reports*, **935**, 1–117, ISSN: 0370-1573, doi:[10.1016/j.physrep.2021.07.001](https://doi.org/10.1016/j.physrep.2021.07.001) (2021).
- Zhu, X., Mathai, V., Stevens, R. J. A. M., Verzicco, R., and Lohse, D., Transition to the ultimate regime in two-dimensional rayleigh-bénard convection, *Phys. Rev. Lett.*, **120**, 144502, doi:[10.1103/PhysRevLett.120.144502](https://doi.org/10.1103/PhysRevLett.120.144502) (2018).
- Zhu, Y. and Antonia, R. A., Temperature dissipation measurements in a fully developed turbulent channel flow, *Experiments in Fluids*, **15**(3), 191–199, doi:[10.1007/BF00189886](https://doi.org/10.1007/BF00189886) (1993).
- Zipser, E. J. and Liu, C., Extreme Convection vs. Extreme Rainfall: a Global View, *Current Climate Change Reports*, **7**(4), 121–130 (2021).